

Dynamics and Optimal Control of Self-Sustained Instabilities in Laminar and Turbulent Swirling Flows: Application to the Part Load Vortex Rope in Francis Turbines

THÈSE N° 8363 (2018)

PRÉSENTÉE LE 16 FÉVRIER 2018

À LA FACULTÉ DES SCIENCES ET TECHNIQUES DE L'INGÉNIEUR
LABORATOIRE DE MACHINES HYDRAULIQUES
PROGRAMME DOCTORAL EN MÉCANIQUE

ÉCOLE POLYTECHNIQUE FÉDÉRALE DE LAUSANNE

POUR L'OBTENTION DU GRADE DE DOCTEUR ÈS SCIENCES

PAR

Simon PASCHE

acceptée sur proposition du jury:

Prof. J.-F. Molinari, président du jury
Prof. F. Avellan, Prof. F. Gallaire, directeurs de thèse
Dr K. Oberleithner, rapporteur
Dr C. Ségoufin, rapporteuse
Prof. T. Schneider, rapporteur



ÉCOLE POLYTECHNIQUE
FÉDÉRALE DE LAUSANNE

Suisse
2018

Success is not final, failure is not fatal:
it is the courage to continue that counts.
— Winston S. Churchill

To my wife, my son and my daughter...

Acknowledgements

I would like to acknowledge the members of the jury Claire Ségoufin, Kilian Oberleithner, Tobias Schneider, François Gallaire and François Avellan for their valuable time spending in reading this thesis and for their relevant questions and comments during the private defense. I also want to acknowledge Jean-François Molinari for presiding over the jury. I am also grateful to the Swiss National Science Foundation, which founded this research work.

Ce travail de doctorat n'aurait pas pu voir le jour sans la contribution du Prof. François Avellan, mon directeur de thèse et directeur du Laboratoire de Machine Hydraulique (LMH), et du Prof. François Gallaire, mon co-directeur de thèse et directeur du Laboratoire de Mécanique des Fluides et Instabilités (LFMI). Je leur exprime ma sincère gratitude pour m'avoir soutenu dès le début de ma thèse et de m'avoir pleinement intégré dans leurs deux laboratoires sans réserve. Je remercie tout particulièrement le Prof. François Avellan pour m'avoir offert la possibilité de réaliser ce travail de recherche et pour son soutien inconditionnel. Je le remercie aussi de m'avoir intégré au sein du projet européen Hyperbole dans ces débuts, qui m'a permis de rencontrer des partenaires académiques et industriels liés au secteur des turbomachines hydrauliques et aussi de m'avoir offert l'opportunité de présenter mes travaux de recherche dans des congrès internationaux. J'ai beaucoup apprécié son soutien et je lui exprime toute ma gratitude pour la confiance qu'il me porte quant à la gestion de mon travail.

Je remercie aussi particulièrement mon co-directeur de thèse, le Prof. François Gallaire qui m'a toujours soutenu et ceci depuis mon Master à l'EPFL. Ces idées percutantes ont toujours alimentés nos discussions. Ses conseils m'ont toujours été d'une grande aide. Sa passion pour la science, son énergie infinie et son envie de partager ces connaissances sont des qualités que j'ai beaucoup appréciées durant mon doctorat.

Je souhaite remercier toute l'équipe de l'atelier mécanique du LMH pour l'aide qu'ils m'ont apportée et pour les bons moments que nous avons passés ensemble. Je remercie le bureau d'étude du LMH, Vincent Berruex, Alain Renaud et Philippe Faucherre pour leur soutien technique, et le Dr. Philippe Cerrutti pour son support informatique et sans qui cette thèse n'aurait pas vu le jour à cause de la grande quantité de données que j'ai générée. Un grand merci également à toute l'équipe d'ingénieurs d'essai du LMH, dont Alberto Bullani avec qui j'ai fait mes études à l'EPFL. Je remercie aussi Isabelle Stoudmann-Schmutz pour son travail administratif et son aide efficace.

Je remercie sincèrement les doctorants et post-docs du LMH, Andreas, Arthur, Matthieu,

Acknowledgements

Martino, Marc, Phillipe K., Keita, Ebrahim, Sebastian, Siamak, Joao G.P., Joao G.B., Takashi, Audrey, Christian L., Pascal, Ali, Alexis, pour leur discussions et les parties de volley inoubliable. Je tiens à remercier particulièrement Christian V. pour m'avoir aidé dans les débuts de ma thèse et pour avoir concocté des mets dignes d'un chef étoilé à quelques pauses de midi; Loïc A. avec qui j'ai partagé des jolis moments d'escalade et d'évasions intellectuelles au sujet de la montagne; Elena V. et Outi S. pour notre aventure en terre Américaine lors de la conférence APS DFD à Portland; Je souhaite à toutes ces personnes plein de succès pour leurs carrières et je souhaite aussi bonne chance pour leurs thèses à toutes les personnes concernées.

I would like to thanks Prof. Tobias Schneider, head director of the laboratory of Emergent Complexity in Physical Systems, ECPS, for our interesting discussions, his good humor and for our nice moments talking about the village of Chateau d'Oex. I am also grateful to the ECPS team.

Je remercie aussi toute l'équipe de Power Vision Engineering, dont Dr. C. Nicolet, Dr. S. Alligné et toute l'équipe de la HES de Sion, dont Prof. C. Münch-Alligné, Dr. V. Hasmatuchi, Dr. J. Decaix pour les bons moments passés ensemble.

Je souhaite aussi remercier sincèrement l'équipe du LFMI, Francesco, Gioele, Giacomo, Isha, Vladislav, Lailai, Nicolas, Edouard, Laura, Mathias N., Andrea, Gaëtan, Mathias B., Lorenzo, Eunok pour les discussions, les bons moments passer ensemble, les diners au bord du lac et surtout pour m'avoir accueilli à bras ouvert au sein de ce laboratoire. Je remercie particulièrement Francesco, Goele, Giacomo pour notre incroyable excursion en Andalousie lors de la conférence EFMCI1. Je souhaite bonne chance à Isha, Giacomo et Gioele pour vos thèses et je souhaite également à tous les autres plein de succès pour vos carrières respectives. Je remercie aussi Petra Erika Bendel et Nicolas Borboën pour leurs supports administratif et informatique. Je remercie aussi la Prof. Elise Lorenceau pour nos discussions lors de son séjour au LFMI.

En tout cas, j'aimerais vous dire que j'ai eu énormément de plaisir et de chance de tous vous côtoyer!!!

Je remercie particulièrement mes parents et mes soeurs qui m'ont soutenu et encouragé lors de ces années d'études et qui me soutiendront toujours. Je remercie aussi ma belle-famille pour sa présence et pour sa bienveillance.

Je remercie tout particulièrement mon épouse qui m'a soutenu et m'a donné la force de réaliser ce travail de doctorat. Son courage et sa patience m'ont été d'une grande aide. Et pour finir, Un énorme merci à mes enfants qui m'apportent une joie immense chaque jour grâce à leurs sourires et leurs énergies infinies.

Lausanne, le 7 Décembre 2017

S. Pasche

Abstract

The current energetic transition planned by the European commission targets to reduce the greenhouse gas emission level to 80% below 1990 at the time horizon of 2050. Electric energy is therefore encouraged as main driving force, which in fact promotes the development of renewable energy sources, such as photovoltaic and wind energy, due to their large and imminent potential. The growing contribution of these energy sources on the power distribution and transmission system can jeopardize the stability of the electric grid due to their intermittent nature, which are strongly correlated to the weather conditions and impact therefore randomly the balance of the electric consumption and production. In this context, hydropower plays an important role and will increasingly do so, on one hand, to contribute to renewable energy production and, on the other hand, to preserve the grid stability through the provision of further advanced system services to mitigate power fluctuations.

The overarching objective of this research work is, as a result, the enhancement of hydropower plant value by extending the operating range of the most worldwide and powerful generating units: the Francis turbine, while improving their long-term availability. Off-design operating conditions of Francis turbines are, however, hindered by large pressure fluctuations, which causes risks of operating instability, and, fatigue and resonance of the mechanical structures. These pressure fluctuations are induced by the cavitation vortex rope, which develops as a single helical precessing vortex inside the turbine draft tube at part load regime. The control of this part load vortex rope is therefore addressed in the present work using optimal fluid flow control technique, based on the hydrodynamic instability properties of draft tube flow field.

The control strategy adopted is first developed on an academic benchmark flow, the spiral vortex breakdown to assess the feasibility and the validity of the approach. The stabilization of the flow is targeted by reducing the most unstable eigenvalue growth rate exhibited by global stability analysis. Stability analysis distinguishes two cases: base flow stability analysis, which correctly predicts the exponential growth of disturbances close to the instability threshold and mean flow stability analysis, which correctly predicts the frequency of the nonlinear dynamical system further away from the threshold. This fact is confirmed for the case of the spiral vortex breakdown and the stabilization of the eigenvalue growth rate of the mean flow is successfully achieved. This result emphasizes the physical significance and practical usefulness of mean flow stability analysis and related optimal control strategies.

Nonlinear interactions of purely hydrodynamic instabilities are also investigated in this re-

Abstract

search work by direct numerical flow simulations of the spiral vortex breakdown for a fixed swirl number $S = 1.095$. A Ruelle-Takens-Newhouse scenario is identified and leads to the onset of chaos as the Reynolds number increases to $Re = 220$. The mechanism leading to this route to chaos is supported by studying the emergence of self-sustained instabilities in this flow, which is provided by global stability analysis.

The transposition of the idealized uncluttered theoretical framework of fundamental research at low Reynolds number $Re = O(10^2)$ is then accomplished to include the inherent complexity of industrial design in our approach, embedding in particular turbulence modeling to reach high Reynolds number flows around $Re = O(10^6)$. Global stability analysis of the mean turbulent flow of the Francis turbines draft tube flow is performed including turbulent eddy viscosity and interprets the part load vortex rope as an inviscid global unstable eigenmode. In close resemblance to spiral vortex breakdown, a single-helix self-sustained disturbance develops around the time-averaged flow field and grows in time to finally form the vortex rope. The frequency and the structure of this unstable linear disturbance are found in good agreement with respect to the 3-D numerical flow simulations.

The identification of the part load vortex rope as a self-sustained instability has allowed us to investigate the origin of the synchronous pressure wave in elbow draft tubes. An asymptotic expansion around the mean turbulent flow, constituted by a domain perturbation method and a global stability analysis, shows that the mode of the part load vortex rope and the mode of the wall disturbance interact and produce an axisymmetric pulsating force at the next order composed of their intercrossed Reynolds stresses, exciting therefore the synchronous wave at the frequency of the vortex rope.

Based on the hydrodynamic instability properties of the part load vortex rope, the predictive control of this vortex is performed by targeting the most unstable eigenvalue growth rate of the draft tube mean turbulent flow. An optimal force distribution is determined, which successfully quenches the vortex rope and sketches the design of a realistic control appendage. This result brings a promising solution to control the part load vortex rope and to increase the operation flexibility of Francis turbines.

This research work, based on the control and the study of self-sustained instabilities, contributes to explaining fundamental issues in hydraulic turbomachines and the transition to turbulence in open swirling flows.

Key words: Francis turbines, Chaos, Part load vortex rope, Pressure fluctuation, Optimal fluid flow control, Spiral vortex breakdown, Hydrodynamic instability, Turbulent swirling flow, Nonlinear dynamics

Résumé

L'actuelle transition énergétique planifiée par la commission Européenne a pour objectif de réduire le niveau d'émission de gaz à effet de serre à un taux de 80% au-dessous du niveau de 1990, d'ici à l'année 2050. L'énergie électrique est ainsi encouragée comme force motrice principale, qui de ce fait promeut le développement des énergies renouvelables, telles que l'énergie photovoltaïque et éolienne en raison de leurs forts potentiels disponibles. La contribution croissante de ces énergies dans le système de distribution et de transmission de puissance peut compromettre la stabilité du réseau électrique à cause de leurs intermittences, qui sont fortement corrélées aux conditions météorologiques et impactent ainsi aléatoirement l'équilibre entre la consommation électrique et la production électrique. Dans ce contexte, l'hydroélectricité joue un rôle prépondérant, en contribuant d'une part à la production d'énergie renouvelable et en préservant d'autre part la stabilité du réseau, maintenue par des systèmes de contrôle avancé atténuant les fluctuations de puissances électriques.

L'objectif final de ce travail de recherche est d'améliorer la contribution des centrales hydroélectriques en augmentant la plage de fonctionnement de la turbine la plus répandue au monde et la plus puissante : la turbine Francis, tout en garantissant la longévité de ces centrales. Les turbines Francis opérant hors conditions nominales sont néanmoins sujettes à de fortes fluctuations de pression qui induisent des risques d'instabilité de fonctionnement ainsi que de résonance et fatigue de la structure mécanique. Ces fluctuations de pression sont principalement produites par la torche de cavitation qui, à charge partielle, est caractérisée par un tourbillon à simple hélice ayant un mouvement de précession dans le diffuseur de la turbine. Le contrôle de cette torche de charge partielle est ainsi étudié dans le présent travail en utilisant des techniques issues du contrôle optimal des écoulements fluides et basées sur les propriétés d'instabilités hydrodynamiques du champ de vitesse dans l'aspirateur de la turbine.

La stratégie de contrôle adoptée est premièrement développée sur un écoulement académique de référence, soit l'éclatement tourbillonnaire spiralé, pour évaluer la faisabilité et la validité de l'approche. La stabilisation de cet écoulement est recherchée en réduisant le taux de croissance de la valeur propre la plus instable déterminée par une analyse de stabilité globale. L'analyse de stabilité distingue deux cas : celui de la stabilité autour de l'écoulement de base qui prédit correctement la croissance exponentielle de perturbations proche du seuil de cette instabilité, et celui de la stabilité autour de l'écoulement moyen qui prédit correctement la fréquence de la dynamique du système non-linéaire plus loin de son seuil. Ce fait est vérifié

dans le cas de l'éclatement tourbillonnaire spiralé où la stabilisation du taux de croissance de la valeur propre originaire de l'écoulement moyen est atteinte avec succès. Ce résultat souligne la signification physique et l'utilité pratique du critère utilisé, à savoir celui du taux de croissance de la valeur propre issue de l'écoulement moyen, et de la stratégie de contrôle associée.

Les interactions non-linéaires d'instabilités purement hydrodynamiques sont aussi étudiées dans ce travail de recherche par la simulation directe des écoulements de l'éclatement tourbillonnaire spiralé à un nombre de swirl fixé à $S = 1.095$. Un scénario de Ruelle-Takens-Newhouse est identifié et met en évidence l'apparition du chaos lorsque le nombre de Reynolds croît jusqu'à la valeur de $Re = 220$. Le mécanisme conduisant à ce chaos est confirmé par l'étude de l'émergence d'instabilités auto-entretenues dans cet écoulement qui est fourni par l'analyse de stabilité globale.

La transposition du cadre théorique idéalisé et épuré de la recherche fondamentale à bas nombre de Reynolds $Re = O(10^2)$ est ensuite accomplie dans notre approche pour inclure la complexité intrinsèque des configurations industrielles, en intégrant en particulier la modélisation de la turbulence pour atteindre des écoulements à haut nombre de Reynolds autour de $Re = O(10^6)$. L'analyse de stabilité globale de l'écoulement turbulent dans le diffuseur de la turbine Francis moyenné en temps est réalisée en incluant la viscosité turbulente des tourbillons et interprète la torche à charge partielle comme un mode propre globalement instable. De manière similaire à l'éclatement tourbillonnaire spiralé, l'instabilité auto-entretenu à une seule hélice se développe autour du champ de vitesse moyenné en temps et évolue pour finalement former la torche. La valeur de la fréquence et la structure de cette perturbation linéaire instable se trouvent en bon accord avec les simulations numériques 3-D des écoulements.

L'identification de la torche à charge partielle comme une source d'instabilité auto-entretenu nous a permis d'investiguer l'origine de l'onde de pression synchrone dans les aspirateurs coulés. Un développement asymptotique autour de l'écoulement turbulent moyenné en temps, constitué d'une méthode de perturbation de domaine et d'une analyse de stabilité globale, montre l'interaction du mode de la torche à charge partielle et de celui de la perturbation de la paroi produisant une force pulsante axisymétrique à l'ordre suivant. Cette force est composée de la contraintes de Reynolds entrecroisées de ces modes, excitant ainsi l'onde synchrone à la fréquence de la torche.

Par la suite, le contrôle prédictif de ce tourbillon, basé sur les propriétés des instabilités hydrodynamiques de la torche à charge partielle, est réalisé en ciblant le taux de croissance de la valeur propre la plus instable provenant de l'écoulement turbulent moyenné en temps. Cette méthode a permis de déterminer la force distribuée optimale qui supprime la torche et dessine le design d'un réel appendice de contrôle. Ce résultat apporte la solution la plus favorable pour contrôler la torche de charge partielle et aussi pour augmenter la flexibilité d'opération des turbines Francis.

Ce travail de recherche, basé sur le contrôle et l'étude des instabilités auto-entretenues contri-

bue à l'explication des problèmes fondamentaux des machines hydrauliques et de la transition à la turbulence des écoulements tournants dans un domaine semi-infini.

Mots clefs : Turbines Francis, chaos, torche à charge partielle, fluctuation de pression, control optimal des écoulements fluides, éclatement tourbillonnaire spiralé, instabilité hydrodynamique, écoulement tournant turbulent, dynamique non-linéaire.

Contents

Acknowledgements	i
Abstract (English/Français)	iii
List of figures	xiii
List of tables	xxi
Nomenclature	xxiii
1 Introduction	1
1.1 Present work	12
1.2 Outline	13
2 Stability analysis and predictive control of spiral vortex breakdown	15
<i>PAPER: Predictive control of spiral vortex breakdown</i>	15
2.1 Introduction	16
2.2 Flow configuration	20
2.2.1 Governing equations	20
2.2.2 Direct numerical flow simulation	21
2.2.3 Axisymmetric flow	22
2.2.4 Global stability analysis	23
2.3 Flow dynamics and stability analyses	24
2.3.1 Three dimensional flow	24
2.3.2 Axisymmetric flow	26
2.3.3 Global stability analysis	27
2.4 Optimal control: flow stabilization and flow manipulation controls	29
2.4.1 Optimal control theory	29
2.4.2 Minimization and numerical methods	31
2.5 Flow control results	31
2.5.1 Base flow manipulation control at $Re = 180$	31
2.5.2 Base flow stabilization control at $Re = 180$	32
2.5.3 Mean flow stabilization at $Re = 180$	34
2.5.4 Mean flow stabilization at $Re = 300$	36
2.6 Discussion & Conclusion	36

Contents

2.7	Appendix: Validation and convergence studies	39
2.7.1	Validation of the 3-D DNS	39
2.7.2	Eigenvalue convergence of the base flow	40
2.7.3	Eigenvalue convergence of the mean flow	40
2.8	Appendix: Optimal control problem	40
2.8.1	Optimal control theory	40
2.8.2	Validation of the optimal control problem	45
2.9	Appendix: Boundary control	46
3	Stability analysis of mean turbulent swirling flows at $Re = O(10^6)$: Application to the Francis turbine part load vortex rope	49
	<i>PAPER: Part Load Vortex Rope as a Global Unstable Mode</i>	49
3.1	Introduction	50
3.2	Problem formulation	53
3.3	Numerical tools	54
3.3.1	3-D flow field	54
3.3.2	2-D global linear stability analysis	55
3.4	3-D flow fields	57
3.5	Time averaged flow field	60
3.6	Global Stability Analysis	63
3.6.1	Frequency prediction	63
3.6.2	Turbulence effects	64
3.6.3	Eigenmodes	64
3.7	Discussion & Conclusion	65
4	Optimal control of self-sustained instabilities in turbulent swirling flows: Application to the Francis turbine part load vortex rope	69
	<i>PAPER: Predictive control of part load vortex rope in Francis turbines</i>	69
4.1	Introduction	70
4.2	Flow configuration	73
4.3	Theoretical framework	73
4.4	Numerical methods	76
4.4.1	Three-dimensional numerical flow simulations	76
4.4.2	Minimization problem	77
4.5	Results	77
4.5.1	Optimal control of the part load vortex rope	77
4.5.2	Flow control in reduced scale model geometry	80
4.6	Conclusion	83
4.7	Appendix	84
4.7.1	Optimal control	84
4.7.2	Linear sensitivity-based finite amplitude control	86
4.8	Discussion	88

5	Pressure surge and synchronous pressure fluctuations in Francis turbines	89
	<i>PAPER: Origin of the synchronous pressure fluctuations in the draft tube of Francis turbines operating at part load conditions</i>	89
5.1	Introduction	90
5.2	Methodology	93
5.3	Numerical methods	95
5.3.1	Three dimensional flow field	95
5.3.2	Fourier series analysis	95
5.3.3	Asymptotic expansion	97
5.4	Results	102
5.4.1	Fourier series analysis	102
5.4.2	Asymptotic expansion	109
5.5	Conclusion & Discussion	112
5.6	Appendix	113
5.6.1	Two dimensional axisymmetric computational domain	113
5.6.2	Asymptotic expansion complementary equations	113
6	Nonlinear interaction of self-sustained instabilities in laminar swirling flows: Route to chaos	115
	<i>PAPER: Onset of chaos in helical vortex breakdown at low Reynolds number</i>	115
6.1	Introduction	116
6.2	Flow configuration	118
6.3	Numerical methods	119
6.3.1	Direct numerical flow simulations	119
6.3.2	Temporal-azimuthal Fourier decomposition	120
6.3.3	Global stability analysis	121
6.4	Instantaneous flow	122
6.5	Bifurcation analysis	124
6.6	Nonlinear time series analysis	125
6.6.1	Nonlinear time series	125
6.6.2	Sensitivity to initial disturbance	127
6.6.3	Attractor cross sections	128
6.6.4	Amplitude Fourier spectrum	130
6.7	Mode interactions	134
6.7.1	Stability analysis	135
6.7.2	Temporal-azimuthal Fourier series cascade	136
6.7.3	Temporal-azimuthal Fourier series modes	138
6.8	Conclusions	142
6.9	Appendix	144
6.9.1	Validation of the 3D DNS	144
6.9.2	Frequency validation	146

Contents

7 Conclusions & Perspectives	147
7.1 Conclusions	147
7.2 Perspectives	150
Bibliography	164
Curriculum Vitae	165

List of Figures

1.1	Reduce scale FLINDT Francis turbine (a) and section cut (b).	2
1.2	Francis turbine runner geometry as a function a the specific speed v (Häckert [1]).	3
1.3	Efficiency hillchart η of a Francis turbine as a function of the energy coefficient ψ , the flow coefficient ϕ and the guide vane opening GVO (a) and typipcal cavitation regime (b), see Franck et al. [2].	4
1.4	Inlet and outlet velocity triangle relation of a runner at the best efficiency point (BEP), at part load operating condition and full load operating condition and its assocaited vortex rope.	5
1.5	Flow oscillator example, the Von-Karman vortex street (a) and flow amplifier example, jet flow (b), see Van Dyke [3].	7
1.6	Space-time evolution of a disturbance located close to $X = 0$ at time $t = 0$, from a base state with positive advection. (a) stable base state, (b) convectively unstable base state, (c) absolutely unstable base state (see Charru [4]).	8
1.7	Stability analysis performed by Barkley [5] around the base and mean clinder wake flow at $Re = 100$. (a) Instantaneous vorticity, (b) base flow, (c) mean flow, (d) frequency of the leading eigenmode, (e) growth rate of the leading eigenmode.	9
1.8	Variations of the growth rate (a) as a function of the location of the steady force. Results are given for the critical Reynolds number $Re = 46.8$ performed by Marquet et al [6]. (b) Results of passive control by Stykowski & Sreenivasan [7]. A control cylinder 10 times smaller than the main cylinder is placed at various locations of the flow. For each location of the control cylinder and for various Reynolds numbers, the growth rate of the perturbations is measured. Contours where the growth rate is nul are represented for each Reynolds number.	10
2.1	Three-dimensional schematic of the flow configuration.	21
2.2	Iso-surfaces of axial vorticity contour of the 3-D DNS flow solution for (a) $Re = 180$ and (b) $Re = 300$, for $S = 1.095$	24
2.3	Discrete Fourier amplitude spectrum of the time signal of the 3-D DNS of the radial velocity component located at $(R, \theta, Z) = (0.1, 0.0, 5.0)$ for $Re = 180$ and $Re = 300$, for $S = 1.095$	25

List of Figures

2.4	Time averaged solution of the 3-D Navier Stokes equations, $\bar{\mathbf{C}}$, for $S = 1.095$ and $Re = 180$ (a) and $Re = 300$ (b). The upper part of the graph shows the tangential velocity component and on the lower part, the streamsurfaces colored by the magnitude of the axial velocity component.	26
2.5	Solution of the steady axisymmetric Navier Stokes equations, \mathbf{C}_B , for $S = 1.095$ and $Re = 180$ (a) and $Re = 300$ (b). The upper part of the graph shows the tangential velocity component and on the lower part, the streamsurfaces colored by the magnitude of the axial velocity component.	26
2.6	Eigenvalue spectrums of the global linear stability of mode $m = 1$ about the base (a) and mean (b) flow at $Re = 300$ and $S = 1.095$. Unstable eigenvalues are labeled respectively B_1, B_2, B_3 and M_1 and M_2	27
2.7	Growth rate and angular frequency of the global linear stability of the mean, M_1, M_2 and base flow, B_1, B_2, B_3, B_4 , for azimuthal wave number $m = 1$ compared to the 3-D angular frequency from the DNS, computed by discrete Fourier transform at location $(R, \theta, Z) = (0.1, 0.0, 5.0)$	28
2.8	Navier Stokes solutions for the base flow manipulation control at $Re = 180$ (b) and the associated volume force (a) at the minimum of the functional \mathcal{J}_{Manip}	32
2.9	Base flow dominant growth rate normalized by the most unstable uncontrolled eigenvalue at $Re = 180$ as a function of the norm of the control (a) and of the angular frequency of the mode (b) for the "flow manipulation control" (blue solid curve) and "base flow stabilization control" (red solid curve), and the "linear sensitivity-based finite amplitude control" (red dashed curve).	33
2.10	Optimal "base flow stabilization control" force (a) and associated flow solution (b) at $Re = 180$ and $S = 1.095$	33
2.11	Suboptimal "linear sensitivity-based finite amplitude control" (a) and associated flow solution (b) at $Re = 180$ and $S = 1.095$	33
2.12	Mean flow dominant growth rate, normalized by the most unstable uncontrolled mean flow eigenvalue at $Re = 180$ (red curves) and $Re = 300$ (blue curves) as a function of the norm of the control (a) and of the angular frequency of the mode (b) for the nonlinear mean flow stabilization (solid curves) and the "linear sensitivity-based finite amplitude control" (dashed curves).	35
2.13	Time averaged 3-D Navier Stokes solution of the "mean flow stabilization control" (b) and the related force applied (a) for $Re = 180$ at convergence.	35
2.14	Suboptimal "linear sensitivity-based finite amplitude control" about the mean flow at $Re = 180$ (a) and $Re = 300$ (b) for a swirl number of $S = 1.095$	35
2.15	Time averaged 3-D Navier Stokes solution of the mean flow stabilization control (b) and the related force applied (a) for $Re = 300$ at convergence.	36
2.16	3-D Navier Stokes vorticity of the optimal mean flow stabilization control solution for $Re = 180$ (a) and $Re = 300$ (b). These 3D-flows are steady solutions and they correspond to the mean flows (and therefore base) reported in fig. 2.13 and 2.15.	37
2.17	Objective function evolution as a function of iteration steps and normalized error.	45

2.18	Dominant growth rate as a function of the norm of the control (a) and of the angular frequency of the mode (b) for the "flow manipulation control".	45
2.19	Dominant growth rate as a function of the norm of the control (a) and of the angular frequency of the mode (b) for different minimization algorithms.	46
2.20	Optimal inlet velocity profile to stabilize the spiral vortex breakdown at a Reynolds value of $Re = 180$, determined by controlling the eigenvalue growth rate from the base flow (a) and the associated flow distribution (b).	47
2.21	Base flow dominant growth rate normalized by the most unstable uncontrolled eigenvalue at $Re = 180$ as a function of the norm of the control (a) and of the angular frequency of the mode (b) for the "flow manipulation control" (blue solid curve), the "base flow stabilization distributed control" (red solid curve), the "linear sensitivity-based finite amplitude distributed control" (red dashed curve), and the "base flow stabilization inlet control" (yellow solid curve).	48
3.1	Cross section of the FLINDT geometry with the location of the section 1.3 and 1.75 and their cross planes where pressure sensors are located.	54
3.2	Phase averaged of the wall pressure signals at section 1.3 (a) and 1.75 (b) at the sensor 1,2,3 and 4 of the experimental data [8] and the present 3-D numerical flow simulation of the original elbow.	58
3.3	Time averaged velocity profile for the axial and tangential component at the center line of sections 1.3 (a), (c) and 1.75 (b), (d) for the original and Moody draft tube of the present 3-D numerical flow simulations and the LDV measurements [9].	59
3.4	Vortex rope appearing in the original draft tube (a) and in the Moody draft tube (b), highlighted by a blue iso-pressure and the corresponding instantaneous axial velocity field on the ZX-cross section.	60
3.5	Time averaged axial velocity field of the vortex rope (a), where the solid black curve is the iso-contour $\bar{C}_Z = 0$. Zoom on the recirculation region at the tip of the runner cone (b).	61
3.6	Velocity profiles of the time averaged flow field of the Moody draft tube for different location along the cone, (a) just after the runner, (b) at section 1.3 and (c) between section 1.3 and 1.75.	61
3.7	Time averaged turbulent Reynolds number used for the stability analysis.	62
3.8	Eigenvalue spectra of the vortex rope for azimuthal wave number (a) $m = 0$, (b) $m = 2$ and (c) $m = 1$ with standard deviation of the eigenvalues with respect to the mean flow resolution, highlighted by error bars.	63
3.9	Single unstable eigenvalue computed with the spatially varying eddy viscosity (dash line) and variation of the unstable eigenvalue (circle) with respect to the turbulent Reynolds number $Re_t = 140 - 30'000$ when frozen approach is used, the pulsation (a) and the growth rate (b).	64

List of Figures

3.10	Three dimensional reconstruction of the axial velocity field for the unstable eigenmode $\omega = 1.43 - 0.20i$, $m = 1$ (a) and the 3-D axial velocity disturbance from the 3-D numerical flow simulation (b).	65
4.1	Reduce scale model of the FLINDT Francis turbine (a), pressure sensor location (b), the original elbow draft tube (c), and the axisymmetric Moody type draft tube used to compute the minimization algorithm (d).	74
4.2	Schematic of the minimization algorithm for the mean turbulent flow stabilization.	75
4.3	Uncontrolled (a) and controlled (b) axial flow solutions carried out by minimizing the dominant unstable eigenmode of the mean flow, superimposed with a pressure iso-contour ($C_p = -4.1$) materializing the part load vortex rope.	78
4.4	Influence of the control norm on the peak-to-peak pressure coefficient amplitude (a) and growth rate normalized by uncontrolled dominant eigenvalue (b) during the minimization procedure. Each symbol corresponds to an iteration.	79
4.5	Eigenvalue spectrum of azimuthal wavenumber $m = 1$ from the mean turbulent flow of the initial iteration (a), the penultimate iteration (b) and the ultimate iteration (c). The symbol (*) represents the direct eigenvalue from eqn. (4.7) and the symbol (o) represents the complex conjugate adjoint eigenvalue from eqn. (4.8), only displayed in subfigure (a)	79
4.6	Radial (a) and axial (b) volume force obtained by minimizing the dominant growth rate of the mean turbulent flow that stabilizes the part load vortex rope.	81
4.7	Monitored coefficient pressure on section S1.3 at the sensor location 1, 2, 3, 4, during the transient control of the part load vortex rope in the elbow geometry.	82
4.8	Temporal snapshots of the axial velocity and the pressure iso-contour of value $C_p = -4.1$, exhibiting the part load vortex rope quenched by the 2-D axisymmetric optimal force obtained by minimizing eqn. (4.2).	82
4.9	Surface specific energy of static E_s , kinetic E_k and total E_{tot} pressures on cross sections along the draft tube curvilinear distance normalized by the kinetic specific energy at the draft tube inlet.	83
4.10	Influence of the control norm on the peak-to-peak pressure coefficient amplitude for the "mean turbulent flow stabilization control" (solid curves) and the "linear sensitivity-based finite amplitude control" (dash curves) at the monitoring points of section 1.3 (black curves) and the section 1.75 (gray curves) for the axisymmetric draft tube. Each symbol corresponds to an iteration.	86
4.11	Controlled axial flow solutions of the axisymmetric draft tube (a) and elbow draft tube (b) carried out by the "linear sensitivity-based finite amplitude control", superimposed with a pressure iso-contour ($C_p = -4.1$) materializing the part load vortex rope.	87
4.12	Radial (a) and axial (b) volume force obtained from the "linear sensitivity-based finite amplitude control" that stabilizes the part load vortex rope.	88

5.1	Flindt reduced scale physical CAO model (a) with the wall pressure sensor at two different cross section S1.3 and S1.75 (b), and the different hydraulic draft tube domain investigated by numerical flow simulations, (c) the original elbow draft tube, (d) the axisymmetric Moody type draft tube, (e) the disturbed Moody type draft tube case I and (f) the disturbed Moody type draft tube case II.	94
5.2	Methodology applied to the vortex rope to investigate the development of the synchronous pressure, left branch the nonlinear analysis of the axisymmetric Moody draft tube, right branch analysis of the disturbed Moody draft tube, in red the asymptotic analysis and the curved gray arrows show the flow field comparison carried out in the present study. The boxes represent the computational operations.	100
5.3	Boundary condition applied for domain disturbance using the matching prefactor γ on the associated Fourier mode. The disturbance of the Fourier decomposition domain is enlarged to help understanding the analysis.	102
5.4	Pressure isocontour of the vortex rope ($Cp = -4.1$) and axial velocity distribution on the YZ plane for the instantaneous URANS solution in the elbow draft tube .	103
5.5	convective part (dashed curve) and synchronous part (solid curve) of the wall pressure measurements at the sensor $N^\circ 1,2,3,4$ on the cross section S1.3 for elbow (a), disturbed case I (c), axisymmetric (e) draft tube and at the cross section S1.75 for elbow (b), disturbed case I (d), axisymmetric (f) draft tube. . .	104
5.6	Volume integral of kinetic energy of temporal-azimuthal ($m-q$) Fourier modes of the disturbed Moody draft tube case I (a) and the axisymmetric Moody draft tube (b). The energy of the diagonal terms is scaled by $1/4$	105
5.7	Fourier series decomposition of the disturbed Moody draft tube case I and their related 3-D reconstruction of axial and pressure components for the vortex rope Fourier mode $m = 1, q = 1$, (a) and (b), the stationary wall disturbance Fourier mode $m = 1, q = 0$, (c) and (d), and the synchronous Fourier mode $m = 0, q = 1$, (e) and (f) at an arbitrary chosen time t	107
5.8	Time evolution of the vortex rope materialized by a pressure iso-contour of value $Cp = -4.1$ (a) and associated instantaneous pressure field of the azimuthal Fourier series decomposition for the vortex rope disturbance $m = 1, q = 1$ left (b) and the synchronous pressure $m = 0, q = 1$ right (b).	108
5.9	Kinetic and potential energy per unit length of the synchronous Fourier mode as a function of Z for the disturbed Moody draft tube case II.	109
5.10	Axisymmetric turbulent eddy viscosity (a) and axisymmetric mean velocity distribution (b) where the flow is linearized around in the asymptotic expansion . .	110
5.11	Azimuthal-temporal Fourier series decomposition of the disturbed Moody type draft tube case II, compared with the asymptotic expansion for the vortex rope Fourier mode and its eigenvalue ($m = 1, q = 1$) (a) and (b), the stationary wall disturbances ($m = 1, q = 0$) (c) and (d), and the synchronous waves ($m = 0, q = 1$) (e) and (f).	111
5.12	Two dimensional axisymmetric domain used to compute the asymptotic analysis.	113

List of Figures

6.1	3D schematic of the flow configuration.	119
6.2	Time evolution of the swirling flow induced by a Grabowski and Berger vortex for a swirl number of $S = 1.095$ and a Reynolds number of $Re = 220$, materialized by axial vorticity iso-contours.	123
6.3	Bifurcation diagram of the min/max temporal series of the radial velocity C_R at $(R, \theta, Z) = (0.1, 0.0, 6.0)$ (point symbole). The instability threshold of Pasche et al. [10], at $Re = 143.5$, is illustrated as a cross symbole.	124
6.4	Discrete temporal Fourier transform of the azimuthal time serie monitored at $(R, \theta, Z) = (0.1, 0.0, 6.0)$ for a swirl number of $S = 1.095$ and several Reynolds numbers, (a) $Re = 180$, (b) $Re = 200$, (c) $Re = 205$, (d) $Re = 215$, (e) $Re = 220$, (f) $Re = 230$, (g) $Re = 250$, (h) $Re = 300$. The end of each time series use a zoomed scale.	126
6.5	Time series of the reference flow and the disturbed flow with a random noise of amplitude 10^{-8} at the initial time step at a Reynolds value of $Re = 215$ (a) and $Re = 220$ (b), at the location $(R, \theta, Z) = (0.1, 0.0, 6.0)$	127
6.6	L_2 -norm of the distance between the reference and disturbed dynamical state at the location $(R, \theta, Z) = (0.1, 0.0, 6.0)$ at a Reynolds value of $Re = 205$ (a), $Re = 215$ (b) and $Re = 220$ (c).	128
6.7	Attractor cross section of the velocity time serie at $(R, \theta, Z) = (0.1, 0.0, 6.0)$, for $C_\theta = 0.001$, a swirlnumber of $S = 1.095$ and several Reynolds numbers, (a) $Re = 180$, (b) $Re = 200$, (c) $Re = 205$, (d) $Re = 215$, (e) $Re = 220$, (f) $Re = 230$, (g) $Re = 250$, (h) $Re = 300$	129
6.8	Fast Fourier transform of the velocity time series at $(R, \theta, Z) = (0.1, 0.0, 6.0)$ for a swirl number of $S = 1.095$ and Reynolds numbers, (a, b) $Re = 180$, (c, d) $Re = 200$, (e, f) $Re = 205$, (g, h) $Re = 215$, and snapshots of the associated vorticity iso-contours.	131
6.8	Fast Fourier transform of the velocity time series at $(R, \theta, Z) = (0.1, 0.0, 6.0)$ for a swirl number of $S = 1.095$ and Reynolds numbers, (i, j) $Re = 220$, (k, l) $Re = 230$, (m, n) $Re = 250$, (o, p) $Re = 300$, and snapshots of the associated vorticity iso-contours.	132
6.9	Growth rate and angular frequency comparison of the 3D fft and the stability analysis for $m = 1$, eigemodes of azimuthal wavenumber ($m = 0, 2$) have no correlation with DNS frequencies.	135
6.10	Primary and downstream eigenmode axial velocity iso-contour at a Reynolds value of $Re = 200$	136
6.11	Temporal-azimutahl Fourier decomposition of the DNS solutions for the Reynolds value $Re = 200$ (a), $Re = 220$ (b), $Re = 230$ (c) and $Re = 250$ (d). Amplitude Fourier spectrum for $R = 0.6$ along Z location ($Z = [0.6, 2, 3, 4, 6, 8, 10, 15, 20]$) with the fifth first azimuthal wavenumber m plotted in parallel with the streamlines of the time-average flow.	137

6.12 Axial velocity iso-contour of temporal-azimuthal Fourier series modes at $Re = 200$, associated to the primary spiral at frequency f_1 (a) and the downstream spiral at frequency f_2 (b) at an arbitrary selected phase.	139
6.13 Axial velocity iso-contour of temporal-azimuthal Fourier series modes at $Re = 220$, associated to the primary spiral at frequency f_1 (a), downstream spiral at frequency f_2 (b), near-wake spiral at frequency f_3 (c) and the axisymmetric pulsation at frequency c (d) at an arbitrary selected phase.	140
6.14 Axial velocity iso-contour of temporal-azimuthal Fourier series modes at $Re = 230$, associated to the primary spiral at frequency f_1 (a), downstream spiral at frequency f_2 (b), near-wake spiral at frequency f_3 (c) and the axisymmetric pulsation at frequency c (d) at an arbitrary selected phase.	141
6.15 Axial velocity iso-contour of temporal-azimuthal Fourier series modes at $Re = 250$, associated to the primary spiral at frequency f_1 (a), downstream spiral at frequency f_2 (b), double helix first harmonic (c) (labeled a in fig. 6.8m) at an arbitrary selected phase.	142
6.16 Time series, attractor cross section and amplitude Fourier spectrum at the monitoring point $(R, \theta, Z) = (0.1, 0.0, 6.0)$ and at the Reynolds value of $Re = 220$ computed on the finer discretization M3.	145

List of Tables

2.1	Boundary conditions on the axisymmetric axis applied to the disturbances for different azimuthal wave numbers.	23
2.2	Convergence of the 3-D numerical flow simulations and eigenvalues of mean flow for $Re = 200$, $S = 1.095$	39
2.3	Eigenvalue sensitivity to the mesh configuration for $Re = 200$, $S = 1.095$	40
3.1	Boundary conditions imposed on the symmetry axis of the domain	57
3.2	Frequency of the vortex rope obtains by the FFT of the experimental data [8], CFD of the original and Moody draft tube and the present global linear stability analysis.	66
6.1	Boundary conditions on the axisymmetric axis applied to the disturbances for different azimuthal wave numbers.	121
6.2	Convergence of the 3D numerical flow simulations and eigenvalues of mean flow	145
6.3	Frequency interaction for $Re = 230$, $S = 1.095$ at $R = 0.2$, $Z = 6.0$ measured and approximated by the formulas using f_1 , f_2 , f_3 and f_4	146

Nomenclature

Acronyms

BEP	B est E fficiency P oint
CFD	C omputational F luid D ynamics
DNS	D irect N umerical S imulation
EPFL	É cole P olytechnique F édérale de L ausanne
EU	E uropean U nion
FLINDT	F low I nvestigation in D raft T ube
GVO	G uide V ane O pening
LDV	L aser D oppler V elocimetry
LFMI	L aboratory for F luid M echanic and I nstabilities
LMH	L aboratoire de M achine H ydraulique
PIV	P article I mage V elocimetry
RANS	R eynolds A veraged N avie S tokes equation
RES	R enewable e nergy s ources
rpm	r evolutions p er m inute
SAS	S cale A daptive S imulation
URANS	U nsteady R ANS

Superscripts

*	complex conjugate or optimal solution
†	adjoint
B	base flow
H	transconjugate
T	transpose
(\cdot)	ϵ power order

Subscripts

1	runner high pressure reference section
$\bar{1}$	runner low pressure reference section

Nomenclature

I	power unit high pressure reference section
\bar{I}	power unit low pressure reference section
\bar{B}	tailwater reservoir reference section
B	headwater reservoir reference section
b	blade
atm	atmospheric condition
c	convective
in	inlet
n	nominal
$P - P$	peak-to-peak
ref	reference
v	precessing vortex rope

Latin letters

X, Y, Z	Cartesian coordinates	(m)
R, θ, Z	Cylindrical coordinates	(m)
\vec{C}	absolute flow velocity vector	(m s ⁻¹)
\mathbf{C}	velocity vector	(m s ⁻¹)
C_m, C_Z	meridional (axial) velocity component	(m s ⁻¹)
C_u, C_θ	circumferential (azimuthal) velocity component	(m s ⁻¹)
C_R	radial velocity component	(m s ⁻¹)
C_Q	discharge velocity; $C_Q = Q / A$	(m s ⁻¹)
$\bar{\mathbf{C}}$	mean velocity field	(m s ⁻¹)
$\langle \mathbf{C} \rangle$	phase averaged velocity field	(m s ⁻¹)
$\tilde{\mathbf{C}}$	coherent velocity fluctuation	(m s ⁻¹)
\mathbf{C}'	turbulent velocity fluctuation	(m s ⁻¹)
\mathbf{c}	velocity eigenvector	(m s ⁻¹)
\vec{W}	relative flow velocity vector	(m s ⁻¹)
\vec{U}	peripheral runner velocity vector	(m s ⁻¹)
\mathbf{U}	state vector $\mathbf{U} = (\mathbf{C}, P)$	(m s ⁻¹)
\mathbf{u}	state eigenvector $\mathbf{u} = (\mathbf{c}, p)$	(m s ⁻¹)
$\bar{\mathbf{U}}$	mean state vector	(m s ⁻¹)
A	Area	(m ²)
D	diameter	(m)
H	head; $H = p / (\rho \cdot g) + Z + C^2 / (2 \cdot g)$	(m)
\mathcal{J}	objective function	(-)
E	specific energy; $E = g \cdot (H_I - H_{\bar{I}})$	(J kg ⁻¹)
E_k	kinetic energy	(-)
e_k	kinetic energy per unit length	(-)
E_p	potential energy	(-)
e_p	potential energy per unit length	(-)

E_S	Surface specific energy of static pressure $E_S = \int_{\Omega} P/\rho \, d\Omega$	(-)
E_k	Surface specific energy of kinetic pressure $E_k = \int_{\Omega} 0.5\mathbf{C}^2 \, d\Omega$	(-)
E_{tot}	Surface specific energy of total pressure $E_{tot} = \int_{\Omega} P/\rho + 0.5\mathbf{C}^2 \, d\Omega$	(-)
f	frequency	(Hz)
H	head; $H = p/(\rho \cdot g) + Z + C^2/(2 \cdot g)$	(m)
k	specific turbulence kinetic energy	(m ² s ⁻²)
l	length	(m)
m	azimuthal wave number	(-)
q	integer factor	(-)
\mathbf{n}	normal vector	(m)
NPSE	net Positive Suction Energy; $NPSE = gH_I - gZ_{ref} - p_v/\rho$	(J kg ⁻¹)
p_{atm}	atmospheric pressure	(Pa)
p_v	vapor pressure	(Pa)
P	pressure	(Pa)
p'	turbulent pressure fluctuation	(Pa)
\tilde{P}	coherent pressure fluctuation	(Pa)
p	pressure eigenvector	(Pa)
Q	discharge	(m ³ s ⁻¹)
R_{Ie}	reference radius	(m)
S	swirl number	(-)
S_{ij}	strain tensor	(-)
\mathbf{T}	Reynolds stresses of self-sustained instability	(m s ⁻²)
t	time	(s)
y^+	dimensionless wall distance	(-)
Z	elevation	(m)

Greek letters

α	absolute flow angle, or control weight	(°, -)
β	relative flow angle	(°)
Γ	Boundary	(-)
η	efficiency	(-)
θ	angular position	(rad)
μ	dynamic viscosity	(Pa s)
ν	kinematic viscosity	(m ² s ⁻¹)
ν_t	turbulent kinematic viscosity	(m ² s ⁻¹)
$\bar{\nu}_t$	mean turbulent kinematic viscosity	(m ² s ⁻¹)
ρ	density	(kg m ⁻³)
σ	Thoma cavitation number	(-)
τ	minimization step length	(-)

Nomenclature

ϕ	flow rate coefficient	(-)
χ	pressure recovery factor	(-)
Ψ	energy coefficient	(-)
Ω	control volume	(m ³)
Ω_a	axisymmetric control volume	(m ³)
ω	eigenvalue	(s ⁻¹)

Dimensionless number

Cp	pressure factor; $Cp = (p - \bar{p}) / (0.5\rho C^2)$	(-)
Re	Reynolds number; $Re = R_{ref}C/\nu$	(-)
Re_t	turbulent Reynolds number; $Re = R_{ref}C/\nu_t$	(-)
σ	Thoma cavitation number; $\sigma = NPSE/E$	(-)
S	Swirl number	(-)
ψ	Energy coefficient; $\psi = 2E/(\omega_n^2 R^2)$	(-)
ϕ	Flow coefficient; $\phi = Q/(\pi\omega_n R^3)$	(-)
ν	Specific speed; $\nu = \omega_n \cdot (Q_n/\pi)^{1/2} / (2E_n)^{3/4}$	(-)

Bracket notations

$\langle . \rangle$	phase averaged
$\langle ., . \rangle$	inner product $\langle a, b \rangle = \int_{\Omega} a \cdot b^* d\Omega$

Operators

L	linearized Navier Stokes operator
N	singular operator

1 Introduction

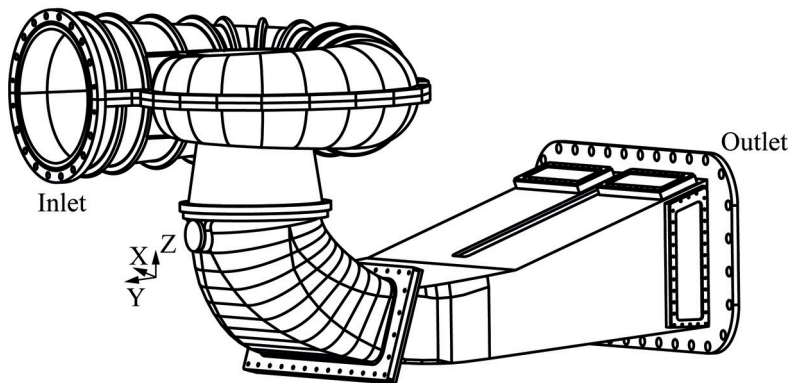
In 2050, the European commission plans to achieve actual energetic transition, which contributes in meeting the climate change challenges by moving away from the fossil fuels and by developing a competitive low-carbon economy. This transition edited as a road-map since 2009, has almost reach the first objectives established for 2020, known as the "20-20-20" targets enacted in the climate and energy package. These objectives plans:

- A 20% reduction in EU greenhouse gas emissions from 1990 levels
- Raising the share of EU energy consumption produced from renewable resources to 20%
- A 20% improvement in the EU's energy efficiency.

Future aims according to this road-map, are to target 40% reduction emissions in 2030, 60% in 2040 and finally the EU greenhouse gas emissions should be cut to 80% at least below 1990 levels at the time horizon of 2050. The action plan of these ambitious objectives are supported by two main strategies, first, the use of energy from renewable sources is promoted, and second, a broad deployment of energy efficiency initiatives and technologies in each economy branch, i.e. power generation and distribution, buildings, industry, agriculture and transport, are encouraged.

In this context, renewable energies are rising up by developing their power capacity since 2005 in Europe. This increase is mainly attributed to the photovoltaic and wind energy sources, which represents 11% and 16.7% in 2016 of the installed capacity instead of 0.3% and 6%, respectively in 2005. This impressive growth is made available by the technology development and the large potential of implementation sites of these energies compare to other renewable energies such as large hydropower, which has 120GW installed capacity in 2005 compare to 138GW in 2016 in Europe. However, to meet the 2050 objectives, an increase of hydroelectricity production is also encouraged by developing the small hydroelectricity, run-of-river hydroelectricity, the installation of new reservoirs and the enhancement of the

(a) FLINDT reduced scale physical model



(b) FLINDT reduced scale physical model YZ section

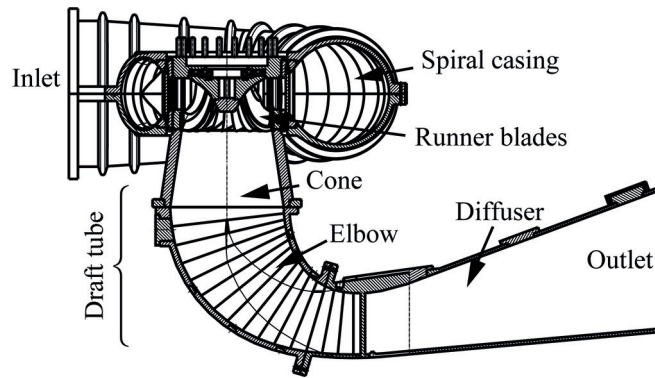


Figure 1.1 – Reduce scale FLINDT Francis turbine (a) and section cut (b).

actual reservoir capacity by removing sediment of the lake bed and increasing the height of the dams. The current trend in renewable energies will therefore continue, as expected, to reach the energy and climate objectives targeted by the European policies. While the path toward a competitive low-carbon economy seems realistic, the growing contribution from the wind and photovoltaic energy on the power distribution and transmission system can jeopardize the stability of the electric grid due to their short-time intermittent nature, which are strongly correlated to the weather conditions and impact therefore the balance of the electric consumption and production randomly.

The new power apportionment of energy sources needs first a sufficient base load production, acting as a large inertial mass to avoid voltage drop of the grid and second powerful, flexible and reactive systems to deal with the future massive intermittent renewable power production. The run-of-river hydroelectricity delivers a constant production, which accounts for the grid base load as the nuclear power plant production and becomes even more important due to the insecure future of the nuclear power, in sight of the recent catastrophe of Fukushima. The large hydroelectric turbines match the latter system characteristics which are indeed currently used to regulate the grid. Further improvements are, however, needed to continue to support the growth of intermittent renewable energies. They are provided by the electric and hydraulic

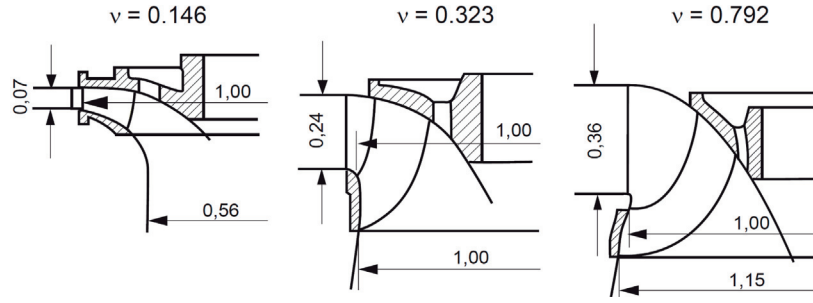


Figure 1.2 – Francis turbine runner geometry as a function of the specific speed v (Häckert [1]).

machine of these generating units with the development of variable speed generators and the extension of the hydraulic operating range. Therefore, the grid stability will be preserved by coupling the power production of high efficiency turbines to that of extremely flexible turbines in operating conditions, without forgetting pumped storage capacity, which can increase the water driving force by refilling reservoirs.

In the present manuscript, the increase of operation flexibility of the most worldwide and powerful generating units is considered i.e. Francis turbines, see fig 1.1, which represent around 60% of the actual installed capacity. Francis turbines easily modulate power generation by changing the hydraulic torque of the runner, which is prescribed by the runner blade pressure distribution and therefore controlled by the incoming flow incidence. Francis turbines are equipped with pivoting guide vanes, which are the unique regulator of the turbine and control the discharge flowing through the turbine by opening or closing them (GVO = guide vane opening) and define the flow incidence on the runner blades. In contrast, the head of the turbine is almost constant for existing installations, which is imposed by the topography of the construction site and only varies with the seasons due to the water level of the headwater reservoir. This head defines the specific energy E_n available for the turbine, which is a prerequisite to design the runner. Once the rated discharge Q_n and the angular frequency of the generator ω_n is known, the specific speed of the turbine can be computed: $v = \omega_n \cdot (Q_n/\pi)^{1/2} / (2E_n)^{3/4}$. This dimensionless number defines the geometrical characteristics of the runner design, see fig. 1.2. In a second step, this design is improved using shape optimization to achieve the highest efficiency η , around 95%, at the nominal conditions, therefore called best efficiency point (BEP). The effective efficiency of the turbine is at the end carried out by experimental measurements, which leads to the typical efficiency hillchart (see fig. 1.3a). This diagram displays the efficiency as a function of the operating conditions, it means the flow coefficient $\phi = Q/(\pi\omega_n R^3)$ (discharge), the energy coefficient $\psi = 2E/(\omega_n^2 R^2)$ (head) and the guide vane opening (GVO). As the implementation sites of hydraulic turbines are always different, each runner design is unique and leads to an unique efficiency hillchart.

While operation at the best efficiency point (BEP) is favored to monetize the machine, off-design operating conditions within a small range around the nominal discharge are acceptable to mitigate the power grid fluctuations. Further extension is however prohibited due to hazards

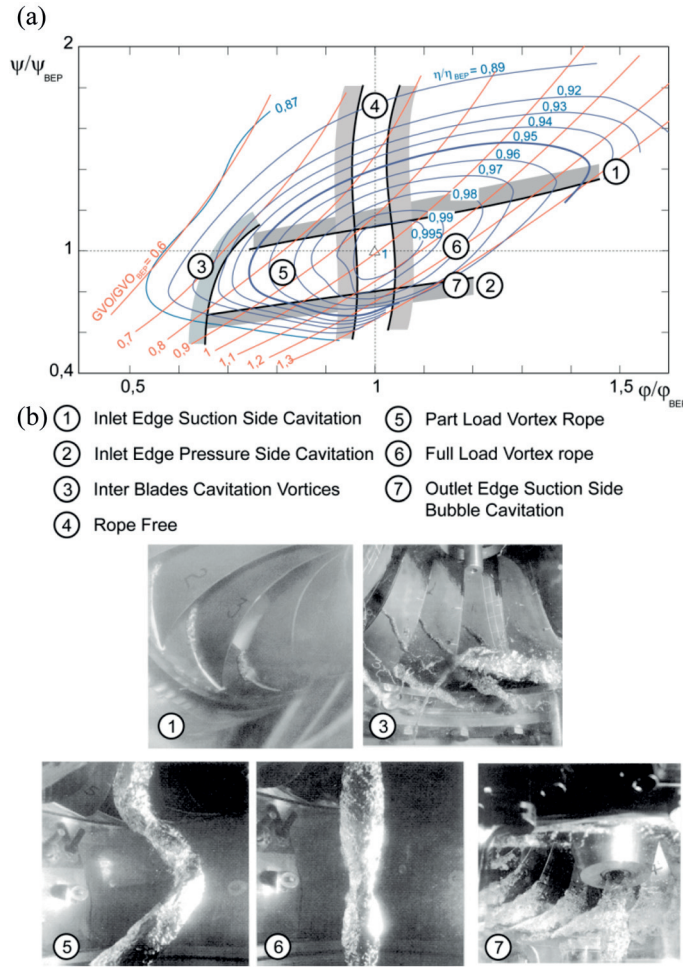


Figure 1.3 – Efficiency hillchart η of a Francis turbine as a function of the energy coefficient ψ , the flow coefficient ϕ and the guide vane opening GVO (a) and typical cavitation regime (b), see Franck et al. [2].

risks induced by operating instability and fatigue, and resonance of the mechanical structures in response to the appearance of a vortex flow in the draft tube of the turbine, which produces large pressure fluctuations. Figure 1.3(b) illustrates these vortical structures. As mentioned, when the guide vane opening (GVO) is controlled in a real turbine, which has an equivalent representation in this diagram by moving along a horizontal line centered on the best efficiency point, the vortex rope free region (labeled 4) is left to either the part load vortex rope (labeled 5) or the full load vortex rope (labeled 6 in fig. 1.3). This figure 1.3 represents also the others typical cavitation regimes, which also bound the vortex free zone along the energy coefficient direction by inlet edge suction side cavitation and outlet edge suction side bubble cavitation.

These vortex ropes appear with the residual swirling flow at the runner outlet. Such operation variations are better visualized using the flow velocity diagram, see fig. 1.4. This diagram is based on the velocity composition law that allows one to transfer the velocity vector of fluid

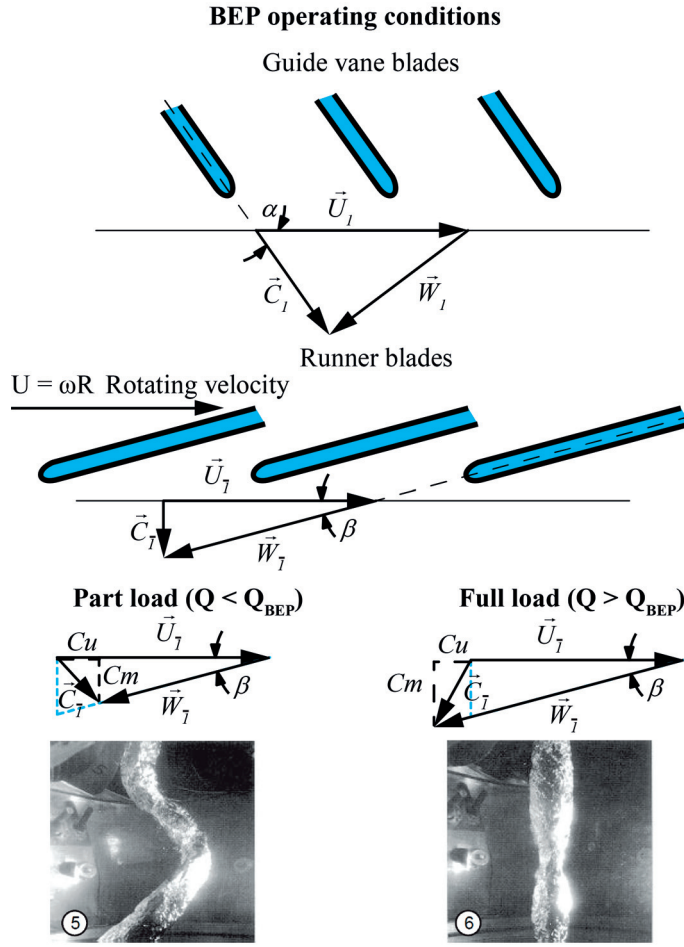


Figure 1.4 – Inlet and outlet velocity triangle relation of a runner at the best efficiency point (BEP), at part load operating condition and full load operating condition and its associated vortex rope.

particles from the stator reference frame to the rotor reference frame and vice-versa. In the hydraulic turbomachine context, the absolute velocity vector \vec{C} in the stationary reference frame is given by the guide vane opening α and the velocity of the rotating reference frame is imposed by the runner rotation $\vec{U} = R\vec{\omega}$. At the outlet of the runner the velocity vector is prescribed by the blade angle β . Since we consider incompressible fluid flow, the meridional component of the absolute velocity is obtained by dividing the discharge by the area at the runner inlet or outlet and the velocity triangle is completed using the guide vane angle α and the blade angle β . The velocity diagram results in the absolute velocity vector at the runner outlet, which give access to the flow direction in the draft tube. At the best efficiency point, the hydraulic losses are minimized and therefore the runner design should drive an axial flow in the draft tube. In contrast, at off-design operating conditions, the residual swirling flow leads to a vortex core, see fig. 1.4. More precisely, at full load regime, it means at larger discharge than the BEP, the pulsating vortex rope, which spins in the opposite direction of the runner

rotation, is observed, or at part load regime i.e. at lower discharge than the BEP, the precessing helical vortex rope, which spins temporally in the same direction of the runner rotation, is observed. The part load vortex rope is characterized by a coherent structure and a periodic frequency around 0.2 to 0.4 times the runner frequency Nishi et al. [11]. The dynamics of these vortical structures is still investigated nowadays using experimental measurements such as pressure sensor, Laser Doppler Velocimetry (LDV) and two-phase flow Particule Image Velocimetry (PIV), see Nishi et al. [12], Nishi et al [13], Nishi & Liu [14], Avellan [15], Arpe & Avellan [8], Iliescu et al. [16] and Favrel et al. [17] among others. Numerical flow simulation is also widely used to design turbines and investigate the flow distribution, see Ruprecht et al. [18], Mauri et al. [19], Paik et al. [20], Buntić et al. [21], Wang & Zhou [22], Ciocan et al. [9], Trivedi et al. [23] and Brammer et al. [24] among others.

As mentioned earlier, the vortex rope causes the onset of large pressure fluctuations at off-design operating conditions. The increase of operation flexibility of Francis turbines therefore call for advanced fluid flow control techniques to mitigate the pressure fluctuations at these operating conditions. Passive strategies were investigated such as stabilizer fins [25] or J-groove (Kurokawa et al. [26]) to decrease the residual swirl of the draft tube flow. A different blade design with shaped outlet was also studied by Brekke [27] to correcting the swirling flow at the runner outlet. Mitigation of the recirculation zone close to the runner was also attempt by using appendage at the tip of the runner cone (Qian et al. [28]). Other passive strategies, which do not require a modification of the geometry were investigated, such as constant wall blowing. A jet flow acting at the center line of the draft tube and issuing from the crown tip of the runner has successfully mitigated the pressure fluctuations over a large operating range by controlling the jet velocity around 10% to 12% of the turbine discharge (Susan-Resiga et al. [29], Zhang et al. [30] and Foroutan & Yavuzkurt [31]). Active feedback control were also investigated to mitigate the first harmonic of the part load vortex rope by injecting mass flow at the end of the draft tube cone (Blommaert et al. [32]). Despite the large number of control techniques which have been tested over the years, the best control strategy still needs to be assessed. From this perspective we therefore use an optimization technique, following the optimal control theory, to compute an optimal volume force to control the part load vortex rope.

Cavitation is usually encountered in Francis turbines, see fig. 1.3. This phase change occurs when the local pressure of the water is below the vapor pressure. Low pressure zone such as vortices or blade suction sides are, therefore, more sensitive to cavitation inception. The vapor volume fraction is highly correlated to the reference pressure of the water phase, which in our case is a function of the height from the tail-water level or atmospheric pressure to the turbine setting level. This characteristic is attributed to the Thoma cavitation dimensionless number $\sigma = NPSE/E$ (Net Positive Suction Energy divided by the specific energy of the turbine), where a low value of this number indicates a high risk of cavitation development.

Not only can cavitation induce erosion, it can also play the role of catalyst for the synchronous pressure surge effect. This critical phenomenon appears when the synchronous pressure

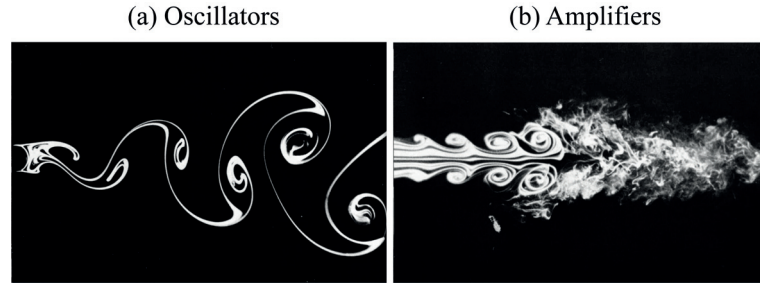


Figure 1.5 – Flow oscillator example, the Von-Karman vortex street (a) and flow amplifier example, jet flow (b), see Van Dyke [3].

fluctuations excites the natural frequency of the piping system. This frequency matching is enabled by the satisfaction of two conditions, the natural frequency of the piping system and the local wave speed are reduced as the cavitation increases inside the draft tube of the turbine (Landry et al. [33]), and second, the part load vortex rope induces a planar wave or a synchronous wave, which acts as an excitation source (Nicolet [34], Alligné et al. [35], Favrel et al. [17] and Landry et al. [36]). This planar wave can be identified by an azimuthal Fourier serie decomposition in the circular section of the draft tube, the convective wave represents therefore the non-axisymmetric coefficients of the part load vortex rope and the synchronous wave represents the temporal azimuthal-averaged variation of the state variable (Nishi et al. [12]). In this context, the characterization of the eigenfrequency of the piping system is obtained by 1-D hydroacoustic model including elastic pipe developed by Nicolet [34], based in the method of the transfer matrices (Zielke & Hack [37]). The origin and the amplitude of the synchronous pressure remains however poorly understood except the fact that it appears in elbow draft tubes (Fanelli [38] and Nishi & Liu [14]). In the present research work, the origin of the synchronous pressure wave is investigated.

The turbine fluid flow can belongs to the class of open flows characterized by fluid particles continuously entering and leaving the experimental domain, in contrast to wall enclosed flow. The periodic motion of the part load vortex rope is an archetype shared by many other open fluid flow examples: boundary layers, mixing layers, wakes, jets and Pipe flows, among many others. With respect to a bifurcation parameter, which can be the Reynolds number or the swirl number (associated to the discharge in Francis turbines $S = \int_0^R \rho C_m C_u r^2 dr / \int_0^R \rho C_m^2 r dr$ Gupta [39]), the flow, which is initially stationary at low Reynolds number or at the BEP, suddenly changes its topology as the Reynolds number or swirl number increases. This change or bifurcation takes its physical meaning by studying the development of intrinsic perturbation of the flow, i.e modal analysis and non-modal stability analysis. In real flows, fluid particles entering an experimental domain are always submitted to infinitesimal stochastic fluctuations, which in certain case can develop, supported by an amplification mechanism, to modify the flow. These mechanisms are illustrated in fig. 1.5 with two examples, the cylinder wake flow and the jet flow. The former case is defined as a flow oscillator, in which a self-sustained instability emerges and induces an intrinsic oscillating dynamics, the von

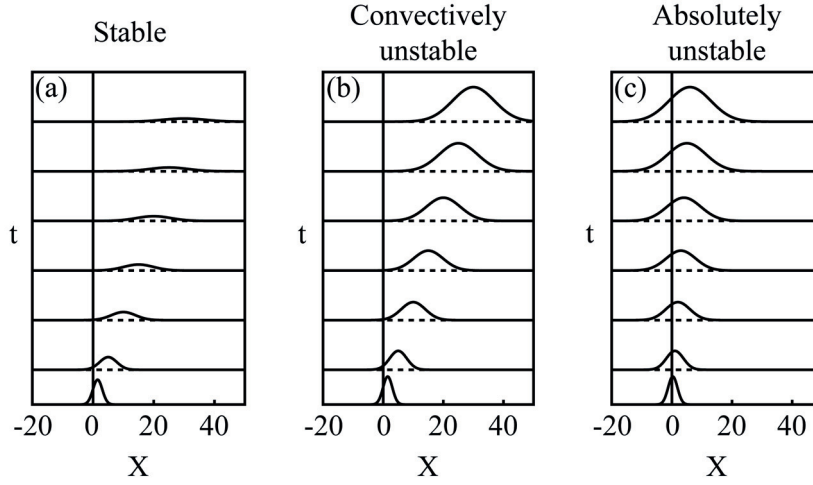


Figure 1.6 – Space-time evolution of a disturbance located close to $X = 0$ at time $t = 0$, from a base state with positive advection. (a) stable base state, (b) convectively unstable base state, (c) absolutely unstable base state (see Charru [4]).

Karman vortex street. The latter case is defined as a flow amplifier, in which a strong sensitivity to external disturbance is observed. If harmonic forcing is applied to these systems, an oscillator will typically lead to nonlinear interactions between the forcing and its natural frequency, while an amplifier will adopt the frequency imposed by the harmonic forcing with an amplified response. This amplification mechanism is due to the non-normality of the linearized evolution operator, in contrast to the development of an unstable global eigenmode of an oscillator. The non-normality corresponds to the non-orthogonal basis formed by the eigenvector space of the linearized evolution operator, see Schmid [40] and Chomaz [41]. Hence, non-normality can also produce large transient growth (Trefethen et al. [42]) due to the superposition of the eigenvectors, which described linear evolution of perturbations.

The dynamical analysis of disturbance evolution can be computed by two approaches, the local linear stability analysis or the global linear stability analysis. Both methods solve an eigenvalue problem linearized around a base state. The local framework is suitable for weakly nonparallel flows, which assume slow variation along the streamwise direction of the base state. The instability properties of the flow is therefore built as a superposition of instability waves of each station location. Locally the response of the system can exhibit three different behaviors. The flow is either linearly stable when all disturbances decay to zero as time tends to infinite, or the flow is linearly unstable and wavy perturbations in space grow exponentially in time. Two different scenarii are distinguished in the second case, the flow is either convectively unstable or absolutely unstable leading to weakly non-parallel interpretation of the differentiation of amplifier flows or oscillator flows, see fig. 1.6. Instead of considering only the temporal stability (perturbation of the form $c(R)\exp(i(kz - \omega t))$ with the axial wavenumber $k \in \mathbb{R}$ and the eigenvalue $\omega \in \mathbb{C}$) that is the case for linear stable or unstable flows, the convective/absolute properties are determined by assessing a spatio-temporal stability analysis, which consider

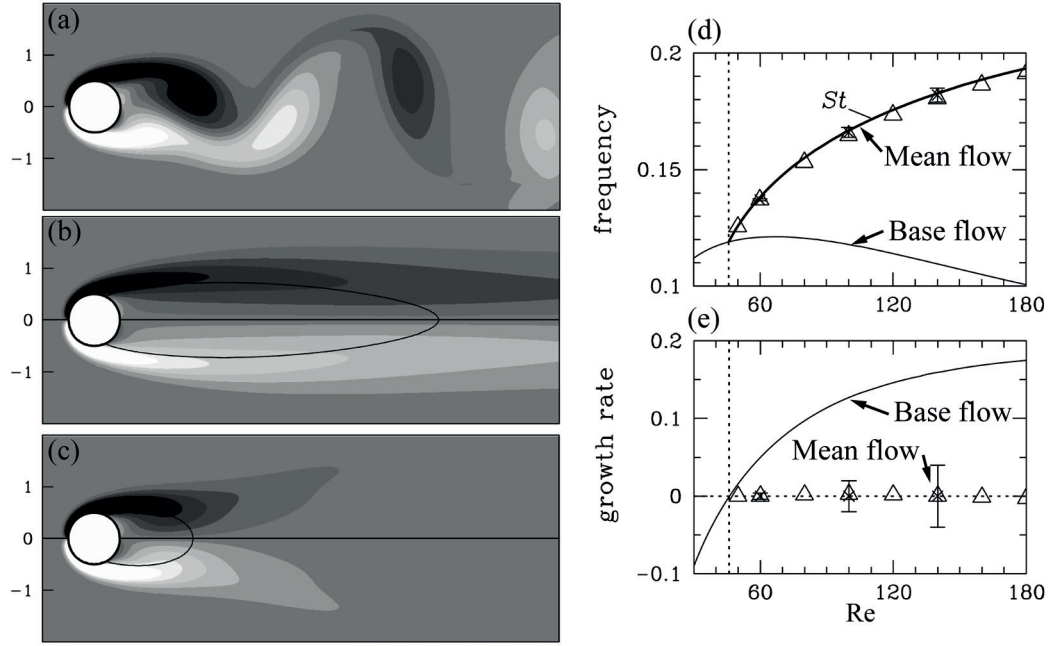


Figure 1.7 – Stability analysis performed by Barkley [5] around the base and mean clinder wake flow at $Re = 100$. (a) Instantaneous vorticity, (b) base flow, (c) mean flow, (d) frequency of the leading eigenmode, (e) growth rate of the leading eigenmode.

both eigenvalue and spatial wavenumber as complex ($k \in \mathbb{C}$ and $\omega \in \mathbb{C}$), Bers [43] and Huerre & Monkewitz [44].

Global stability analysis consider strongly nonparallel flow by keeping the base state as global, while locale stability analysis partitions the physical domain. Globally unstable flows are therefore oscillators as absolutely unstable flow but globally stable flow can be either linearly stable or convectively locally unstable. Disturbance evolution of oscillator characterized by an unstable global mode explains the first transition of such flows, which occurs through a supercritical Hopf bifurcation and leads to a limit cycle solution. This concept was further extended to unsteady laminar flow using instead of base state, which is equal to the stationary solution of the flow field, the mean flow, defined as the time averaged of the flow field Barkley [5].

The base flow, computed far away from the instability threshold, is known to yield natural frequencies, which deviate from the limit cycle frequency. In contrast, the stability analysis around the mean flow is known to correctly capture the frequency of the instability, see fig. 1.7. While the Reynolds number is often the bifurcation parameter of flows, swirling flow have a second bifurcation parameter, which is the swirl number and therefore we can investigate in the case of the part load vortex rope, the stability at high Reynolds number with respect to the swirl bifurcation parameter. The success of this approach to low-Reynolds number flows in recent years is impressive: it ranges from wake flows around obstacles (Barkley [5]) to idealized configurations of swirling wakes (Meliga et al. [45]) as well as jets-in-cross flows

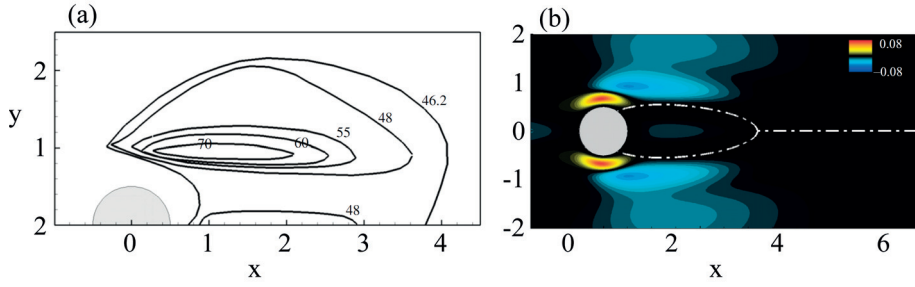


Figure 1.8 – Variations of the growth rate (a) as a function of the location of the steady force. Results are given for the critical Reynolds number $Re = 46.8$ performed by Marquet et al [6]. (b) Results of passive control by Stykowski & Sreenivasan [7]. A control cylinder 10 times smaller than the main cylinder is placed at various locations of the flow. For each location of the control cylinder and for various Reynolds numbers, the growth rate of the perturbations is measured. Contours where the growth rate is nul are represented for each Reynolds number.

(see Theofilis [46] for a review). Its generalization to the global stability analysis of turbulent flows at high Reynolds number has been found recently successful by Meliga et al. [47]. Recently local and global stability analyses about mean and mean turbulent swirling flows experiencing vortex breakdown were investigated in several confined geometries. Among others, Tammisola & Juniper [48] investigated the flow in a swirl generator setup at a Reynolds number of $4.8 \cdot 10^3$, Oberleithner et al. [49] and Paredes et al. [50] studied the precessing vortex core in a combustion chamber at Reynolds number around $3 \cdot 10^4$, Grimble et al. [51] considered the flow in a cyclone separator setup at a Reynolds number around 10^4 . These studies successfully predict the frequency of the helical mode and its unstable nature, which structure the flow and can act as an excitation source in the associated industrial applications. The eigenvalue resulting from the stability analysis moreover, can define a measure to assess control efficiency or can be used as an input to investigate relevant control strategies such as feedback or predictive control.

The stability properties of the flow can be altered by small modification of the base flow, such as the advection rate, the presence of localized forces, turbulence level or boundary conditions. These modifications can be represented as sensitivity maps localizing the most receptivity region of the flow, where passive control could be applied see Camarri [52] for a review. The most famous example is the passive control of vortex shedding of the cylinder wake flow. Strykowski & Sreenivasan [7] have experimentally investigated how a small control cylinder suitably placed in the wake of the main cylinder alters the vortex shedding, see fig. 1.8(a). For various diameter ratios of the two cylinders they determined the regions of the flow where the placement of the control cylinder leads to a complete suppression of the phenomenon over a specific range of Reynolds numbers. The same optimal positions were found by Kim & Chang [53] and Mittal & Raghuvanshi [54], from direct numerical simulations, who performed a global stability analysis of cylinder flow in the presence of a small control cylinder. All these approaches successfully determined the optimal placement of a control cylinder to suppress the vortex shedding, but required that various locations of the control cylinder be tested and

either experimental measurements, direct numerical simulations or global stability analyses be carried out in each case. A systematic approach was developed by Giannetti & Luchini [55] and Marquet et al. [6]. It consists of assessing the variations of the eigenvalue induced by generic structural modifications of the linearized Navier-Stokes operator. They proposed modeling the feedback mechanisms triggering the global instability by a specific structural modification of the perturbation operator: a local force proportional to the perturbation velocity acting as a momentum source in the perturbation equations. Marquet et al. [6], and Giannetti & Luchini [55] show through sensitivity maps, see fig. 1.8(b), that the insertion of a small cylinder just above the main cylinder (red location of fig. 1.8(b)) increases the amplitude and diminishes the frequency of the vortex shedding. On the contrary the addition of a small cylinder in the blue region of fig. 1.8(b) diminishes the amplitude and increases the critical Reynolds number. Recent results of Meliga et al. [47] have shown how an algebraic viscosity model could be included in the linear stability analysis for that purpose. Sensitivity maps analogous to those shown in fig. 1.7 in the laminar case could be obtained in the turbulent regime, where the sensitivity map of the frequency of the vortex shedding as a function of the control cylinder location is compared to a robotized experimental campaign of Parezdonic & Cadot [56].

These sensitivity map provide relevant information to control self-sustained instability close to its threshold because only small modification of the flow are needed to stabilize the flow. However far away from this threshold or in turbulent regime, small modifications of the flow are not sufficient and the optimal amplitude of the control need to be determined. The linear approximation of the sensitivity map can be therefore used as iteration step for computing nonlinear sensitivity maps, which is assessed in the present research work.

1.1 Present work

The primary aim of this research work consists in increasing the operation flexibility of Francis turbines at part load regime, which is thought to be one of the main solutions to mitigate the large power fluctuations of the electric grid arising from the foreseeable massive introduction of intermittent renewable energies in the distribution systems. An intense cavitation vortex rope is however known to appear in these operating conditions and prohibits power generation due to large pressure fluctuations at a well-defined frequency, which causes risks of operating instability, and, fatigue and resonance of the mechanical structures. The control of the part load vortex rope is therefore assessed in this research work using optimal predictive control technique.

Control algorithms need a physically-based target about this helical structure, which is brought by investigating the hydrodynamic instability properties of the draft tube flow distribution, in similarity to the recent development on helical vortex breakdown phenomenon affecting swirling jets and wakes. It requires, however to transpose the idealized uncluttered theoretical framework of fundamental research to the complexity inherent to industrial design, including in particular turbulence modeling to reach high Reynolds number flows $Re = O(10^6)$. The present work has bridged this gap and presents a linear framework to investigate the flow in hydraulic turbines based on global stability analysis.

The linear dynamics and the optimal predictive control of the draft tube flow field of a Francis turbine operating at part load conditions are assessed in the present research work for the reference case study, the FLINDT project - flow investigation in draft tube — project, Eureka No. 1625.

This linear framework is also used to investigate the origin of the synchronous pressure at part load operating conditions. This excitation source, associated to a planar wave oscillating at the same frequency as the precessing vortex rope, induces critical pressure surges when it enters in resonance with the eigenfrequency of the hydraulic piping system. An asymptotic expansion around the mean turbulent flow, constituted by a domain perturbation to include wall disturbance interactions and by a global stability analysis, is performed to show the origin and the mechanism of the synchronous pressure associated to this fluid-solid interaction.

The control algorithm used in the part load vortex rope case is first developed on an academic test case, the spiral vortex breakdown, to assess the feasibility and the validity of the approach. In addition, the direct numerical flow simulation of the spiral vortex breakdown has revealed the onset of chaos at a Reynolds value of $Re = 220$ induced by purely hydrodynamic interactions. A bifurcation analysis is performed and the nonlinear interactions of several self-sustained instability revealed by stability analysis are investigated to identify the route to chaos in this flow.

This research work is supported by the Swiss National Science Foundation (SNSF) - grant no. 200021 149818.1

1.2 Outline

This thesis is a compilation of published articles or submitted articles in peer-reviewed journal. Each chapter is composed by an introductory paragraph following by one article. Chapter 2 presents the stability analysis and the predictive control algorithm developed on the academic benchmark flow, spiral vortex breakdown. Chapter 3 transposes the idealized uncluttered theoretical framework of fundamental research to the complexity inherent to industrial design. The stability analysis of high Reynolds flows is assessed on the part load vortex rope appearing the draft tube of Francis turbines at a Reynolds number around $Re = O(10^6)$. The control of the part load vortex rope is then reported in the chapter 4, where the optimal predictive control algorithm previously validated is applied. Chapter 5 presents the origin of the synchronous pressure using the framework of the global linear stability analysis of the part load vortex rope embedded in an asymptotic expansion, which shows the interaction of the part load vortex rope and the draft tube wall. Chapter 6 comes back on the spiral vortex breakdown to present the nonlinear interaction of several self-sustained modes, which lead to the onset of chaos at a Reynolds number of $Re = 220$. Finally a conclusion and the perspectives are drawn in Chapter 7.

2 Stability analysis and predictive control of spiral vortex breakdown

Barkley's study [5] on the stability analysis around the base and mean flow of the cylinder wake is revisited in the first part of this chapter. Self-sustained instability emerging from laminar swirling flows experiencing spiral vortex breakdown are investigated using global stability analysis. The deviation of the frequency prediction from the eigenvalue of the base flow is less pronounced but remains valid compare to the cylinder wake and the excellent frequency prediction of the the stability analysis around mean flow is further emphasized, while two unstable eigenmodes are observed. The second part of this chapter introduces the predictive control of the spiral vortex breakdown. The neutral assumption of unstable eigenvalue around the mean flow is revoked by successfully stabilizing the instantaneous flow using a minimization algorithm, which targets the eigenvalue growth rate of the most unstable eigenmode. This encouraging results obtained close and far from the instability threshold has allowed us to envisage to quench the part load vortex rope.

The variables used in this document are susceptible to change in comparison to the submitted version of the article to keep the document consistency. Additional paragraph and results could be also added.

PAPER: Predictive control of spiral vortex breakdown

Predictive control of spiral vortex breakdown

Simon Pasche¹, François Gallaire², François Avellan¹

¹ LMH, Swiss Federal Institute of Technology (EPFL), CH-1007, Lausanne, Switzerland

² LFMI, Swiss Federal Institute of Technology (EPFL), CH-1015, Lausanne, Switzerland

Preprint version of the article submitted in *Journal of Fluid Mechanics* including reviewers' comments, (2017)

The predictive control of the self-sustained single spiral vortex breakdown mode is addressed in the three-dimensional flow geometry of Ruith, Chen, Meiburg & Maxworthy [57] for a constant swirl number $S = 1.095$. Based on adjoint optimization algorithms, two different control strategies have been designed. First, a quadratic objective function minimizing the radial velocity intensity, taking advantage of the physical mechanism underpinning spiral vortex breakdown. The second strategy focuses on the hydrodynamic instability properties using as objective function the growth rate of the most unstable global eigenmode. These minimization algorithms seek for an optimal volume force in an axisymmetric domain avoiding therefore expensive 3-D computations. In addition to considering eigenvalues around the base flow, we also investigate the stability around the mean flow and we find that it correctly predicts the frequency of the self-sustained single spiral vortex breakdown mode for Reynolds numbers up to $Re = 500$. Close to the instability threshold, at a Reynolds value of $Re = 180$, all these control strategies successfully quench the spiral vortex breakdown. The related volume force is found identical for the base and mean flow eigenvalue control even if the uncontrolled growth rates differ significantly. The control of the least unstable eigenvalue of the mean flow is not only found optimal at $Re = 180$, it also stabilizes the flow at a Reynolds value as large as $Re = 300$, which opens promising extensions to industrial applications.

2.1 Introduction

Vortex breakdown is a characteristic phenomenon affecting swirling jet and wake flows. It is associated to a sudden change of the flow topology when the swirl number S , defined as the ratio between the characteristic tangential velocity and the centerline axial velocity, reaches a critical value. While the flow remains columnar below this threshold, it suddenly changes topology into several possible vortex breakdown states, which have been observed and labeled across the last decades. As first observed by Lambourne & Bryer [58] on delta-wings, both the bubble vortex breakdown characterized by an axisymmetric recirculation region and the spiral vortex breakdown can exist in similar flow conditions. Even richer dynamics and

structures have been observed in tube experiments by Hall [59], Leibovich [60] and Escudier & Zehnder [61] where the bubble breakdown may be followed by columnar, single spiral or double spiral flows, depending on the parameters. In this vein, Sarpkaya [62] reported a flow map of the different possible states with respect to the bifurcation parameters. Vortex flows possibly experiencing vortex breakdown are found in several industrial applications, such as flow over delta-wings, thermal and hydraulic turbomachines as well as combustion chambers. In these industrial situations, vortex breakdown often results in performance degradation and structure fatigue although in certain case it may be also beneficial, for example in burner stabilization where the stagnation point play the role of flame anchor. High performance industrial exploitation of these systems under secure operating conditions therefore calls for flow control techniques which could enable to operate at off design regime and thereby increase operating flexibility (European policy [63]), see among others Susan-Resiga et al. [64], Favrel et al. [17], Pasche et al. [65] for hydraulic turbomachines and Gursul et al. [66] for leading-edge vortices and Paschereit et al. [67], Syred [68] for thermal turbomachines.

To interpret the variety of observed vortex breakdown states, two different physical mechanisms were mainly highlighted over the years. First, the transition from columnar flow to bubble breakdown was interpreted by Squire [69] as the consequence of an infinitesimal standing wave, which exists only when the swirl surpasses a certain threshold. In addition, Benjamin [70] showed that this threshold coincides with the super/subcritical transition where Kelvin waves hosted by the vortex core start propagating upstream. This led him to draw an analogy with the hydraulic jump phenomenon, known to be also associated to a super/subcritical transition of gravity waves. Since then, Wang & Rusak [71] have proposed a unifying view connecting these local wave propagation properties to the global stability properties of inviscid vortex flows of finite length.

Second, the hydrodynamic instabilities of swirling jets and wakes have been analyzed in great detail with emphasis on the development in space and time of helical disturbances. While several mechanisms can be active for velocity profiles with strong axial or azimuthal shear (Gallaire & Chomaz[72]), even vortex flows with Gaussian axial vorticity and velocity distributions, referred to as the Batchelor vortex, were found very unstable at intermediate values of swirl, as the result of the so-called generalized centrifugal instability (Leibovich & Stewartson [73]). The observation that helical instability could become absolutely unstable (Huerre & Monkewitz [44]) in swirling wakes (Delbende et al. [74]) has led to the interpretation of spiral vortex breakdown as a secondary instability of axisymmetric vortex breakdown (Gallaire et al. [75]). The absolutely or convectively unstable nature of the flow was determined by computing numerically the linear impulse response of a localized disturbance on the numerically computed axisymmetric flow solution, as previously performed by Ruith et al. [57]. The self-sustained instability accounting for spiral vortex breakdown was interpreted as the consequence of the existence of an absolutely unstable region.

Ruith et al.'s [57] direct numerical simulations (DNS) of the incompressible Navier-Stokes equations were probably the first attempt to break the dependence on the lateral boundary

condition in comparison with previous studies such as Spall et al. [76], Althaus et al. [77]. In addition to axisymmetric direct numerical simulations (DNS), the author also performed full three-dimensional (3-D) DNS, using convective radial boundary condition mimicking a semi-infinite domain, in order to analyze the mode selection in a free vortex breakdown phenomenon. The flow solutions were initiated by the inlet Grabowski & Berger[78] vortex profile and this vortex now appears as a benchmark model for disturbance analysis of the vortex breakdown in the more recent work of Vyazmina et al. [79], Meliga et al. [45], Qadri et al. [80] and Rusak et al. [81]. Both Meliga et al. [45] and Qadri et al. [80] performed a global linear stability analysis about the axisymmetric base flow, and successfully described the Hopf bifurcation and the development of the spiral vortex breakdown spinning in time around the axisymmetric breakdown bubble for Reynolds number and swirl number close to $Re = 200$ and $S = 1$, confirming the weakly non parallel local analysis of Gallaire et al. [75]. Furthermore Meliga et al. [45] used the global stability analysis to rigorously derive coupled weakly nonlinear amplitude equations that helped understanding the mode selection between a single spiral $m = 1$ and a double spiral $m = 2$ in the vicinity of the codimension-2 point $Re = 71.95$ and $S = 1.436$.

Such global stability analyses about the axisymmetric base flow is relevant at the instability onset but one may question its validity further away from threshold. This fundamental issue related to the application of global stability analysis to real flows was revived by Barkley [5]. Considering the Bénard-von-Karman vortex street in the cylinder wake, Barkley [5] showed that the Strouhal number was correctly captured by a global linear stability analysis around the mean flow while the prediction from the linearization around the base flow quickly failed when the Reynolds number was increased. This can be interpreted as a consequence of the mean-flow distortion (Maurel et al. [82]) resulting from the nonlinear Reynolds stresses, which both account for the difference between the base and mean flow and for the saturation of the disturbance, as demonstrated by Sipp & Lebedev [83] using a weakly nonlinear multiple-scale expansion to derive a Landau amplitude equation. More recently, this approach was extended further away from threshold (Mantič-Lugo et al. [84]) by a semilinear coupling of, on one hand, the correction to the base flow through the Reynolds stresses, to, on the other hand, a linearized disturbance equation. Without going into that level of analysis, we will in the present study address the quality of the frequency prediction resulting both from the stability analysis about the base and mean flows in Ruith et al.'s [57] semi-infinite swirling flow configuration by considering Reynolds numbers up to $Re = 500$.

Recently local and global stability analyses about mean and turbulent mean swirling flows experiencing vortex breakdown were investigated in several confined geometries. Among others, Tammisola & Juniper [48] investigated the flow in a swirl generator setup at a Reynolds number of $4.8 \cdot 10^3$, Oberleithner et al. [49] and Paredes et al. [50] studied the precessing vortex core in a combustion chamber at Reynolds number around $3 \cdot 10^4$, Grimble et al. [51] considered the flow in a cyclone separator setup at a Reynolds number around 10^4 and Pasche et al. [65] who investigated the part load vortex rope in Francis turbines at a Reynolds number around 10^6 . These studies successfully predict the unstable nature of the helical

mode and its frequency, which structures the flow and acts as an excitation source in these industrial applications. The growth rate resulting from the stability analysis moreover can define a measure to assess control efficiency or can be used as an input to investigate relevant control strategies such as feedback or predictive control. Control techniques applied to Navier-Stokes equations were reviewed by Kim & Bewley [85], and can be categorized for our purpose into two main approaches: the closed-loop and open-loop control strategies. Among open-loop control strategies, one distinguishes between passive and active strategies, the latter being subcategorized into steady and unsteady. All these control approaches seek flow manipulations which aim at optimizing some features of the flow. The control target can be an eigenvalue, the drag on an obstacle, among many other possible choices of objectives.

Regarding first closed-loop control, foundations were laid out by Lions [86], who demonstrated the existence and the uniqueness of the optimal control solution for linear partial differential equations and quadratic objectives. Such predictive techniques were initiated by Joslin et al. [87] and Bewley et al. [88]. They are computationally extremely demanding, because of the need to perform unsteady direct and adjoint calculations, with the associated memory requirements. With the recent advent of high performance computing facilities (HPC), there is a certain revival in the approach (Passaggia & Ehrenstein [89] and Goit & Meyers [90]). An alternative closed-loop control approach, inspired by automatic control and based on direct feedback control, was promoted in the hydrodynamic instability context by Bewley & Liu [91], among others. The closed-loop control couples actuators to sensors for optimal disturbance rejection using a feedback gain matrix that is determined by solving a matrix Riccati equation. While several examples of direct feedback control can be found in the literature (see Kim & Bewley [85] for a review), they most often need to be combined with a model reduction technique.

Focusing next on steady open-loop control, although it can be based on trial and error (Strykowski & Sreenivasan [7]), it can also be determined within an adjoint-based optimization approach. This approach is derived in the Lagrangian functional framework and uses the adjoint fields as Lagrangian multipliers to determine a closed-form expressions of the gradient direction in a very cost-effective way (Gunzburger [92] and Giannetti & Luchini [93]). The first gradient direction may be viewed as the sensitivity field, following Giannetti & Luchini [55] or Marquet et al. [6]. The sensitivity is defined as the gradient of the objective (for instance the eigenvalue) with respect to the control variable (for instance a distributed volume force). The sensitivity to base flow modification were applied to the stabilization of the cylinder wake flow by Marquet et al. [6]. More rarely does the adjoint-based optimization approach seem to have been used in its entire nonlinear spirit (Camarri & Iollo [94]). The sensitivity analysis of the laminar and steady base flow solution was extended to the mean flow for turbulent flows by Meliga et al. [47], focusing on nominally 2-D flow configurations, followed more recently by Mettot et al. [95] and Carini et al. [96].

Turning back to axisymmetric vortex breakdown, Gallaire et al. [97] applied Ricatti-based feedback control to quench the global axisymmetric unstable mode above the transition from

supercritical to subcritical state for the inviscid flow in pipe of finite length, while Rusak et al. [81] recently implemented a more efficient physically-based feedback control on the same flow. Steady open-loop wall control through blowing and suction was explored by Meliga & Gallaire [98] for viscous flow in a confined geometry and analyzed in the framework of sensitivity analysis by determining the effect of the control on the amplitude equation governing the steady bifurcation. In the present study we will consider different steady open-loop flow control strategies to mitigate the development of the spiral mode in Ruith et al.'s flow [57]. We will first attempt to minimize the radial velocity intensity as a proxy for the flow non-parallelism i.e. quenching the axisymmetric bubble, a strategy referred to as "optimal base flow manipulation" and then we devise an iterative scheme to optimally quench the dominant eigenvalue growth rate of the base and mean flows. This "optimal flow stabilization control" determines what could be called a nonlinear sensitivity field to a steady force and determines the control amplitude, which becomes relevant to design efficient control appendages (Lacis et al. [99]).

The paper is organized as follows: the open geometry of Ruith et al. [57] leading to spiral vortex breakdown is described together with the governing equations in section 2.2, while we perform unsteady 3-D DNS of the spiral vortex breakdown at various Reynolds numbers and determine the prevailing axisymmetric laminar base flow solution in section 2.3. This section is completed by a comparison of the stability properties of the base and mean flows, which are also compared to the limit cycle frequency obtained from the DNS. The theoretical framework for the optimal flow control problem is described in section 2.4 both for the optimal base flow manipulation and the base and mean flow stabilization approaches. The results of these different control strategies are compared in section 2.5, before conclusions are drawn.

2.2 Flow configuration

2.2.1 Governing equations

We consider the dimensionless incompressible Navier-Stokes equations in a semi-infinite domain Ω ,

$$\begin{aligned} \frac{\partial \mathbf{C}}{\partial t} + (\mathbf{C} \cdot \nabla) \mathbf{C} &= -\nabla P + Re^{-1} \nabla^2 \mathbf{C} \quad \text{in } \Omega \\ \nabla \cdot \mathbf{C} &= 0 \quad \text{in } \Omega, \end{aligned} \tag{2.1}$$

where (\mathbf{C}, P) are the state variables and Re the Reynolds number, built on the fluid's kinematic viscosity and on the vortex core radius and incoming centerline streamwise velocity prevailing at inlet. This system is written in compact form as

$$\mathcal{N} \partial_t \mathbf{U} + \mathcal{M}(\mathbf{U}) = \mathbf{0} \quad \text{in } \Omega, \tag{2.2}$$

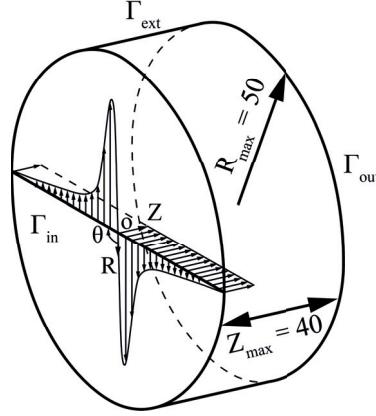


Figure 2.1 – Three-dimensional schematic of the flow configuration.

where $\mathbf{U} = (\mathbf{C}, P)$, \mathcal{M} is the nonlinear evolution operator and \mathcal{N} is the singular operator premultiplying the time-derivative. We consider the dynamics governed by equations (2.1) and resulting from an inlet Grabowski & Berger [78] vortex profile

$$\begin{aligned} C_R(R) &= 0, & C_\theta(R) &= S\Psi, & C_Z(R) &= 1, & \text{on } \Gamma_{in} \\ \Psi(R \leq 1) &= R(2 - R^2), & \Psi(R > 1) &= 1/R, \end{aligned} \quad (2.3)$$

This vortex is composed of a unitary uniform dimensionless axial velocity component $C_Z = 1$, a null radial velocity component, and a tangential velocity component with maximum intensity assigned by the swirl number S and composed of a vortex core of dimensionless radius 1 in solid body rotation and a potential decay outside the vortex core. In the present study, we fix the swirl number to $S = 1.095$ but let vary the Reynolds number up to $Re = 500$, thereby restricting our investigation to the spiral vortex breakdown case, in contrast to pure bubble vortex breakdown or multiple helix vortex breakdown observed respectively at lower and larger swirl numbers (Ruith et al. [57] and Meliga et al. [45]).

2.2.2 Direct numerical flow simulation

Direct numerical flow simulations (DNS) have been performed on a 3-D cylindrical domain based on a cartesian coordinate system (X, Y, Z) . The main axis of the cylinder is oriented along the Z -component and its origin is located at the center of the inlet, see fig. 2.1. A second, cylindrical, coordinate system is introduced (R, θ, Z) , which is more convenient to study vortex flows, its axial axis Z and origin remaining identical. The transformation matrix between the two reference frames is defined as follows: the X -axis is oriented along R for $\theta = 0$, while the Y -axis completes the reference frame to obtain a right-handed coordinate system and corresponds therefore to $\theta = \pi/2$. The radial extension of the domain equals $R_{max} = 50$ while its length is $Z_{max} = 40$. Such dimensions were necessary to guarantee an unconfined radial boundary condition (see appendix 2.7.1) because the vortex breakdown resulting from these flow conditions is known to be very sensitive to confinement effects, as experimented

by Ruith et al. [57]. The computational domain is bounded by the Grabowsky and Berger vortex (2.3) on the inlet boundary Γ_{in} , a free-outflow condition $(-P\mathbf{I} + Re^{-1} \cdot (\nabla \mathbf{C})) \cdot \mathbf{n} = 0$ on the external boundary Γ_{ext} , and a convective condition $\partial_t \mathbf{C} + \mathbf{C}_c \cdot \partial_{\mathbf{n}} \mathbf{C} = 0$ on the outlet boundary Γ_{out} . We have fixed the convective velocity to be equal to the free-stream velocity $\mathbf{C}_c = \mathbf{e}_Z$. The governing equations are solved numerically with NEK5000 a spectral element solver developed by Fischer et al. [100]. The temporal discretization of the nonlinear terms is treated explicitly by a third order backward-differentiation scheme (BDF3) combined with a third order extrapolation scheme (EXT3). The linear terms are treated implicitly in time and a pressure-velocity decoupling method is used for the spatial discretization. The velocity and pressure space are represented by a tensor-product array of Gauss-Lobatto-Legendre (GLL) and Gauss-Legendre (GL) points of polynomial orders N and $N - 2$. In the present study, $P_{10} - P_8$ polynomial orders for velocity-pressure with 11040 hexahedral elements are required to compute the flow field. This represents a computation of 8 millions of degree of freedoms. The validation of the 3-D DNS is presented in appendix 2.7.1.

2.2.3 Axisymmetric flow

The steady axisymmetric flow solution developing from the inlet Grabowsky and Berger vortex (2.3) is also investigated, with governing equations written in compact form as

$$\mathcal{M}(\mathbf{U}_B) = \mathbf{0} \quad \text{in } \Omega_a, \quad (2.4)$$

with $\mathbf{U}_B = (\mathbf{C}_B, P_B)$ the base flow state variables. An axisymmetric domain Ω_a , with the same dimensions as those of the 3-D domain is used $R_{max} = 50$ and $Z_{max} = 40$, except that a sponge region is added along the Z -component at the end of the domain. The length of this sponge region is equal to $L_{sponge} = 60$, using the same smoothing function as in Meliga et al. [45]. The inlet and external boundary conditions are equivalent to those of the 3-D case but a symmetry condition is applied on the axis Γ_{axis} that equals to $C_{BR} = C_{B\theta} = 0, \partial_R C_{BZ} = 0$, while the outlet boundary has a free-outflow condition.

The flow solution is carried out by the means of the finite element library Freefem++ [101]. The steady axisymmetric incompressible Navier-Stokes equations are first premultiplied by R to avoid the axis singularity and then solved numerically via a Newton-Raphson iterative method. The related linear system is carried out by the Unsymmetric Multifrontal sparse LU Factorization PACKage (UMFPACK) [102]. The computational domain is meshed by 408'866 triangular Taylor-Hood elements, $P_2 - P_1$ polynomial order elements for the velocity-pressure unknowns. A convergence criterion of 10^{-8} on the H_1 -norm is reached in the Newton-Raphson iterative method, which leads to the base flow solution.

2.2.4 Global stability analysis

The small disturbance dynamics, $\tilde{\mathbf{U}} = (\tilde{\mathbf{C}}, \tilde{P})$, of the Navier-Stokes equations are investigated by global linear stability analyses around the base flow \mathbf{U}_B and the mean flow $\bar{\mathbf{U}} = (\bar{\mathbf{C}}, \bar{P})$ in the axisymmetric domain Ω_a . The disturbances $\tilde{\mathbf{U}}$ are expanded in normal modes for different azimuthal wave numbers $m \in \mathbb{Z}$,

$$\tilde{\mathbf{U}}(R, \theta, Z, t) = \mathbf{u}(R, Z) \exp(i(m\theta - \omega t)) + c.c., \quad (2.5)$$

where $c.c.$ is the complex conjugate. We assume mean flow solutions unperturbed at first order by the Reynolds stresses (Barkley [5], Meliga et al. [47], Mantić-Lugo et al. [84] for discussion on this hypothesis). Therefore the eigenvalue problems related to the base and mean flow state become similar and may be written in a compact form using a generic flow solution $\mathbf{U}_0 = (\mathbf{C}_0, P_0)$ as

$$(-i(\omega_r + i\omega_i)\mathcal{N} + \mathcal{L}_m(\mathbf{C}_0))\mathbf{u} = \mathbf{0}, \quad \text{in } \Omega_a, \quad (2.6)$$

where \mathcal{L}_m is the operator for the linearized Navier-Stokes equations of azimuthal wave number m and \mathbf{U}_0 the linearization point that is equal to \mathbf{U}_B for base flow eigenvalue problem and $\bar{\mathbf{U}}$ for mean flow eigenvalue problem. The time-averaged flow distribution $\bar{\mathbf{U}}$ is computed on the fly in NEK5000 with a minimum of 160 periods of the characteristic oscillation, after the transient phase has died out. In addition, an interpolation step is needed to transfer the mean flow from the 3-D mesh to the axisymmetric mesh. This is carried out by a spectral interpolation of 10^{-13} accuracy integrated in NEK5000. At this level the mean flow is assumed purely axisymmetric and only a slice at $X = 0$ and $Y > 0$ is interpolated and exported to the eigenvalue solver.

In this context we use the definition that a positive azimuthal wavenumber $m > 0$ corresponds to a spiral coiling in space in the anti-trigonometric direction and therefore, since $S > 0$, in the opposite direction as that of the ambient flow while $m < 0$ designates a spiral coiling in the same direction as the flow. The boundary conditions applied to the disturbances are homogeneous Dirichlet conditions when Dirichlet conditions are imposed on the base flow and remain unchanged in case of a Neumann condition. Specific boundary conditions, which

Azimuthal wave number	Boundary conditions
$m = 0$	$c_R = v_\theta = 0, \partial_R c_Z = 0$
$m = \pm 1$	$c_Z = p = 0, \partial_R c_R = \partial_R c_\theta$
$m > 1$	$c_R = c_\theta = c_Z = 0$

Table 2.1 – Boundary conditions on the axisymmetric axis applied to the disturbances for different azimuthal wave numbers.

are recalled in Table 2.1, are applied on the symmetry axis due to the azimuthal expansion. They are obtained by symmetry considerations of the perturbations (Khorrami [103]).

The global stability analysis is carried out by finite element method implemented in the Freefem++ software [101]. The eigenvalue problem is first premultiplied by R and then the discretized equations are solved by the implicit restarted Arnoldi method of the ARPACK library [104]. The eigenvalues are obtained with a tolerance of 10^{-6} of the ARPACK solver. The axisymmetric mesh described in section 2.2.3 is used to compute the eigenvalue problem of the base and mean flow, except that the sponge region is removed for the latter. A validation of the eigenvalue calculations of the base and mean flows is presented in appendices 2.7.2 and 2.7.3 respectively.

2.3 Flow dynamics and stability analyses

2.3.1 Three dimensional flow

The 3-D instantaneous flow computations are illustrated for two specific Reynolds values, $Re = 180$ and $Re = 300$, by axial vorticity contours in fig. 2.2(a) and (b), respectively. These

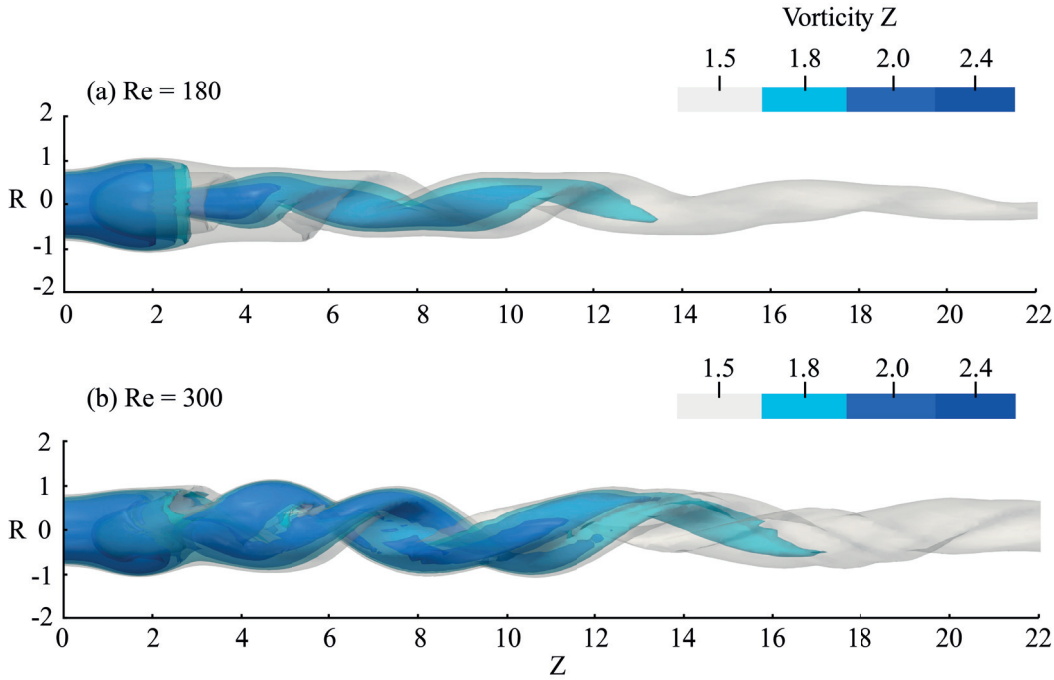


Figure 2.2 – Iso-surfaces of axial vorticity contour of the 3-D DNS flow solution for (a) $Re = 180$ and (b) $Re = 300$, for $S = 1.095$.

contours highlight the recirculation bubble and the spiraling motions of the flow. In the case of $Re = 180$, the recirculation bubble is accompanied by a single helical vortex structure coiling in its wake, fig. 2.2(a). The spiral spins temporally in the same direction as the Grabowsky

& Berger vortex but coils spatially in the opposite direction, which is consistent with the previous results of Ruith et al. [57]. The temporal discrete Fourier amplitude spectrum of the radial velocity at the location $(R, \theta, Z) = (0.1, 0.0, 5.0)$, see fig. 2.3(a), exhibits a quasi-sinusoidal signal at the frequency $f = 0.189$. The system has reached a limit cycle that arises from a self-sustained instability. In contrast, at $Re = 300$, the wake of the bubble is followed by two helical spirals, which have the same spatial coiling and temporal spinning as for $Re = 180$. The axial vorticity contours in fig. 2.2(b) exhibit a second, slaved, spiral in the vicinity of first, master, spiral. They are differentiated by their axial vorticity magnitudes, the slaved structure exhibiting a modulated axial vorticity iso-contour when compared to the master structure, characterized by a dense iso-contour, at a value of 2.4. The temporal discrete Fourier amplitude spectrum is richer than that prevailing at $Re = 180$, see fig. 2.3(b). This amplitude spectrum exhibits four peaks: a main one with a frequency of $f = 0.204$ corresponding to the master helical vortex, a smaller peak close to the main peak with a frequency of $f = 0.167$, a low frequency peak at a frequency of $f = 0.003$, as well as the main peak's second harmonic at $f = 0.408$. The low frequency component and the broad base of the main peak, which is not a lack of FFT accuracy, are markers of the nonlinear interactions between the two spirals.

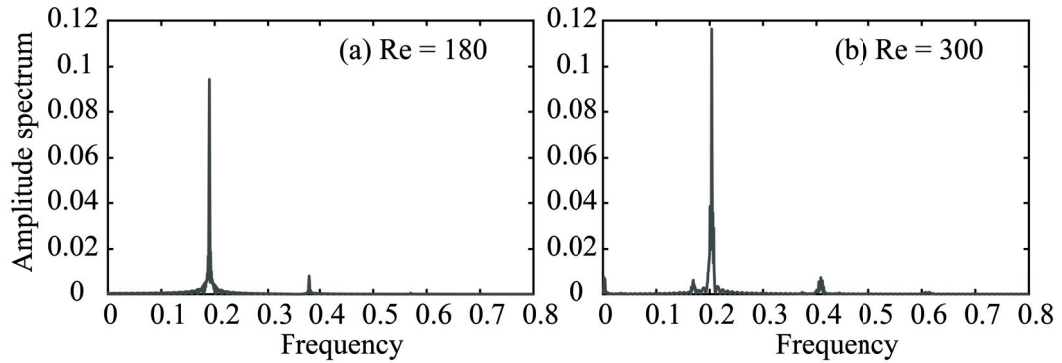


Figure 2.3 – Discrete Fourier amplitude spectrum of the time signal of the 3-D DNS of the radial velocity component located at $(R, \theta, Z) = (0.1, 0.0, 5.0)$ for $Re = 180$ and $Re = 300$, for $S = 1.095$.

The axisymmetric time-averaged flow fields, to be investigated by global stability analysis are displayed in fig. 2.4. These figures are composed by the tangential velocity component on the upper part, $R > 0$, and streamsurfaces colored by the magnitude of the axial velocity component on the lower part, $R < 0$. The time-averaged streamsurfaces exhibit a recirculation bubble, characteristic of vortex breakdown. At $Re = 180$, the bubble is elongated and lifted up from the centerline in its downstream part while the bubble has a more round shape for $Re = 300$, and additionally a second decelerated region is observed at $Z = 5$. We have observed that the extension of the time-averaged bubble decreases with the Reynolds number while the intensity of the undulating wake in the lee of the bubble increases with the Reynolds number.

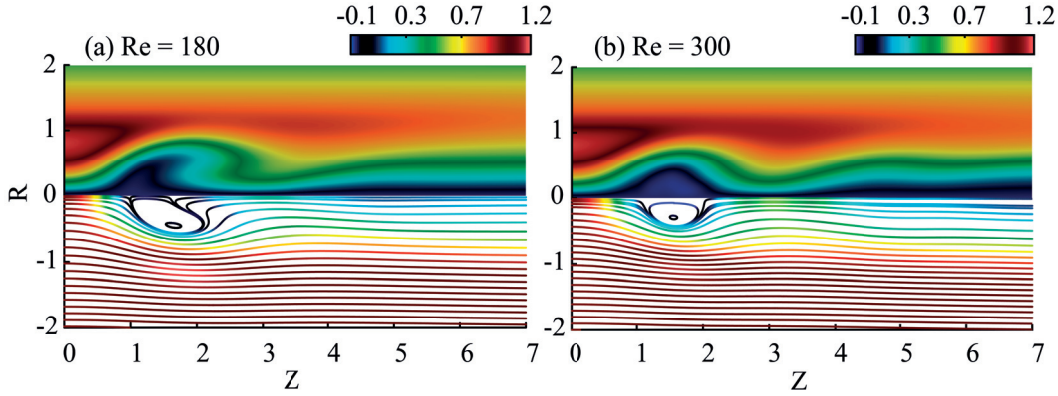


Figure 2.4 – Time averaged solution of the 3-D Navier Stokes equations, $\bar{\mathbf{C}}$, for $S = 1.095$ and $Re = 180$ (a) and $Re = 300$ (b). The upper part of the graph shows the tangential velocity component and on the lower part, the streamsurfaces colored by the magnitude of the axial velocity component.

2.3.2 Axisymmetric flow

The axisymmetric base flow, governed by eqn. (2.4), is displayed in fig. 2.5(a) and (b) for $Re = 180$ and $Re = 300$, respectively, for $S = 1.095$. At a Reynolds value of $Re = 180$, the difference between the mean flow (fig. 2.4a) and the base flow (fig. 2.5a) is almost invisible. The mean flow correction resulting from the saturation of the self-sustained instability is therefore best observed at $Re = 300$, see fig. 2.5(b) and fig. 2.4(b), where the mean flow strongly deviates from the base flow, supporting the observations already reported by Ruith et al. [57].

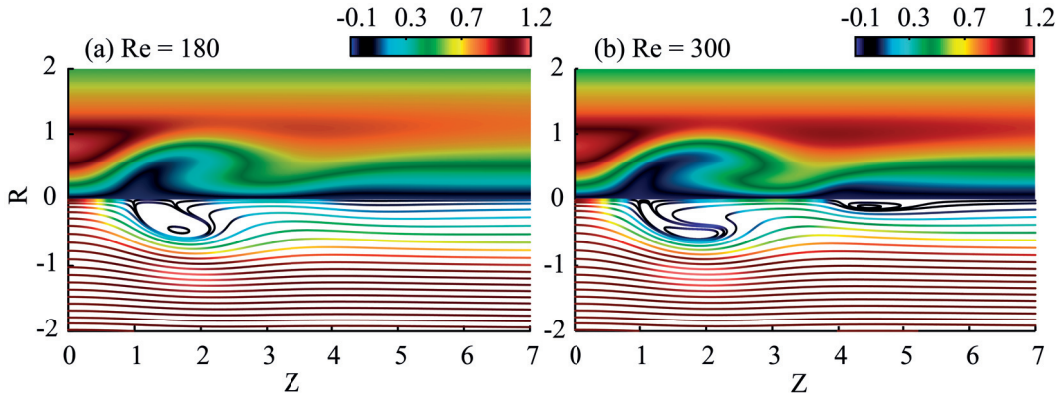


Figure 2.5 – Solution of the steady axisymmetric Navier Stokes equations, \mathbf{C}_B , for $S = 1.095$ and $Re = 180$ (a) and $Re = 300$ (b). The upper part of the graph shows the tangential velocity component and on the lower part, the streamsurfaces colored by the magnitude of the axial velocity component.

2.3.3 Global stability analysis

The global stability of the base flow and the mean flow has been investigated, with focus on the first helical mode $m = 1$. A representative example is presented in fig. 2.6 at a Reynolds value of $Re = 300$. Up to three unstable eigenmodes, labeled B_n for $n = 1, 2, 3$ can be identified in the eigenvalue spectrum of the base flow, while only two unstable modes M_1 and M_2 are detected in the mean flow eigenvalue spectrum. The associated growth rates are significantly larger when the linearization is performed around the base flow than around the mean flow, in agreement with mean flow modification based saturation mechanisms reported in different flow geometries (Barkley [5] and Mantić-Lugo et al. [84]).

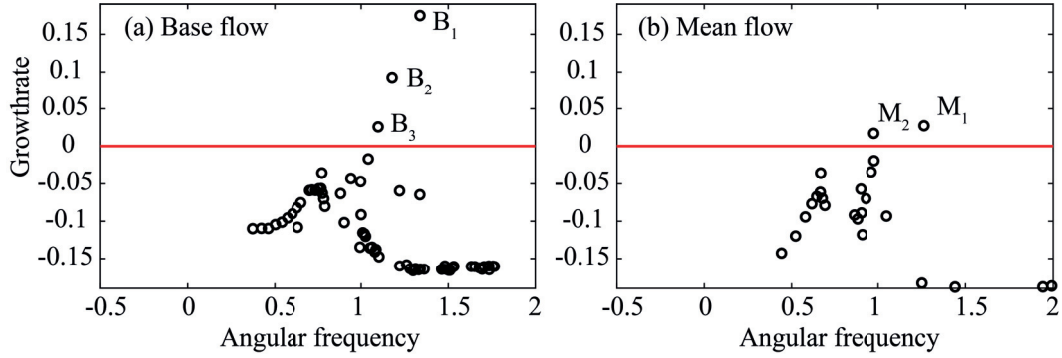


Figure 2.6 – Eigenvalue spectra of the global linear stability of mode $m = 1$ about the base (a) and mean (b) flow at $Re = 300$ and $S = 1.095$. Unstable eigenvalues are labeled respectively B_1 , B_2 , B_3 and M_1 and M_2 .

We have then systematically compared the frequency prediction of the base and mean flow stability analyses for different Reynolds values $Re = 100 - 500$ by keeping constant the swirl number $S = 1.095$, focusing only on unstable modes and on the azimuthal wavenumber $m = 1$, since other azimuthal wavenumbers were all found linearly damped. The instability threshold was found at $Re = 143.5$ for the base flow and approximately at $Re = 143.7$ for the mean flow, where the dying out of the transient in the DNS become prohibitively long close to threshold. In the vicinity of the threshold, the linear frequency predictions (respectively in red and blue for the base and mean flow) are in agreement with the limit cycle frequency extracted from discrete Fourier transform of the 3-D DNS signal (in green), see fig. 2.7(a). As the Reynolds number increases, the growth rate of the dominant unstable mode linearized about the base flow (B_1) increases rapidly, followed by a second unstable mode (B_2) bifurcating at $Re = 200$ and subsequently emerging unstable eigenvalues B_3 and B_4 . At $Re = 350$, where the base flow stability analysis has been stopped, the base flow is found to be unstable to no less than four unstable modes, as seen in fig. 2.7(b). The frequencies of the four eigenvalues considered are all around $\omega_r \approx 1.08$ at their respective instability thresholds, beyond which they increase

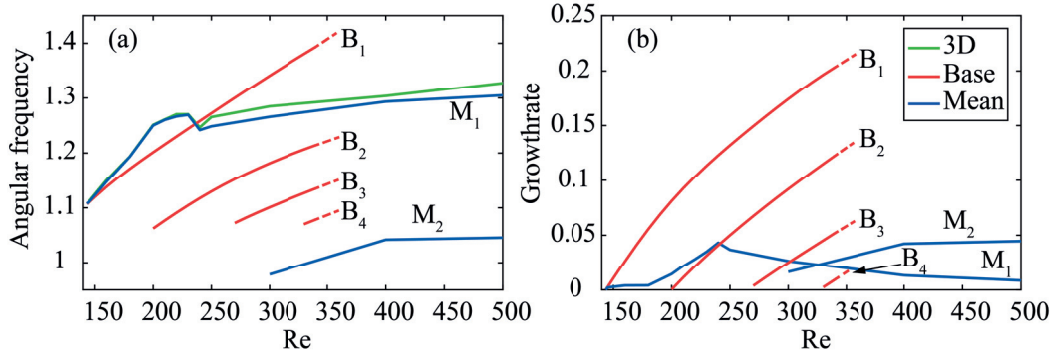


Figure 2.7 – Growth rate and angular frequency of the global linear stability of the mean, M_1 , M_2 and base flow, B_1 , B_2 , B_3 , B_4 , for azimuthal wave number $m = 1$ compared to the 3-D angular frequency from the DNS, computed by discrete Fourier transform at location $(R, \theta, Z) = (0.1, 0.0, 5.0)$.

linearly with the Reynolds number. The base flow frequency prediction of the dominant unstable mode remains acceptable before it crosses the non-monotonic limit cycle frequency evolution (in green) around $Re = 235$. This appears as an *a posteriori* justification of the validity range of the linear stability analysis about the base flow of Meliga et al. [45] and Qadri et al. [80].

The limit cycle frequency (in green) indeed first strongly increases away from threshold until it drops for $Re > 230$ and finally slowly increases with the Reynolds number for $Re > 240$. The frequency of the leading eigenvalue (M_1) of the mean flow (in blue) closely follows the limit cycle frequency (in green) along the whole Reynolds number range, demonstrating a correct frequency prediction by the global stability analysis around the mean flow, as found in the canonical cylinder wake flow (Barkley [5]). Similarly the maximum growth rate of the mean flow remains much smaller than the growth rate of the dominant mode of the base flow that stays close to zero. Above $Re > 300$, a second unstable eigenvalue is found with a frequency that corresponds to the second peak observed in the temporal discrete Fourier amplitude spectrum (the angular frequencies ω_r should be divided by 2π to compare to the frequencies obtained in fig. 2.3, for example at $Re = 300$, $f_{M_2} = 0.156$, and $f_{DNS} = 0.167$). The most unstable eigenmode is likely to correspond to the master helix. The second unstable eigenmode would be associated the slaved helix. These frequency predictions, together with the global stability of the base and mean flows with respect to $m = 2$ (not shown for brevity) are a confirmation that the snapshot of fig. 2.2(b) at $Re = 300$ does not correspond to an $m = 2$ instability but rather to the superimposition of two $m = 1$ spirals, each corresponding to a separate frequency peak and without any phase correlation.

These results on the frequency prediction of the stability analysis about the mean flow support the recent extension of this technique to high Reynolds number industrial flows, such as the frequency prediction of the precessing vortex core in combustion chamber Oberleithner et al.

[49], Paredes et al. [50], Tammisola & Juniper [48] or of the part load vortex rope in Francis hydraulic turbines Pasche et al. [65]. Moreover, we identify up to two unstable eigenmodes, which may offer a relevant test case for the need to take into account mode interaction in generalizing the self-consistent model for saturation dynamics developed by Mantič-Lugo et al. [84], in the spirit of the generalized quasi-linear models developed by Marston et al. [105].

2.4 Optimal control: flow stabilization and flow manipulation controls

2.4.1 Optimal control theory

Although it can be beneficial to improve mixing, the self-sustained instability in the spiral vortex breakdown is a source of perturbations that is undesirable in several applications Rheingans [106], Syred [68], Gursul et al. [66], Nishi & Liu [14]. The finite amplitude nonlinear predictive control of such perturbations is investigated for two specific Reynolds values $Re = 180$ and $Re = 300$, with the aim to stabilize the periodic fluctuations by applying a constant volume force. In the present study, we have chosen to minimize two different objectives to achieve this goal, a "flow stabilization control" which targets a zero value of the growth rate of the most unstable eigenvalue declined into two versions controlling the base and mean flow eigenvalue, and a "flow manipulation control" which targets a minimal radial velocity intensity. The rationale behind this latter choice is to minimize the radial flow associated to the bubble formation and thereby to maintain the flow as columnar as possible. This strategy is based on the physical mechanism underpinning spiral vortex breakdown: the wake induced by the bubble triggers an absolute instability region that leads to the spiral vortex oscillation (Gallaire et al. [75] and Qadri et al. [80]). The mathematical framework required in these minimization problems is the optimal control theory. The objective functions for the two control strategies, to be defined in eqn. (2.7) and (2.8), are derived for the axisymmetric domain where the base flows and the relevant base and mean flow stability analyses were computed, bypassing larger and more expensive 3-D computations. This dimensionality reduction from the 3-D domain to a 2-D axisymmetric domain is performed thanks to the azimuthal Fourier decomposition naturally appearing in the eigenvalue analysis involved in the "flow stabilization control". In the context of the "flow manipulation control", only the axisymmetric base flow is considered, which is 2-D by definition. To be more specific the following objective function are defined,

Flow manipulation control

$$\text{Min } \mathcal{J}_{Manip}(\mathbf{F}) = \frac{1}{2} \iint_{\Omega_a} C_R(\mathbf{F})^2 d\Omega_a + \frac{\alpha}{2} \iint_{\Omega_a} \|\mathbf{F}\|^2 d\Omega_a, \quad (2.7)$$

Flow stabilization control

$$\text{Min } \mathcal{J}_{Stab}(\mathbf{F}) = |\Im(\omega)| + \frac{\alpha}{2} \iint_{\Omega_a} \|\mathbf{F}\|^2 d\Omega_a, \quad (2.8)$$

where \mathcal{J} is the objective function, \mathbf{F} the control variable (here a volume force), (\mathbf{C}, P) the state variables, ω the eigenvalue of the most unstable eigenmode linearized around the base (ω_{B_1}) or mean flow (ω_{M_1}) and α the scalar weight penalizing of the control cost (here the L_2 -norm of the volume force). We control the flow on the entire axisymmetric domain Ω_a through the radial and axial volume force components only. We made this choice to avoid trivial control solutions, which would simply decrease the tangential velocity magnitude, and to consider simple control distributions that are easier to visually translate in terms of potential appendage control devices. At convergence, the distributed control investigated will end to an optimal volume force (F_R^*, F_Z^*) and optimal state variables (\mathbf{C}^*, P^*) .

The gradient direction of these objective functions allows us to look for the minimum of \mathcal{J} through an iterative algorithm such as a conjugate-gradient method. This gradient is computed by the use of the Frechet derivative applied to a specific Lagrangian functional related to each optimal control problems. These Lagrangian functionals which are expressed in appendix 2.8.1, use the adjoint variables as Lagrange multipliers, $(\mathbf{C}^\dagger, P^\dagger)$ for the Navier-Stokes equations and $(\mathbf{c}^\dagger, p^\dagger)$ for the eigenvalue problem. The gradient direction is defined by eqn. (2.9) for the distributed control

$$\nabla \mathcal{J} = \mathbf{C}^\dagger + \alpha \mathbf{F} \text{ in } \Omega_a. \quad (2.9)$$

We should mention that the computation of the "flow stabilization control", where the leading eigenvalue directly intervenes, uses the sensitivity to a steady force $\nabla_F \omega_i$ as gradient direction, see Giannetti & Luchini [55] and Marquet et al. [6]. Since however the steady force is no more expected to remain infinitesimal, the non-linearity of the controlled Navier-Stokes equations is included in our optimization strategy, which can therefore be seen as a "nonlinear sensitivity" to a steady force. Since in the case of the canonical cylinder wake flow (Strykowski & Streenivasan [7] and Marquet et al. [6]), the linear sensitivity to a steady force, mimicking a small control cylinder, was sufficient to stabilize the flow close to the instability threshold, we have also investigated the efficiency of this linear sensitivity approach in the case of the spiral vortex breakdown. In this called "linear sensitivity-based finite amplitude control", the first

gradient direction $\nabla_F \omega_i = \mathbf{F}^{(o)}$ is multiplied by a finite amplitude A determined by a bisection method until the growth rate of the controlled leading eigenvalue is equal to zero. Next, we compute the "base flow manipulation control", the "base flow stabilization control", the "mean flow stabilization control" and the "linear sensitivity-based finite amplitude control" of the base and mean flow at a Reynolds value of $Re = 180$, before turning to a Reynolds value of $Re = 300$, further away from instability threshold, where only the "mean flow stabilization method" and the "linear sensitivity-based finite amplitude control" of the mean flow are determined.

2.4.2 Minimization and numerical methods

The optimal control problems are solved by a conjugate-gradient method where the direction is updated by a Polak-Ribiere method [107] and the step length is defined by an Armijo line search method, see Polak [108]. The initial step τ is dependent on the flow case and has been chosen to ensure convergence (see appendix 2.8.2) and the control weight is set to $\alpha = 10^{-5}$. Since the "base flow stabilization" is a nonconvex problem, the solution invariance was checked with respect to the parameter α , the initial step lengths and the optimization methods. The results are presented in appendix 2.8.2, where the solution has been found to be quasi-invariant under these choices in the methods.

The optimization algorithms for the "flow manipulation control" and the "base flow stabilization control" have been solved numerically with Freefem++ software in the same spirit as the base flow and eigenvalue problem computations, the same mesh and discretization technique are applied. In the case of the "mean flow stabilization control", the time averaged flow field is computed by DNS in NEK5000 before being transferred on the axisymmetric mesh. The other minimization steps of the conjugate-gradient algorithm are computed within Freefem++ until the next updated control (updated volume force) is obtained and returned to the 3-D DNS. The optimization process is stopped when the objective function \mathcal{J} reaches a minimum, see appendix 2.8.2.

2.5 Flow control results

2.5.1 Base flow manipulation control at $Re = 180$

The predictive control of the axisymmetric bubble base flow minimizing the quadratic objective function eqn. (2.7) at $Re = 180$ is displayed through the associated volume forcing in fig. 2.8(a) and the flow solution \mathbf{C}^* in fig. 2.8(b). The radial velocity component exhibited by the streamsurfaces is clearly reduced by the minimization algorithm, starting with a maximum value of $C_R^{max} = 0.3$ and ending with a value of $C_R^{max} = 0.037$ at convergence, leading to a columnar solution contrasting with the uncontrolled bubble breakdown, see fig. 2.5(a). Although the control target is not the recirculation bubble itself (in contrast to what was proposed in Boujo & Gallaire [109] for plane flows) or the recirculation intensity, we

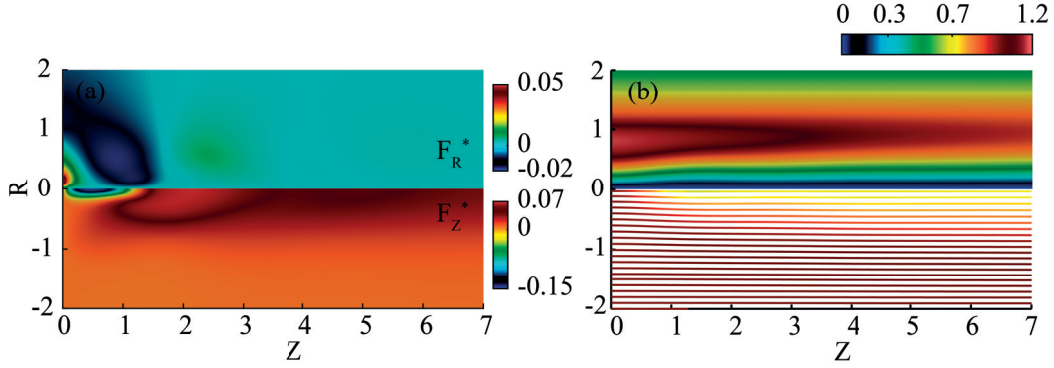


Figure 2.8 – Navier Stokes solutions for the base flow manipulation control at $Re = 180$ (b) and the associated volume force (a) at the minimum of the functional \mathcal{J}_{Manip} .

note that the use of our physical mechanism inspired surrogate objective entirely suppresses the recirculation: the minimum centerline axial velocity evolves from an uncontrolled value of $C_Z^{min} = -0.08$ to a controlled value of $C_Z^{min} = 0.8$. The volume force needed to restore a breakdown-free columnar solution is a predominating axial suction upstream of the nominal breakdown bubble combined with a subdominant radial correction, see fig. 2.8(a), both resulting in a control amplitude at convergence of $\|\mathbf{F}^*\| = 0.084$, see fig. 2.18 in appendix 2.8.2.

We have verified that the suppression of the recirculation bubble results in the stabilization of the spiral mode, as anticipated by the understanding of the underlying physical mechanism. Figure 2.9(a) (blue solid curve) demonstrates that the stabilization is achieved for a control amplitude of $\|\mathbf{F}\| = 0.028$, far beyond the minimizing control amplitude $\|\mathbf{F}^*\| = 0.084$. Note that this stabilization is accompanied by a 10% frequency shift (see the blue solid curve in fig. 2.9b). While physically well motivated the "flow manipulation control" will appear as suboptimal when compared to the "flow stabilization control" presented in section 2.5.2. As we will see, the comparison of fig. 2.8(a) and 2.10(a) will show that a lot of control authority is spent in reducing the radial velocity in regions of low receptivity of the instability. We therefore now turn our efforts to base flow stabilization control, trading the conservative but quadratic cost-functional, eqn. (2.7) for a more precise but nonconvex cost-functional, eqn. (2.8).

2.5.2 Base flow stabilization control at $Re = 180$

Despite the absence of mathematical proof, we have observed that the minimization algorithm targeting the eigenvalue growth rate of the spiral vortex breakdown mode developing on the base flow, herein referred to as "base flow stabilization control", succeeds in stabilizing the flow. As seen by the red solid curve in fig. 2.9(a), the normalized eigenvalue growth rate progressively decreases until stabilization for $\|\mathbf{F}^*\| = 0.0058$, i.e. 5 times less than the "flow manipulation control" approach. Interestingly, a finite amplitude recirculation bubble is still present in the stable, optimally controlled flow reported in fig. 2.10(b). The comparison with the uncontrolled base flow (see fig. 2.5a) shows that minimal changes in the recirculation

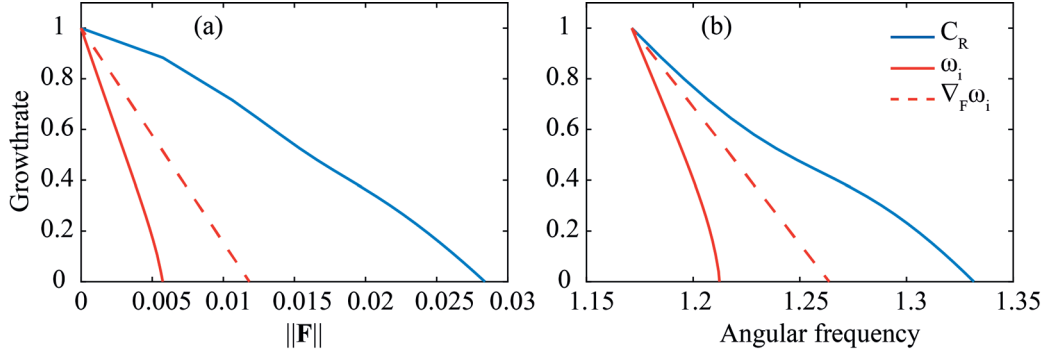


Figure 2.9 – Base flow dominant growth rate normalized by the most unstable uncontrolled eigenvalue at $Re = 180$ as a function of the norm of the control (a) and of the angular frequency of the mode (b) for the "flow manipulation control" (blue solid curve) and "base flow stabilization control" (red solid curve), and the "linear sensitivity-based finite amplitude control" (red dashed curve).

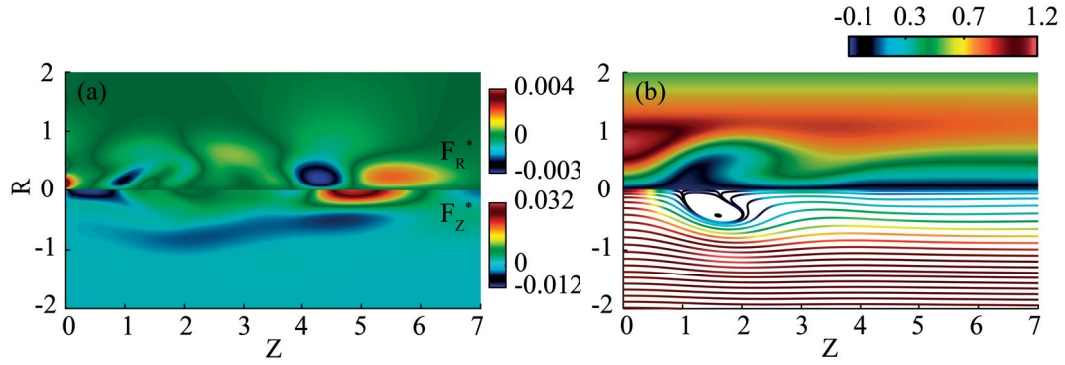


Figure 2.10 – Optimal "base flow stabilization control" force (a) and associated flow solution (b) at $Re = 180$ and $S = 1.095$.

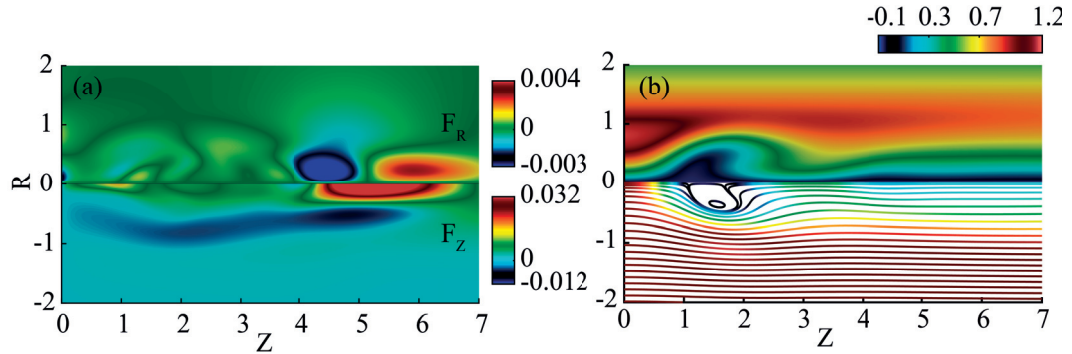


Figure 2.11 – Suboptimal "linear sensitivity-based finite amplitude control" (a) and associated flow solution (b) at $Re = 180$ and $S = 1.095$.

bubble are sufficient to restore the stability of the flow and this stabilization goes together with a small frequency shift reported in fig. 2.9(b).

The determination of this optimal, nonlinear, predictive control requires a computationally expensive iterative minimization procedure. A linear sensitivity-based finite amplitude control therefore provides a promising alternative. The latter is included in red dashed curve in fig. 2.9(a), showing that, although linearity is preserved, flow stabilization is achieved for approximately two times more control amplitude. A comparison of both volume force distributions in fig. 2.10(a) and 2.11(a) shows in addition that the first gradient direction may deviate quite substantially from the nonlinear optimal control. While the latter suggests to decelerate the flow in the inlet region, thereby pulling on the recirculation bubble, the sensitivity-based centerline axial force accelerates the flow upstream of the bubble, thereby pushing the bubble downstream. This results in slightly different flow topologies (see fig. 2.10b and 2.11b), noting that in both cases, the bubble is slightly smaller than in the nominal, unstable, base flow reported in fig. 2.5(a). In contrast the volume forces acting in bubble wake around $Z = 5$ are very similar and act to accelerate the flow in the wake region. This is also clearly visible from the resulting controlled flows (fig. 2.10b and 2.11b) when compared to the base flow (fig. 2.5a). All these results illustrate that, even for moderate growth rates, the finite amplitude linear sensitivity to a steady force can remain significantly suboptimal.

We now turn our attention to the mean flow stabilization control, first at $Re = 180$.

2.5.3 Mean flow stabilization at $Re = 180$

The control magnitude and eigenvalue path during the minimization process are exhibited in solid red lines in fig. 2.12(a) and (b) for the "mean flow stabilization control" at $Re = 180$, together with the "linear sensitivity-based finite amplitude control" of the mean flow (red dashed lines). The optimal mean flow stabilization control is reached for a norm of $\|\mathbf{F}^*\| = 0.0057$ while the linear sensitivity-based finite amplitude control stabilizes the flow for $\|\mathbf{F}^*\| = 0.014$. These values compare very well with those obtained for the base flow stabilization control. The volume force and controlled solution, see fig. 2.13, are also very similar to those of the base flow control, see fig. 2.10. This indicates the consistency of both approaches targeting the dominant growth rate of the mean and base flows respectively, for parameters close to the bifurcation threshold, even if the least unstable eigenvalues of the base and mean flow differ by a factor 10. The 3-D vorticity contour of the controlled flow solution is plotted in fig. 2.16(a), demonstrating that the axisymmetry of the flow is restored and the inspection of the time-dependent traces remains stationary.

The linear sensitivity-based finite amplitude control about the mean flow is presented in fig. 2.14(a) and represents the initial sensitivity to a steady force for $Re = 180$. The receptivity distribution, while suboptimal, is very similar to the nonlinear sensitivity map, and enables a correct identification of the maximum and minimum locations.

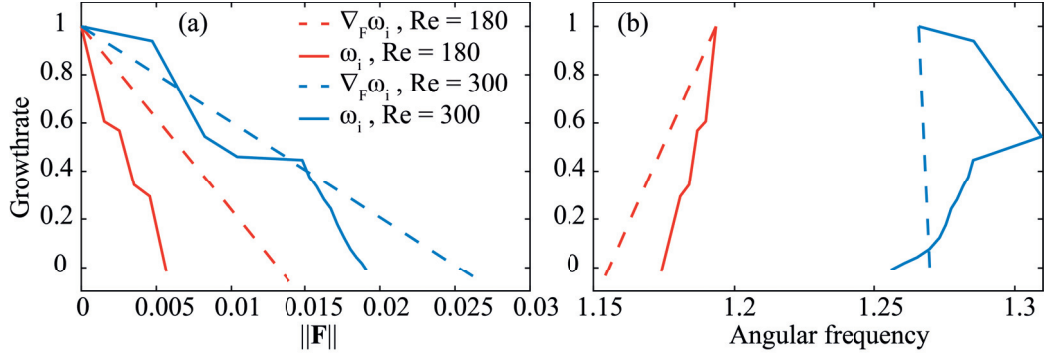


Figure 2.12 – Mean flow dominant growth rate, normalized by the most unstable uncontrolled mean flow eigenvalue at $Re = 180$ (red curves) and $Re = 300$ (blue curves) as a function of the norm of the control (a) and of the angular frequency of the mode (b) for the nonlinear mean flow stabilization (solid curves) and the "linear sensitivity-based finite amplitude control" (dashed curves).

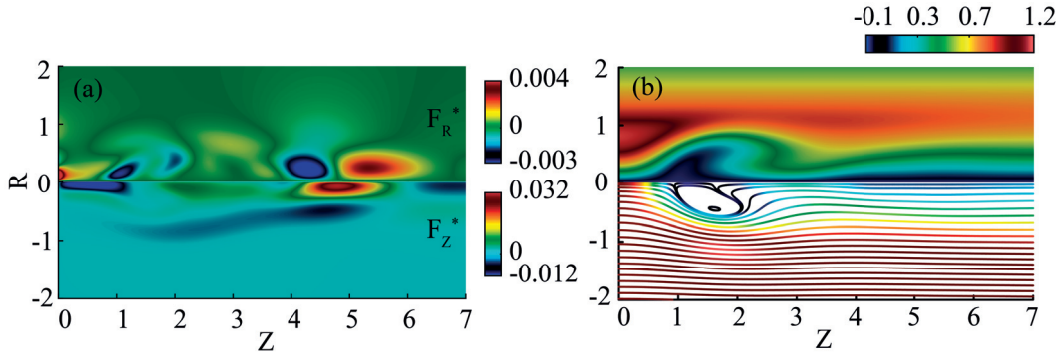


Figure 2.13 – Time averaged 3-D Navier Stokes solution of the "mean flow stabilization control" (b) and the related force applied (a) for $Re = 180$ at convergence.

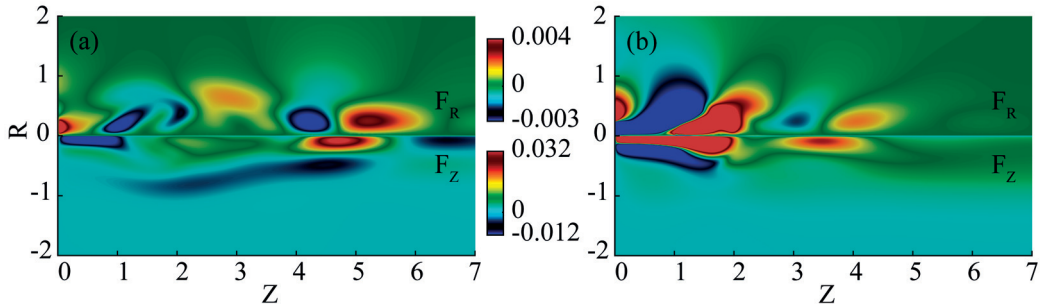


Figure 2.14 – Suboptimal "linear sensitivity-based finite amplitude control" about the mean flow at $Re = 180$ (a) and $Re = 300$ (b) for a swirl number of $S = 1.095$.

2.5.4 Mean flow stabilization at $Re = 300$

At $Re = 300$, the minimization path is less straight, and the optimal solution (solid blue line in fig. 2.12) seems to oscillate around the trajectory of the "linear sensitivity-based finite amplitude control" (dashed blue line in fig. 2.12) before eventually sensibly reducing the eigenvalue growth rate at the end of the algorithm. The control magnitude is $\|\mathbf{F}^*\| = 0.019$ at convergence, to be compared with the value of $\|\mathbf{F}^*\| = 0.027$ required for the mean flow "linear sensitivity-based finite amplitude control". The optimal volume force as well as the resulting controlled flow solution are exhibited in fig. 2.15. In contrast to the Reynolds number $Re = 180$ case, most of the control effort is located in the recirculating bubble region while little forcing acts in the wake region. The upstream forcing blows the bubble downstream, as opposed to the optimal forcing at $Re = 180$, where the bubble was sucked. The controlled flow solution has no recirculation, but adopts instead a wavy form and demonstrates therefore that a large modification of the mean flow is required to restore its stability, while a small modification is required at a Reynolds value of $Re = 180$. The 3-D solution is displayed in fig. 2.16(b), demonstrating the axisymmetrization of the controlled flow. Although several waves are observed on the vorticity contour, we have checked that the controlled flow remains steady. In addition, the "linear sensitivity-based finite amplitude control" about the mean flow is presented in fig. 2.14(b) and represents the initial sensitivity to a steady force for $Re = 300$. Similarly to the "mean flow stabilization control" at a Reynolds value of $Re = 180$, the linear receptivity well identifies the maximum and minimum of the nonlinear receptivity map (see fig. 2.15a), although it remains suboptimal (see fig. 2.12).

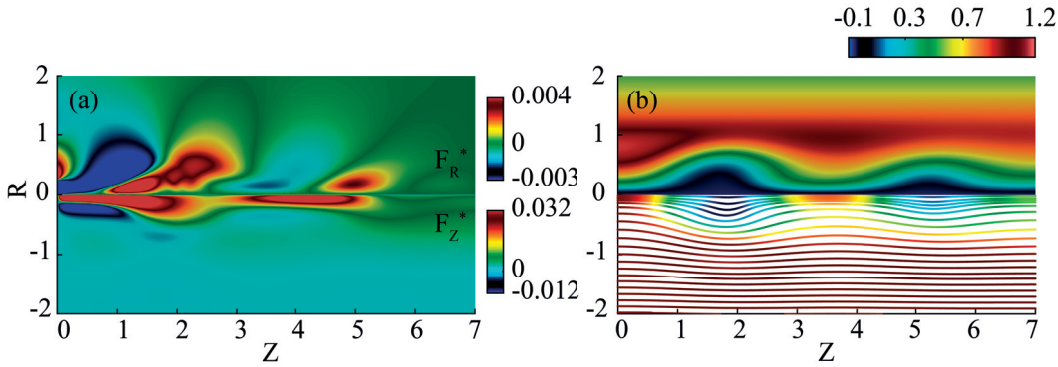


Figure 2.15 – Time averaged 3-D Navier Stokes solution of the mean flow stabilization control (b) and the related force applied (a) for $Re = 300$ at convergence.

2.6 Discussion & Conclusion

In this study, we have first discussed the validity of the base flow and mean flow stability analysis in predicting the frequency of the self-sustained single spiral vortex breakdown mode appearing for sufficient swirl and Reynolds numbers in the flow geometry of Ruith et al. [57]. Fixing the swirl number to $S = 1.095$, we have seen that the two stability analyses coincide

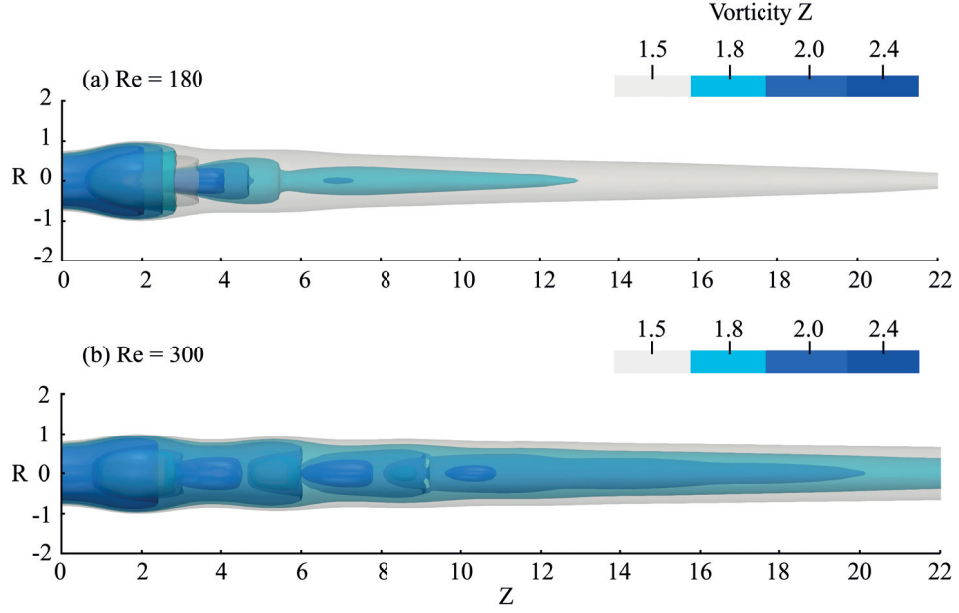


Figure 2.16 – 3-D Navier Stokes vorticity of the optimal mean flow stabilization control solution for $Re = 180$ (a) and $Re = 300$ (b). These 3D-flows are steady solutions and they correspond to the mean flows (and therefore base) reported in fig. 2.13 and 2.15.

with the limit cycle frequency close to the bifurcation threshold until $Re \sim 200$. For larger Reynolds number, the mean flow stability analysis provides an excellent prediction of the dominant frequency in the nonlinear simulations, in contrast to the base flow stability analysis, as the consequence of an important mean flow modification: while the base flow has two recirculation bubbles at $Re = 300$, the mean flow has only one much smaller recirculation bubble. This result emphasizes the successful prediction provided by the stability analysis around the mean flow, which was also recently reported for turbulent mean flow in industrial applications (Oberleithner et al. [49], Paredes et al [50], Tammisola & Juniper [48] and Pasche et al. [65]). Moreover in the present study, we observe a second unstable global mode above a Reynolds value of $Re = 300$. This second instability should be interpreted in light of the self-consistent model for saturation dynamics of self-sustained instabilities (Mantić-Lugo et al. [84]).

We have then investigated the predictive control of the spiral vortex breakdown based on adjoint optimization method. The spiral vortex breakdown was quenched by an axisymmetric steady volume force distribution on $(\mathbf{e}_R, \mathbf{e}_Z)$ obtained by minimizing two different objective functions, a nonconvex objective function targeting the most unstable eigenvalue growth rate of the base or mean flow stability analyses, that directly acts on the instability marker ("flow stabilization control") and a quadratic objective function minimizing the norm of the radial velocity distribution that is inspired by the physical mechanism governing spiral vortex breakdown ("flow manipulation control"). These control strategies were computed in an axisymmetric domain avoiding expensive 3-D minimization computations. This dimensionality

reduction from the 3-D domain to a 2-D axisymmetric domain is performed thanks to the azimuthal Fourier decomposition naturally appearing in the eigenvalue analysis involved in the "flow stabilization control". We can therefore expect to tackle self-sustained instability control at larger Reynolds numbers. The gradient direction involved in the minimization of the "flow stabilization control" uses the linear sensitivity to a steady force (Giannetti & Luchini [55] and Marquet et al. [6]) at each iteration step. A simpler approach has also been followed where the first gradient direction is chosen and only the amplitude varied referred to as "linear sensitivity-based finite amplitude control".

The "flow manipulation control" succeeded in stabilizing the flow at $Re = 180$, to the price of a significant control cost. This surrogate control was found suboptimal in contrast to the "flow stabilization control" but the direction of the volume force upstream of the bubble is identical and pulls on the recirculation bubble. The "linear sensitivity-based finite amplitude control" was found also successful but suboptimal. While the force distribution was correct in the vortex breakdown bubble wake, its sign was opposite to the optimal stabilization control upstream of the bubble, demonstrating the fragility of this computationally cheaper method.

The control of the mean flow was found equivalent to the base flow control at $Re = 180$. Both yielded a controlled flow preserving its recirculation bubble. The same control norm and force distribution are found for the base and mean flow control, while the growth rate differs by a factor 10 between the base and mean eigenvalue, showing the consistency of the base and mean flow eigenvalues control. This result emphasizes the non-neutrality of the eigenvalue growth rate and its practical usefulness to apply such control strategies. This encouraged us to explore the mean flow stabilization control at a much larger Reynolds number of $Re = 300$. Targeting only the dominant mean flow growth rate, the optimal control was found successful in quenching all spiral modes for a control cost four times higher than at $Re = 180$, yielding a controlled flow solution where recirculation regions were quenched by a volume force pushing the bubble downstream. The "linear sensitivity-based finite amplitude control" was also found successful, although suboptimal.

This also suggests using this technique to stabilize instabilities prevailing in a turbulent background, i.e. in turbulent flows dominated by a self-sustained periodic instability, by using the sensitivity computed by Meliga et al. [47] for turbulent flows. In the context of spiral vortex breakdown, a natural extension of the present work is the control of the precessing vortex rope in Francis turbines operating at off-design conditions (Pasche et al. [110]). While the finite amplitude volume force projected on the radial and axial component may appear as a pure theoretical concept, it can be in principle practically realized by an axisymmetric appendage to control the flow without external energy or it can be used as a design step to access the most receptive region of the instability by applying blowing or suction along a suitable region. Alternatively the present control strategy can be generalized to boundary control. First attempts (section 2.9) indicate that the instability can be quenched successfully at Reynolds $Re = 180$ by pure radial inlet injection. This result contrasts with the distributed control, which shows a larger contribution of the axial component (fig. 2.13). Turning back

to distributed control, we underline the correct identification by the mean flow based linear sensitivity map of the minimum and maximum of the nonlinear receptivity regions, both close to the threshold $Re = 180$ and far away from it $Re = 300$. Linear sensitivity maps may therefore be sufficient to develop an appendage accessing these locations, although their validity cannot be ensured *a priori*. Optimal nonlinear sensitivity maps, as developed in this study, appear therefore as the most consistent and promising approach for industrial applications (Paredes et al. [50] and Pasche et al. [110]).

2.7 Appendix: Validation and convergence studies

2.7.1 Validation of the 3-D DNS

The 3-D direct numerical flow simulations have been validated by changing the mesh size, the mesh topology, the boundary conditions, the domain dimensions and the time step for a fixed swirl number $S = 1.095$ and Reynolds number $Re = 200$. The convergence criterion is based on the deviation of the frequency and the amplitude of the radial velocity component of the single helical vortex flow. These values are monitored at $(R, \theta, Z) = (0.1, 0.0, 5.0)$ which is located after the bubble, in the helical flow region. The results of this convergence study are displayed on Table 2.2. The topology of the mesh is an O-grid type with two different cell arrangements in the center: diamond cells that almost preserve the azimuthal symmetry of the problem and square cells. All cells have a P_{10} and P_8 spectral discretizations with a uniform number of nodes $n_x \times n_y \times n_z = 10 \times 10 \times 10$ and $n_x \times n_y \times n_z = 8 \times 8 \times 8$ for velocities and pressure respectively. The robustness of the solutions with respect to the convective boundary

Case	Topology	BC on Γ_{ext}	Z_{max}	R_{max}	n_e	CFL	3-D (Amp,freq)	Eigenvalue
M5	Diamonds	free-outflow	40	50	11040	0.37	(0.1299,0.1991)	(0.01427,1.25009)
M6	Diamonds	free-outflow	60	50	16320	0.37	(0.1224,0.1991)	(0.01454,1.25193)
M7	Diamonds	free-outflow	40	50	29696	0.44	(0.1284,0.1984)	(0.01475,1.25175)
M8	Squares	No slip	40	50	12512	0.34	(0.1231,0.1991)	-
M9	Diamonds	free-outflow	40	50	11040	0.18	(0.1267,0.1991)	-

Table 2.2 – Convergence of the 3-D numerical flow simulations and eigenvalues of mean flow for $Re = 200$, $S = 1.095$.

condition on the outlet Γ_{out} is investigated by changing the length of the reference domain to $Z_{max} = 60$ for mesh M6 instead of $Z_{max} = 40$. The radial unconfinement is guaranteed by the invariance in regard to the lateral boundary conditions (free-outflow or no-slip). The CFL number invariance is also investigated on the mesh M9 and finally a refined mesh M7 concludes the convergence analysis. In the present study the mesh M5 is the reference mesh for the results presented.

2.7.2 Eigenvalue convergence of the base flow

The mesh of the axisymmetric domain is designed in a way that the convergence of the most unstable eigenvalue is obtained when solving the eigenvalue problem related to eqn. (2.6). Therefore different domain sizes and meshes have been investigated, and the values of the most eigenvalue are resumed on Table 2.3. The mesh M1 has been selected for the present study and the same mesh is used for the base flow computation.

Mesh	Z_{max}	R_{max}	Sponge length	n_e	Eigenvalue
M1	40	50	60	408866	(0.081167,1.20117)
M2	40	50	60	633502	(0.081610,1.20010)
M3	80	50	60	556443	(0.081277,1.20091)
M4	40	60	60	416488	(0.081175,1.20116)

Table 2.3 – Eigenvalue sensitivity to the mesh configuration for $Re = 200$, $S = 1.095$.

2.7.3 Eigenvalue convergence of the mean flow

The mesh designed for the eigenvalue problem of the base flow is kept for the eigenvalue problem of the mean flow except that the sponge region is removed. The domain without the sponge region exactly fits the 3-D domain avoiding the need for an extrapolation procedure. A spectral interpolation is solely required to transfer the time averaged flow field to the axisymmetric velocity space. We have to mention that the convective boundary condition at the outlet of the 3-D domain is replaced by a free-outflow condition at the outlet of the axisymmetric domain. This does not have any impact on the convergence of the eigenvalues, as supported by the invariance of the eigenvalue with respect to the length of the 3-D domain (see the last column of Table 2.2). For the reference mesh M5, the refined mesh M7 and the longer domain mesh M6, both the frequency and the growth rates of the eigenvalues are similar.

2.8 Appendix: Optimal control problem

2.8.1 Optimal control theory

The formalism of the optimal control problem for the "flow manipulation control" and the "flow stabilization control" is introduced in this appendix. Our aim is to solve the following

general constrained minimization problem:

$$\begin{aligned}
 &\text{find } \mathbf{F} \in \mathcal{U}, \quad \mathbf{F} = \min \mathcal{J}(\mathbf{F}, \mathbf{C}) \quad \text{with} \\
 &(\mathbf{C} \cdot \nabla) \mathbf{C} = -\nabla P + Re^{-1} \nabla^2 \mathbf{C} + \mathbf{F} && \text{in } \Omega_a \\
 &\nabla \cdot \mathbf{C} = 0 && \text{in } \Omega_a \\
 &-i\omega \mathbf{c} + (\mathbf{C} \cdot \nabla) \mathbf{c} + (\mathbf{c} \cdot \nabla) \mathbf{C} = -\nabla p + Re^{-1} \nabla^2 \mathbf{c} && \text{in } \Omega_a \\
 &\nabla \cdot \mathbf{c} = 0 && \text{in } \Omega_a \\
 &G(\mathbf{C}) = 0 && \text{on } \Gamma \\
 &g(\mathbf{c}) = 0 && \text{on } \Gamma,
 \end{aligned} \tag{2.10}$$

where \mathcal{J} is the objective function, $(\mathbf{C}, P) \in \mathcal{V}$ the state variables, \mathbf{F} the control variable, $[\mathbf{c}, p]$ the global eigenmodes, Ω the domain, Γ the boundaries of the domain, G and g the associated boundary conditions and \mathcal{V} and \mathcal{U} two Hilbert spaces.

We consider first the "flow manipulation problem" for a distributed control, the objective function of which reads:

$$\mathcal{J}_{Manip}(\mathbf{F}) = \frac{1}{2} \int_{\Omega_a} \|\mathbf{C}(\mathbf{F}) - \mathbf{z}_d\|^2 d\Omega_a + \frac{\alpha}{2} \int_{\Omega_a} \|\mathbf{F}\|^2 d\Omega_a, \tag{2.11}$$

with $\mathbf{z}_d = \mathbf{0}$, $\mathbf{C} = (C_R, 0, 0)$ and $\mathbf{F} = (F_R, 0, F_Z)$. This objective function targets a minimal radial velocity component controlled by radial and axial distributed volume forces. Since we have defined the objective function, the associated Lagrangian functional with respect to the governing equations expresses as

$$\begin{aligned}
 \mathcal{L}([\mathbf{C}, P], \mathbf{F}, [\mathbf{C}^\dagger, P^\dagger]) &= \mathcal{J}(\mathbf{C}, \mathbf{F}) - a(\mathbf{C}, \mathbf{C}^\dagger) - d(\mathbf{C}, \mathbf{C}, \mathbf{C}^\dagger) \\
 &\quad - b(\mathbf{C}^\dagger, P) - b(\mathbf{C}, P^\dagger) + \langle \mathbf{F}, \mathbf{C}^\dagger \rangle, \tag{2.12}
 \end{aligned}$$

where $a(.,.)$, $b(.,.)$ are the bilinear form of the viscous, pressure and divergence, $\langle ., . \rangle$ is the Hermitian inner product, $d(.,.,.)$ is the trilinear form and $[\mathbf{C}^\dagger, P^\dagger]$ are the Lagrange multipliers, also called adjoint variables. Observe that the eigenvalue equation does not appear in this Lagrangian, since it is not a control target, as we manipulate the base flow by targeting the radial velocity intensity as a proxy for flow non-parallelism. The distinct set of equations systems solved in the minimization problem are derived by satisfying the first order optimal condition of the Lagrangian, according to

$$\left. \frac{d}{d\epsilon} \mathcal{L}([\dots + \epsilon \Phi]) \right|_{\epsilon=0} = 0. \tag{2.13}$$

This condition is computed by the Frechet derivative, where $\Phi \in \mathcal{V}$, is test function associated

to each variable and leads to the state equations, the adjoint problem and the optimality condition. These systems of equations are expressed in strong form with the boundary conditions related to our problem in eqns. (2.14), (2.15) and (2.16).

State equations:

$$\begin{aligned}
 \nabla \mathbf{C} \cdot \mathbf{C} &= -\nabla P + Re^{-1} \nabla^2 \mathbf{C} + \mathbf{F} && \text{in } \Omega_a \\
 \nabla \cdot \mathbf{C} &= 0 && \text{in } \Omega_a \\
 C_R(R) = 0, C_\theta(R) = S\Psi, C_Z(R) = 1 &&& \text{on } \Gamma_{in} \\
 C_R = C_\theta = \partial_R C_Z = 0 &&& \text{on } \Gamma_{axis} \\
 Re^{-1} \partial_{\mathbf{n}} \mathbf{C} - P \mathbf{n} &= 0 && \text{on } \Gamma_{ext}, \Gamma_{out}
 \end{aligned} \tag{2.14}$$

Adjoint equations:

$$\begin{aligned}
 \nabla^T \mathbf{C} \cdot \mathbf{C}^\dagger - \nabla \mathbf{C}^\dagger \cdot \mathbf{C} &= -\nabla P^\dagger + Re^{-1} \nabla^2 \mathbf{C}^\dagger + \mathbf{C} - \mathbf{z}_d && \text{in } \Omega_a \\
 \nabla \cdot \mathbf{C}^\dagger &= 0 && \text{in } \Omega_a \\
 \mathbf{C}^\dagger &= 0 && \text{on } \Gamma_{in} \\
 C_R^\dagger = C_\theta^\dagger = \partial_R C_Z^\dagger = 0 &&& \text{on } \Gamma_{axis} \\
 Re^{-1} \partial_{\mathbf{n}} \mathbf{C}^\dagger - P^\dagger \mathbf{n} + (\mathbf{C} \cdot \mathbf{n}) \mathbf{C}^\dagger &= 0 && \text{on } \Gamma_{ext}, \Gamma_{out}
 \end{aligned} \tag{2.15}$$

Optimality condition:

$$\nabla \mathcal{J} = \mathbf{C}^\dagger + \alpha \mathbf{F} \tag{2.16}$$

As highlighted in the body of the paper, the main advantage of this flow manipulation control approach is to ensure a quadratic objective function.

We next consider the direct so-called "flow stabilization control" problem for a distributed control, the objective function of which reads:

$$\mathcal{J}_{Stab}(\mathbf{F}) = |\Im(\omega)| + \frac{\alpha}{2} \iint_{\Omega_a} \|\mathbf{F}\|^2 d\Omega_a. \tag{2.17}$$

The Lagrangian functional of this minimization problem is expressed as:

$$\begin{aligned} \mathcal{L}(\omega, [\mathbf{c}, p], [\mathbf{C}, P], [\mathbf{c}^\dagger, p^\dagger], [\mathbf{C}^\dagger, P^\dagger], \mathbf{F}) = & \mathcal{J}(\omega, \mathbf{F}) - t(\mathbf{c}, \mathbf{c}^\dagger) - a(\mathbf{c}, \mathbf{c}^\dagger) \\ & - d(\mathbf{c}, \mathbf{C}, \mathbf{c}^\dagger) - d(\mathbf{C}, \mathbf{c}, \mathbf{c}^\dagger) - b(\mathbf{c}^\dagger, p) - b(\mathbf{c}, p^\dagger) - a(\mathbf{C}, \mathbf{C}^\dagger) - d(\mathbf{C}, \mathbf{C}, \mathbf{C}^\dagger) \\ & - b(\mathbf{C}^\dagger, P) - b(\mathbf{C}, P^\dagger) + \langle \mathbf{F}, \mathbf{C}^\dagger \rangle, \end{aligned} \quad (2.18)$$

where $t(.,.)$ is the mass matrix of the time derivative including the eigenvalue ω . Following the same procedure as for the previous problem, the stationary point of the Lagrangian functional leads to a system of 6 equations, the state equation, the direct eigenvalue problem, the adjoint eigenvalue problem, a normalization condition, the adjoint problem and the optimality condition. These problems are expressed in strong form with the boundary conditions related to our study in eqns (2.19), (2.20), (2.21), (2.22), (2.23) and (2.24).

State equations:

$$\begin{aligned} \nabla \mathbf{C} \cdot \mathbf{C} &= -\nabla P + Re^{-1} \nabla^2 \mathbf{C} + \mathbf{F} && \text{in } \Omega_a \\ \nabla \cdot \mathbf{C} &= 0 && \text{in } \Omega_a \\ C_R(R) = 0, \quad C_\theta(R) = S\Psi, \quad C_Z(R) = 1 && \text{on } \Gamma_{in} \\ C_R = C_\theta = \partial_R C_Z = 0 && \text{on } \Gamma_{axis} \\ Re^{-1} \partial_{\mathbf{n}} \mathbf{C} - P \mathbf{n} = 0 && \text{on } \Gamma_{ext}, \Gamma_{out} \end{aligned} \quad (2.19)$$

Direct eigenvalue equations:

$$\begin{aligned} -i\omega \mathbf{c} + \nabla_m \mathbf{c} \cdot \mathbf{C} + \nabla \mathbf{C} \cdot \mathbf{c} &= -\nabla_m p + Re^{-1} \nabla_m^2 \mathbf{c} && \text{in } \Omega_a \\ \nabla_m \cdot \mathbf{c} &= 0 && \text{in } \Omega_a \\ \mathbf{c} &= 0 && \text{on } \Gamma_{in} \\ \text{c.f. Table 2.1} && \text{on } \Gamma_{axis} \\ Re^{-1} \partial_{\mathbf{n}} \mathbf{c} - p \mathbf{n} &= 0 && \text{on } \Gamma_{ext}, \Gamma_{out} \end{aligned} \quad (2.20)$$

Adjoint eigenvalue equations:

$$\begin{aligned}
 i\omega^* \mathbf{c}^\dagger + \nabla_m^T \mathbf{C} \cdot \mathbf{c}^\dagger - \nabla_m \mathbf{c}^\dagger \cdot \mathbf{C} &= -\nabla_m p^\dagger + Re^{-1} \nabla_m^2 \mathbf{c}^\dagger & \text{in } \Omega_a \\
 \nabla_m \cdot \mathbf{c}^\dagger &= 0 & \text{in } \Omega_a \\
 \mathbf{c}^\dagger &= 0 & \text{on } \Gamma_{in} \\
 \text{c.f. Table 2.1} & & \text{on } \Gamma_{axis} \\
 Re^{-1} \partial_n \mathbf{c}^\dagger - p^\dagger \mathbf{n} + (\mathbf{C} \cdot \mathbf{n}) \mathbf{c}^\dagger &= 0 & \text{on } \Gamma_{ext}, \Gamma_{out}
 \end{aligned} \tag{2.21}$$

Normalization condition:

$$1 - \langle \mathbf{c}, \mathbf{c}^\dagger \rangle = 0 \quad \text{in } \Omega_a \tag{2.22}$$

Adjoint equations:

$$\begin{aligned}
 \nabla^T \mathbf{C} \cdot \mathbf{C}^\dagger - \nabla \mathbf{C}^\dagger \cdot \mathbf{C} &= -\nabla P^\dagger + Re^{-1} \nabla^2 \mathbf{C}^\dagger + \nabla_m \mathbf{c}^\dagger \cdot \mathbf{c}^* - (\nabla_m \mathbf{c})^H \cdot \mathbf{c}^\dagger & \text{in } \Omega_a \\
 \nabla \cdot \mathbf{C}^\dagger &= 0 & \text{in } \Omega_a \\
 \mathbf{C}^\dagger &= 0 & \text{on } \Gamma_{in} \\
 C_R^\dagger = C_\theta^\dagger = \partial_R C_Z^\dagger &= 0 & \text{on } \Gamma_{axis} \\
 Re^{-1} \partial_n \mathbf{C}^\dagger - P^\dagger \mathbf{n} + (\mathbf{C} \cdot \mathbf{n}) \mathbf{C}^\dagger - (\mathbf{c}^* \cdot \mathbf{n}) \mathbf{c}^\dagger &= 0 & \text{on } \Gamma_{ext}, \Gamma_{out}
 \end{aligned} \tag{2.23}$$

Optimality condition:

$$\nabla \mathcal{J} = \mathbf{C}^\dagger + \alpha \mathbf{F} \tag{2.24}$$

These systems of equations are solved iteratively by a conjugate gradient method in the FreeFEM++ software, except for the mean flow, which is computed by NEK5000 and then interpolated on the 2-D axisymmetric mesh.

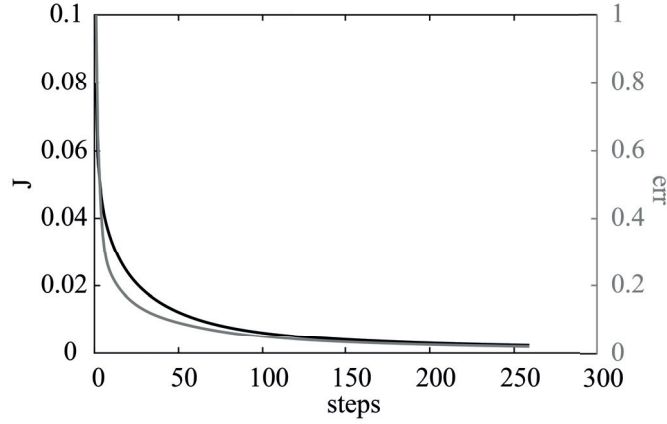


Figure 2.17 – Objective function evolution as a function of iteration steps and normalized error.

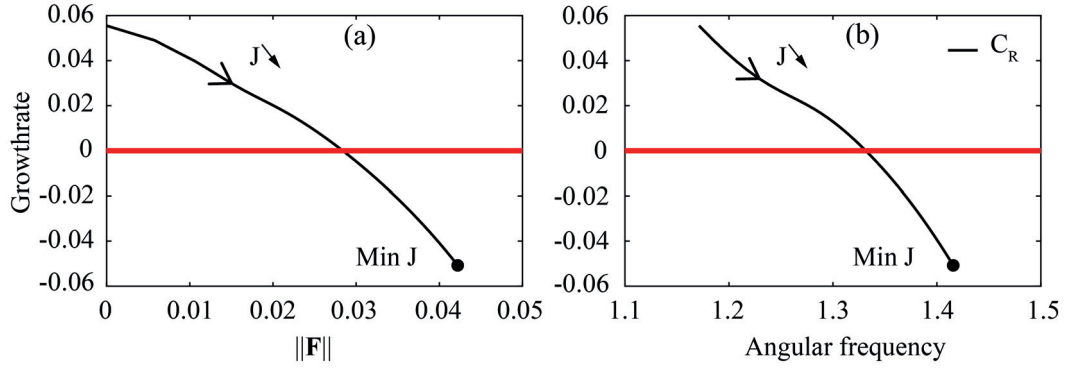


Figure 2.18 – Dominant growth rate as a function of the norm of the control (a) and of the angular frequency of the mode (b) for the "flow manipulation control".

2.8.2 Validation of the optimal control problem

The evolution of the "flow manipulation" objective function and its normalized error between two consecutive steps are displayed in fig. 2.17 and the variation of the eigenvalue during the minimization process is displayed in fig. 2.18. The algorithm converges to a minimum where the radial velocity component of the flow is indeed very small. The most unstable eigenvalue is stabilized before the minimum of the objective function is reached.

The minimization of the objective function associated to the "flow stabilization control" is nonconvex and therefore several solutions may exist. All these solutions are legitimate for the problem but the set of these solutions must be almost invariant with respect to the optimization algorithm to obtain an optimal control. Thus we compute the "flow stabilization control" for different initial step length τ and two different algorithms. The first one is the conjugate gradient method that is used for the previously outlined optimization procedure and the second is the steepest descent method. The results are displayed in fig. 2.19 and we observe that the path of the eigenvalue during the minimization procedure is similar in all

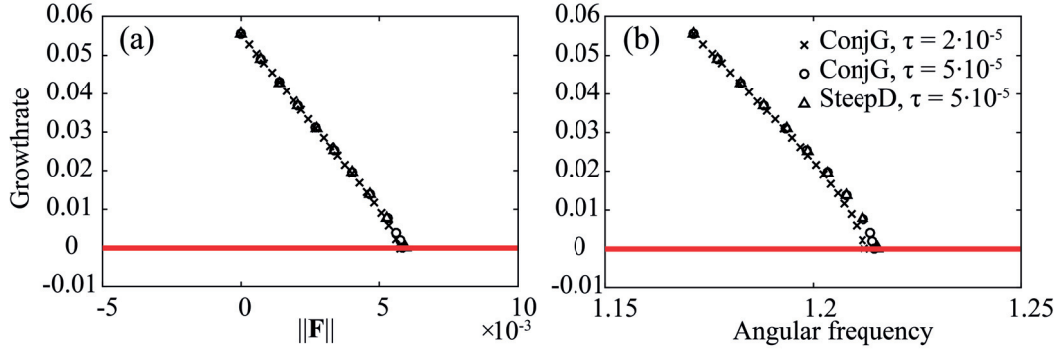


Figure 2.19 – Dominant growth rate as a function of the norm of the control (a) and of the angular frequency of the mode (b) for different minimization algorithms.

cases. The solution thus appears as quasi-independent of the computational parameters, ensuring its robustness and validity. Finally, the influence of α is not presented here because the solutions were seen to be invariant with respect to this parameter. We set $\alpha = 10^{-5}$ in the present study.

2.9 Appendix: Boundary control

The minimization algorithm, presented in this study, can be modified to control the inlet boundary condition of the Grabowski & Berger [78] vortex at $Re = 180$ considering, for instance, the eigenvalue growth rate linearized around the base flow. The objective function is written as

Inlet flow stabilization control

$$\text{Min } \mathcal{J}_{Stab}(\mathbf{f}) = |\Im(\omega)| + \frac{\alpha}{2} \int_{\Gamma_{in}} \|\mathbf{f}\|^2 d\Gamma_{in}, \quad (2.25)$$

where $\alpha = 1 \cdot 10^{-5}$ is kept constant and the force on the inlet boundary is projected on the radial and axial components as for the distributed control. The state equation reads:

State equations:

$$\begin{aligned} \nabla \mathbf{C} \cdot \mathbf{C} &= -\nabla P + Re^{-1} \nabla^2 \mathbf{C} && \text{in } \Omega_a \\ \nabla \cdot \mathbf{C} &= 0 && \text{in } \Omega_a \\ C_R(R) &= 0 + f_R, \quad C_\theta(R) = S\Psi, \quad C_Z(R) = 1 + f_Z && \text{on } \Gamma_{in} \\ C_R &= C_\theta = \partial_R C_Z = 0 && \text{on } \Gamma_{axis} \\ Re^{-1} \partial_{\mathbf{n}} \mathbf{C} - P \mathbf{n} &= 0 && \text{on } \Gamma_{ext}, \Gamma_{out}, \end{aligned} \quad (2.26)$$

and the gradient direction that minimize the eigenvalue growth rate is given by

$$\nabla \mathcal{J} = -\frac{d\mathbf{C}^\dagger}{d\mathbf{n}} + \alpha \mathbf{f} \quad \text{on } \Gamma_{in}, \quad (2.27)$$

This algorithm follows the same step as for the distributed control. The base flow equations, the direct eigenvalue equations, the adjoint eigenvalue equations, the normalization condition, the adjoint equations are solved to compute the optimality condition eqn. (2.27). The results of this control strategy applied to the base flow and for a Reynolds value of $Re = 180$ are displayed in fig. 2.20 and 2.21. The optimal inlet condition reported in fig. 2.20(a) successfully

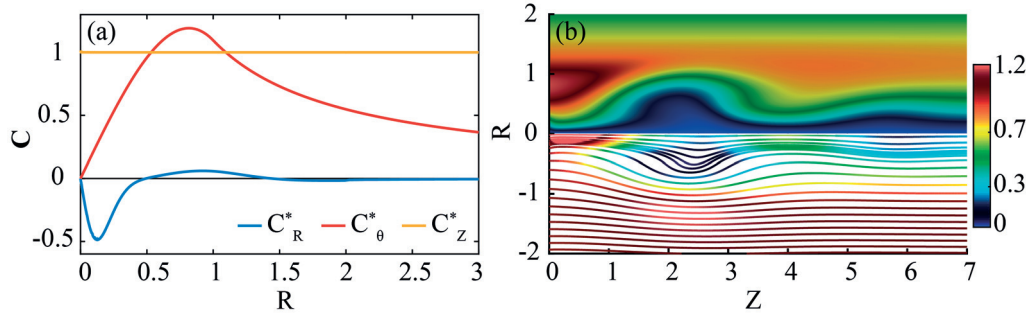


Figure 2.20 – Optimal inlet velocity profile to stabilize the spiral vortex breakdown at a Reynolds value of $Re = 180$, determined by controlling the eigenvalue growth rate from the base flow (a) and the associated flow distribution (b).

stabilizes the spiral vortex breakdown by imposing a negative radial velocity, and no noticeable modification to the axial component. Such inlet velocity profile leads to a controlled flow solution (see fig. 2.20b) suppressing the recirculation zone and having the same wavy form as for the distributed control at a Reynolds value of $Re = 300$ (see fig. 2.15b). The control magnitude and the eigenvalue paths during the minimization process are illustrated in fig. 2.21 (yellow solid curves). These dimensionless curves are superimposed with the distributed control results obtained in this paper, although the the norms of the distributed and boundary controls have different physical meanings. The yellow solid curve in fig. 2.21(a) reports the stabilization of the most unstable eigenvalue growth rate by the inlet flow stabilization control.

We surprisingly observe that the axial velocity component is kept untouched, while solely the radial velocity component is modified to quench the helical instability. This result contrasts with the distributed control, which shows largest control effort on the axial component. We, therefore, observe that a constrained optimization in a more restrictive set of parameters (boundary vs distributed) can distort or even miss the relevant information about the distribution of the receptivity region of the instability, which are mainly carried by the axial component in the present case. In addition, the gradient of the adjoint state in turbulent industrial applications may be oscillating and could jeopardize the robustness of boundary control algorithms.

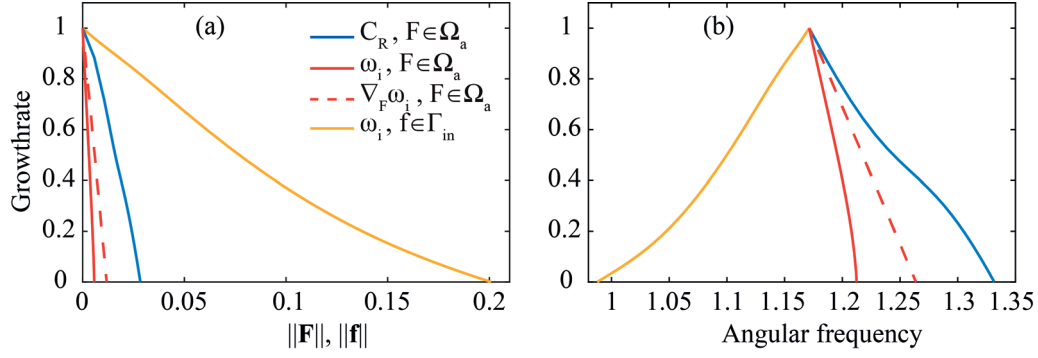


Figure 2.21 – Base flow dominant growth rate normalized by the most unstable uncontrolled eigenvalue at $Re = 180$ as a function of the norm of the control (a) and of the angular frequency of the mode (b) for the "flow manipulation control" (blue solid curve), the "base flow stabilization distributed control" (red solid curve), the "linear sensitivity-based finite amplitude distributed control" (red dashed curve), and the "base flow stabilization inlet control" (yellow solid curve).

3 Stability analysis of mean turbulent swirling flows at $Re = O(10^6)$: Application to the Francis turbine part load vortex rope

The stability analysis of the Francis turbine part load vortex rope is assessed in this chapter. The coherent structure of this vortex flow, which is kept at a high Reynolds number $Re = O(10^6)$, makes this industrial flow an excellent candidate to validate the linear stability analysis around mean turbulent flows. The part load vortex rope often associated to the vortex breakdown phenomenon is definitely shown to come from the same mechanism, the development of a globally unstable disturbance inducing self-sustained oscillations.

The variables used in this document are susceptible to change in comparison to the submitted version of the article to keep the document consistency.

PAPER: Part Load Vortex Rope as a Global Unstable Mode

Part Load Vortex Rope as a Global Unstable Mode

Simon Pasche¹, François Avellan¹, François Gallaire²

¹ LMH, Swiss Federal Institute of Technology (EPFL), CH-1007, Lausanne, Switzerland

² LFMI, Swiss Federal Institute of Technology (EPFL), CH-1015, Lausanne, Switzerland

Preprint version of the article published in *Journal of Fluids Engineering*, (2017), DOI:
10.1115/1.4035640

Renewable energy sources (RES) have reached 23.7% of the worldwide electrical generation production in 2015. The hydraulic energy contribution amounts to 16.6% and comes mainly from large-scale hydropower plants, where Francis turbines represents 60% of the generating units. However, the future massive development of RES will require more advanced grid regulation strategies that may be achieved by increasing the operation flexibility of the Francis generating units. Part load operating condition of these turbines is hindered by pressure fluctuations in the draft tube of the machine. A precessing helical vortex rope develops in this condition, which imperils the mechanical structure and limits the operation flexibility of these turbines. A thorough description of the physical mechanism leading to the vortex rope is a prerequisite to develop relevant flow control strategies. This work, based on a linear global stability analysis of the time-averaged flow field, including a turbulent eddy viscosity, interprets the vortex rope as a global unstable eigenmode. In close resemblance to spiral vortex breakdown, a single-helix disturbance develops around the time-averaged flow field and grows in time to finally form the vortex rope. The frequency and the structure of this unstable linear disturbance are found in good agreement with respect to the 3-D numerical flow simulations.

3.1 Introduction

A massive penetration of alternative renewable energies and a broad deployment of energy efficiency initiatives and technologies reflect the current energy developments. In this context, hydropower already contributes and will increasingly do so, on one hand, to participate to renewable energy production and, on the other, to absorb the highly dynamic energy storage requirements associated to a widely distributed injection of the photovoltaic and wind energy into the transmission and the distribution systems. The hydropower thereby preserves the stability of these systems through the provision of advanced system services.

Hydraulic turbines are able to produce several hundreds of megawatts in a time lapse of

the order of a minute, which makes them excellent candidates for the regulation of grid fluctuations. The use of Francis turbines, which represent the largest turbine market, in this regulation context hinges on the prescriptions on the operating conditions. Standard operating conditions are met at the Best Efficiency operating Point (BEP) of the turbine. At the BEP, which is the design point of the runner, an axial flow is produced in the draft tube of the turbine that minimizes the hydraulic losses. The turbines can however respond to fast and elastic grid fluctuations only by operating at off-design conditions. This not only increases the hydraulic losses at the price of a reduced efficiency, this merely exposes the turbines to risks of operating instability, structural fatigue as well as resonance of the mechanical structures due to the appearance of a vortex flow in the draft tube which produces large pressure fluctuations. Flow control strategies aimed at mitigating the development of hydrodynamic instabilities are therefore desirable to improve the flexibility of the operating regime of Francis turbines.

A detailed understanding of the unsteady vortex flows appearing in the draft tube is a prerequisite for the development of targeted control methods. Two different vortex structures have been observed in Francis turbines: an axisymmetric pulsating vortex rope at full load operating conditions (see Jacob et al. [111] and Tsujimoto et al. [112]) and a helical precessing vortex rope at part load operating conditions, which is relevant in the context of grid regulation and which the present study is focused. The first observations of this precessing vortex rope were reported by Dériaz [113] when he investigated the pressure surge effect, that was discovered in a hydroelectric power plant, see Rheingans [106]. Nishi et al. [12] then characterized the different flow regimes and investigated the frequency dependency against the operating conditions. These authors also identified a synchronous and convective component of the pressure fluctuations by signal decomposition of pressure measurements. Deeper experimental investigations were performed by unsteady wall pressure measurements reported by Arpe & Avellan [8], laser Doppler velocimetry and two-phase flow particle image velocity by Ciocan et al. [9], Iliescu et al. [16], Favrel et al. [17], Müller et al. [114]. From an analytical point of view, idealized models of the instantaneous vortex rope were derived to better describe this phenomenon (Dörfler [115] and Fanelli [38]). Susan-Resiga et al. [116] have succeeded in modeling the mean flow velocity at the runner outlet over a broad range of operating conditions of the Francis turbine by the superposition of three elementary vortices. They also performed a linear wave perturbation analysis of these fitted velocity profiles and showed that the flow is sensitive to axisymmetric disturbances when a sudden variation in the draft tube pressure recovery occurs. This sudden variation results in a transition from supercritical to a subcritical state as the discharge coefficient decreases, and is reminiscent of vortex breakdown. Kuibin et al. [117] have derived an analytical model to predict the time averaged velocity profile at the runner outlet and the frequency of the vortex rope as a function of the discharge coefficient, the dimensionless flux of momentum, and the swirl-free radial velocity profile. In this study, we interpret the vortex rope as the development of an infinitesimal global disturbance of the turbulent mean flow, conducting a so-called global hydrodynamic instability analysis.

Hydrodynamic instability analysis investigates the development of infinitesimal disturbances

Chapter 3. Stability analysis of mean turbulent swirling flows at $Re = O(10^6)$: Application to the Francis turbine part load vortex rope

emerging from a base state. The first theory which has been developed is the so-called local temporal stability analysis, which considers the linearized time-evolution of perturbations superimposed on a streamwise (say \mathbf{e}_x) base flow. Further assuming a wavy dependence of the form $\exp((i(kx - \omega t))$ for a prescribed wavelength $2\pi/k$, this yields a dispersion relation $\omega(k)$. The stable or unstable nature of the flow is then given by the sign of the imaginary part of the dispersion relation. The flow is unstable if there exists at least one wavenumber with positive imaginary part of the frequency. This approach has been very successful in explaining and predicting several instabilities, e.g. the Rayleigh-Plateau, Rayleigh-Taylor or Kelvin-Helmholtz instabilities, among others. However this approach fails to correctly capture the effect of advection on the behavior of a spatially developing flow. In real situations, there is indeed often a dominant advection direction and the question becomes to evaluate the growth in time and space of incoming fluctuations. This has led to the concept of convective and absolute instability, which distinguishes the situation where advection dominates over growth and where instability waves are swept away while they grow (convective instability) from the one where growth dominates over advection and some instability waves withstand the advection and invade the entire domain (absolute instability). In less idealized, spatially developing flows, locally absolutely unstable flows give rise to synchronized oscillator behavior while convectively unstable flows behave as noise amplifiers. Despite their importance in the physical understanding of instabilities, the local stability approaches are limited to weakly non-parallel flows and difficult to apply in real flows. In situations where the geometry is complex, such as draft tubes and where in addition the flow quickly recovers when exiting the rotating vanes, the flow evolves over length scales which are comparable to the wavelength of the instability and the weakly non parallel theories can be questioned. One has then to resort to global stability analysis where the full base flow is considered and yields a 2-D, 2-D axisymmetric or sometimes even 3-D eigenvalue problem, that can now be tackled with the power of modern high performance computers. The success of this approach to low-Reynolds number flows in recent years is impressive: it ranges from wake flows around obstacles (Barkley [5]) to idealized configurations of swirling wakes Meliga & Gallaire [98] as well as jets-in-cross flows (see Theofilis [46] for a review). Its generalization to the global stability analysis of turbulent flows at high Reynolds number has been found recently successful by Meliga et al. [47].

In this study, we apply global hydrodynamic instability analysis to the turbulent mean flow in a draft tube. This contrasts with the local stability analysis of helical modes of Zhang et al. [118]. More recently Topor & Bristrian [119] have investigated the absolute/convective inviscid instability of the mean velocity profile at the runner outlet and obtained a satisfactory prediction of the frequency and wavelength of the vortex rope. A global stability analysis of inviscid flow has also been recently performed by Pochyly et al. [120] on the solution of the Reynolds-Averaged-Navier-Stokes equations, resulting in a myriad of unstable modes, one of which captures the vortex rope frequency. While these studies highlight the unstable character of the flow at part-load conditions, they have only partially succeeded in describing the intrinsic physical mechanism originating in the vortex rope.

The paper is structured as follows: the framework of the global stability analysis applied to the vortex rope is presented under section 3.2 then the numerical tools are presented, section 3.3. The results of the 3-D numerical flow simulations are exhibited and a comparison with experimental measurements is performed under section 3.4. The mean flow quantities are extracted in section 3.5 and the global stability analysis on the turbulent mean flow is carried out in section 3.6. Finally the application of the global stability analysis on the vortex rope is discussed under section 3.7.

3.2 Problem formulation

The precessing vortex rope appearing in the draft tube cone of a Francis turbine operating at part load conditions is investigated by global linear stability analysis for the FLINDT Case study - Flow Investigation In Draft Tube - project, Eureka No. 1625. Since the rotating vortex is an unsteady phenomenon occurring at high Reynolds number, no steady solution of the governing equations can be obtained numerically, only unsteady solutions are available from computations. This restriction results in a modification of the classical formalism of the linear stability analysis. Thus instead of computing the evolution of infinitesimal perturbations emerging from a base flow, or fixed point, defined as a steady solution of the Navier-Stokes equations in our case, the global linear stability analysis is performed on the mean flow, the time averaged solution of the unsteady equations. The shift from base to mean flow is mathematically valid when the Reynolds stresses are unperturbed at leading order, as discussed by Barkley [5]. However the vortex rope is far from this assumption and the validity of applying a global linear stability approach remains questionable. There are only several flows where periodic coherent structures persist at high Reynolds number. Jet flows and shear flows are classical examples where a broadband spectrum appears with the turbulent level in contrast to the bluff body or the vortex rope which robustly exist at high Reynolds number. Thus the vortex rope is an appropriate candidate to evaluate the emergence of infinitesimal perturbations in turbulent flow and therefore the outcomes of instability theory for coherent structure prediction.

The 3-D flow field of the initial geometry of the turbine is computed and validated with experimental results from Arpe & Avellan [8] and Ciocan et al. [9]. The periodic motion of the flow field allows us to design a second geometry of the draft tube, a Moody type draft tube by discharge velocity conservation over the cross sections of the original one. This is the main point to perform accurate linear global stability analysis, by reducing from a 3-D to a 2-D axisymmetric formulation. On the practical side, the main drawback for using a Moody draft tube is the impact on the turbine efficiency but this is out of the scope of this study. We show that the eigenvalues and eigenmodes solutions of the 2-D axisymmetric linear global stability analysis inform us about the frequency values and the growth rates of the developed perturbed modes in the draft tube of the Francis turbine.

3.3 Numerical tools

3.3.1 3-D flow field

Three dimensional numerical flow simulations are performed for the reference part load operating condition of the FLINDT project for a flow rate coefficient of $\phi = 0.27$, a specific energy of $\psi = 1.16$, a Thomas cavitation number of $\sigma = 1.16$ and a Reynolds number based on the runner outlet diameter of $Re \approx 10^6$. At this regime, cavitation free conditions exist. Only the flow in the runner and the draft tube is computed using ANSYS CFX 15.0 software. This computational domain was demonstrated to be sufficient to accurately predict the unsteady behaviour of the vortex rope, see Ciocan et al. [9]. Unsteady Reynolds Average Navier-Stokes

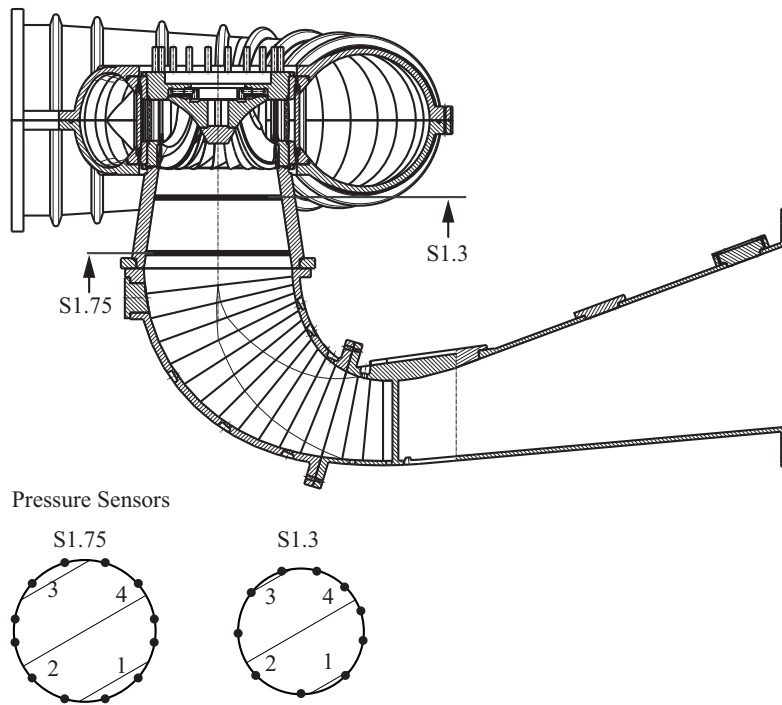


Figure 3.1 – Cross section of the FLINDT geometry with the location of the section 1.3 and 1.75 and their cross planes where pressure sensors are located.

(URANS) equations are solved considering the following boundary conditions: A constant velocity profile and a turbulence intensity are imposed at the inlet boundary where their values come from a previous steady calculation of the spiral casing and distributor, as Ciocan et al. [9], and open conditions are applied at the outlet of the domain. A transient rotor stator interaction allows the flow to transit from the runner domain to the draft tube domain by a general grid connection (GGI) method, which takes into account all interaction effects between components. Mesh is locally refined in the runner and in the draft tube cone to obtain an accurate solution of the flow field in these regions. SAS-SST turbulence model is used to correctly capture flow separation in the runner, Egorov & Menter [121], in order to obtain an accurate flow field at the runner outlet that is the starting point of the vortex rope.

Three different meshes are used to analyze the mesh influence, 3.7 mio, 7.5 mio and 14 mio of cells with a mean y^+ of 136, 90, and 23, respectively. A time step of 1° of runner revolution is used to obtain a rms convergence error of each components of 10^{-4} . The simulation runs for 5 vortex rope revolutions, i.e. about 18 runner revolutions, after an initialization phase that includes the transient effects. Pressure is monitored on two sections (1.3 & 1.75) in the cone by 22 sensors at the same location as the experimental measurements of Arpe & Avellan [8], see fig. 3.1, allowing us to validate the results with experimental data. The time averaged flow field is computed while the simulation is running, and starts after the transient effects to 5 vortex revolutions.

The flow field in the Moody draft tube type designed from the original elbow type is computed using the same numerical setup of the original one excepts that the mesh contains a total of 4.0 mio, 7.5 mio and 10 mio of cells spread in the runner, the draft tube cone and the diffuser.

3.3.2 2-D global linear stability analysis

The stability analysis is performed on the time averaged flow field of the Moody draft tube. Since the mean flow is turbulent, the stability analysis has to consider the spatial variation of eddy viscosity in its formulation which leads to a linear stability analysis of a turbulent mean flow. The dynamical equations driven small amplitude wave disturbances $\tilde{\mathbf{C}}$ in incompressible turbulent flow were first derived by Reynolds & Hussain [122]. The primitive variables are decomposed in a time averaged $\bar{[\cdot]}$, a periodic $\tilde{[\cdot]}$ and turbulent fluctuations $[\cdot]'$, in order that the velocity yields to

$$\mathbf{C} = \bar{\mathbf{C}} + \tilde{\mathbf{C}} + \mathbf{C}', \quad (3.1)$$

where phase averaging operator holds

$$\langle \mathbf{C} \rangle = \bar{\mathbf{C}} + \tilde{\mathbf{C}}. \quad (3.2)$$

The phase averaging operator is applied to the triple decomposed Navier-Stokes equations. The results are subtracted to the time average of the same equations. This leads to the non-linear evolution of the periodic perturbations,

$$\begin{aligned} \frac{\partial \tilde{\mathbf{C}}}{\partial t} + \nabla \tilde{\mathbf{C}} \cdot \bar{\mathbf{C}} + \nabla \bar{\mathbf{C}} \cdot \tilde{\mathbf{C}} &= -\nabla \tilde{P} + Re^{-1} \nabla^2 \tilde{\mathbf{C}} + \nabla \cdot \left(\overline{\tilde{\mathbf{C}} \tilde{\mathbf{C}}} - \tilde{\mathbf{C}} \tilde{\mathbf{C}} \right) + \nabla \cdot \left(\overline{\mathbf{C}' \mathbf{C}'} - \langle \mathbf{C}' \mathbf{C}' \rangle \right) \\ \nabla \cdot \tilde{\mathbf{C}} &= 0 \end{aligned} \quad (3.3)$$

The closure problem of eqn. (3.3) is solved by using Boussinesq approximation for the time averaging $-\overline{C'_i C'_j} = 2\nu_t \bar{S}_{ij} - 2/3 \bar{k} \delta_{ij}$ and phase averaging $-\langle C'_i C'_j \rangle = 2\nu_t \langle S_{ij} \rangle - 2/3 \langle k \rangle \delta_{ij}$, where S_{ij} is the strain tensor defined as $S_{ij} = 1/2(\partial C_i / \partial X_j + \partial C_j / \partial X_i)$, and assuming that the phase averaging process only affects the turbulence structure and not the energy, i.e. $\langle k \rangle = \bar{k}$, see Reynolds & Hussain [122] and Viola et al. [123] for more details.

Chapter 3. Stability analysis of mean turbulent swirling flows at $Re = O(10^6)$: Application to the Francis turbine part load vortex rope

In the frameworks of stability analysis, a linearised version of eqn. (3.3) is derived including the previous assumptions. The term $\nabla \cdot (\tilde{\mathbf{C}}\tilde{\mathbf{C}} - \tilde{\mathbf{C}}\tilde{\mathbf{C}})$ is cancelled due to higher order non-linearity, and the term $\nabla \cdot (\overline{\mathbf{C}'\mathbf{C}'} - \langle \mathbf{C}'\mathbf{C}' \rangle)$ is simplified using the eddy viscosity formulation $\nabla \cdot [\nu_t(\tilde{\mathbf{C}})(\nabla + \nabla^T)\tilde{\mathbf{C}}]$ and the linearisation of the turbulence model $\nabla \cdot [(\nabla\nu_t(\tilde{\mathbf{C}}) \cdot \tilde{\mathbf{C}})(\nabla + \nabla^T)\tilde{\mathbf{C}}]$. The contribution from the linearisation of the turbulence model $\nabla \cdot [(\nabla\nu_t(\tilde{\mathbf{C}}) \cdot \tilde{\mathbf{C}})(\nabla + \nabla^T)\tilde{\mathbf{C}}]$ is assumed to be small and is neglected, as Mettrot et al. [95], Meliga et al. [47], Cossu et al. [124], Delàlamo & Jiminez [125] and Reynolds & Hussain [122]. Finally the periodic disturbance $(\tilde{\mathbf{C}}, \tilde{P})$ is expanded in normal mode according to

$$(\tilde{\mathbf{C}}, \tilde{P})(R, \theta, Z, t) = (\mathbf{c}, p)(R, Z)e^{i(m\theta - \omega t)} + \text{complex conjugate}, \quad (3.4)$$

where (\mathbf{c}, p) are defined as the global eigenmodes and leads to the linearised wave disturbance equations of turbulent flows for azimuthal wave numbers:

$$\begin{aligned} -i\omega\mathbf{c} + \nabla_m\mathbf{c} \cdot \tilde{\mathbf{C}} + \nabla_m\tilde{\mathbf{C}} \cdot \mathbf{c} &= -\nabla_m p + Re^{-1}\nabla_m^2\mathbf{c} + \nabla_m \cdot [\nu_t(\tilde{\mathbf{C}})(\nabla_m + \nabla_m^T)\mathbf{c}] \\ \nabla_m \cdot \mathbf{c} &= 0, \end{aligned} \quad (3.5)$$

where $\nu_t(\tilde{\mathbf{C}})$ is the spatial eddy viscosity and (∇_m) is the gradient operator, $(\nabla_m \cdot)$ is the divergence operator, (∇_m^2) is the laplacian in cylindrical coordinates with the derivative with respect to θ replaced by im . At this level different turbulent viscosity models are available for the stability analysis. The zero order approximation leads to a constant eddy viscosity $\nu_t = Cst$, while in higher order models, the eddy viscosity is a function of the mean flow $\tilde{\mathbf{C}}$. In a general sense, the eddy viscosity is modelled through the combination of several scalars, like the kinetic turbulent viscosity k , which are governed by transport equations. For common models ν_t becomes, $\nu_t = Cst \cdot k^2/\epsilon$ for the $k - \epsilon$ model or $\nu_t = k/\omega$ for the $k - \omega$ model which by definition is locally dependent of the instantaneous velocity. In our case for SAS-SST model the definition of ν_t is a quite tedious and is not presented here, see Egorov & Menter [121]. The spatial eddy viscosity $\nu_t(\tilde{\mathbf{C}})$ is a solution of the 3-D numerical flow simulation and is accessible to perform the stability analysis. This approach is referred to as eddy viscosity model and is used as reference eigenvalue computation. A second approach, with constant eddy viscosity $\nu_t(\tilde{\mathbf{C}}) = \nu_t$, is also defined and allows us to investigate the influence of the eddy viscosity model in the stability analysis. This last definition leads to the simplification of the dissipative term of eqn. (3.5) to $(Re^{-1}\nabla_m^2\mathbf{c} + \nabla_m \cdot [\nu_t(\tilde{\mathbf{C}})(\nabla_m + \nabla_m^T)\mathbf{c}]) = (Re^{-1} + \nu_t)\nabla_m^2\mathbf{c}$. We refer to this formulation, which is similar to the frozen eddy viscosity approach of Mettrot et al. [95]. The spatial eddy viscosity distribution is determined, similar as the mean flow, through successive time and azimuthal averaging procedures. All these variables have been computed in a dimensional framework and they are made dimensionless to be consistent with the stability analysis. The reference length is the runner outlet radius R_{1e} and the reference velocity is the discharge velocity C_{ref} . This defined a Reynolds number of $Re = R_{1e}C_{ref}/\nu = 824'400$ for the present computation and a turbulent Reynolds number defined as $Re_t = R_{1e}C_{ref}/\nu_t$.

The set of equations eqn. (3.5) in axisymmetric form is discretized by finite element methods

in the software Freefem++, see Meliga & Gallaire [98]. A 2-D axisymmetric domain of the Francis turbine from the runner blade trailing edge to the outlet of the Moody draft tube is meshed using P_2 - P_1 triangular finite elements. The resulting eigenvalue problem is solved using Krylov methods from ARPACK libraries, (Lehoucq [104]), where a direct solver is used for matrix inversion through a sparse LU factorization (UMFPACK package, Davis [102]). Dirichlet boundary conditions are imposed at the wall of the turbine and at the inlet. Free-outflow condition is set at the outlet $(-p\mathbf{I} + (Re^{-1} + \nu_t(\tilde{\mathbf{C}}))\nabla\mathbf{c}) \cdot \mathbf{n} = 0$. On the axisymmetric axis, the boundary condition that is recalled in Table 3.1 is dependent of the azimuthal wave number m , see Khorrami [103]. The inlet variables $\tilde{\mathbf{C}}$ and $\nu_t(\tilde{\mathbf{C}})$ are interpolated on the 2-D axisymmetric

Table 3.1 – Boundary conditions imposed on the symmetry axis of the domain

Wave number	Axis boundary conditions
$m = 0$	$c_R = c_\theta = 0, \partial_R c_Z = 0$
$m = \pm 1$	$c_Z = p = 0, \partial_R c_R = \partial_R c_\theta = 0$
$ m > 1$	$c_R = c_\theta = c_Z = 0$

mesh of the eigenvalue problem using Matlab interpolation tools. This mesh is composed of approximately 500'000 triangles to compute accurately the eigenvalue ω of eqn. (3.5). The imaginary part of ω describes the growth or decay of disturbances and the real part of ω informs about the frequency of these disturbances.

The convergence of the eigenvalues is ensured by the tolerance of the ARPACK solver, set to 10^{-6} , and by the invariance of the 2-D axisymmetric mesh size. However the eigenvalue problem incorporates the mean flow, whose native resolution is based on the 3-D mesh size, that may implicitly induce a variation of the eigenvalues. These variations have been evaluated by computing the eigenvalues associated to the 3-D meshes, the coarse, the medium and the fine ones, and reported as error bars in fig. 3.8(c), which is presented in section 3.6.

3.4 3-D flow fields

The 3-D numerical flow simulations of the original draft tube are validated against the experimental measurements, wall pressure and laser Doppler velocimetry measurements on the sections 1.3 and 1.75 from Arpe & Avellan [8] and Ciocan et al. [9]. The Moody draft tube is designed with the aim to conserve the velocity field of the original case. This feature is also evaluated in this section by comparison to the experimental data and the CFD results.

A first relevant parameter of the vortex rope dynamics is its frequency. This frequency is evaluated by fast Fourier transform of the wall pressure signals at both sections. The frequency observed in the experiment is $f_{rope}/f_{runner} = 0.3$ and the numerical flow simulations have a

Chapter 3. Stability analysis of mean turbulent swirling flows at $Re = O(10^6)$: Application to the Francis turbine part load vortex rope

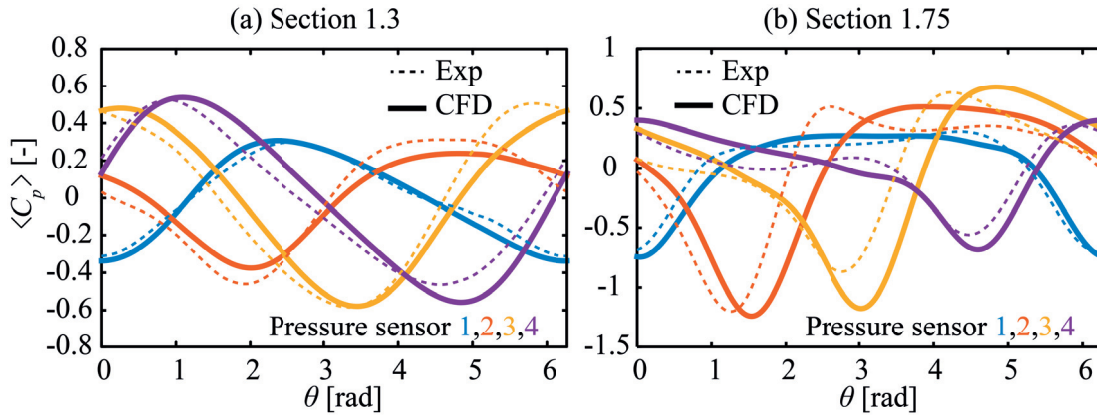


Figure 3.2 – Phase averaged of the wall pressure signals at section 1.3 (a) and 1.75 (b) at the sensor 1,2,3 and 4 of the experimental data [8] and the present 3-D numerical flow simulation of the original elbow.

frequency of $f_{rope}/f_{runner} = 0.34$ for the coarse mesh and $f_{rope}/f_{runner} = 0.33$ for the medium and fine mesh. Note that no discrepancy is observed between the two sections. The relative error between the CFD and the experiments, 10%, is slightly improved compare to Ciocan et al. [9], 13%, but remains in the same order of magnitude. The Moody geometry reproduces the same frequency as the original draft tube, a value of $f_{rope}/f_{runner} = 0.33$ is computed for all meshes. The frequency invariance of the numerical flow simulations ensures mesh independent results for both cases and underlines the self-sustained character of the vortex rope while a symmetry breaking is imposed by the elbow.

The wall pressure signals provide an accurate insight of the vortex rope dynamics by following its evolutions over one rotation. A phase averaged post processing is performed to extract the relevant part of the pressure signal by excluding turbulent fluctuations and noise. A reference signal, sensor 1, provides the phase change for every signals on the same section. Each pieces of signal, between two phase change, are superimposed and averaged for an increment of rotation of 1° , see Müller et al. [114]. In figure 3.2, the phase averaged signal of the section 1.3 and 1.75 are displayed for the fine mesh of the original draft tube and the experimental measurements. Both signals of the different sensors reproduce the fluctuations of the vortex rope. Along section 1.3 the pressure peak and shape are well reproduced. On the section 1.75, sensor 1 is reproduced accurately but the pressure peaks and the signal shapes of the others have more discrepancies. The numerical flow simulation is able to reproduce the vortex rope dynamics in the cone of the draft tube but as it enters the elbow, the results deflect from the experimental measurements.

This deflection is also seen from the time averaged flow field. Figure 3.3 reproduces the LDV measurements of Ciocan et al. [9], without error bars and the present results of the numerical flow simulations. The velocity deficit and the shape of the velocity profile are in good agreement for the section 1.3. For the axial velocity component, the main velocity deficit as well as the velocity increase close to the wall are captured by the CFD. The slope of the

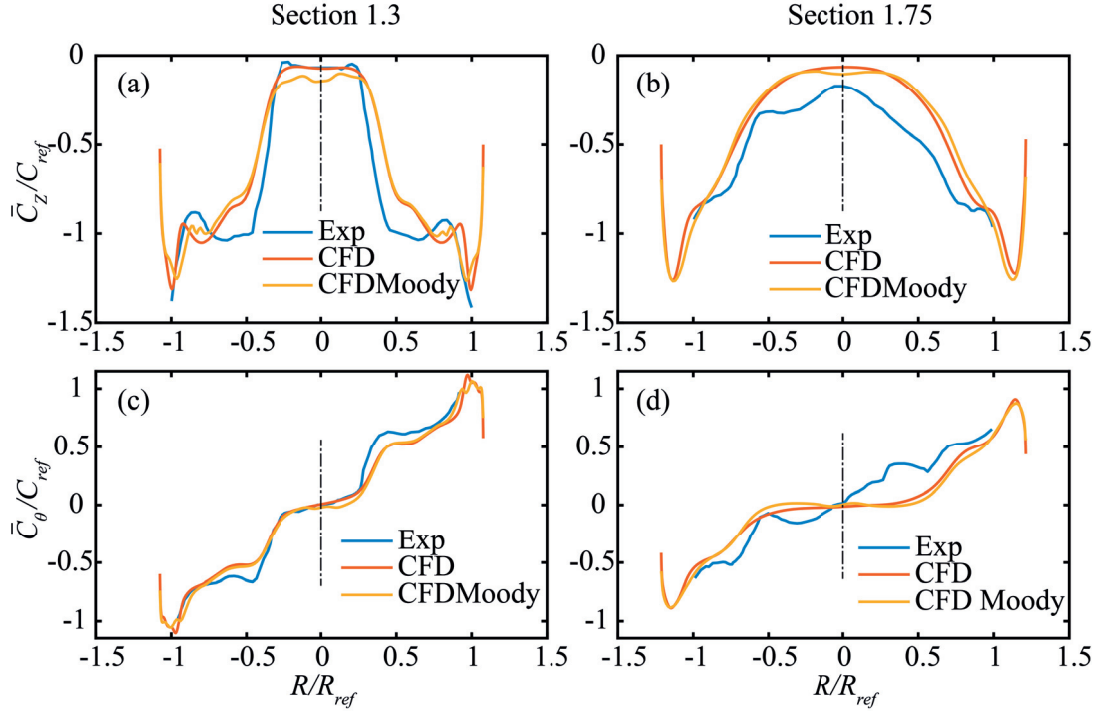


Figure 3.3 – Time averaged velocity profile for the axial and tangential component at the center line of sections 1.3 (a), (c) and 1.75 (b), (d) for the original and Moody draft tube of the present 3-D numerical flow simulations and the LDV measurements [9].

tangential velocity is also captured in the domain except at a radius of 0.5 where the curve is smoothed. At section 1.75 the CFD curves of the tangential velocity are smoothed compare to the experimental results. A plateau appears while in reality the curve has a linear behaviour. The axial deficit is also larger than in reality. As previously seen, a deflection between the CFD and the measurements appears in the elbow of the draft tube. Improving the fine scale resolution by mesh refinement and turbulence model investigation could help obtaining a more realistic dissipation of the vortex rope in the elbow, potentially yielding closer results with the experimental measurements. However the behaviour of the vortex rope is well captured in the cone of the draft tube and the CFD results are in global agreement with the experimental measurements.

The stability analysis is performed on the time averaged flow field which from the point of view of the CFD results are identical for the Moody and original draft tube in the cone as seen in fig. 3.3. This means that the 2-D axisymmetric approximation of the 3-D elbow reflects the real development of the vortex rope and lets envisage a good transportability of the results of the stability analysis to the original draft tube.

In summary our numerical flow simulations of the FLINDT turbine are validated with the experimental data and we succeed in conserving the flow field of the original draft tube with the Moody draft tube. A last figure exhibits this similarity between the original and Moody draft

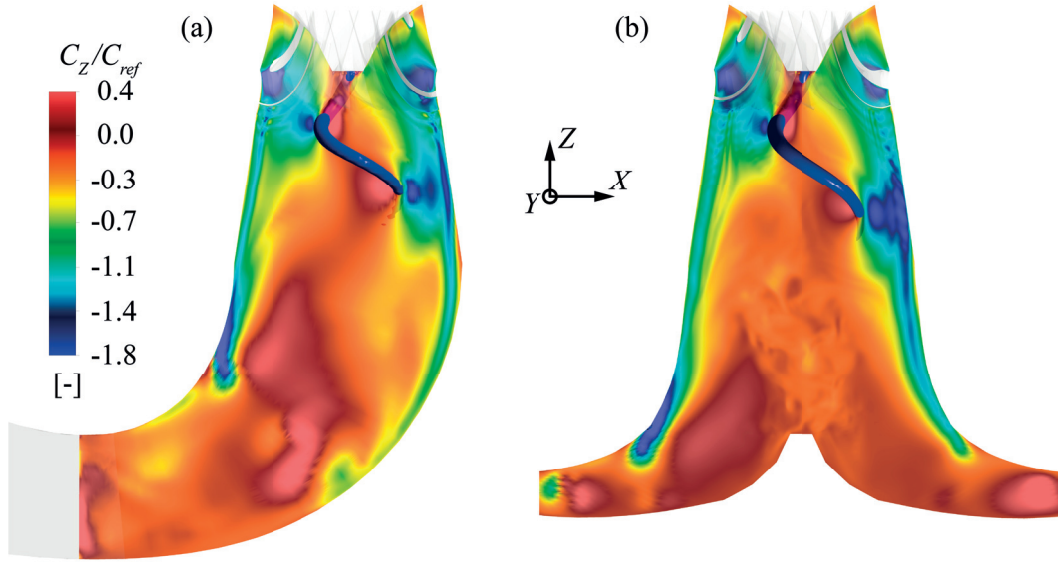


Figure 3.4 – Vortex rope appearing in the original draft tube (a) and in the Moody draft tube (b), highlighted by a blue iso-pressure and the corresponding instantaneous axial velocity field on the ZX-cross section.

tube. A slice plane of the instantaneous axial velocity field and the vortex rope materialized by the same iso-pressure are displayed in fig 3.4(a) and (b) for both cases.

3.5 Time averaged flow field

The time averaged flow field is the reference point where stability analysis is deployed in order to understand the main characteristics of the flow dynamics. The time averaged axial velocity displayed in fig. 3.5(a), highlights two regions, an external region where the axial velocity accelerates along the wall and a center region where the velocity approaches zero. In the second region, a recirculation appears at the tip of the runner cone where the vortex rope starts developing, see fig. 3.5(b).

More details of this flow are shown in fig. 3.6, where the velocity profiles on three different sections are displayed, one just after the runner (fig. 3.6a), one along section 1.3 (fig. 3.6b) and a last in the middle of section 1.3 and 1.75 (fig. 3.6c). The external region has the axial and tangential velocity that approaches the discharge velocity and a radial component with non zero value is observed. The intensity of each component is maximum just after the runner outlet and decreases progressively along the draft tube. This means that the vortex rope interpreted as a self-sustained instability has better chances to develop in the upper part of the cone than at the end of the cone. The center part of the velocity profiles reveals a plateau that has approximately zero value for the radial and tangential velocity. The radial length of this plateau grows along the streamline direction and reflects the radial coiling of the

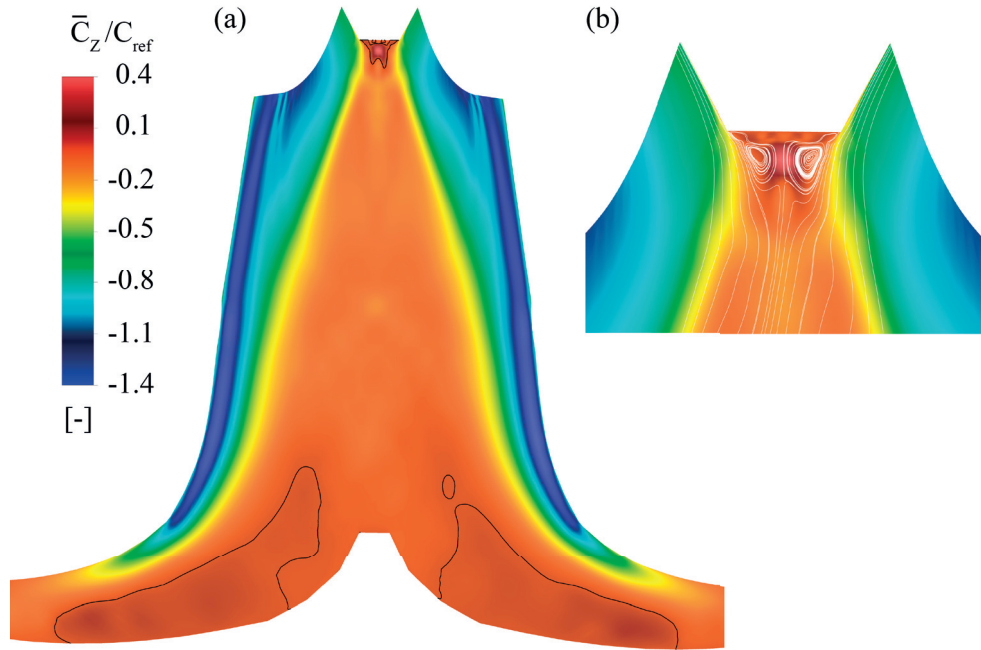


Figure 3.5 – Time averaged axial velocity field of the vortex rope (a), where the solid black curve is the iso-contour $\bar{C}_Z = 0$. Zoom on the recirculation region at the tip of the runner cone (b).

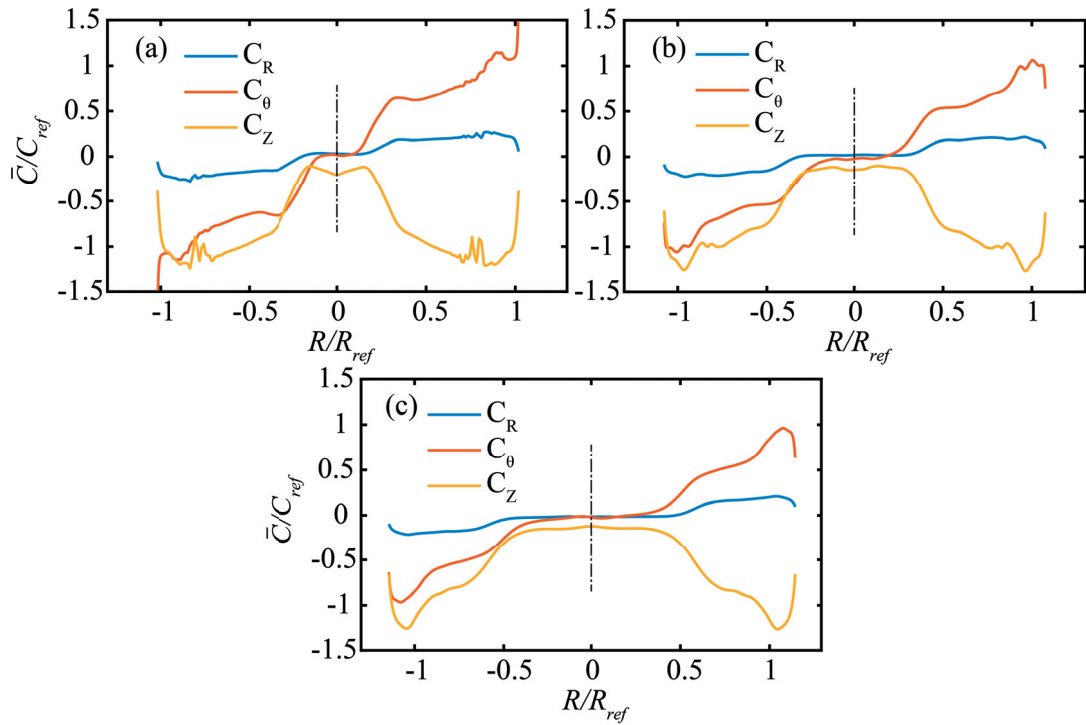


Figure 3.6 – Velocity profiles of the time averaged flow field of the Moody draft tube for different location along the cone, (a) just after the runner, (b) at section 1.3 and (c) between section 1.3 and 1.75.

Chapter 3. Stability analysis of mean turbulent swirling flows at $Re = O(10^6)$: Application to the Francis turbine part load vortex rope

vortex rope. This plateau corresponds to the trace of the center part of the helical filament. All velocity components have a sharp transition between the center and the external region. This transition results in a shear in three components and coincides with the location of the center of the instantaneous vortex rope.

Another important point resulting from the 3-D numerical flow simulations is the time averaged spatial distribution of the eddy viscosity $\nu_t(\bar{C})$ that is used for the global stability analysis. This one is displayed in fig. 3.7 as the turbulent Reynolds number Re_t . The colorscale is limited to 12'000 to be able to observed relevant behaviours.

In the cone center, the turbulent Reynolds number is between $Re_t = 10'050$ and $Re_t = 4'200$. This one drops to a value of $Re_t = 1'000$ in the fluid region, where the vortex rope precesses. This spatial distribution exhibits the work of the turbulence model in the URANS equations which needs to increase locally the fluid viscosity to obtain a solid body rotation in the core of the vortex rope. The global stability analysis, eqn. (3.5), takes into account both the molecular viscosity and the eddy viscosity through the Reynolds number and the turbulent Reynolds number. Recalling that the Reynolds number is $Re = 824'400$ for the studied flow configuration, the eddy viscosity prevails over the molecular viscosity, as clearly exhibited in fig. 3.7.

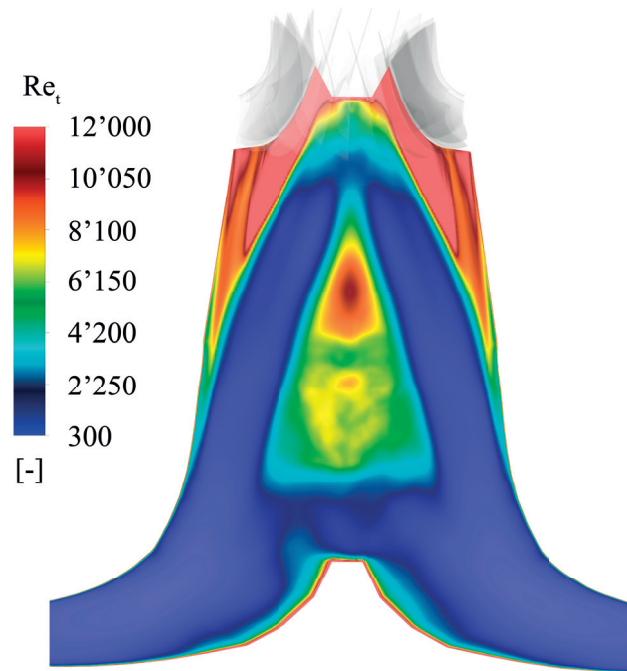


Figure 3.7 – Time averaged turbulent Reynolds number used for the stability analysis.

3.6 Global Stability Analysis

3.6.1 Frequency prediction

Once the mean velocity field and the mean eddy viscosity are azimuthally averaged and interpolated on the 2-D axisymmetric mesh, the stability analysis is performed by the means of the finite element library FreeFEM++. The eigenvalue spectra, using the eddy viscosity model, show only positive eigenvalues for the azimuthal wave number $m = 1$, see fig. 3.8(c), as the single helical vortex observed in the experiments. The eigenvalues for the other azimuthal wave numbers, especially $m = 0$ and $m = 2$, are stable, see fig 3.8(a) and (b). Two eigenvalues

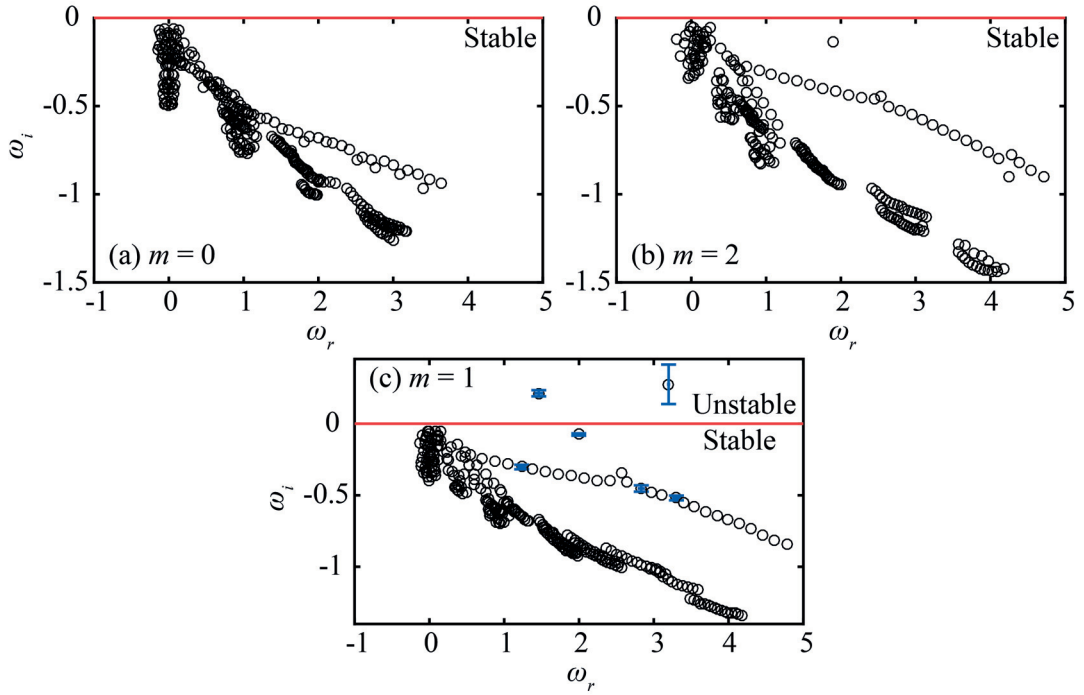


Figure 3.8 – Eigenvalue spectra of the vortex rope for azimuthal wave number (a) $m = 0$, (b) $m = 2$ and (c) $m = 1$ with standard deviation of the eigenvalues with respect to the mean flow resolution, highlighted by error bars.

are unstable for $m = 1$, the first one corresponding to $\omega = 1.43 - 0.20i$ and a second to $\omega = 3.20 - 0.27i$. We recall that $-\Im(\omega)$ represents the growth rate and $\Re(\omega)$ represents the frequency associate to the normal mode expansion eqn.(3.4). Note that the second eigenvalue which has the larger growth rate is sensitive to the mean flow resolution, see the error bars in fig. 3.8(c). These error bars represent the standard deviation of the eigenvalues with respect to the mean flow resolution, the coarse, medium and fine 3-D mesh. This behaviour is only observed for the second unstable eigenvalue while all the others are insensitive. This suggests to exclude this eigenvalue, due to its lack of robustness and convergence (remind that eigenvalues of a $(3 \times 250'000)^2$ eigenvalue problem are practically delicate). The only remaining unstable mode is $\omega = 1.43 - 0.20i$. The dimensionless frequency of this eigenvalue is $f_{rope}/f_{runner} = 0.38$. The

Chapter 3. Stability analysis of mean turbulent swirling flows at $Re = O(10^6)$: Application to the Francis turbine part load vortex rope

frequency prediction of our stability analysis is not far from the reality, a relative error of 15 % from the CFD results is obtained. This result remains relevant, because the condition to apply a linear stability analysis is not all met.

3.6.2 Turbulence effects

The unstable eigenvalues are computed with a spatially varying eddy viscosity. As presented earlier, a constant turbulence model is also used to investigate the involvement of the turbulence in the stability analysis. In the constant model, the turbulent Reynolds number and Reynolds number are just added. As the first one is preponderant in front of the second one, the turbulent Reynolds number prevails. Thus the involvement of the turbulence model in the global stability analysis is investigated by computing the eigenvalue problem for a series of turbulent Reynolds numbers, $Re_t = 140 - 30'000$, see fig. 3.9(a) and (b). Under a turbulent Reynolds number of $Re_t < 190$ all eigenvalues are stable. On contrary for $Re_t > 190$, the single

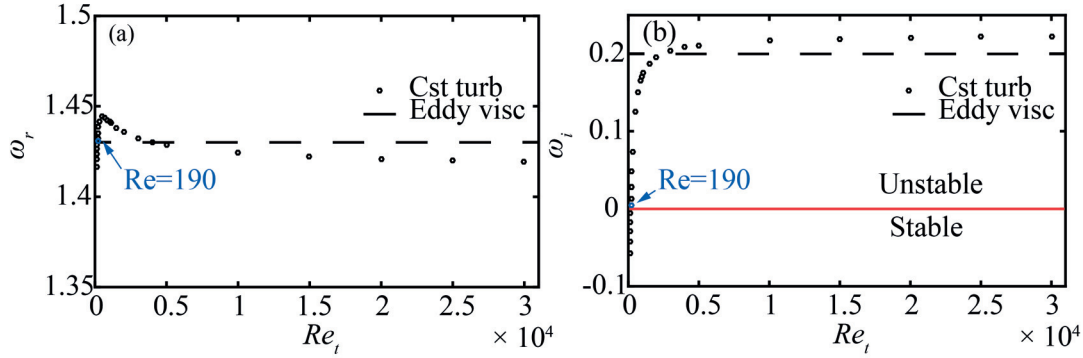


Figure 3.9 – Single unstable eigenvalue computed with the spatially varying eddy viscosity (dash line) and variation of the unstable eigenvalue (circle) with respect to the turbulent Reynolds number $Re_t = 140 - 30'000$ when frozen approach is used, the pulsation (a) and the growth rate (b).

helical mode, $m = 1$, becomes unstable. In fig. 3.9(b), the growth rate increases rapidly with the turbulent Reynolds number and reaches an asymptote of value 0.23 near the growth rate of the eddy viscosity model. The pulsation, in fig. 3.9(a), has a maximum value for $Re_t = 500$ and then decrease to reach an asymptote of value 1.41. The maximum deviation of the pulsation $\delta\omega_i$, over the range of Re_t is 0.025. This deviation corresponds to a frequency variation of the vortex rope of $\delta f_{rope}/f_{runner} = 0.01$. The frequency of the unstable eigenmode is not very affected by the turbulent model. Thus a mean value of the spatial eddy viscosity is sufficient to have a good approximation of the frequency of the mode for turbulent base flow.

3.6.3 Eigenmodes

The global linear stability analysis predicts that the most unstable eigenmode will develop in the flow at infinitely long time. A 3-D reconstruction of the axial velocity of the unstable

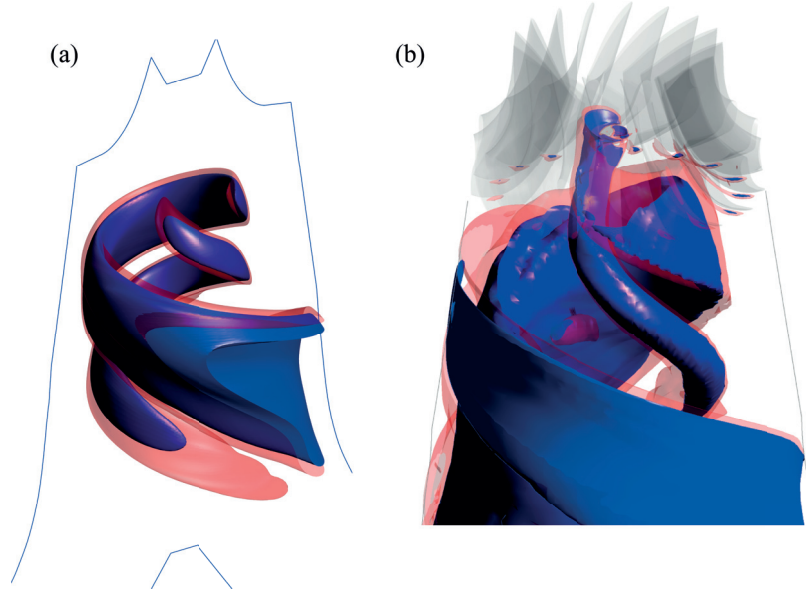


Figure 3.10 – Three dimensional reconstruction of the axial velocity field for the unstable eigenmode $\omega = 1.43 - 0.20i$, $m = 1$ (a) and the 3-D axial velocity disturbance from the 3-D numerical flow simulation (b).

eigenmode is shown in fig. 3.10(a). This eigenmode shows the vortex rope helical structure in the center part of the cone and a second branch along the draft tube wall similar to a tongue. This eigenmode is defined up to a constant; so only qualitative comparison with the real perturbations of the 3-D flow field can be made. The wave disturbance of the 3-D flow field is extracted by removing the time averaged flow from the instantaneous flow $\tilde{\mathbf{C}} = \mathbf{C} - \bar{\mathbf{C}}$ without including the turbulent motion because URANS equations are solved. These two modes for the axial velocity disturbance are in excellent agreement in term of shape, see fig. 3.10(a) and (b). The second branch is also displayed in the instantaneous case that is formed along the draft tube wall too. The center part of the eigenmode that reflects the vortex rope, does not extend up to the tip of the runner cone, in contrast to the nonlinear vortex rope obtained when the full URANS equations are considered. The eigenmode associated to the unstable eigenvalue finally exhibits an excellent agreement with the instantaneous disturbance of the vortex rope.

3.7 Discussion & Conclusion

Three-dimensional numerical flow simulations of the FLINDT geometry have been performed for part load operating conditions, $\phi = 0.27$ and $\psi = 1.16$. Two designs have been investigated, the original one with an elbow draft tube and a simplified one, with a Moody type draft tube. In both cases, a precessing vortex rope appears. The frequency of the vortex rope as well as the time averaged velocity profiles have been validated against experimental measurements and a good agreement has been obtained. The self-sustained character of the vortex rope is

Chapter 3. Stability analysis of mean turbulent swirling flows at $Re = O(10^6)$: Application to the Francis turbine part load vortex rope

highlighted by its frequency invariance against the symmetry breaking of the elbow draft tube. These results enable the further investigation of the main focus of this study: the instability properties of the vortex rope, that is carried out by a global stability analysis. According to this analysis, we investigate the development of infinitesimal disturbances governed by the linearised Navier-Stokes equations around a turbulent mean flow. This turbulent mean flow is obtained by time-averaging the flow field of the previously described 3-D numerical flow simulations. Thanks to the helical structure of the vortex rope and to the axisymmetry of the Moody type draft tube, the 3-D stability problem can be reduced to a 2-D axisymmetric global stability analysis. The mean flow is obtained by azimuthal averaging while each azimuthal wavenumber requires a separate eigenvalue calculation.

The results of this 2-D axisymmetric global stability analysis exhibit only two unstable eigenvalues for the single helical mode $m = 1$. The second unstable eigenvalue, that has the highest frequency can be excluded due to lack of convergence. The frequency of the first unstable eigenvalue $f_{rope}/f_{runner} = 0.38$, see Table 3.2, compares well with the instantaneous frequency of the vortex rope $f_{rope}/f_{runner} = 0.33$, with a relative error of 15%. A similar error, 9%, was observed in the study on the stability of the turbulent flow around a D-shaped cylinder at Reynolds number $Re = 13'000$ by Meliga et al. [47]. Stability analysis of turbulent flows is seen to be less accurate to predict the main frequency of a flow than stability analysis of laminar flows. However the frequency prediction of the vortex rope remains remarkable given the large Reynolds number $Re \approx 10^6$ of the instantaneous flow.

Table 3.2 – Frequency of the vortex rope obtains by the FFT of the experimental data [8], CFD of the original and Moody draft tube and the present global linear stability analysis.

	Experimental	Elbow draft tube fine mesh	Moody draft tube fine mesh	Global linear stability
f_{rope}/f_{runner}	0.30	0.33	0.33	0.38

The eigenmode associated to the unstable eigenvalue is in close agreement with the 3-D disturbance of the vortex rope. This eigenmode exhibits a secondary vortex along the draft wall that is also present in the 3-D simulations and that may be interpreted as a tilting Kelvin-Helmholz mode (see Gallaire & Chomaz [126] and Maxworthy & Liang [127]) due to the combination of the swirling flow and the shear of time averaged axial velocity profile near the draft tube wall, see fig. 3.6. The primary vortical structure of the eigenmode, located in the cone center, is the very reminiscent of the vortical structure that develops in the 3-D flow and forms the precessing vortex rope. In the instantaneous case, when the nonlinear effects are numerically solved, this instability attaches to the tip of the runner cone and extends in the draft tube elbow, an effect not captured by the linear stability analysis. It is striking that these results have been obtained by considering a 2-D axisymmetric Moody type draft tube, but are

still representative of the structure found in the full simulation of the 3-D original draft tube. The geometrical simplification thereby ensures a more accurate eigenvalue calculation.

The linearised wave disturbance equations of turbulent flows for azimuthal wave numbers, eqn. (3.5), takes into account the incompressibility condition and the turbulent fluctuations of the flow. These equations have been derived under several assumptions that finally model these fluctuations by a dissipative viscous term where the viscosity is defined as the time-average of the instantaneous eddy viscosity. The molecular viscosity remains included in the model, but is seen to be negligible with respect to the turbulent viscosity. Indeed, the molecular viscosity has an equivalent Reynolds number of $Re = 824'400$ while the turbulent viscosity has an equivalent turbulent Reynolds number of $Re_t = 1000$ in the precessing cone of the vortex rope. While it has often been observed that the growth rate of the dominant unstable eigenmode of a mean flow was close to zero, Barkley [5], Mantić-Lugo et al. [84], this not the case in our study, as in the turbulent stability analysis of Meliga et al. [47].

The vortex rope captured as an instability in a "viscous framework" (in view of the large turbulent eddy viscosity) is found insensitive to different turbulence models used in the stability analysis. The frequency and the growth rate both reach an asymptotes as the frozen eddy viscosity is decreased, which are close to those computed by including the eddy viscosity turbulence model. This suggests that the vortex rope is an inviscid instability that can be captured by Euler equations using an appropriate 2-D axisymmetric formulation. This approach has been followed by Pochyly et al. [120], by considered as base flow an axisymmetric steady solution of the Navier-Stokes equations in a straight cone draft tube, that mimics the vortex rope time averaged flow field.

The success of our approach relies on the use of global linear stability on a mean flow which was proven to correctly capture the main frequency of the flow (Barkley [5] and Giannetti & Luchini [55]) in comparison to the temporal local stability analysis, which was not able to predict the correct most unstable azimuthal wave number for self-sustained instabilities, see Gallaire & Chomaz [72]. While an absolute/convective instability approach, Huerre & Monkewitz [44], can be sometimes used to obtain a correct prediction, Gallaire et al. [75], Qadri et al. [80], Pasche et al. [128], this approach is restricted to parallel or weakly non parallel flows, which can be questioned in the complex geometry of a Francis turbine draft tube.

In summary, the investigation of the vortex rope as an unstable infinitesimal perturbation by global linear stability analysis around a turbulent mean flow provides insight into the physical understanding of this phenomenon. A global unstable eigenmode develops on the time averaged flow field and leads to the formation of the vortex rope in the draft tube of the Francis turbine operating at part load conditions. This instability is interpreted as an inviscid instability in view of the frequency invariance with respect to the turbulent Reynolds number. To improve the power generation flexibility of Francis turbines for grid compensations, control schemes targeting this unstable eigenmode should be implemented as a natural continuation of this work using sensitivity analysis methods (Marquet et al. [6]).

4 Optimal control of self-sustained instabilities in turbulent swirling flows: Application to the Francis turbine part load vortex rope

The self-sustained character of the part load vortex rope was demonstrated in the third chapter using stability analysis and the control of such instabilities at low Reynolds number $Re = 300$ was performed in the second chapter. As reminder, this control technique minimizes the eigenvalue growth rate from the stability analysis around the mean flow. In this chapter, the control of self-sustained instabilities at high Reynolds number using the same control strategy is addressed. The Francis turbine vortex rope at $Re = O(10^6)$ is controlled.

The variables used in this document are susceptible to change in comparison to the submitted version of the article to keep the document consistency. Additional paragraph and results could be also added.

PAPER: Predictive control of part load vortex rope in Francis turbines

Predictive control of part load vortex rope in Francis turbines

Simon Pasche¹, François Avellan¹, François Gallaire²

¹ LMH, Swiss Federal Institute of Technology (EPFL), CH-1007, Lausanne, Switzerland

² LFMI, Swiss Federal Institute of Technology (EPFL), CH-1015, Lausanne, Switzerland

Preprint version of the article submitted in *Journal of Fluids Engineering*, (2017)

The global trend in reduction of CO_2 emission encourages electric energy as main driving force and promotes the development of renewable energy sources (RES), such as photovoltaic and wind energy, due to their large and imminent potential. The intermittent production of these unsteady RES added to the daily fluctuations of the consumption must be regularized to deliver a safe electric supply. The grid stability can be currently maintained by the reactive and flexible hydropower production but advanced regulation technique must be developed to continue to support the development of intermittent RES. Regarding the Francis turbines that represent 60% of the generating hydro-units, a natural improvement is the enlargement of operation flexibility, nowadays restricted to the design point of the machine. However operating at off-design is hindered by large pressure fluctuations that imperil the mechanical structure, calling for the development of flow control methods. We investigated the optimal control of the flow distribution at the part load operating condition characterized by a precessing helical vortex in the turbine draft tube. This vortex is identified as a self-sustained instability associated to the development of an infinitesimal disturbance, we demonstrate that it can be stabilized by targeting the dominant growth rate of the mean turbulent flow through an adjoint-based minimization algorithm. We determine an optimal force distribution that successfully quenches the part load vortex rope and sketches the design of a realistic control appendage.

4.1 Introduction

The daily fluctuations of the electrical consumption are balanced by flexible electric power generation to insure a safe electric supply. This monitoring capacity is perfectly mastered, but the additional incoming intermittent electric power production from the renewable energy sources (RES) has started to stress the electric grid and will jeopardize in a foreseeable future the grid stability. These variations, resulting both from consumption and production, can be mainly regulated by the flexible power production of hydraulic turbines, which are able to

generate or interrupt hundred of megawatts in less than a minute in certain cases. However this regulation technique has almost reached its limits and further improvements and developments are needed for hydropower to be able to continue to support the future development of the unsteady RES. Among all turbine types that contribute to hydropower capacity, which amounts to 17% of the total electric energy production, the Francis units represent 60% of the world wide market. We, therefore, focus on advanced regulation techniques provided by Francis generating units. A natural improvement may be the enlargement of the Francis turbine operating region, restricted to a limited region between the best efficiency conditions and full load for the moment. Unfortunately off-design operating conditions in Francis turbines result in complex flow patterns in the turbine draft tube that produce large pressure fluctuations and expose the turbines to the risks of operating instability, structural fatigue and resonance of the mechanical structures. These fluctuations originate from large coherent vortex structures, resulting from residual swirling flow at the runner outlet, and characterized by an axisymmetric pulsating vortex at full load conditions and an helical precessing vortex at part load conditions called part load vortex rope. In contrast, at the design point, a nominal flow condition is observed: an axial flow exits the runner and minimizes the hydraulic losses, denominated as best efficiency point (BEP). An extension of operating conditions thus passes through the pressure fluctuations mitigation in hydraulic turbines by controlling the flow, so as to best release the full hydropower potential.

A wide variety of control techniques have been developed over the years, which fall within categories like open-loop, closed-loop, passive or active controls, without forgetting trial and error methods based on designers' intuitions that are always legitimate for complex cases. We refer to Kim & Bewley [85] for an overview of the control techniques applied to Navier-Stokes equations, among all we focus, in the present study, on the so-called predictive control or adjoint-based cost functional minimization approach (Joslin et al. [87], Gunzburger [92] and Bewley et al. [88]). This optimization problem solves the first-order necessary conditions of a Lagrangian functional, suitably built from the governing equations and a defined objective function, to determine a closed-form expression of the gradient direction or optimality condition so as to iteratively minimizes a flow target. This target may be defined as the drag of an obstacle, the turbulent kinetic energy, an eigenvalue associated to an instability, etc. Such predictive techniques are computationally extremely demanding, due to the need of unsteady direct and adjoint computations, although with the recent advent of high performance computing facilities (HPC), there is a certain revival in this approach (Passaggia & Uhrenstein [89] and Goit & Meyers [90]). This adjoint-based method has been applied to self-sustained instabilities in open flows by targeting the most unstable eigenvalue as objective function, in a suboptimal sense through the computation of linear sensitivity maps, to find the most preferable actuation locations (Giannetti & Luchini [55], Marquet et al. [6] and Qadri et al. [80]) or more rarely in an optimal sense for annihilation of the self-sustained instability, Camarri & Iollo [94] in a 2D case, Pasche et al. [10] in a 3D case. Being first investigated in the laminar regime, the global linear stability analysis around a base flow is able to predict the flow bifurcation from a stationary solution of the Navier-Stokes equations to the development of a

Chapter 4. Optimal control of self-sustained instabilities in turbulent swirling flows: Application to the Francis turbine part load vortex rope

self-sustained instability identified by the exponential growth rate of an unstable eigenmode. The frequency prediction of this unstable eigenvalue becomes however often incorrect as the system departs from the instability threshold, while the global stability analysis of the mean flow successfully predicts the limit cycle frequency in some canonical flows (Barkley [5]). This improved frequency approximation from the mean flow stability analysis comes from a flow feedback mechanism associated to the self-sustained instability development. The difference between the base flow and mean flow is imputed to the Reynolds stresses of the self-sustained instability, as demonstrated by Sipp & Lebedev [83] using a weakly nonlinear multiple-scale expansion at the threshold, and by Mantič-Lugo et al. [84] further away from threshold using a self-consistent model that couples the forced base flow by the perturbation's Reynolds stresses to a linear disturbance equation. This correct frequency prediction of laminar limit cycles translates in some cases to turbulent flows. The stability analysis of mean turbulent flow was shown to correctly capture dominant frequencies (Viola et al. [123]) while linear sensitivity maps (Meliga et al. [47]) developed around the mean flow were found predictive. The consistent sensitivity map predictions in turbulent flows let us envisage the mitigation of the part load vortex rope by solving an optimal control problem that targets an unstable eigenvalue of the mean flow in a Francis turbine.

The part load vortex rope was investigated over many years experimentally and numerically. Numerical tools dealing with complex 3-D rotating geometry and two-phase flows were developed, see Trivedi et al. [23] for a review, and experimental measurements using wall pressure acquisitions, laser Doppler velocimetry (LDV), particle image velocimetry (PIV) in two phase flows or high speed visualizations were performed (Ciocan et al. [9], Iliescu et al. [16], Kirschner et al. [129], Favrel et al. [17] and Müller et al. [114]). Numerical flow simulations and experimental measurements result in an accurate description of flow phenomena as well as a data collection for flow models development with the aim to predict for example the swirl at the runner outlet (Susan-Resiga et al. [116]), or acoustic resonance of the machine (Alligné et al. [35] and Landry et al. [130]). The control of the vortex rope was investigated by trial and error or physical intuitions due to the lack of a significant target to build a minimization problem. One approach, related to passive control, is to decrease the swirl at part load regime by applying stabilizer fins (Nishi et al. [25]) or J-groove (Kurokawa et al. [26]), on the draft tube wall. A different blade design with shaped outlet was investigated by Brekke [27] that also aims to correct the swirling flow distribution at the draft tube inlet. Another approach is to modify the recirculation region close to the runner by adding an extension to the crown tip (Qian et al. [28]). However such techniques are only able to mitigate the pressure fluctuations in a narrow operating regime and can create additional undesirable hydraulic losses due to permanent geometry modification. Regarding active controls, a feeding pipe in the turbine draft tube controlled by a rotating valve is able to cancel the first harmonic of the part load vortex rope by producing an inverse signal (Blommaert et al. [32]). However this technique has amplified the second and third harmonic, reducing the total pressure fluctuations by only one quarter. Susan-Resiga et al. [29] have investigated an axial water injection from the crown tip, and have successfully mitigated the pressure fluctuations over a large operating range by controlling the

jet velocity. This technique allows one to suppress the part load vortex rope by letting the jet velocity reaches a value of 10% to 12% of the turbine discharge (Zhang et al. [30]). The same conclusions were obtained using a swirling vane (Bosioc et al. [131]). In addition a parametric study of the jet velocity and discharge is proposed by Foroutan & Yavuzkurt [31] to obtain a better combination to eliminate the pressure fluctuations in a straight draft tube.

Despite the large number of control techniques which have been tested over the years, the best control strategy still needs to be assessed. From this perspective we therefore use an optimization technique, following the optimal control theory, to compute a relevant volume force to control the vortex rope. Since the part load vortex rope is an unstable eigenmode associated to an unstable eigenvalue (Pasche et al. [65]), we choose to minimize the growth rate of this unstable eigenvalue as target for the flow stabilization, a direct way to suppress this self-sustained instability. While a volume force cannot be imposed in practice, it illustrates where to act to effectively control the part load vortex rope.

The paper is structured as follows: the case studied is presented in section 4.2. Then an adjoint-based algorithm is described in section 4.3 and its computation is introduced in section 4.4. Then the results are presented in section 4.5 and a conclusion is drawn.

4.2 Flow configuration

We have investigated numerically flow control applied to the Francis turbine geometry of the FLINDT case study - flow investigation in draft tube - project, Eureka No. 1625, see Avellan [15]. This turbine is composed of a high specific speed runner followed by an elbow draft tube and a pier, see fig. 4.1(a) and (c). In the present study, we have introduced a second draft tube geometry, an axisymmetric Moody type [132] draft tube fig. 4.1(d), designed by discharge conservation over cross sections of the elbow draft tube (Pasche et al. [65]). We have considered the flow distribution bounded by these geometries for prescribed part load operating conditions, a flow rate coefficient of $\phi = 0.27$, a specific energy of $\psi = 1.16$ and a Thoma cavitation number of $\sigma = 1.16$. At these conditions, 67% of the BEP discharge flows across the turbine, and the residual swirling flow appearing at the runner outlet leads to a precessing cavitation-free vortex rope inside the draft tube. The time evolution of this vortex has been monitored by wall pressure points at two cross sections, S1.3 and S1.75, in the draft tube cone fig. 4.1(b), localized at the same positions as the pressure sensors in the experimental measurements performed by Arpe & Avellan [8].

4.3 Theoretical framework

As detailed in Pasche et al. [65], the part load vortex rope develops through the exponential growth of an infinitesimal disturbance whose amplitude saturates by a nonlinear feedback mechanism and leads to its final self-sustained rotating vortex structure. A natural control strategy is therefore to prevent the development of this disturbance, which can be caught by a

Chapter 4. Optimal control of self-sustained instabilities in turbulent swirling flows: Application to the Francis turbine part load vortex rope

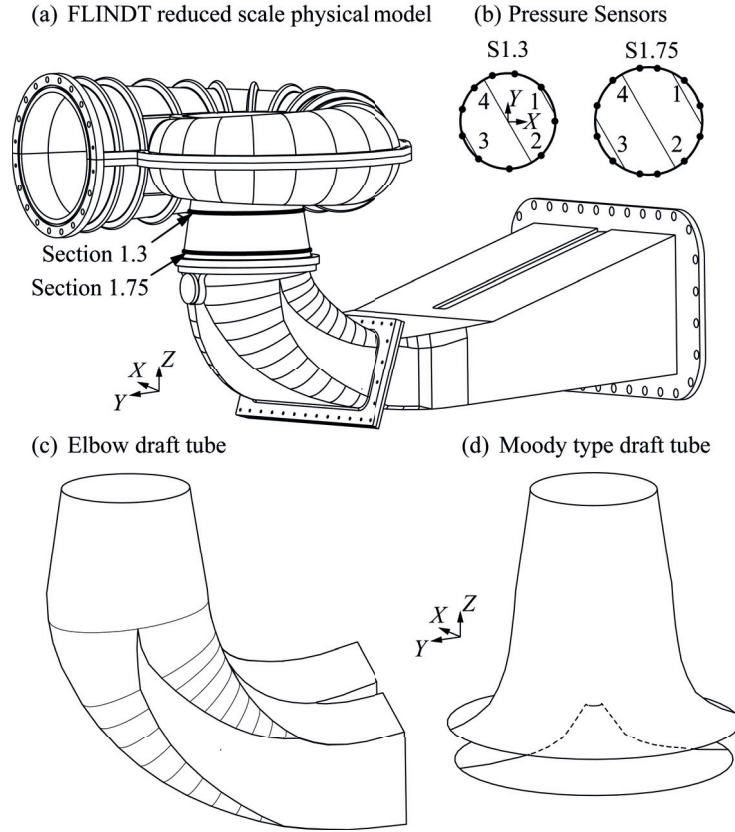


Figure 4.1 – Reduce scale model of the FLINDT Francis turbine (a), pressure sensor location (b), the original elbow draft tube (c), and the axisymmetric Moody type draft tube used to compute the minimization algorithm (d).

global stability analysis around the mean turbulent flow from an infinitesimal disturbance decomposed in an azimuthal-temporal complex Fourier series:

$$(\tilde{\mathbf{C}}, \tilde{P})(R, \theta, Z, t) = (\mathbf{c}, p)(R, Z) \exp(i(m\theta - \omega t)) + c.c., \quad (4.1)$$

with $c.c.$ the complex conjugate, m the azimuthal wavenumber and ω the eigenvalue. The part load vortex rope disturbance is characterized by an unstable eigenmode associated to an unstable eigenvalue ω_v of azimuthal wavenumber $m = 1$. Since the stability analysis results in a large set of eigenvalues, we choose as control target the eigenvalue associated to the vortex rope disturbance on the basis of its frequency (real part) and eigenfunction. We have developed a minimization algorithm to stabilize the flow, based on the optimal control theory whose objective function targeted the growth rate of the unstable eigenmode $-\Im(\omega_v)$. This minimization problem writes as:

$$\text{Min } \mathcal{J}(\omega_v, \mathbf{F}) = |\Im(\omega_v)| + \frac{\alpha}{2} \iint_{\Omega_a} \|\mathbf{F}\|^2 d\Omega_a, \quad (4.2)$$

where \mathcal{J} is the objective function, \mathbf{F} the control variable, α the scalar weight penalizing of the control intensity and ω_ν the targeted eigenvalue. The control variable is defined as a volume force distributed along $(\mathbf{e}_R, \mathbf{e}_Z)$, that at convergence ended to (F_R^*, F_Z^*) . We reformulate this optimization problem using Lagrangian functional \mathcal{L} , expressed in appendix eqn. (4.4), where the adjoint fields are used as Lagrangian multipliers: $(\mathbf{C}^\dagger, P^\dagger)$ for the state variable and $(\mathbf{c}^\dagger, p^\dagger)$ for the disturbance. We derive the set of equations that sought for a gradient direction of this problem by satisfying the stationary condition of \mathcal{L} . This set of equations expressed in appendix eqns. (4.6-4.11), leads to the following general form of the gradient direction for a distributed control force F :

$$\nabla \mathcal{J} = \mathbf{C}^\dagger + \alpha \mathbf{F}. \quad (4.3)$$

This gradient direction coupled with a steepest descent method allowed us to minimize our objective function eqn. (4.2). A schematic of the minimization algorithm is displayed in fig. 4.2. Instead of computing this minimization problem in a full 3-D domain we are able to

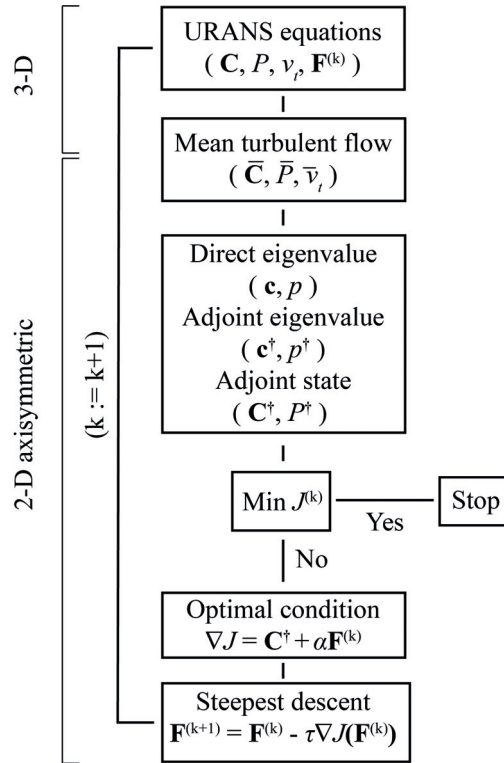


Figure 4.2 – Schematic of the minimization algorithm for the mean turbulent flow stabilization.

compute it partially in a 2-D axisymmetric domain (on a slice of the 3-D domain), thanks firstly to the symmetry properties of the part load vortex rope that can be caught by azimuthal Fourier decomposition eqn. (4.1) and secondly to the axisymmetric Moody type draft tube design that preserves the frequency of the vortex rope (Pasche et al. [65]). The algorithm solves the following steps: The Unsteady Reynolds-Averaged Navier Stokes (URANS) equations

Chapter 4. Optimal control of self-sustained instabilities in turbulent swirling flows: Application to the Francis turbine part load vortex rope

bounded by the Moody type draft tube geometry are first solved numerically. On the fly, the time averaged solutions of the velocity, pressure and eddy viscosity distribution are computed. The dimensionality reduction from the 3-D to the 2-D axisymmetric domain is obtained by azimuthal averaging procedure leading to an axisymmetric mean turbulent flow solution about which linear disturbance developments are investigated. The iterative computation of the direct eigenvalue problem eqn. (4.7), the adjoint eigenvalue problem eqn. (4.8), the normalization condition eqn. (4.9) and the adjoint flow equations eqn. (4.10) results in the gradient direction (optimal condition) eqn. (4.3). Coupled to a steepest descent method, this gradient direction minimizes our objective function. As the first loop is performed, an axisymmetric volume force is obtained and is included in the URANS equations of the next step, and so forth, until the vortex rope is quenched. Finally the 2-D axisymmetric optimal volume force is applied to the elbow draft tube geometry by solving the associated forced URANS equations.

We focus in this Chapter on the mean turbulent flow stabilization control, issued from the computation of the linear sensitivity map (Giannetti & Luchini [55] and Marquet et al. [6]) at each iterative step. However, with the thought to provide an overview and to increase the pertinence of the proposed method in turbulent swirling flows, we also compute the "linear sensitivity-based finite amplitude control" of the part load vortex rope, similar to the spiral vortex breakdown control in laminar swirling flow (Chapter 2 and Pasche et al. [10]), while this second approach appears to be suboptimal to control the spiral vortex breakdown. As reminder, in this called "linear sensitivity-based finite amplitude control", the first gradient direction $\nabla_F \omega_i = \mathbf{F}^{(0)}$ is multiplied by a finite amplitude A determined by a bisection method until the growth rate of the controlled leading eigenvalue is equal to zero. The results of this second approach are presented in appendix 4.7.2.

4.4 Numerical methods

4.4.1 Three-dimensional numerical flow simulations

The solution of the URANS equations for the two geometries considered, the elbow draft and the axisymmetric Moody type draft tube, are computed with ANSYS CFX 16.0. We reused the solver configurations and the meshes from the previous study on stability analysis of the part load vortex rope in Pasche et al. [65], where the numerical solution from these pre-processing steps were already validated against experimental measurements. The fluid domain includes the runner, the draft tube and a draft tube extension to avoid backward perturbations from the outlet. The velocity and the turbulence intensity is distributed at the inlet of the runner coming from a previous steady calculation of the spiral casing and guide vane cascade. An open condition is set at the outlet and the flow is transferred from the rotational to the stationary domain by a general grid connection (GGI). A time step of 1 deg of runner revolution and a rms convergence error of 10^{-4} are imposed and the turbulence is modeled by a shear stress transport-based scale-adaptive simulation (SST-SAS) model. The

meshes have a total of 7.5 mio of hexahedral cells for the axisymmetric Moody type draft tube and 7.5 mio for the elbow draft tube case. The time averaged variables, velocity and eddy viscosity, is computed on the fly while the simulation is running and they start to be averaged after the transient dies out corresponding to time lap from 1.5 to 5 vortex rotations. The pressure is also monitored on the two different section S1.3 and S1.75. The mean flow velocity and mean eddy viscosity, around which the minimization algorithm is computed to control the vortex rope, is azimuthally averaged to obtain a 2-D axisymmetric solution.

4.4.2 Minimization problem

Except the mean turbulent flow, the optimization algorithm is solved numerically on a 2-D axisymmetric domain by the means of the finite element solver Freefem++ [101] for the axisymmetric Moody type draft tube only. The meshe satisfies the inf-sup conditions by using P_2 - P_1 shape functions on triangular elements. The fluid domain ends at the outlet 3-D draft tube domain and starts as close as possible to the runner blade to avoid inlet perturbations. This domain is discretized by a total of 300'000 triangular cells suitably distributed. The direct and adjoint eigenvalue problem are solved using a Krylov method from ARPACK libraries [104] with a tolerance of 10^{-6} where matrix inversions are performed with UMFPACK package, a sparse lower-upper triangular matrix factorization. After obtaining the gradient direction, a steepest descent method is used to update the control with a step length defined by an Armijo line search method [108]. The initial step $\tau = 5 \cdot 10^{-4}$ and a weight control parameter of $\alpha = 10^{-2}$ are set. The algorithm is computed until the part load vortex rope is stabilized.

4.5 Results

4.5.1 Optimal control of the part load vortex rope

The effect of the predictive control of the part load vortex rope minimizing eqn. (4.2) is displayed in fig. 4.3. The uncontrolled flow (fig. 4.3a) shows a single helical vortex core in the turbine draft tube, materialized by a pressure iso-contour. This vortex rotates in time in the same direction as the ambient swirling flow and coils spatially in the opposite direction. This precession induces a local flow acceleration along the draft tube wall in the free-stream direction and a counter flow acceleration in the draft tube center. In opposition, the controlled flow (fig. 4.3b) displays a columnar vortex confined along the draft tube center line. This columnar vortex appears disorganized, without coherent vortex core and it disintegrates at the draft tube cone end. This vortex is characterized by counter flow regions of high intensity in its center, surrounded by accelerated flow regions in the free-stream direction. The shear stress between these flow regions not only produces small scale velocity fluctuations that increase the turbulence intensity, but also increases the pressure level inside the draft tube as shown by the constant pressure iso-contour $C_P = -4.1$. The flow topology change demonstrates the achievement of the control goal, which minimizes the unstable eigenvalue of the mean

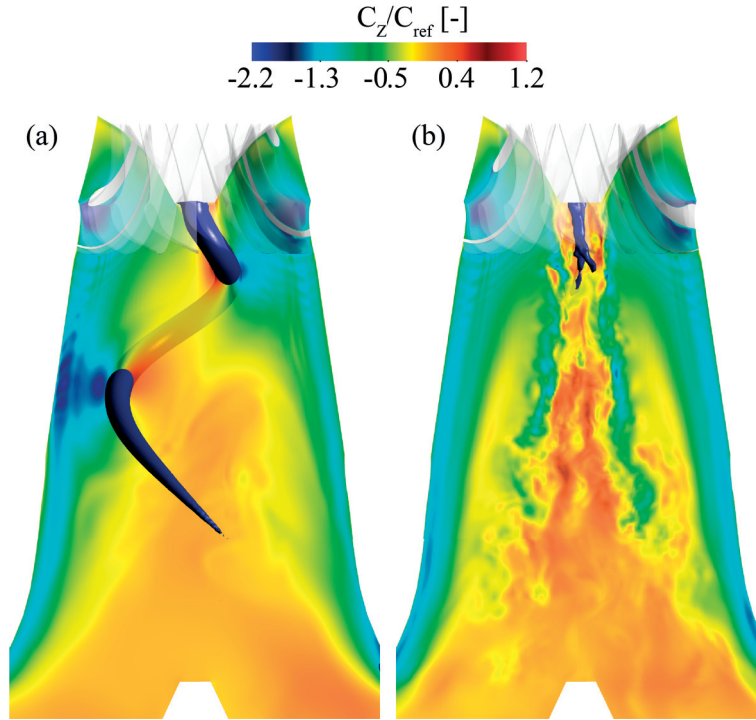


Figure 4.3 – Uncontrolled (a) and controlled (b) axial flow solutions carried out by minimizing the dominant unstable eigenmode of the mean flow, superimposed with a pressure iso-contour ($C_p = -4.1$) materializing the part load vortex rope.

turbulent flow associated to the part load vortex rope.

The influence of the minimization procedure on the part load vortex rope is monitored by two parameters, the amplitude of the peak-to-peak pressure coefficient at the monitoring points of sections S1.3 and S1.75 and the growth rate of the unstable eigenvalue computed from the mean turbulent flow. These parameters are reported as a function of the volume force norm in fig. 4.4. The peak-to-peak amplitudes (fig. 4.4a) of the vortex rope slowly decrease following a linear trend until the penultimate update of the volume force is carried out. The pressure fluctuations are damped by 30% before being totally mitigated by the ultimate volume force update, which quenches the vortex rope. This sudden mitigation of the vortex rope has also been reported in experimental setup using axial water jet injection at the tip of the runner cone (Bosio et al. [131]). The same curve behavior is observed for the unstable eigenvalue evolution (fig. 4.4b), except for one iteration where the growth rate increases, pointing to the fragility of computing eigenvalues of high Reynolds number flows, although the peak-to-peak pressure amplitudes monotonically decrease. At the ultimate iteration, the dimensionless force norm requires to quench the part load vortex rope was equal to $\|\mathbf{F}^*\| = 0.56$.

The eigenvalue spectrum of the azimuthal wavenumber $m = 1$ is displayed for the initial, penultimate and ultimate iteration of the minimization procedure in fig.4.5(a), (b) and (c), respectively. As remainder, only eigenmodes of azimuthal wavenumber $m = 1$ are shown to be

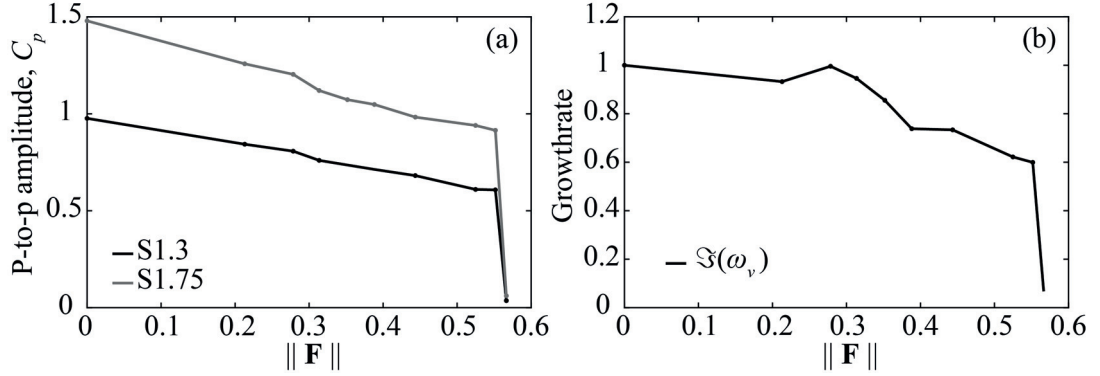


Figure 4.4 – Influence of the control norm on the peak-to-peak pressure coefficient amplitude (a) and growth rate normalized by uncontrolled dominant eigenvalue (b) during the minimization procedure. Each symbol corresponds to an iteration.

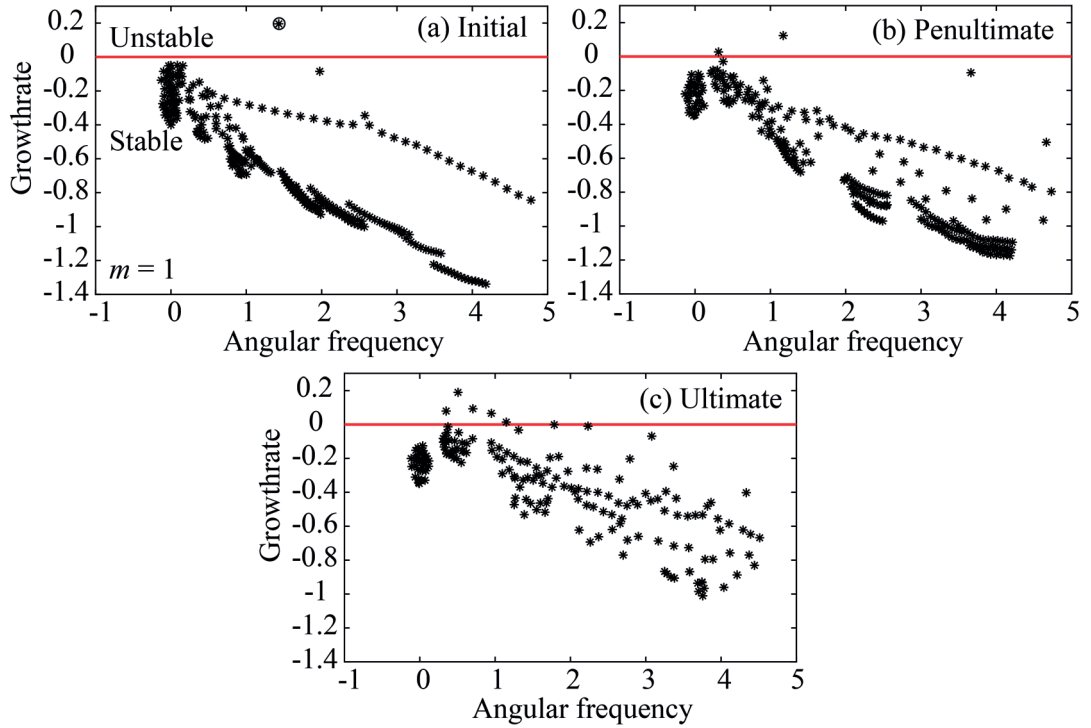


Figure 4.5 – Eigenvalue spectrum of azimuthal wavenumber $m = 1$ from the mean turbulent flow of the initial iteration (a), the penultimate iteration (b) and the ultimate iteration (c). The symbol $(*)$ represents the direct eigenvalue from eqn. (4.7) and the symbol (\circ) represents the complex conjugate adjoint eigenvalue from eqn. (4.8), only displayed in subfigure (a)

Chapter 4. Optimal control of self-sustained instabilities in turbulent swirling flows: Application to the Francis turbine part load vortex rope

unstable (Pasche et al. [65]), which corresponds to single helical disturbances coiling spatially in the opposite direction of the ambient flow rigorously identical as the part load vortex rope. Initially the unstable eigenvalue of the vortex rope is clearly apart from the other stable eigenvalue. At the penultimate iteration, an additional marginally unstable eigenvalue at low frequency appears beside the eigenvalue associated to the part load vortex rope disturbance. The growth rate and frequency of the vortex rope eigenvalue is slightly inferior as compared to the uncontrolled flow, and remains clearly dissociated from the other eigenvalues. At the ultimate iteration, several unstable eigenvalues located at low frequency appear. Among all, the eigenvalue associated to the vortex rope is selected on a narrow band width filter from the frequency of the previous iteration, and its associated eigenmode is found to be confined in the center of the draft tube. Since the other eigenmodes are also concentrated in the columnar vortex observed in fig. 4.3(b), we speculate that the increase of turbulence intensity is produced by small scale fluctuations as well as the disintegration of the columnar vortex at the cone end might be explained by the interactions of these $m = 1$ instabilities. The emergence of other unstable eigenmodes while the dominant growth rate is minimized, can compromise the algorithm convergence but in the present study, the marginally unstable eigenvalue of the penultimate iteration remains ineffective allowing us to quench the part load vortex rope by our control strategy.

While the force norm is updated, we observe a sudden flow transition from the penultimate iteration, where a coherent single helical state (one unstable eigenvalue) is observed to a columnar centralized vortex state (several unstable eigenvalue) at the ultimate iteration. We expect a smooth stabilization of the unstable eigenvalue associated to the vortex rope. However, the eigenvalue growth rate drops suddenly. This behaviour can be the consequence of the mean flow distortion by the nonlinear mode interactions, such as harmonic mode generations (Sipp & Lebedev [83]) that is additionally accounted in the eigenvalue growth rate.

The radial and axial volume forces that quench the part load vortex rope are exhibited in fig. 4.6(a) and (b), respectively. The radial volume force acts in two locations, under the runner crown tip rising to the runner crown wall, and in the middle of the draft tube. The axial volume force acts along the whole draft tube center line until the end of the draft tube cone. The control effort are mainly achieved by the axial volume force that accelerates the flow along the draft tube center line and decelerates it around the tip of the runner crown. Both forces display a control free region at the tip of the runner cone and along the draft tube wall where the part load vortex rope is not sensitive to control strategies.

4.5.2 Flow control in reduced scale model geometry

The optimal volume force obtained by minimizing eqn. (4.2) quenches successfully the part load vortex rope in the axisymmetric Moody type draft tube, we have next tested this volume force on the reduced scale model geometry designed with the elbow draft tube. For that purpose, the axisymmetric optimal volume force is interpolated on the elbow draft tube mesh.

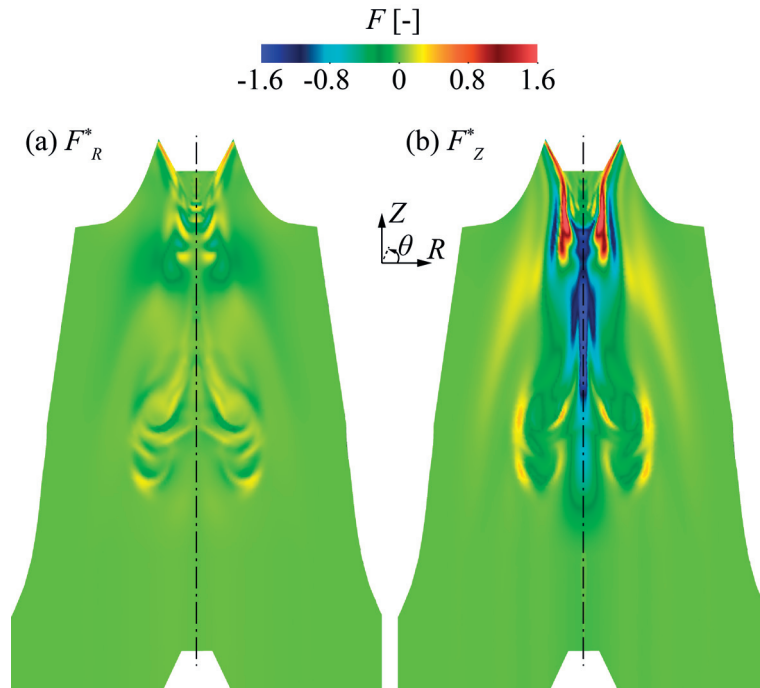


Figure 4.6 – Radial (a) and axial (b) volume force obtained by minimizing the dominant growth rate of the mean turbulent flow that stabilizes the part load vortex rope.

The pressure monitored at the section S1.3 during the transient phase of the vortex rope control is displayed in fig. 4.7 for the sensor 1, 2, 3, 4. The pressure fluctuations decrease in amplitude to reach a quasi steady state after 5 initial vortex rope precessions, showing the successful annihilation of the part load vortex rope by the computed axisymmetric volume force. In addition, we observe that the different pressure signals merge at time $t = 0.82$ s and therefore the flow becomes axisymmetric as the coherent structure of the vortex rope is destroyed. The vortex flow associated to these pressure temporal signals is exhibited in fig. 4.8 by temporal snapshots of axial velocity superimposed with a constant pressure iso-contour. The vortex intensity starts first to decrease until $t = 0.82$, where the vortex, which keeps its helical shape, is shrunk at the runner outlet and its tail is no longer extending in the elbow. From $t = 0.82$ on, the coherent structure is destroyed and small scale fluctuations are increased, leading finally to a columnar vortex in the draft tube center line similar to the controlled flow of the Moody type draft tube, fig. 4.3(b).

Time averaged global parameters, such as the runner torque and the turbine specific energy, are calculated in the uncontrolled flow regime and in the quasi stationary regime of the controlled flow. We obtain identical parameter values for both cases, showing that our optimal volume force does not modify the flow condition in the runner. Time-averages of local parameters are also investigated for the controlled and uncontrolled cases. Figure 4.9 exhibits the surface integral of the specific energies associated to the static E_S , the kinetic E_k and the total E_{tot} pressures on cross sections along the draft tube curvilinear center line, normalized

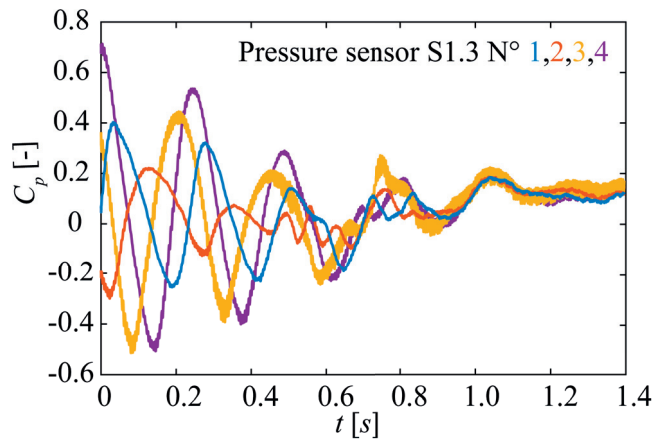


Figure 4.7 – Monitored coefficient pressure on section S1.3 at the sensor location 1, 2, 3, 4, during the transient control of the part load vortex rope in the elbow geometry.

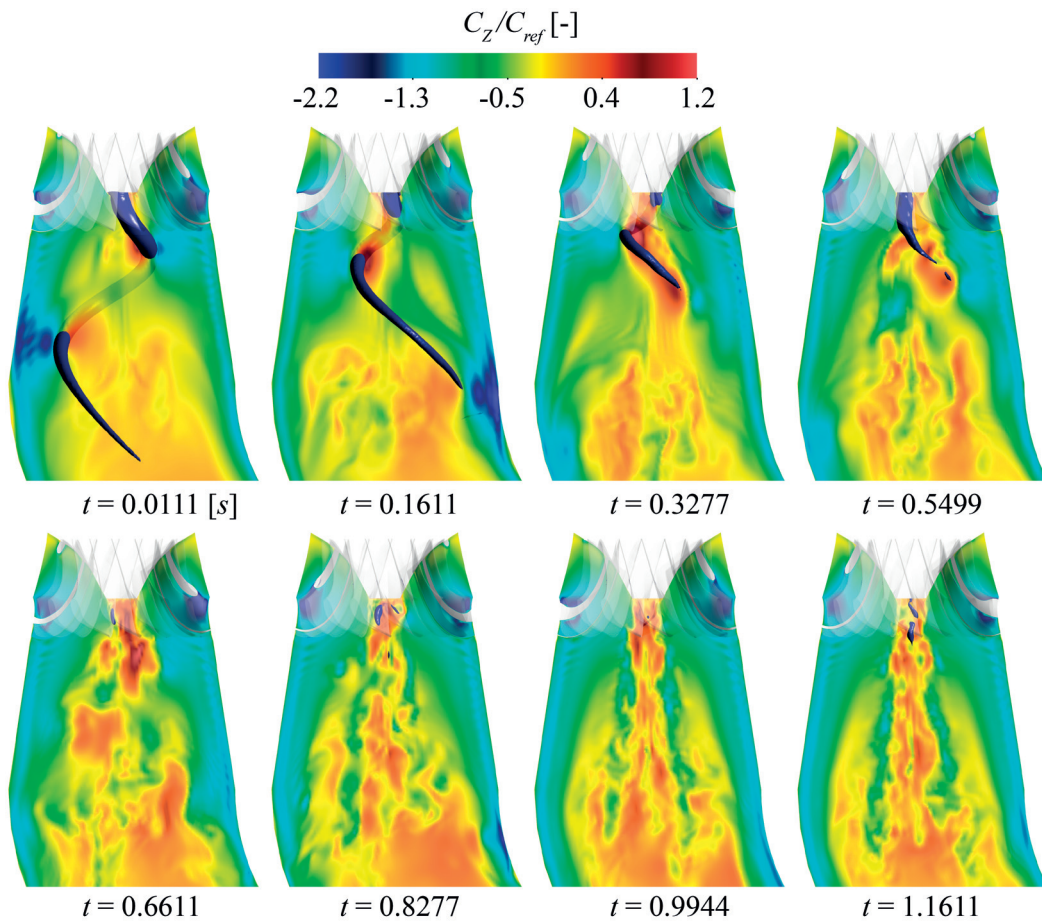


Figure 4.8 – Temporal snapshots of the axial velocity and the pressure iso-contour of value $C_p = -4.1$, exhibiting the part load vortex rope quenched by the 2-D axisymmetric optimal force obtained by minimizing eqn. (4.2).

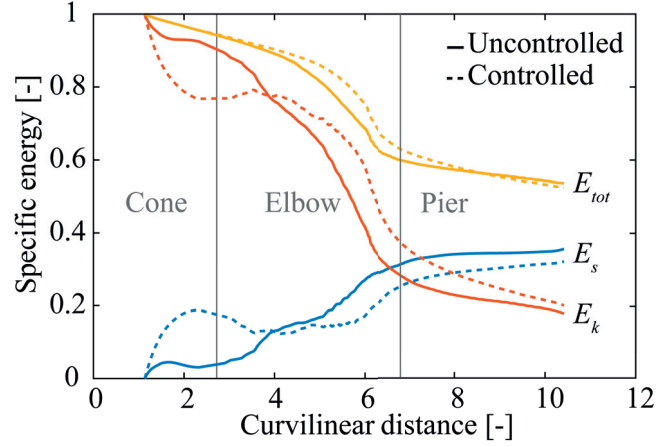


Figure 4.9 – Surface specific energy of static E_s , kinetic E_k and total E_{tot} pressures on cross sections along the draft tube curvilinear distance normalized by the kinetic specific energy at the draft tube inlet.

by the dynamic pressure at the draft tube inlet. The total pressure specific energy drops inside the elbow as a consequence of the part load operating condition due to hydraulic losses, in opposition to the BEP condition where the total pressure specific energy is kept close to a value of 1 and delivers therefore a high turbine efficiency. The static pressure specific energy was increased in the draft tube cone when the vortex rope was controlled, but this specific energy returned to the uncontrolled energy level of the elbow draft tube after the cone.

4.6 Conclusion

We have investigated the predictive control of the part load vortex rope. We have defined a relevant objective function that targets an intrinsic property of this flow. Since the vortex rope is an infinitesimal disturbance growing about the mean turbulent flow, which is expressed as an unstable eigenmode (Pasche et al. [65]), we choose to minimize the growth rate of this dominant unstable eigenmode. Using the optimal control framework, we have derived the gradient direction that minimizes our objective function, by satisfying the first order necessary condition of the Lagrangian functional of our problem. Coupled with a steepest descent method, this gradient direction leads to an optimal volume force that successfully quenches the part load vortex rope and reduces the pressure fluctuations to a quasi-stationary state.

Starting from a coherent single helical vortex, the ultimate control shrinks the part load vortex rope in the center of the draft tube, and produces turbulence fluctuations in this region. The remaining flow does not have any coherent single spiral. When the control is activated, the flow needs 5 initial vortex rope precessions to quench the self-sustained instability.

The volume force controlling the radial and axial flow distribution is located along the center line of the draft tube cone. This force has a largest intensity on the axial component and

Chapter 4. Optimal control of self-sustained instabilities in turbulent swirling flows: Application to the Francis turbine part load vortex rope

accelerates the flow in the draft tube center line starting at the runner outlet location and keeps the region of the tip of the runner cone control-free. A decelerated axial force is also showed along the runner crown wall. The blade torques and the specific energy as well as the energy distribution in the draft tube are investigated but no significant change are observed, the torques and specific energies remaining identical.

We have developed a minimization algorithm to find an optimal volume force that is able to quench a self-sustained instability in turbulent swirling flows. The resulting bulk force can be used to design a control device that mitigates the part load vortex rope and therefore can open part load operating conditions of Francis turbines.

4.7 Appendix

4.7.1 Optimal control

We consider the constrained minimization problem associated to eqn. (4.2) that minimizes the dominant growth rate of the mean turbulent flow. The Lagrangian functional framework is used to find a close form expression of the gradient direction. This Lagrangian functional is expressed as:

$$\begin{aligned} \mathcal{L}(\omega_\nu, [\mathbf{c}, p], [\bar{\mathbf{C}}, \bar{P}], [\mathbf{c}^\dagger, p^\dagger], [\mathbf{C}^\dagger, P^\dagger], \mathbf{F}) = & \mathcal{J}(\omega_\nu, \mathbf{F}) - t(\mathbf{c}, \mathbf{c}^\dagger) - a(\mathbf{c}, \mathbf{c}^\dagger) \\ & - d(\mathbf{c}, \bar{\mathbf{C}}, \mathbf{c}^\dagger) - d(\bar{\mathbf{C}}, \mathbf{c}, \mathbf{c}^\dagger) - b(\mathbf{c}^\dagger, p) - b(\mathbf{c}, p^\dagger) - a(\bar{\mathbf{C}}, \mathbf{C}^\dagger) - d(\bar{\mathbf{C}}, \bar{\mathbf{C}}, \mathbf{C}^\dagger) \\ & - b(\mathbf{C}^\dagger, P) - b(\bar{\mathbf{C}}, P^\dagger) + \langle \mathbf{F}, \mathbf{C}^\dagger \rangle + \langle \mathbf{T}, \mathbf{C}^\dagger \rangle, \end{aligned} \quad (4.4)$$

where $a(.,.)$, $b(.,.)$ are the bilinear form of the viscous, pressure and divergence, $\langle ., . \rangle$ is the Hermitian inner product, $d(.,.,.)$ is the trilinear form, $t(.,.)$ is the mass matrix of the time derivative including the eigenvalue ω_ν , $(\mathbf{C}^\dagger, P^\dagger)$ are the Lagrange multipliers of the mean flow and $(\mathbf{c}^\dagger, p^\dagger)$ are the Lagrange multipliers of the perturbed flow, both called adjoint variables. A minimum if it exists is defined as a stationary point of the Lagrangian functional that is derived using the Frechet derivative

$$\left. \frac{d}{d\epsilon} \mathcal{L}([\dots + \epsilon \phi]) \right|_{\epsilon=0} = 0. \quad (4.5)$$

where ϕ is test functions associated to each variable. This computation leads to 6 sets of equations, the state equation, the direct eigenvalue problem, the adjoint eigenvalue problem, a normalization condition, the adjoint problem and the optimality condition. These problems are expressed in strong form in eqn. (4.6-4.11). The state equation considered in this problem are the mean flow equations, a RANS equations forced by the Reynolds stresses of the self-sustained instability that compensate for the mean flow distortion (Barkley [5], Sipp & Lebedev

[83] and Mantič-Lugo et al. [84]).

State equations:

$$\begin{aligned}\nabla \bar{\mathbf{C}} \cdot \bar{\mathbf{C}} &= -\nabla P + Re^{-1} \nabla^2 \bar{\mathbf{C}} + \nabla \cdot [\bar{\mathbf{v}}_t (\nabla + \nabla^T) \bar{\mathbf{C}}] + \mathbf{F} + \mathbf{T} \\ \nabla \cdot \bar{\mathbf{C}} &= 0,\end{aligned}\tag{4.6}$$

where \mathbf{F} is the control force and \mathbf{T} is the Reynolds stresses of the self-sustained mode.

Direct eigenvalue equations:

$$\begin{aligned}-i\omega \mathbf{c} + \nabla_m \mathbf{c} \cdot \bar{\mathbf{C}} + \nabla \bar{\mathbf{C}} \cdot \mathbf{c} &= -\nabla_m p + Re^{-1} \nabla_m^2 \mathbf{c} + \nabla \cdot [\bar{\mathbf{v}}_t (\nabla + \nabla^T) \mathbf{c}] \\ \nabla_m \cdot \mathbf{c} &= 0\end{aligned}\tag{4.7}$$

Adjoint eigenvalue equations:

$$\begin{aligned}i\omega^* \mathbf{c}^\dagger + \nabla_m^T \bar{\mathbf{C}} \cdot \mathbf{c}^\dagger - \nabla_m \mathbf{c}^\dagger \cdot \bar{\mathbf{C}} &= -\nabla_m p^\dagger + Re^{-1} \nabla_m^2 \mathbf{c}^\dagger + \nabla \cdot [\bar{\mathbf{v}}_t (\nabla + \nabla^T) \mathbf{c}^\dagger] \\ \nabla_m \cdot \mathbf{c}^\dagger &= 0\end{aligned}\tag{4.8}$$

Normalization condition:

$$1 - \langle \mathbf{c}, \mathbf{c}^\dagger \rangle = 0\tag{4.9}$$

Adjoint flow equations:

$$\begin{aligned}\nabla^T \bar{\mathbf{C}} \cdot \mathbf{C}^\dagger - \nabla \mathbf{C}^\dagger \cdot \bar{\mathbf{C}} &= -\nabla P^\dagger + Re^{-1} \nabla^2 \mathbf{C}^\dagger + \nabla_m \mathbf{c}^\dagger \cdot \mathbf{c}^* - (\nabla_m \mathbf{c})^H \cdot \mathbf{c}^\dagger + \nabla \cdot [\bar{\mathbf{v}}_t (\nabla + \nabla^T) \mathbf{C}^\dagger] \\ \nabla \cdot \mathbf{C}^\dagger &= 0\end{aligned}\tag{4.10}$$

Optimality condition:

$$\nabla \mathcal{J} = \mathbf{C}^\dagger + \alpha \mathbf{F}\tag{4.11}$$

All this equations are solved in a 2-D axisymmetric domain by the means of the Freefem++ software [101] and lead to the gradient direction that is updated by a steepest descent method

Chapter 4. Optimal control of self-sustained instabilities in turbulent swirling flows: Application to the Francis turbine part load vortex rope

and allow us to compute the optimal force to control the part load vortex rope.

We have verified that the targeted eigenvalue in the minimization problem eqn. (4.2) obtained by computing the direct eigenvalue equations eqn. (4.7) is the complex conjugate of the adjoint eigenvalue computed from the adjoint eigenvalue equations eqn. (4.8). These eigenvalues are exhibited in fig. 4.5(a).

Practically the state equations eqn. (4.6) are not solved in the presented form, it allows us to derived consistent equations. The mean flow $(\bar{\mathbf{C}}, \bar{P})$ is computed by taking the time averaged of the URANS flow solution, solved in a 3-D domain defined by equations:

$$\begin{aligned} \frac{\partial \mathbf{C}}{\partial t} + \nabla \mathbf{C} \cdot \mathbf{C} &= -\nabla P + Re^{-1} \nabla^2 \mathbf{C} + \nabla \cdot [\nu_t (\nabla + \nabla^T) \mathbf{C}] \\ \nabla \cdot \mathbf{C} &= 0. \end{aligned} \quad (4.12)$$

Then a slice of the time and azimuthal averaging flow solution is taken to reduce the 3-D domain to a 2-D axisymmetric domain to compute the minimization procedure.

4.7.2 Linear sensitivity-based finite amplitude control

Although the "linear sensitivity-based finite amplitude control" of the spiral vortex breakdown in laminar swirling flow appears as suboptimal compared to the "mean flow stabilization control" (Chapter 2), the former approach well identifies the minima and maxima of the nonlinear receptivity region of this laminar flow. Therefore the outcomes of the "linear sensitivity-based

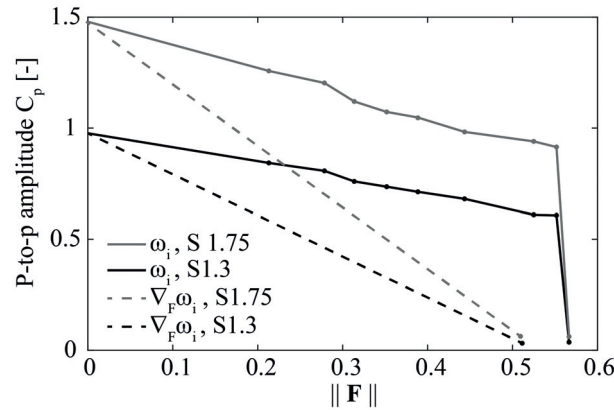


Figure 4.10 – Influence of the control norm on the peak-to-peak pressure coefficient amplitude for the "mean turbulent flow stabilization control" (solid curves) and the "linear sensitivity-based finite amplitude control" (dash curves) at the monitoring points of section 1.3 (black curves) and the section 1.75 (gray curves) for the axisymmetric draft tube. Each symbol corresponds to an iteration.

finite amplitude control" applied to the part load vortex rope are now assessed in this turbulent swirling flow.

The "linear sensitivity-based finite amplitude control" uses the first gradient direction ($\nabla_F \omega_i = \mathbf{F}^{(0)}$) of the minimization algorithm (fig. 4.2) or equivalently the linear sensitivity map (Giannetti & Luchini [55] and Marquet et al. [6]) multiplied by a finite amplitude A , determined by a bisection method until the growth rate of the controlled leading eigenvalue is equal to zero (Chapter 2). As we have seen for the ultimate minimization step of the "mean turbulent flow stabilization control" of the draft tube flow distribution (see fig. 4.5c), the eigenvalue associated to the part load vortex rope is very difficult to identify in the stabilized regime. The determination of the amplitude A is therefore supported by the assessment of the the peak-to-peak pressure coefficient amplitude at the draft tube cone sections 1.3 and 1.75. Figure 4.10 displays these peak-to-peak oscillations as a function of the distributed force norm for the two control methods. Both approaches reduce the flow oscillations close to zero in the draft tube cone. More surprisingly, we observe that the "linear sensitivity-based finite amplitude control" has a smaller norm than the "mean turbulent flow stabilization control", possibly because of the increase of the growth rate at one iteration during the minimization process (see fig. 4.4b).

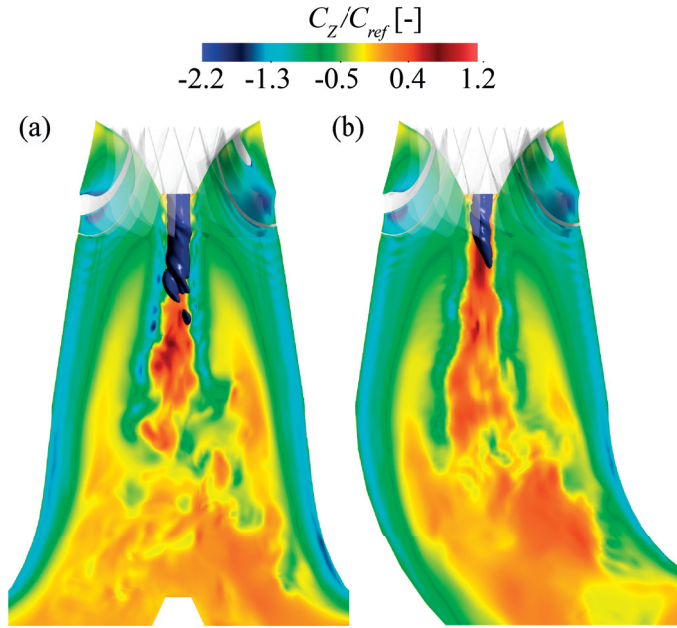


Figure 4.11 – Controlled axial flow solutions of the axisymmetric draft tube (a) and elbow draft tube (b) carried out by the "linear sensitivity-based finite amplitude control", superimposed with a pressure iso-contour ($C_p = -4.1$) materializing the part load vortex rope.

The controlled flow of the "linear sensitivity-based finite amplitude control" is displayed in fig. 4.11 for the axisymmetric draft tube and the elbow draft tube. Note that the axisymmetric draft tube is used to determine the ultimate distributed force, while this force is only transferred to the elbow draft tube as final validation step. In both geometries, the part load vortex rope is quenched and a columnar vortex remains in the draft tube center line, which appears disorganized and disintegrates at the draft tube cone end. These results are similar to the "mean turbulent flow stabilization control", see fig. 4.3 and 4.8.

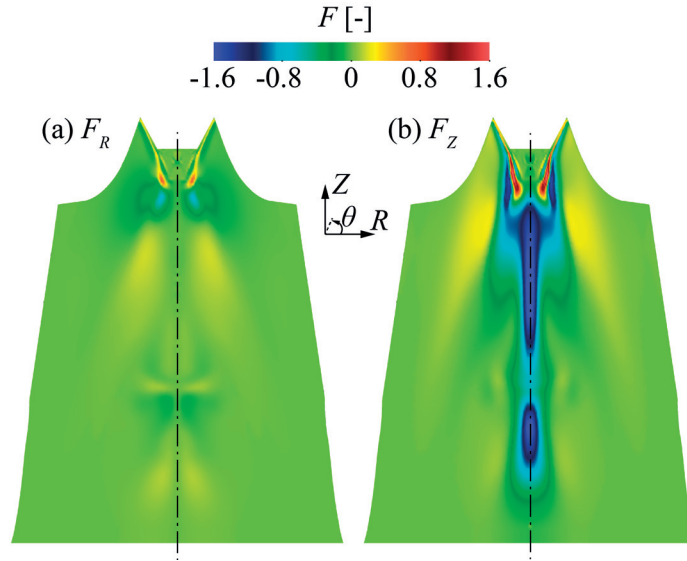


Figure 4.12 – Radial (a) and axial (b) volume force obtained from the "linear sensitivity-based finite amplitude control" that stabilizes the part load vortex rope.

The associated distributed force which quenches the part load vortex rope is displayed in fig. 4.12. This force differs from the "mean turbulent flow stabilization control" (see fig. 4.6), except for the draft tube cone center line region where the bulk force pushes the flow toward the streamwise direction in both approaches. The linear receptivity, provided by the first gradient direction, well identifies , therefore, the minimum of the nonlinear receptivity map in this turbulent swirling flow.

4.8 Discussion

Linear sensitivity maps correctly identify the min/max nonlinear receptivity regions of the part load vortex rope and therefore appear to be sufficient to develop an appendage to access these regions in order to control the flow. However the validity of this approach cannot be ensured *a priori*. The proposed minimization algorithm appears therefore promising to design a robust control, which aims at stabilizing self-sustained instability of turbulent swirling flows.

The identification of the near optimal amplitude A of the "linear sensitivity-based finite amplitude control" is difficult in practice. An approximated amplitude A based on the first gradient direction is not suitable due to the sudden drop of the control curves during the minimization process (see fig. 4.4). We should mention that we have finally required in the bisection method as many steps as the minimization process to obtain this near-optimal amplitude A . Therefore the "linear sensitivity-based finite amplitude control", which should be *a priori* computationally cheaper than a nonlinear receptivity is in reality equivalent if the marginally stable solution is sought.

5 Pressure surge and synchronous pressure fluctuations in Francis turbines

In this chapter, we investigate the origin of the synchronous pressure fluctuations in Francis turbines. This synchronous pressure, associated to a planar wave, can excite the hydraulic piping systems of the power plant and can lead to dangerous pressure surges when the frequency resonance occurs. The interaction between the solid wall of the draft tube and the part load vortex rope is investigated using asymptotic analysis to provide further insight of the mechanism generating the synchronous pressure wave.

The variables used in this document are susceptible to change in comparison to the submitted version of the article to keep the document consistency. Additional paragraph and results could be also added.

PAPER: Origin of the synchronous pressure fluctuations in the draft tube of Francis turbines operating at part load conditions

Origin of the synchronous pressure fluctuations in the draft tube of Francis turbines operating at part load conditions

Simon Pasche¹, François Avellan¹, François Gallaire²

² LFMI, Swiss Federal Institute of Technology (EPFL), CH-1015, Lausanne, Switzerland

¹ LMH, Swiss Federal Institute of Technology (EPFL), CH-1007, Lausanne, Switzerland
Preprint version of the article submitted in *Journal of Fluids and Structures*, (2017)

The synchronous pressure surge effect is a critical phenomenon occurring in Francis turbines operating at part load conditions. In this regime, pressure fluctuations are predominantly coming from the temporal rotation of a single helical vortex inside the turbine draft tube, called the part load vortex rope. However the combination of multi-physics interactions, geometry, cavitation, swirling flow and acoustic waves leads to a pressure amplification, called the synchronous pressure surge effect, which is more dangerous than the fluctuations resulting from the precessing vortex rope. This amplification is caused by the frequency match between the natural frequency of the hydraulic piping system and an excitation source consisting of a synchronous wave. While the synchronous pressure is only observed in elbow draft tube, the physical mechanism originating in the synchronous pressure wave remains poorly understood. We have therefore investigated the starting position and the growth of the synchronous pressure wave in Francis turbines. By energy consideration of an azimuthal-temporal Fourier decomposition of the flow in an axisymmetric draft tube geometry that was slightly disturbed at the wall, the source of the synchronous pressure and its amplification region were identified. In addition, the origin of this wave as the interaction of a wall disturbance with the part load vortex rope, was investigated using an asymptotic analysis and brought deeper comprehension of the synchronous wave generation mechanism.

5.1 Introduction

Electric production from renewable energy sources (RES) contributed a quarter of the world-wide electrical generation in 2016. The continuing development of these sources is currently reaching a level where the production assigned to intermittent RES, which are dependent of the input available-energy, needs to be regulated to guarantee the stability of the electrical grid. One major actor for providing advanced regulation techniques is the hydroelectric power capacity that is representing more than the 50% the total RES. Through the reactive electric

production of hydraulic turbines, hydropower already compensates for the fluctuations of the electrical consumption and allows up to now to integrate the actual fluctuations of the intermittent RES production. The future development of the intermittent RES power capacity may become problematic but it may be still and further supported by improvements of regulation techniques from the hydroelectric power plant through the extension of the operating range of hydraulic turbines that will allow electric production at off-design operating conditions.

Unfortunately off-design operating conditions of Francis turbines, that represent 60% of the hydraulic turbine installed capacity, are hindered by complex flow patterns, which has led to the development of control strategies to overcome pressure fluctuations (Susan-Resiga et al. [29], Zhang et al. [30], Bosioc et al. [131], Tănasă et al. [133], Foroutan et al. [31] and Pasche et al. [110]). These patterns differ according to the off-design operating conditions. In opposition to the runner design regime that coincides to the best efficiency point (BEP) where an axial flow exits the runner, the off-design regime is characterized by a residual swirling flow at the runner outlet that results in fluctuating velocity and pressure distributions in the draft tube. These unsteadiness develop as a pulsating axisymmetric cavitation vortex rope at full load operating condition, for higher discharge than the one at BEP or as a helical precessing vortex called part load vortex rope, for lower discharge than the one at BEP. In addition to these vortex flows implying pressure and velocity surge, a critical phenomenon may occur at off-design condition, when the cavitation vortex flow and the natural frequency of the entire power plant enter in resonance (Dörfler [115]). At part load operating conditions, this resonance phenomenon is called synchronous pressure surge and was first reported by Reinghans [106] with the power swing of a generator. Exclusively observed in elbow type draft tube turbines, this critical effect produces severe pressure fluctuations of higher amplitude than the internal pressure pulsation of the precessing vortex rope. Furthermore Nishi et al. [12] underlined the contribution of a synchronous fluctuation at the frequency of the part load vortex rope in this surge phenomenon by experimental measurements, highlighting the amplification of the synchronous pressure depending on the cavitation parameters of the vortex flow. The synchronous wave is defined as the unsteady azimuthal-averaged component of the flow, which is equivalent to a planar wave by assuming long wave length with respect to the runner diameter. Nishi et al. [12] described also a convective fluctuation, which is associated to the precessing motion of the vortex rope. Therefore the synchronous pressure surge prediction becomes essential to avoid critical situations in power plants and leads to the characterization of the hydraulic system eigenfrequency and of the cavitation parameters of the vortex flow.

A significant improvement of the system eigenfrequency characterization is brought by the 1-D model of mass and momentum flow conservation including elastic pipe wall derived by Nicolet [34]. This hydro-acoustic model, in analogy to an electric circuit, not only describes eigenfrequencies but also transient and unsteady phenomena in hydraulic systems. In particular, Alligné [134] have developped a relevant model of the Francis turbine cavitation vortex rope, by adding among others the flaring of the draft tube, the dissipation induced by the compressibility of the cavitation volume, and the cavitation compliance. In the case of the part load vortex rope, the synchronous pressure that is observed to promote the syn-

chronous surge effect is modeled by an external ad-hoc momentum source. The piping system indeed has a much higher eigenfrequency than the frequency of the cavitation vortex rope, but their interaction becomes possible when the system eigenfrequency is lowered by the local decrease of the traveling pressure wave speed due to the development of the cavitation inside the draft tube. However this 1-D model become only predictive after the definition of calibration curves, associated to the specific geometry and part load operating conditions, as investigated by Landry et al. [130]. Experimental measurements on a reduced scale Francis turbine model were performed with a mass flow source in the feeding pipe, by harmonic excitation techniques and ensured a proper calibration.

Cavitation vortex ropes were experimentally and numerically investigated by many researchers, see Jacob [135], Ruprecht et al. [18], Mauri et al. [19], Paik et al. [20], Buntic et al. [21], Wang & Zhou [22], Pacot et al. [136] and Wilhelm et al. [137] among others. They have contributed to the complete description of the flow conditions appearing at different operating regimes in Francis turbines. They have also developed numerical methods to perform simulations of the complex flow inside rotating hydromachines. Technology development has enabled systematic wall pressure measurements over the whole draft tube (Arpe & Avellan [8], providing a global description of the acoustic phenomenon. In particular, the position of the synchronous pressure maximum amplitude was measured on the inner part of the draft tube elbow. Others experimental measurements such as laser Doppler velocimetry (LDV) and two-phase flow particle image velocimetry (PIV) have brought pressure-velocity correlations (Ciocan et al. [9], Iliescu et al. [16] and Kirschner et al. [129]), which were compared to numerical flow simulations, see Trivedi et al. [23] for a review.

A recent experimental study of Favrel et al. [17] compared the part load vortex rope frequency as a function of the discharge coefficient, as well as on focuses on the dependence of the flow modifications associated to the synchronous pressure amplification. The intrinsic frequency of the part load vortex rope, that is induced by its self-sustained global instability character (Pasche et al. [65]), is observed to linearly decrease in the lower part load regime and to be constant in the upper part load regime as the discharge grows. The synchronous pressure amplification emphasizes a wider vortex rope trajectory and circulation intensity. The cavitation vortex rope, viewed as an excitation source in the hydraulic systems, indeed produces a synchronous wave that is capable to excite the piping system eigenfrequency but the way the synchronous wave emerges from the precessing vortex rope remains an open topic of discussion.

In the present paper, we investigate the origin of the physical mechanism responsible for the generation of the synchronous pressure from the part load vortex rope. The system is viewed as a fluid solid interaction problem due to the symmetry breaking of the elbow draft tube, and it is studied by means of numerical flow simulations (CFD). In addition, an asymptotic development of the flow field is derived to highlight the interactions responsible for the development of the synchronous pressure.

5.2 Methodology

The case studied is the FLINDT geometry - Flow Investigation In Draft Tube - project Eureka No. 1625, where the turbine is composed of a high specific speed runner and an elbow draft tube, see fig. 5.1(a), (c). The origin of the synchronous pressure is investigated for a part load operating regime of the turbine with a flow rate coefficient of $\phi = 0.27$, a specific energy of $\psi = 1.16$ and a Thomas cavitation number of $\sigma = 1.16$. In this regime, the flow field is cavitation free and a precessing vortex rope develops in the elbow draft tube. We use dimensionless variables made by the radius of the runner outlet R_{1e} and the discharge velocity $C_{ref} = Q/(\pi R_{1e}^2)$. Therefore our operating condition defines a Reynolds number built on the fluid's kinematic viscosity of value $Re = R_{1e} C_{ref} / \nu = 824400$. The pressure is reported as a pressure coefficient defined as $Cp = P/(0.5\rho C_{ref}^2)$, with ρ the water density. In the present study, we consider three other draft tube designs. The first geometry is an axisymmetric draft tube (Moody draft tube) based on a discharge velocity conservation over the cross sections of the original elbow draft tube, see fig. 5.1(d), identical to Pasche et al. [65]. The second is an axisymmetric draft tube disturbed at the wall, at the Z locations $Z_0^I = 2.6$ and of relative amplitude $\epsilon^I = 0.1$ (Disturbed Moody draft tube case I), see fig. 5.1(e). The third geometry is an axisymmetric draft tube disturbed at a different wall location $Z_0^{II} = 3.375$ and of relative amplitude $\epsilon^{II} = 0.04$ (Disturbed Moody type draft tube case II), see fig. 5.1(f). The wall disturbance case I is located at the end of the draft tube cone to mimic the elbow start while the wall disturbance case II is located more downstream with a smaller amplitude on an expanded region to be compared to an asymptotic analysis. The chosen disturbances break the symmetry of the draft tube by an eccentric displacement of a circular section of the wall following a Gaussian function along Z , of variance $\sigma^I = 0.1$ and $\sigma^{II} = 0.25$ for case I and II, respectively. These configurations allow us to dissociate the flow pattern induced by the structure and by the self-sustained vortex, by the means of a double azimuthal-temporal Fourier series decomposition of 3-D numerical flow simulations that is previously carried out.

We investigate the physical mechanism originating in the synchronous pressure by performing an asymptotic analysis. Starting from the mean flow of the unperturbed geometry (axisymmetric Moody draft tube) at the zero order, we derive first order equations associated to the part load vortex rope leading to a stability analysis and to the effect of the wall disturbance using a domain perturbation method. Then, the synchronous pressure equation is obtained at the second order. Due to symmetry consideration of the problem, we are able to compute this asymptotic analysis in a 2-D axisymmetric domain instead of a 3-D domain (appendix 5.6.1), where the governing equations are written in a cylindrical coordinate system. The asymptotic results are then compared to the azimuthal-temporal Fourier series decomposition of 3-D numerical flow simulation.

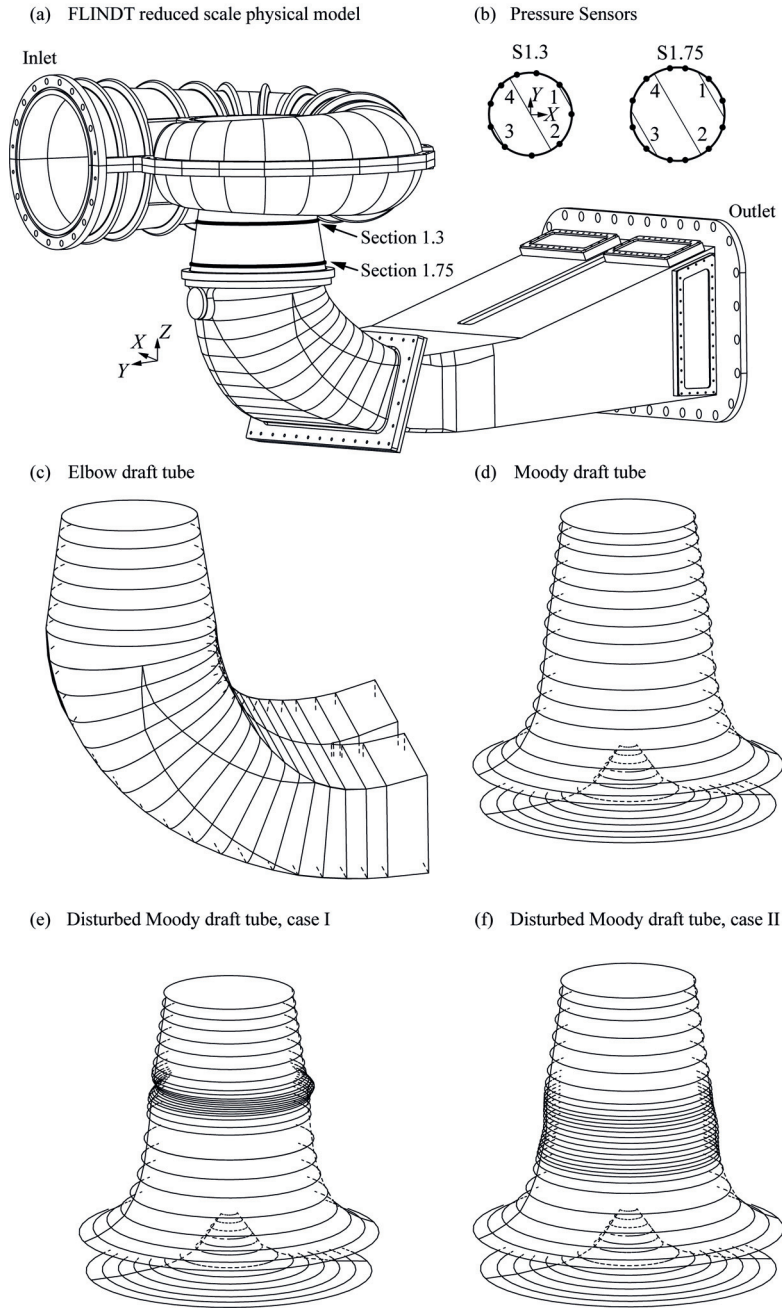


Figure 5.1 – Flindt reduced scale physical CAO model (a) with the wall pressure sensor at two different cross section S1.3 and S1.75 (b), and the different hydraulic draft tube domain investigated by numerical flow simulations, (c) the original elbow draft tube, (d) the axisymmetric Moody type draft tube, (e) the disturbed Moody type draft tube case I and (f) the disturbed Moody type draft tube case II.

5.3 Numerical methods

5.3.1 Three dimensional flow field

The 3-D flow solutions of the elbow and the Moody draft tube are recovered from a previous study, see Pasche et al. [65]. The same numerical setup is used to compute the flow field in the other geometries, the disturbed Moody draft tube case I and case II. The Unsteady Reynolds Averaged Navier-Stokes equations (URANS), eqn. (5.1), are solved with ANSYS CFX 16.0. We use a shear stress transport-based scale-adaptive simulation (SST-SAS) turbulence model that is not reported here for the sake of simplicity (Egorov & Menter [121]). This turbulence model defines the spatial varying turbulence eddy viscosity $\nu_t(\mathbf{C})$.

$$\begin{aligned} \frac{\partial \mathbf{C}}{\partial t} + \nabla \mathbf{C} \cdot \mathbf{C} &= -\nabla P + Re^{-1} \nabla^2 \mathbf{C} + \nabla \cdot [\nu_t(\mathbf{C}) (\nabla + \nabla^T) \mathbf{C}] \\ \nabla \cdot \mathbf{C} &= 0, \end{aligned} \quad (5.1)$$

The computational domain is composed of the runner and the draft tube only, which is demonstrated to be sufficient to compute the flow distribution in the draft tube (Ciocan et al. [9]). The applied boundary conditions are an open condition at the outlet, and a constant velocity and turbulence intensity profile at the inlet, coming from a previous steady calculation of the spiral casing and guide vane cascade. A general grid connection (GGI) method is used to transfer the flow field between the rotational and the stationary domain. A time step of 1 deg of runner revolution and a rms convergence error of 10^{-4} are set in the computational setup. While the simulation is running, the time averaged flow field is computed and the pressure is monitored on the wall of the draft tube cone, at two different sections S1.3 and S1.75 (fig. 5.1b), over five vortex rope precessions. The mesh from the previous computation of the Moody draft tube of Pasche et al. [65] is kept except that the cells are translated to follow the wall disturbances of the present geometry (distributed Moody draft tube case I and II). This mesh is made of a total of 7.5 mio of hexahedral cells.

5.3.2 Fourier series analysis

The interactions of the fluid and the structure are then exhibited by the double azimuthal-temporal ($m - q$) Fourier series decomposition, eqn. (5.2), of the phase averaged state variable

$\langle \mathbf{U} \rangle = \langle (\mathbf{C}, P) \rangle$, for $m \in \mathbb{N}$ and $q \in \mathbb{N}$:

$$\begin{aligned} \langle \mathbf{U}(R, \theta, Z, t) \rangle &= \bar{\mathbf{U}}(R, \theta, Z) + \tilde{\mathbf{U}}(R, \theta, Z, t) = \\ &= \sum_{m=0}^{\infty} [\bar{\mathbf{a}}_{m0}(R, Z) \cos(m\theta) - \bar{\mathbf{b}}_{m0}(R, Z) \sin(m\theta)] + \\ &= \sum_{m=0}^{\infty} \sum_{q=1}^{\infty} [\tilde{\mathbf{a}}_{mq}(R, Z) (\cos(q\omega_v t) \cos(m\theta) - \sin(q\omega_v t) \sin(m\theta)) \\ &\quad - \tilde{\mathbf{b}}_{mq}(R, Z) (\sin(q\omega_v t) \cos(m\theta) + \cos(q\omega_v t) \sin(m\theta))] \\ &= \Re \left(\sum_{m=0}^{\infty} \sum_{q=1}^{\infty} \mathbf{U}_{mq}(R, Z) e^{i(m\theta + q\omega_v t)} \right) \end{aligned} \quad (5.2)$$

where $\bar{\mathbf{a}}_{m0}, \bar{\mathbf{b}}_{m0}$ are the Fourier coefficients of the time averaged flow field and $\tilde{\mathbf{a}}_{mq}, \tilde{\mathbf{b}}_{mq}$ are the Fourier coefficients of the periodic wave. \mathbf{U}_{mq} is not computed on the full domain of the axisymmetric Moody draft tube but in the reduced domain of the disturbed Moody draft tube case I and II, delimited by circular cross-section centered on the axis of the inward wall disturbance radius. This decomposition is carried out in Matlab, after interpolating the state variable $\mathbf{U} = (\mathbf{C}, P)$ over 5 vortex rope precessions, on a 3-D cylindrical point distribution performed by the batch post-processing tool of Ansys 16.0. The phase average process is computed using a trigger signal of the vortex rope frequency $\omega_v / \omega_{runner} = 0.33$. Thus the term $q\omega_v$ for $q \geq 1$ designates the fundamental or the harmonics of the precessing vortex rope. From these definitions, we are able to identify the Fourier coefficients to the disturbance mode of the vortex rope: $\mathbf{U}_{11} = \tilde{\mathbf{a}}_{11} + i\tilde{\mathbf{b}}_{11}$, to the draft tube disturbance: $\mathbf{U}_{10} = \tilde{\mathbf{a}}_{10} + i\tilde{\mathbf{b}}_{10}$ and to the synchronous component: $\mathbf{U}_{01} = \tilde{\mathbf{a}}_{01} + i\tilde{\mathbf{b}}_{01}$. The kinetic energy computed by

$$E_k = \int_{\Omega} \mathbf{C}_{mq} \cdot \mathbf{C}_{mq}^* d\Omega, \quad (5.3)$$

on the control volume assuming Einstein summation convention, assesses the contribution of the different modes. Similarly the potential energy is computed as

$$E_p = \int_{\Omega} \sqrt{P_{mq} \cdot P_{mq}^*} d\Omega. \quad (5.4)$$

A kinetic energy per unit length is also defined

$$e_k(Z) = 2\pi \int_0^R \mathbf{C}_{mq} \cdot \mathbf{C}_{mq}^* R dR, \quad (5.5)$$

as well as a potential energy per unit length

$$e_p(Z) = 2\pi \int_0^R \sqrt{P_{mq} \cdot P_{mq}^*} R dR, \quad (5.6)$$

both being functions of Z .

5.3.3 Asymptotic expansion

An asymptotic analysis is performed to approximate the flow solution of the disturbed Moody draft tube case II. We consider a solution in a power series form of the state variable $\mathbf{U} = (\mathbf{C}, P)$, written as

$$\mathbf{U} = \bar{\mathbf{U}} + \epsilon \mathbf{U}^{(1)} + \epsilon^2 \mathbf{U}^{(2)}, \quad (5.7)$$

where ϵ represents the disturbance amplitude of the geometry and is assumed small $\epsilon \ll 1$, for case II, $\epsilon^{II} = 0.04$. The obstacle equation is written as

$$R = G(\theta, Z) = G_0(Z) + \epsilon G_1(Z) \cos(\theta), \quad (5.8)$$

with $G_0(Z)$ the axisymmetric Moody type draft tube wall function and $G_1(Z) = \exp(-(Z - Z_0)^2/\sigma^2)$ a Gaussian perturbation located at Z_0 of variance $\sigma^{II} = 0.25$, for case II. The following convention is used, $\theta = 0$ designated the most outward disturbance while the $\theta = \pi$ designated the most inward disturbance. Substituting the asymptotic expansion in the governing equations, eqn. (5.1), we obtain a series of systems of equations at various ϵ orders. These systems are written in a 2-D axisymmetric domain (see appendix 5.6.2), so that $\Gamma_{wall} = G_0(Z)$ for all systems.

Order ϵ^0

At order ϵ^0 , we assume that the steady mean turbulent flow equations, that govern the time averaged state variable $\bar{\mathbf{U}}$ are retrieved, according to eqn. (5.9). Following the same assumptions as Barkley [5], Meliga et al. [47] and Mantič-Lugo et al. [84], we obtain that the mean turbulent flow is a steady solution of the governing equations (5.1) forced by the constant Reynolds stresses of the coherent fluctuations of the flow field, symbolized by $\bar{\mathbf{F}}$. The mean turbulent flow is bounded by the same conditions as the instantaneous flow except at the outlet where a free-outflow condition is applied, because a finite element solver is used for this asymptotic analysis. This change does not affect the solutions because the outlet is far enough. Since we consider a 2-D axisymmetric domain, the mean flow satisfies a supplementary axisymmetric boundary condition on Γ_{axis} . As expected at this order, no corrections from the disturbed geometry appears. In addition, the mean turbulent eddy viscosity $\bar{\nu}_t(\bar{\mathbf{C}})$ is also involved in eqn.

(5.9) to correctly capture the mean flow.

$$\begin{aligned}
 \nabla \bar{\mathbf{C}} \cdot \bar{\mathbf{C}} + \nabla \bar{P} - Re^{-1} \nabla^2 \bar{\mathbf{C}} - \nabla \cdot [\bar{v}_t(\bar{\mathbf{C}})(\nabla + \nabla^T) \bar{\mathbf{C}}] &= \bar{\mathbf{F}} \\
 \nabla \cdot \bar{\mathbf{C}} &= 0 \\
 \bar{C}_R = \bar{C}_\theta = \frac{\partial \bar{C}_Z}{\partial R} &= 0 \quad \text{on } \Gamma_{axis} \\
 \bar{\mathbf{C}} &= 0 \quad \text{on } \Gamma_{wall} \\
 \bar{\mathbf{C}} &= \mathbf{C}_{in} \quad \text{on } \Gamma_{in} \\
 (-P\mathbf{I} + Re^{-1} \nabla \bar{\mathbf{C}} + \bar{v}_t(\bar{\mathbf{C}})(\nabla + \nabla^T) \bar{\mathbf{C}}) \cdot \mathbf{n} &= 0 \quad \text{on } \Gamma_{out}
 \end{aligned} \tag{5.9}$$

Order ϵ^1

at order ϵ^1 , the linearized URANS equations around the mean flow are obtained with specific boundary conditions that arise from the disturbed geometry, eqn. (5.8). Taylor series are used to derive these conditions that read $\mathbf{C}^{(1)} = G_1(Z) \cdot \partial_R \bar{\mathbf{C}}$ on Γ_{wall} . Since we deal with a linear system of equations, the superposition principle applies, and \mathbf{U}_1 reads therefore after normal-mode decomposition of azimuthal wavenumbers m and eigenfrequency ω :

$$\mathbf{U}^{(1)}(R, \theta, Z, t) = A \mathbf{U}_{11}^{(1)}(R, Z) e^{i(m\theta - \omega t)} + \epsilon \mathbf{U}_{10}^{(1)}(R, Z) e^{im\theta} + \text{c.c.} \tag{5.10}$$

At this order we choose the distinguished limit such that the amplitude of the vortex rope disturbance and the amplitude of the wall disturbance are of the same order of magnitude, $A = \mathcal{O}(\epsilon)$. The general solution $\mathbf{U}_{11}^{(1)}$ is associated to the eigenvalue problem linearized about the mean turbulent flow equations with homogeneous boundary conditions, written as

$$\begin{aligned}
 -i\omega \mathbf{C}_{11}^{(1)} + \nabla_m \mathbf{C}_{11}^{(1)} \cdot \bar{\mathbf{C}} + \nabla_m \bar{\mathbf{C}} \cdot \mathbf{C}_{11}^{(1)} &= -\nabla_m P_{11}^{(1)} + Re^{-1} \nabla_m^2 \mathbf{C}_{11}^{(1)} + \nabla_m \cdot [\bar{v}_t(\bar{\mathbf{C}})(\nabla_m + \nabla_m^T) \mathbf{C}_{11}^{(1)}] \\
 \nabla_m \cdot \mathbf{C}_{11}^{(1)} &= 0 \\
 C_{11Z}^{(1)} = P_{11}^{(1)} = \frac{\partial C_{11R}^{(1)}}{\partial R} = \frac{\partial C_{11\theta}^{(1)}}{\partial R} &= 0 \quad \text{on } \Gamma_{axis} \\
 \mathbf{C}_{11}^{(1)} &= 0 \quad \text{on } \Gamma_{wall} \\
 \mathbf{C}_{11}^{(1)} &= 0 \quad \text{on } \Gamma_{in} \\
 (-P_{11}^{(1)} \mathbf{I} + Re^{-1} \nabla \mathbf{C}_{11}^{(1)} + \bar{v}_t(\bar{\mathbf{C}})(\nabla + \nabla^T) \mathbf{C}_{11}^{(1)}) \cdot \mathbf{n} &= 0 \quad \text{on } \Gamma_{out}.
 \end{aligned} \tag{5.11}$$

The most relevant solution of this eigenvalue problem is the unstable mode, which well describes the vortex rope disturbance of eigenvalue ω_v for $m = 1$, found by Pasche et al. [65]. The capacity of stability analysis on turbulent mean flows to correctly capture helical structures like the part load vortex rope has been also assessed by recent studies on swirling injectors (Oberleithner et al. [138] and Tammisola & Juniper [48]).

The particular solution $\mathbf{U}_{10}^{(1)}$ is associated to the wall disturbance system of equation, written as

$$\begin{aligned}
 \nabla_m \mathbf{C}_{10}^{(1)} \cdot \bar{\mathbf{C}} + \nabla_m \bar{\mathbf{C}} \cdot \mathbf{C}_{10}^{(1)} = \\
 -\nabla_m P_{10}^{(1)} + Re^{-1} \nabla_m^2 \mathbf{C}_{10}^{(1)} + \nabla_m \cdot \left[\bar{\mathbf{v}}_t (\bar{\mathbf{C}}) (\nabla_m + \nabla_m^T) \mathbf{C}_{10}^{(1)} \right] \\
 \nabla_m \cdot \mathbf{C}_{10}^{(1)} = 0 \\
 C_{10Z}^{(1)} = P_{10}^{(1)} = \frac{\partial C_{10R}^{(1)}}{\partial R} = \frac{\partial C_{10\theta}^{(1)}}{\partial R} = 0 \quad \text{on } \Gamma_{axis} \\
 \mathbf{C}_{10}^{(1)} = G_1(Z) \cdot \frac{\partial \bar{\mathbf{C}}}{\partial R} \quad \text{on } \Gamma_{wall} \\
 \mathbf{C}_{10}^{(1)} = 0 \quad \text{on } \Gamma_{in} \\
 \left(-P_{10}^{(1)} \mathbf{I} + Re^{-1} \nabla \mathbf{C}_{10}^{(1)} + \bar{\mathbf{v}}_t (\bar{\mathbf{C}}) (\nabla + \nabla^T) \mathbf{C}_{10}^{(1)} \right) \cdot \mathbf{n} = 0 \quad \text{on } \Gamma_{out}.
 \end{aligned} \tag{5.12}$$

The boundary condition on Γ_{wall} obtained by applying a domain perturbation method, mimic the wall disturbance. $\mathbf{U}_{10}^{(1)}$ is time independent because a static solution to the eccentric disturbance of the draft tube wall is sought. We should mention that the linearized solution only projects onto the azimuthal wavenumber $m = 1$ due to the disturbance shape of our prescribed geometry.

Order ϵ^2

At order ϵ^2 , systems of linear equations including interactions between the previous order solutions appears. The separation of the systems by frequency and by azimuthal wavenumber leads to five different solutions, according to

$$\begin{aligned}
 \mathbf{U}^{(2)}(R, \theta, Z, t) = \mathbf{U}_{22}^{(2)}(R, Z) e^{i(2\theta - 2\omega t)} + \mathbf{U}_{00}^{(2)}(R, Z) \\
 + \mathbf{U}_{20}^{(2)}(R, Z) e^{i2\theta} + \mathbf{U}_{21}^{(2)}(R, Z) e^{i(2\theta - \omega t)} + \mathbf{U}_{01}^{(2)}(R, Z) e^{-i\omega t} + \text{c.c.}
 \end{aligned} \tag{5.13}$$

These solutions are respectively the second harmonic self-interaction of the vortex rope disturbance, the mean flow correction by the coherent fluctuations, the second harmonic self-interaction of the geometrical disturbance, the second harmonic of the geometrical disturbance with the vortex rope disturbance and, eventually, the synchronous component.

The last solution $\mathbf{U}_{01}^{(2)}$ is of particular interest, and is governed by

$$\begin{aligned}
 & -i\omega_v \mathbf{C}_{01}^{(2)} + \nabla_m \mathbf{C}_{01}^{(2)} \cdot \bar{\mathbf{C}} + \nabla_m \bar{\mathbf{C}} \cdot \mathbf{C}_{01}^{(2)} + \nabla_m P_{01}^{(2)} - Re^{-1} \nabla_m^2 \mathbf{C}_{01}^{(2)} \\
 & - \nabla_m \cdot \left[\bar{v}_t (\bar{\mathbf{C}}) (\nabla_m + \nabla_m^T) \mathbf{C}_{01}^{(2)} \right] = - \nabla_m \mathbf{C}_{11}^{(1)} \cdot \mathbf{C}_{10}^{*(1)} - \nabla_m \mathbf{C}_{10}^{*(1)} \cdot \mathbf{C}_{11}^{(1)} \\
 & \nabla_m \cdot \mathbf{C}_{01}^{(2)} = 0 \\
 & C_{01R}^{(2)} = C_{01\theta}^{(2)} = \frac{\partial C_{01Z}^{(2)}}{\partial R} = 0 \quad \text{on } \Gamma_{axis} \\
 & \mathbf{C}_{01}^{(2)} = 0 \quad \text{on } \Gamma_{wall} \\
 & \mathbf{C}_{01}^{(2)} = 0 \quad \text{on } \Gamma_{in} \\
 & \left(-P_{01}^{(2)} \mathbf{I} + Re^{-1} \nabla \mathbf{C}_{01}^{(2)} + \bar{v}_t (\bar{\mathbf{C}}) (\nabla + \nabla^T) \mathbf{C}_{01}^{(2)} \right) \cdot \mathbf{n} = 0 \quad \text{on } \Gamma_{out}
 \end{aligned} \tag{5.14}$$

This system describes the synchronous wave disturbance, i.e. an axisymmetric pulsation of the flow, coming from the interaction between the geometric elbow disturbance and the dynamic vortex rope disturbance synchronized at the vortex rope frequency as observed in the experimental measurements of Arpe & Avellan [8].

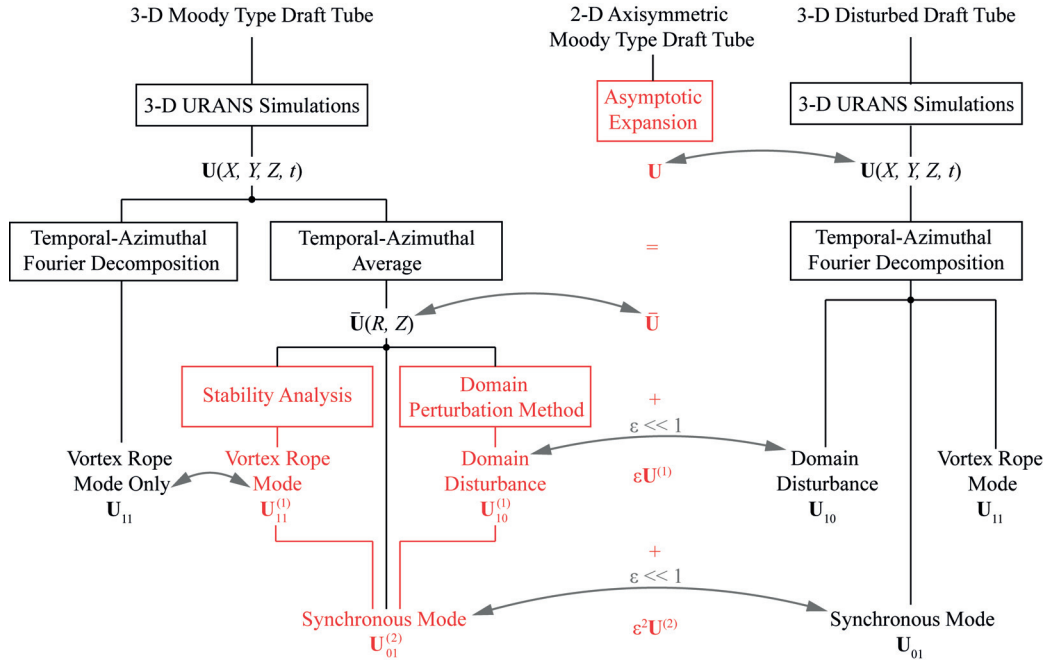


Figure 5.2 – Methodology applied to the vortex rope to investigate the development of the synchronous pressure, left branch the nonlinear analysis of the axisymmetric Moody draft tube, right branch analysis of the disturbed Moody draft tube, in red the asymptotic analysis and the curved gray arrows show the flow field comparison carried out in the present study. The boxes represent the computational operations.

The solutions obtained by the asymptotic analysis are next compared to the Fourier series decomposition of the 3-D numerical flow simulation. The different links between these analysis and solutions are sketched in fig. 5.2. In this schematic, the boxes represent computational operations. The left branch summarizes the methodology applied to the 3-D axisymmetric Moody draft tube and the right branch summarizes it for the 3-D disturbed draft tube. The red parts summarize the asymptotic expansion and comparisons between the different analyses are showed by curved gray arrows.

Numerical computation

The systems of equations, eqns. (5.11), (5.12) and (5.14) are written in weak form and solved numerically with the finite element solver Freefem++ [101] on a 2-D axisymmetric domain, see appendix 5.6.1. The mesh has approximately 500'000 triangle elements using P_2 - P_1 shape functions for the velocity-pressure fields. No further validations are provided because this mesh is identical to the mesh used in Pasche et al [65], in which the computation of the eigenvalue problem associated to the part load vortex rope was carried out. These different systems of equations are solved using (Unsymmetric Multifrontal sparse LU Factorization) UMFPACK package, that was combined with the ARPACK library [104] for solving the eigenvalue problem.

The mean turbulent flow is given by the solution of eqn. (5.9) theoretically, but in practice this set of equations is not solved. The mean turbulent flow $\bar{\mathbf{C}}$ is determined from the time averaged flow distribution that is evaluated on the fly while the 3-D numerical flow simulation of the axisymmetric Moody type draft tube geometry is running. The time averaged flow field obtained on the 3-D mesh is then azimuthally averaged and interpolated on the 2D axisymmetric mesh using matlab interpolation tool. The set of equations eqns. (5.11), (5.12), (5.14) needs not only the mean turbulent flow but also the time averaged spatial distribution of the turbulent eddy viscosity $\bar{\nu}_t(\bar{\mathbf{C}})$, that is computed in the same way.

Several assumptions are performed to proceed to the asymptotic analysis. Since the eigenvector magnitude $\|\mathbf{C}_{11}^{(1)}\|$ associated to the vortex rope disturbance, solution of eqn. (5.11), is left undefined, its norm is identified to the norm of \mathbf{C}_{11} , as extracted from the Fourier series decomposition of the 3-D flow field of the vortex rope associated to the axisymmetric Moody type draft tube geometry without disturbance. The wall boundary condition, imposed for $\mathbf{C}_{10}^{(1)}$ in eqn. (5.12), defined by $\mathbf{C}_{10}^{(1)}|_{\Gamma_{wall}} = G_1(Z) \cdot \partial_R \bar{\mathbf{C}}|_{\Gamma_{wall}}$, could not be computed directly in this way. Since we deal indeed with URANS equations, the boundary layer is modeled by a wall function and its derivative is strongly oscillating. We identify therefore the velocity at the boundary of the Fourier series decomposition associated to the same mode \mathbf{C}_{10} , extracted from the 3-D URANS of the disturbed flow, so as to avoid computing derivatives in the near wall region. We impose $\mathbf{C}_{10}^{(1)}|_{\Gamma_{wall}} \approx \gamma \mathbf{C}_{10}|_{\tilde{\Gamma}_{wall}}$ as boundary condition in eqn. (5.12), in which a scalar correction factor γ appears and compensates for the reduced domain of the Fourier series decomposition, since the disturbed region $G_1(Z)$ has to be excluded, see fig. 5.3. In the asymptotic analysis, the value of this correction factor is 1.73 minimizing the least square fit of the velocity profiles at the maximum wall disturbance Z_0^{II} .

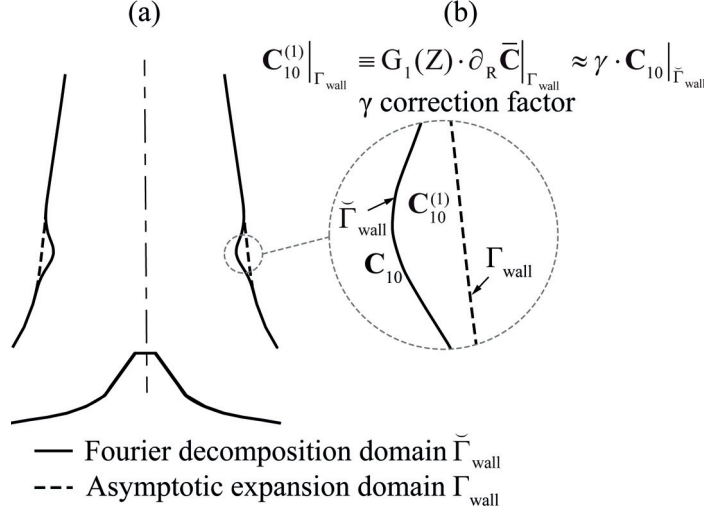


Figure 5.3 – Boundary condition applied for domain disturbance using the matching prefactor γ on the associated Fourier mode. The disturbance of the Fourier decomposition domain is enlarged to help understanding the analysis.

5.4 Results

5.4.1 Fourier series analysis

The instantaneous 3-D flow distribution of the elbow draft tube geometry is reported in fig. 5.4. The axial velocity is plotted on a YZ slice and the vortex core of the part load vortex is materialized by a pressure iso-contour of value $Cp = -4.1$. On the side of the draft tube center line, positive axial velocity regions appear close to the vortex core, that are surrounded by a stagnant axial flow. Along the wall of the draft tube, in contrast, the axial flow has a strong negative value oriented in the free-stream direction. The inlet flow discharge is therefore recovered in the confined region delimited by this negative axial velocity, which presents locally the largest value close to the vortex core strengthened by its rotation.

The pressure monitored on the section 1.3 and 1.75 is a first indicator of the apparition of the synchronous component. The pressure periodic wave are reported in fig. 5.5, for the elbow draft tube (a and b), for the axisymmetric Moody draft tube (c and d), and for the disturbed Moody type draft tube case I (e and f), on sections 1.3 and 1.75 respectively. The synchronous and convective waves in the draft tube are obtained by phase averaged computation based on the reference pressure sensor $N^\circ 2$. The synchronous pressure coefficient, reported by the solid curves, is experienced in both sections in the elbow draft tube (fig. 5.5a and b). Since a single phase numerical flow simulation is performed and the remaining hydraulic system is not computed, no resonance effect can be induced and the synchronous component amplitude in the cone is therefore smaller than the convective components, which are reported by dash curves. Furthermore the synchronous pressure signal is also observed in the case of the wall disturbance case I (fig. 5.5c and d). The localized wall displacement is sufficient to generate

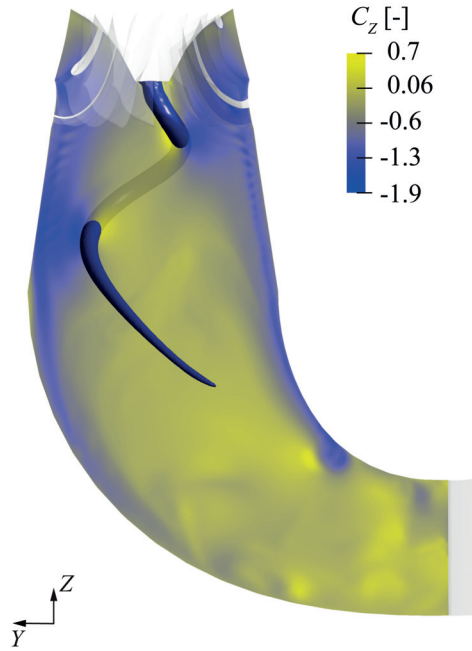


Figure 5.4 – Pressure isocontour of the vortex rope ($C_p = -4.1$) and axial velocity distribution on the YZ plane for the instantaneous URANS solution in the elbow draft tube

a synchronous fluctuation. A similar amplitude as the elbow draft tube is obtained in the section 1.75 but the synchronous pressure is spread and phase shifted in section 1.3. On the contrary, no synchronous fluctuation is observed in the axisymmetric Moody draft tube, and only the convective oscillation remains (fig. 5.5e and f). In agreement with Nishi et al. [12], the synchronous wave appears exclusively when the symmetry axis of the draft tube axis is broken.

The part load vortex rope passage in front of each sensor is felt as a pressure minimum of the convective oscillations (dashed curves) in fig. 5.5, due to the low pressure inside the vortex core. Regarding the axisymmetric Moody type draft tube (fig. 5.5c and d), this minimum is around $\tilde{C}_p \approx -0.45$ in section 1.3 compared to $\tilde{C}_p \approx -1$ in section 1.75. This discrepancy shows the faring angle of the vortex rope that brings it closer to the wall at section 1.75 than at section 1.3 and therefore strengthens the pressure minimum. This pressure minimum of the convective oscillations in the axisymmetric Moody type draft tube is at the same level. In contrast, this level is modulated at section 1.75 of the elbow draft tube and disturbed draft tube case I (fig. 5.5b and f), which is representative of the helical mode distortion induced by the symmetry breaking of the draft tube.

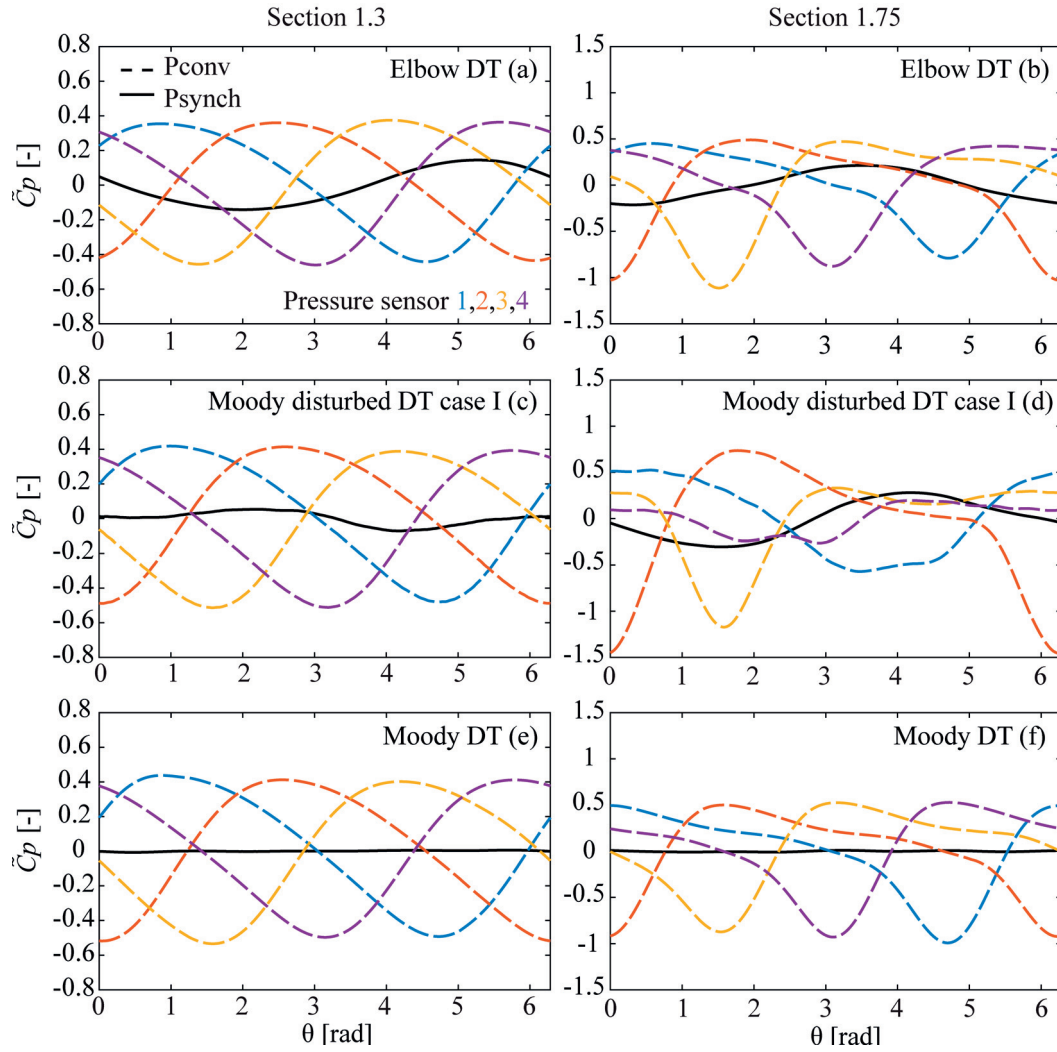


Figure 5.5 – convective part (dashed curve) and synchronous part (solid curve) of the wall pressure measurements at the sensor $N^{\circ} 1,2,3,4$ on the cross section S1.3 for elbow (a), disturbed case I (c), axisymmetric (e) draft tube and at the cross section S1.75 for elbow (b), disturbed case I (d), axisymmetric (f) draft tube.

Regarding the disturbed axisymmetric draft tube case I, we investigate the nonlinear interactions by computing an azimuthal-temporal $m - q$ Fourier series decomposition. This method allows us to separate the wall disturbance mode from the fluid flow modes by our setup definition. Thus the wall disturbance is completely assigned to a stationary, $q = 0$, azimuthal wavenumber $m = 1$ mode. The synchronous component of the vortex rope is therefore defined by the Fourier mode $m = 0$ and $q = 1$, and the vortex rope mode by $m = 1$ and $q = 1$. The kinetic energy of each m -azimuthal and q -temporal modes are computed using eqn. (5.3) and are reported in fig. 5.6(a) for the axisymmetric Moody draft tube and in fig. 5.6(b) the disturbed Moody draft tube case I. For both cases, the strongest contribution to the total kinetic energy

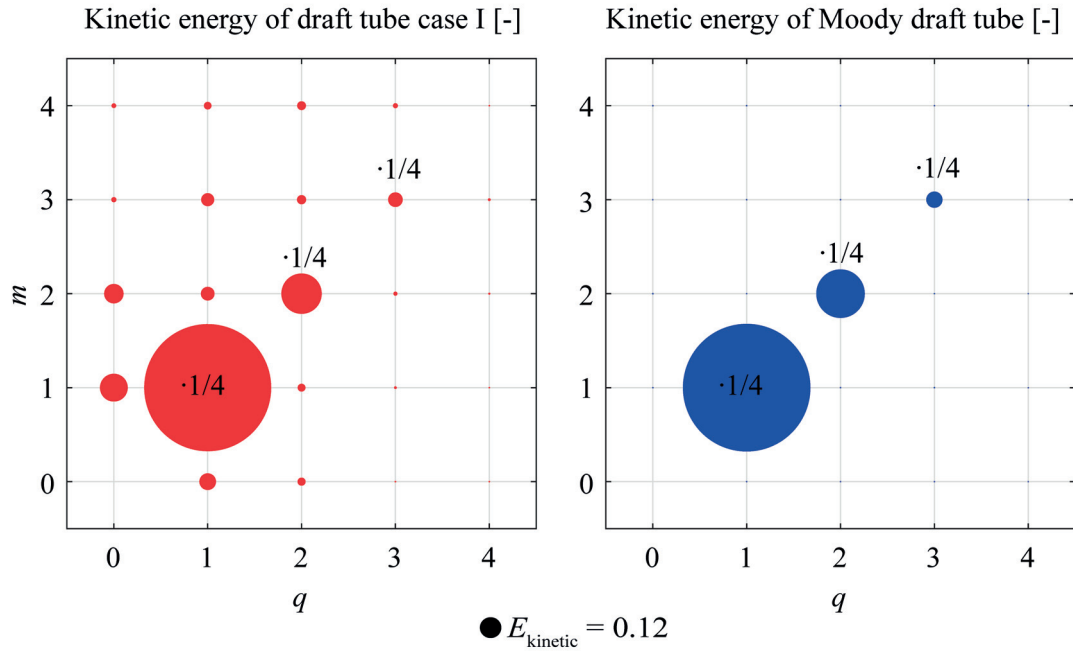


Figure 5.6 – Volume integral of kinetic energy of temporal-azimuthal (m - q) Fourier modes of the disturbed Moody draft tube case I (a) and the axisymmetric Moody draft tube (b). The energy of the diagonal terms is scaled by $1/4$.

is the mode $m = 1$, $q = 1$, the part load vortex rope, that is also observed in the CFD. The harmonics of this mode, the $m = q$ pairs (2, 2) and (3, 3), follow in the energy cascade. The mode energy repartition demonstrates the absence of synchronous fluctuations for axisymmetric draft tubes (fig. 5.6b). The introduction of a small disturbance on the wall, however, generates several Fourier modes coming from the quadratic nonlinearity of the Navier-Stokes equations. Figure 5.6(a) shows the onset of the synchronous mode $m = 0$, $q = 1$ with the sixth highest amplitude of kinetic energy after the vortex fundamental and its harmonics, and the wall disturbance $m = 1$, $q = 0$ and its harmonic. We should mention that the potential energy, eqn. (5.4) is found to follow the same energy distribution as the kinetic energy.

The Fourier modes of interest are reported in fig. 5.7 as a 2-D axisymmetric and 3-D representation of the axial velocity and pressure coefficient. The Fourier mode of the vortex rope, $m = 1$ and $q = 1$, is displayed in fig. 5.7(a) and (b). The pressure iso-contour and the axial velocity iso-contour materialize the shape of the vortex flow. Only negative pressure iso-contours are displayed and therefore show the spatial location of the vortex. In contrast the axial velocity iso-contours show positive and negative values and therefore display simultaneously the flow when the vortex rope hits the inward wall disturbance (negative iso-contour) or hits the outward wall disturbance (positive iso-contour), and vice versa due to symmetry consideration of the Fourier series decomposition. In the left fig. 5.7(b) the vortex rope disturbed by the wall causes a secondary tiny iso-contour of value $Cp = -1$, observed on the top of the inward disturbance. This pressure perturbation of the vortex rope is also observed by a tightened negative axial velocity iso-contour on the right side of fig. 5.7(a) due to the flow acceleration over the wall disturbance.

The Fourier mode of the wall disturbance, $m = 1$ and $q = 0$, is displayed in fig. 5.7(c) and (d). Although this mode has a similar amplitude as the vortex rope mode, it remains in contrast localized in the wall disturbance region. Since this Fourier mode is stationary, the 3-D representations show the inward disturbance on the left part of the iso-contour graphs and the outward disturbance on the right part of the iso-contour graphs. The axial velocity of the inward disturbance shows a flow acceleration on the free-stream direction (negative value) on the top of the wall disturbance and a flow deceleration (positive value) above and below the wall bump. In contrast, the axial velocity iso-contour of the outward disturbance shows only an accelerated flow on a larger region.

The Fourier mode of the synchronous wave, $m = 0$ and $q = 1$, is displayed in fig. 5.7(e) and (f). The synchronous wave is spatially located along the draft tube wall starting from the wall disturbance. A series of minima and maxima along the wall are observed on the axial velocity (right fig. 5.7e). These peaks are separated by a distance that is observed to be set by the axial convective velocity of the vortex rope. The synchronous wave minimum is reached when the vortex hits the outward wall disturbance and its maximum when the vortex rope hits the inward wall disturbance. The time evolution of the synchronous pressure for one precession of the vortex rope is presented in fig. 5.8 and shows the onset of the synchronous pressure formed by the interaction of two single helical disturbances, rhythmized by the self-sustained frequency of the vortex rope.

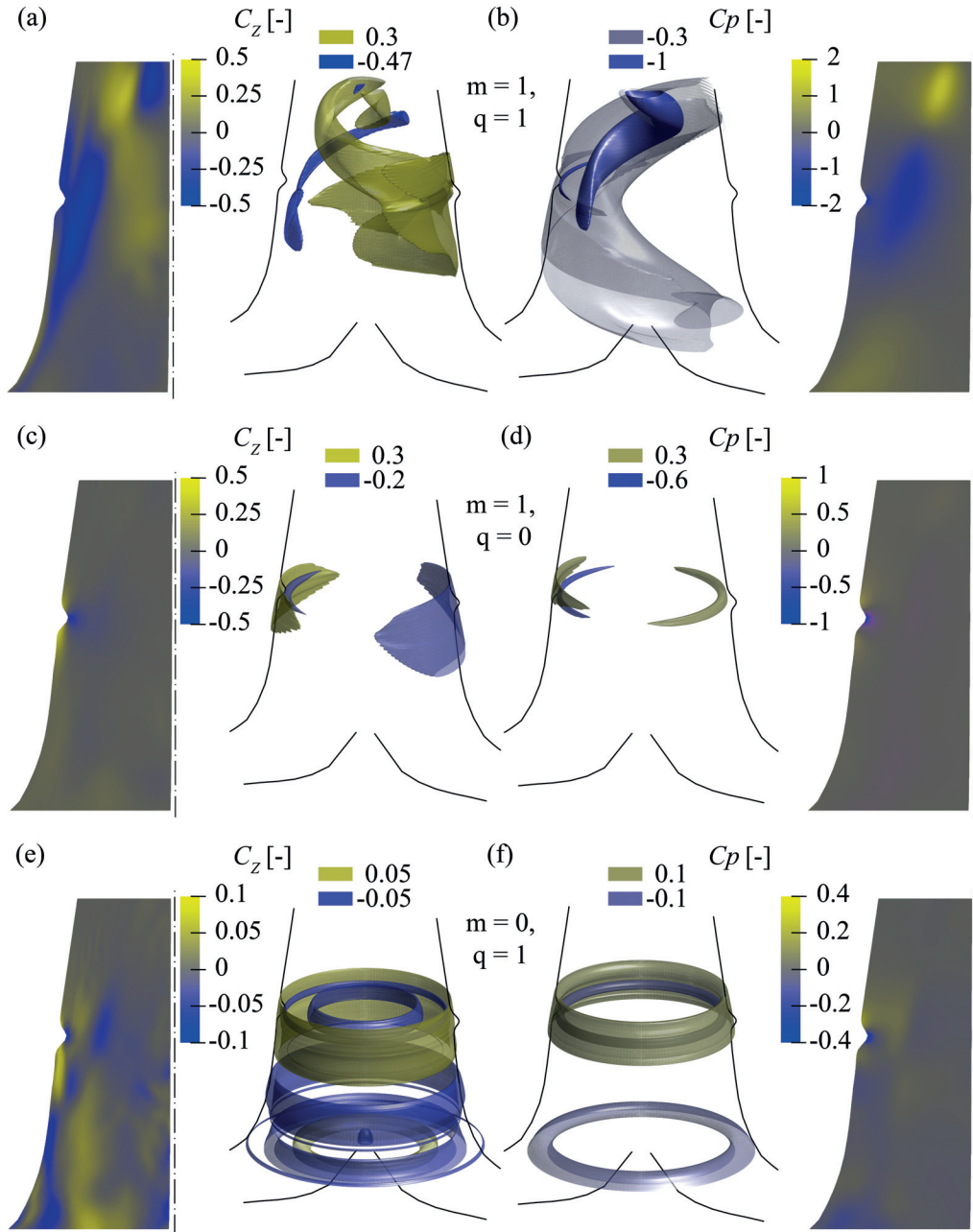


Figure 5.7 – Fourier series decomposition of the disturbed Moody draft tube case I and their related 3-D reconstruction of axial and pressure components for the vortex rope Fourier mode $m = 1, q = 1$, (a) and (b), the stationary wall disturbance Fourier mode $m = 1, q = 0$, (c) and (d), and the synchronous Fourier mode $m = 0, q = 1$, (e) and (f) at an arbitrary chosen time t .

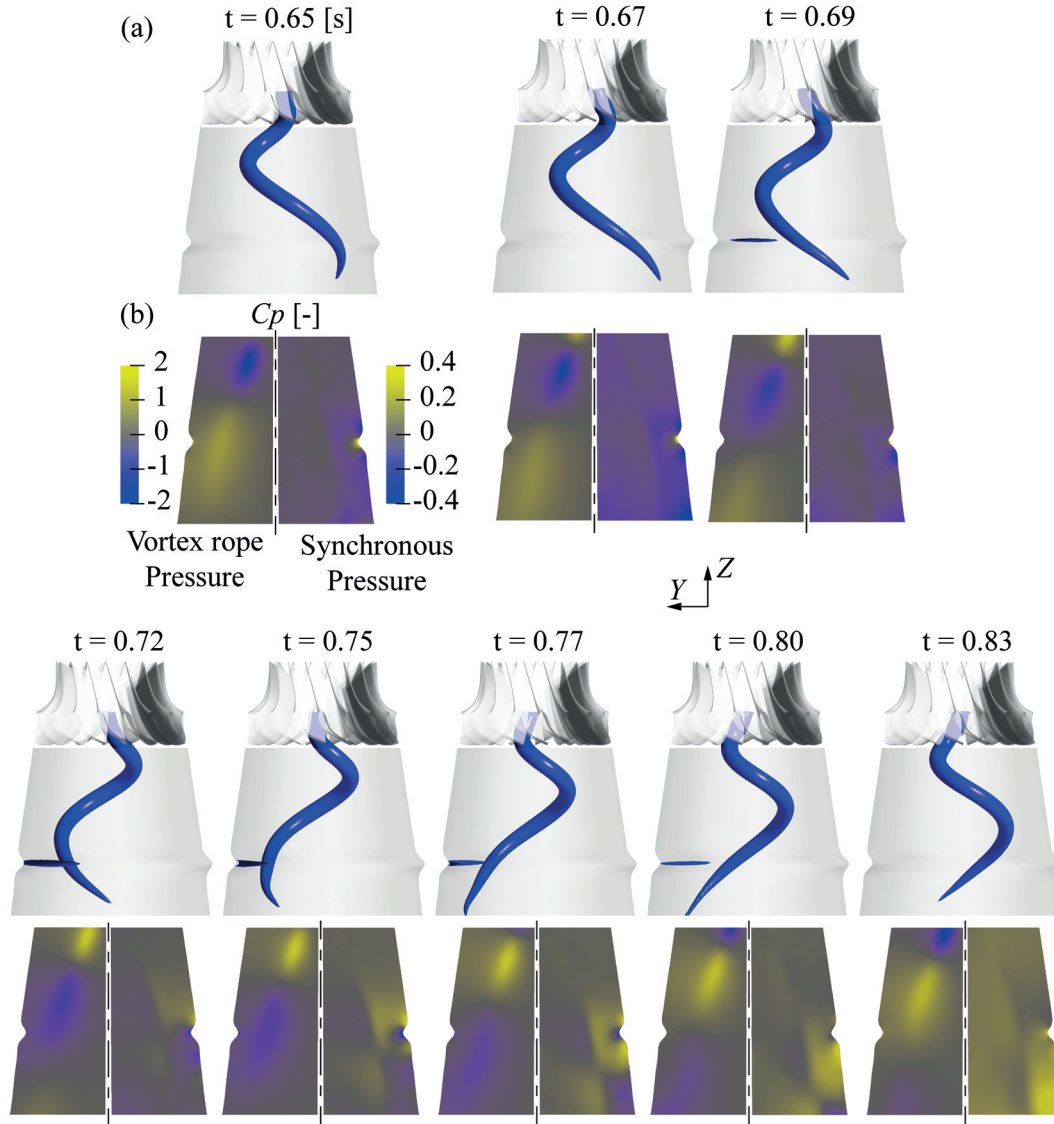


Figure 5.8 – Time evolution of the vortex rope materialized by a pressure iso-contour of value $C_p = -4.1$ (a) and associated instantaneous pressure field of the azimuthal Fourier series decomposition for the vortex rope disturbance $m = 1, q = 1$ left (b) and the synchronous pressure $m = 0, q = 1$ right (b).

The kinetic and potential energy per unit length, eqns. (5.5) and (5.6) of the synchronous Fourier mode are reported in fig. 5.9 as a function of the Z coordinate. The two curves have a similar behaviour, tightened peaks over a plateau located at the wall disturbance $Z_0^{(I)} = 2.6$ that are surrounded by a minimum value of energy at the runner outlet and a maximum value of energy in the axisymmetric elbow. These peaks are associated to the excitation source of the synchronous component, and are due to the axisymmetry breaking of the draft tube. However the excitation source does not correspond to the maximum of energy, this maximum is located in the axisymmetric elbow. Therefore an amplification mechanism occurs when the synchronous wave travels downstream the turbine. In contrast, the synchronous wave is damped at the runner outlet because waves seem to hardly travel upstream in this geometry.

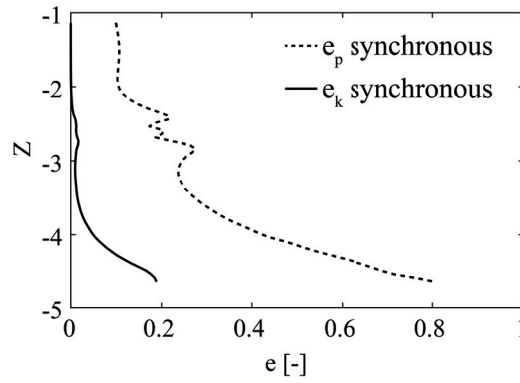


Figure 5.9 – Kinetic and potential energy per unit length of the synchronous Fourier mode as a function of Z for the disturbed Moody draft tube case II.

We now focus on the physical mechanism behind the synchronous wave by investigating the interactions of the different observed disturbances in an asymptotic framework for the disturbed Moody type draft tube case II.

5.4.2 Asymptotic expansion

At zero order, the axisymmetric mean flow solution, defined by eqn. (5.9) is displayed in fig. 5.10(a). The axial velocity shows two regions, a strong velocity along the wall in the free-stream direction and a center region flowing slowly that has one recirculation region close to the tip of the runner cone, for detailed results see Pasche et al. [65]. Not only is the axisymmetric mean flow used in the asymptotic expansion, but also the axisymmetric turbulent eddy viscosity. Figure 5.10(b) illustrates the mean turbulent eddy viscosity where also two different regions are shown, a high eddy viscosity region along the vortex rope path of magnitude $\nu_t \sim 1 \cdot 10^{-3}$, and a low eddy viscosity region at the runner exit and in the draft tube center around $\nu_t \sim 1 \cdot 10^{-4}$. In any case the turbulent eddy viscosity is dominant compared to the molecular viscosity that is equal to $1/Re = 1.2 \cdot 10^{-6}$ in this study.

The first and second order solutions are illustrated in fig. 5.11 and are compared to the Fourier series decomposition of the 3-D CFD for the disturbed Moody type draft tube case II. Figures

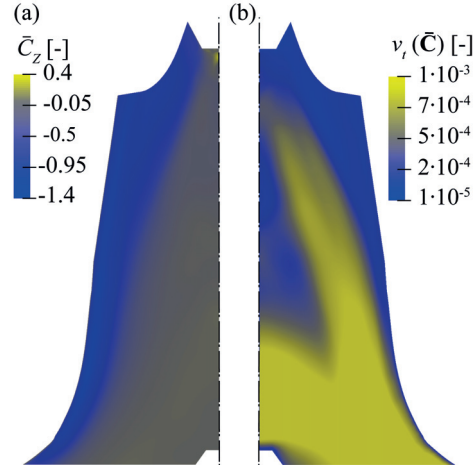


Figure 5.10 – Axisymmetric turbulent eddy viscosity (a) and axisymmetric mean velocity distribution (b) where the flow is linearized around in the asymptotic expansion

5.11(a) and (b) compare the solution $\mathbf{U}_{11}^{(1)}$ to \mathbf{U}_{11} , that are defined as, from left to right in (a), the Fourier series decomposition of the 3-D CFD for $m = 1$ and $q = 1$, and the unstable eigenvector associated to the vortex rope for $m = 1$ and $q = 1$, and in (b) their associated velocity profiles on three different sections, at Z_0 centered on the wall disturbance, at $Z_1 = Z_0 - 25\%$ of the Gaussian variance and at $Z_2 = Z_0 + 25\%$ of the Gaussian variance. In a similar way fig. 5.11(c) and (d) compare $\mathbf{U}_{10}^{(1)}$ to \mathbf{U}_{10} , the axial velocity distribution and the velocity profiles of the Fourier series decomposition $m = 1$ and $q = 0$ of 3-D CFD and the wall disturbance solution of eqn. (5.12). Finally fig. 5.11(e) and (f) compare $\mathbf{U}_{01}^{(2)}$ to \mathbf{U}_{01} , the Fourier series decomposition $m = 0$ and $q = 1$ of 3-D CFD with the solution of eqn. (5.14) that approximates the synchronous components $m = 0$ and $q = 1$.

The unstable eigenvector $\mathbf{U}_{11}^{(1)}$, illustrated in fig. 5.11(a) is found to be slightly different when compared to the CFD result in the axisymmetric Moody draft tube, as discussed in Pasche et al. [65]. However the radial and axial velocity profile traced in fig. 5.11(b) are similar in the region of the wall disturbance. The tangential velocity profiles have similar shapes but their magnitudes differ slightly.

The solution of eqn. (5.12) is reported in fig. 5.11(c) and (d). This solution is localized on the wall disturbance position and has a positive velocity along the wall and a negative on the top of the bump. It is found to correctly approximate the wall disturbance perturbation at ϵ order.

Figures 5.11(e) and (f) report the synchronous wave of the disturbed type Moody draft tube case II. The synchronous wave from the asymptotic analysis has indeed a larger amplitude than the associated Fourier mode but the location and the shape are found similar in the region of the disturbance. A negative region of axial velocity is obtained at the disturbance location followed by a positive region along the draft tube wall in both cases, and the velocity profiles have the same shapes but their amplitudes are larger. The discrepancy is may be linked to the chosen distinguished limit $\epsilon = A$ or to feedbacks of higher order modes.

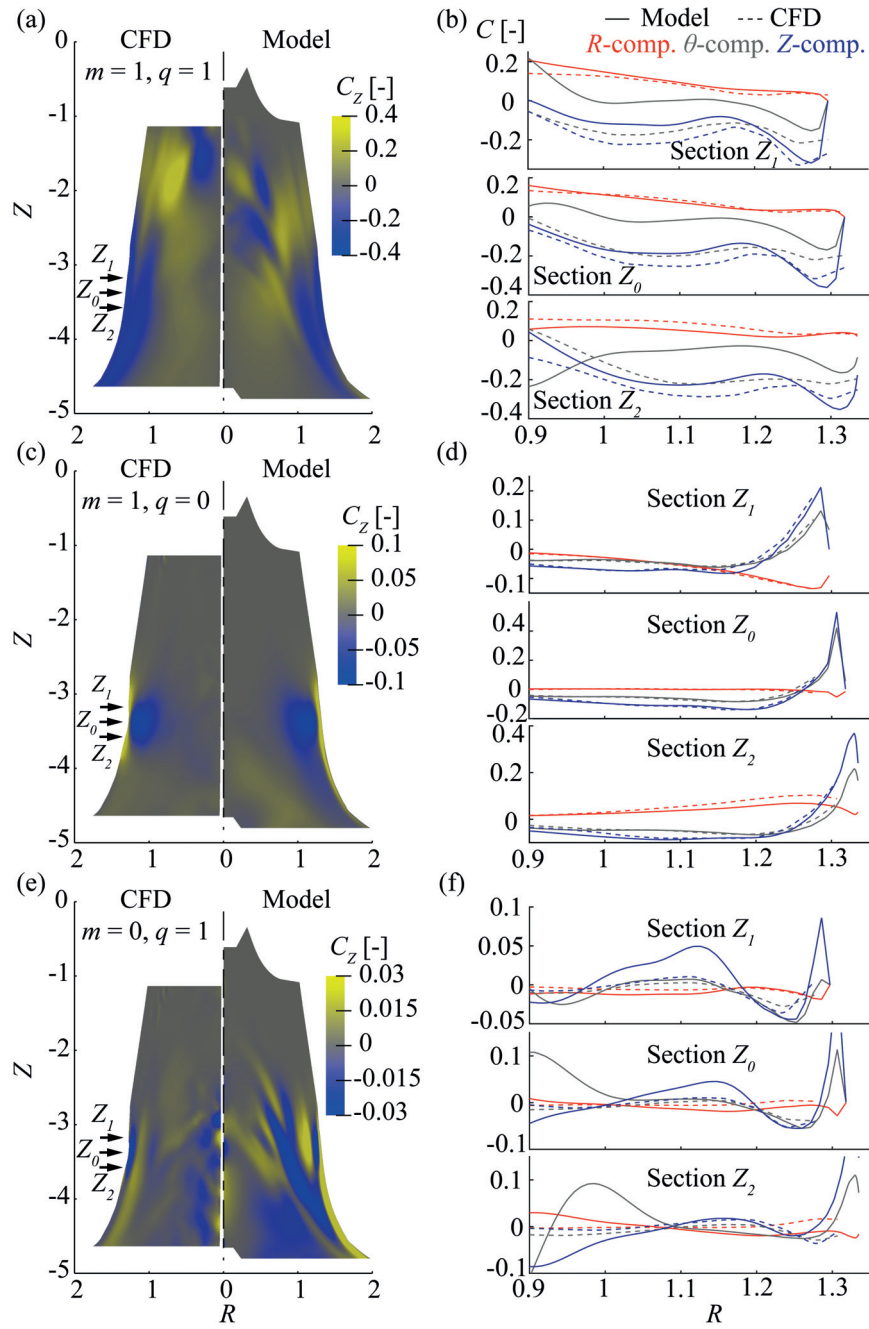


Figure 5.11 – Azimuthal-temporal Fourier series decomposition of the disturbed Moody type draft tube case II, compared with the asymptotic expansion for the vortex rope Fourier mode and its eigenvalue ($m = 1, q = 1$) (a) and (b), the stationary wall disturbances ($m = 1, q = 0$) (c) and (d), and the synchronous waves ($m = 0, q = 1$) (e) and (f).

5.5 Conclusion & Discussion

We have investigated the origin of the synchronous pressure in Francis turbines by the means of 3-D numerical flow simulations. A synchronous wave is observed in the original elbow draft tube by phase averaging of the pressure signal of the wall monitoring points. The frequency of this wave is found identical to the frequency of the vortex rope, consistently with previous studies (Nishi et al. [12] and Arpe & Avellan [8]). Since the numerical domain is reduced to the runner and the draft tube, no acoustic resonance is possible with the piping system, therefore the magnitude of the synchronous pressure wave is inferior than the convective pressure magnitude of the vortex rope. In contrast this synchronous pressure wave is totally absent in the 3-D numerical flow simulations of an axisymmetric Moody draft tube for the same flow regime. The synchronous wave is therefore a fluid-solid interaction between the draft tube geometry and the vortex rope as Nishi et al. [12] have reported in experimental measurements.

We further investigate this interaction using two other draft tube designs, case I and case II where the axisymmetric Moody draft tube is disturbed on the wall at two different places and with different magnitudes. These disturbances are specially designed as an azimuthal wave disturbance $m = 1$, meaning that on a region the draft tube wall sections are translated along one axis only. This setup allows us to separate by double azimuthal-temporal Fourier series decomposition the modes coming from the structure and from the fluid. The energy distributions of these modes shows explicitly the development of a stationary $m = 1$ azimuthal mode, the mode of the structure, that has the largest energy after the vortex rope mode and its harmonics $(m, q) = (1, 1)$, $(2, 2)$ and $(3, 3)$, as well as the development of the synchronous mode $(m, q) = (0, 1)$ with lower energy. Thus the temporal rotation of a single helical vortex in a slightly deformed geometry of an equivalent wavenumber shape produces by nonlinear interactions a planar wave. In these axisymmetric disturbed draft tubes, the origin of the synchronous pressure is located at the disturbance position but its maximum amplitude is observed in the downstream axisymmetric elbow. A second mechanism, yet to be investigated, amplifies the synchronous wave as it travels along the draft tube.

An asymptotic expansion of the flow around the axisymmetric mean turbulent flow helps to formalize the interaction mechanism of the synchronous wave development. A domain perturbation method allows us to include the wall disturbance as a modified boundary condition. By assuming a distinguished limit for the amplitude of the vortex rope similar to the geometrical disturbance, these modes interact and produce an axisymmetric pulsating force at the next order composed of their intercrossed Reynolds stresses, exciting therefore the synchronous wave at the frequency of the vortex rope. This asymptotic analysis compare well to the azimuthal-temporal Fourier series decomposition of the 3-D CFD.

Regarding elbow draft tube turbines where large wall deformation are imposed, the synchronous wave development is expected to affect a broader region, starting at the beginning of the elbow. Its maximum intensity is likely to take place where the vortex rope starts to hit the elbow wall.

5.6 Appendix

5.6.1 Two dimensional axisymmetric computational domain

The asymptotic expansion was computed on a 2-D axisymmetric domain displayed in fig. 5.12. The inlet went back to the runner blade and the outlet was pushed to this end of the 3-D computational domain to isolate these boundary from the computed solution. This domain is identical as Pasche and allowed us to compute an accurate unstable eigenvalue corresponding to the vortex rope, eqn. (5.11)

2-D axisymmetric computational domain

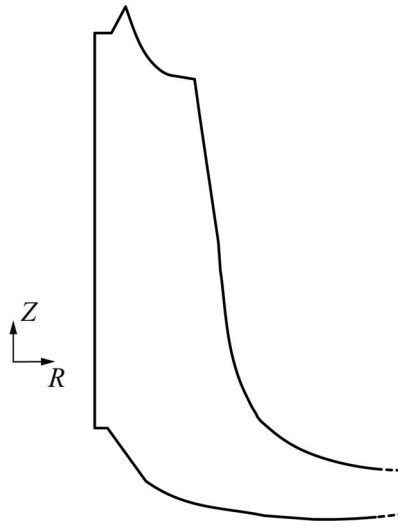


Figure 5.12 – Two dimensional axisymmetric domain used to compute the asymptotic analysis.

5.6.2 Asymptotic expansion complementary equations

The four systems of equations at the order ϵ^2 were reported in the following section. Each systems were related to different variables: $\mathbf{C}_{22}^{(2)}$ the self-interaction of the vortex rope, $\mathbf{C}_{00}^{(2)}$ the Reynolds stresses correction of the mean turbulent flow, $\mathbf{C}_{20}^{(2)}$ the wall disturbance self-interaction, $\mathbf{C}_{21}^{(2)}$ the interaction of the wall disturbance and the vortex rope for azimuthal wavenumber $m = 2$.

$$m = 2, q = 2:$$

$$-i\omega_v \mathbf{C}_{22}^{(2)} + \nabla_m \mathbf{C}_{22}^{(2)} \cdot \bar{\mathbf{C}} + \nabla_m \bar{\mathbf{C}} \cdot \mathbf{C}_{22}^{(2)} + \nabla_m P_{22}^{(2)} - Re^{-1} \nabla_m^2 \mathbf{C}_{22}^{(2)} \quad (5.15)$$

$$-\nabla_m \cdot \left[\mathbf{v}_t(\bar{\mathbf{C}}) (\nabla_m + \nabla_m^T) \mathbf{C}_{22}^{(2)} \right] = -\nabla_m \mathbf{C}_{11}^{(1)} \cdot \mathbf{C}_{11}^{(1)}$$

$$\nabla_m \cdot \mathbf{C}_{22}^{(2)} = 0$$

$m = 0, q = 0$:

$$\begin{aligned}
 & \nabla_m \mathbf{C}_{00}^{(2)} \cdot \bar{\mathbf{C}} + \nabla_m \bar{\mathbf{C}} \cdot \mathbf{C}_{00}^{(2)} + \nabla_m P_{00}^{(2)} - Re^{-1} \nabla_m^2 \mathbf{C}_{00}^{(2)} \\
 & - \nabla_m \cdot \left[\nu_t (\bar{\mathbf{C}}) (\nabla_m + \nabla_m^T) \mathbf{C}_{00}^{(2)} \right] = - \nabla_m \mathbf{C}_{11}^{(1)} \cdot \mathbf{C}_{11}^{*(1)} - \nabla_m \mathbf{C}_{01}^{(1)} \cdot \mathbf{C}_{01}^{*(1)} \\
 & \nabla_m \cdot \mathbf{C}_{00}^{(2)} = 0
 \end{aligned} \tag{5.16}$$

$m = 2, q = 0$:

$$\begin{aligned}
 & \nabla_m \mathbf{C}_{20}^{(2)} \cdot \bar{\mathbf{C}} + \nabla_m \bar{\mathbf{C}} \cdot \mathbf{C}_{20}^{(2)} + \nabla_m P_{20}^{(2)} - Re^{-1} \nabla_m^2 \mathbf{C}_{20}^{(2)} \\
 & - \nabla_m \cdot \left[\nu_t (\bar{\mathbf{C}}) (\nabla_m + \nabla_m^T) \mathbf{C}_{20}^{(2)} \right] = - \nabla_m \mathbf{C}_{10}^{(1)} \cdot \mathbf{C}_{10}^{(1)} \\
 & \nabla_m \cdot \mathbf{C}_{20}^{(2)} = 0
 \end{aligned} \tag{5.17}$$

$m = 2, q = 1$:

$$\begin{aligned}
 & -i\omega_v \mathbf{C}_{21}^{(2)} + \nabla_m \mathbf{C}_{21}^{(2)} \cdot \bar{\mathbf{C}} + \nabla_m \bar{\mathbf{C}} \cdot \mathbf{C}_{21}^{(2)} + \nabla_m P_{21}^{(2)} - Re^{-1} \nabla_m^2 \mathbf{C}_{21}^{(2)} \\
 & - \nabla_m \cdot \left[\nu_t (\bar{\mathbf{C}}) (\nabla_m + \nabla_m^T) \mathbf{C}_{21}^{(2)} \right] = - \nabla_m \mathbf{C}_{11}^{(1)} \cdot \mathbf{C}_{10}^{(1)} - \nabla_m \mathbf{C}_{10}^{(1)} \cdot \mathbf{C}_{11}^{(1)} \\
 & \nabla_m \cdot \mathbf{C}_{21}^{(2)} = 0
 \end{aligned} \tag{5.18}$$

These ancillary systems reflected the other interactions coming from the quadratic nonlinearities of the Navier-Stokes equations that appeared in the energy distribution of the different modes in fig. 5.6.

6 Nonlinear interaction of self-sustained instabilities in laminar swirling flows: Route to chaos

Fluid-solid interactions were investigated in the previous chapter. Nonlinear dynamics of fluid motion governed by self-sustained instabilities are presently investigated. Global stability analysis about the mean flow of the spiral vortex breakdown has revealed two unstable global modes. Their interactions are assessed using direct numerical flow simulations, where a route to chaos is revealed.

The variables used in this document are susceptible to change in comparison to the submitted version of the article to keep the document consistency. Additional paragraph and results could be also added.

PAPER: Onset of chaos in helical vortex breakdown at low Reynolds number

Onset of chaos in helical vortex breakdown at low Reynolds number

Simon Pasche¹, François Gallaire², François Avellan¹

¹ LMH, Swiss Federal Institute of Technology (EPFL), CH-1007, Lausanne, Switzerland

² LFMI, Swiss Federal Institute of Technology (EPFL), CH-1015, Lausanne, Switzerland

Preprint version of the article submitted in *Physical Review Fluids*, (2017)

The nonlinear dynamics of a swirling flow stemming from a Graboswski and Berger vortex in a semi-infinite domain is addressed at low Reynolds numbers and at a fixed swirl number of $S = 1.095$. In this system, only purely hydrodynamic instabilities develop and interact through the quadratic nonlinearities of the Navier-Stokes equations, leading to the onset of chaos at a Reynolds value of $Re = 220$. This chaotic state is reached by following a Ruelle-Takens-Newhouse scenario, which is initiated by a Hopf bifurcation - the spiral vortex breakdown - as the Reynolds number increases. At larger Reynolds value, a frequency synchronization regime is also observed. Nonlinear time series analyses corroborate this scenario. Stability analysis around the time-average flow in association with double azimuthal-temporal Fourier decomposition of the nonlinear flow distributions identify the developing vortices, and provide deeper insight on the development of the flow patterns leading to this route to chaos. Three single helical vortices, the primary spiral associated to the spiral vortex breakdown, a downstream spiral and a near-wake spiral interact together to form a strong axisymmetric mode. As the frequency of the downstream spiral becomes closer to the primary spiral, nonlinear interaction are amplified leading to the chaotic state.

6.1 Introduction

Swirling flows experience vortex breakdown for sufficiently large Reynolds number, as soon as the swirl intensity reaches a critical value. Crossing this threshold, the columnar state of the vortex may bifurcate to several states characterized by a bubble, a spiral or a double spiral breakdown configuration, which have all been reported in many experimental and numerical studies of the last decades, see Lucca-Negro & O'Doherty [139] for a review. This sudden topology change impacts several industrial applications. It affects leading edge vortices that result in a poor flight performance (Gursul et al. [66]), or it prohibits operating conditions in Francis turbines due to the development of large pressure fluctuations (Paschet et al. [10]). In contrast vortex breakdown may be also beneficial, especially in turbomachinery applications, to stabilize the flame of burners or to enhance the mixing of species (Paschereit et al. [67]).

Hydrodynamic instability theory for open flow has shed a new light in this domain with the concept of absolute/convective spatially developing flows of Huerre & Monkewitz [44]. The presence of an advective dominant direction on incoming fluctuations leads to two distinguished situations. In convectively unstable flows, instability waves are swept away as they grow and the flow acts as a noise amplifier. In contrast, in absolutely unstable flows, instability waves invade the entire domain withstanding the advection giving birth to a synchronized oscillator. This concept applied to the Batchelor parallel vortex profile has demonstrated that helical instabilities could become absolutely unstable (Delbende et al. [74]). Weakly non parallel local stability analysis of the spiral vortex breakdown from the velocity profile of the 3-D direct numerical simulation (DNS) of Ruith et al. [57] has led to the interpretation of the spiral vortex breakdown as an absolute instability, triggered by the wake of the upstream bubble (Gallaire et al. [75]). This interpretation was further validated by global stability analysis of non-parallel flow where eigenvalues of the 3-D linearized Navier-Stokes (Theofilis [46]) equations around a base flow were carried out, see Meliga et al. [47] and Qadri et al. [80]. Stemming from a Grabowski & Berger vortex, this open flow has become a benchmark model for disturbance analysis of vortex breakdown, see Vyazmina et al. [79] and Rusak et al. [81].

A bifurcation diagram of this benchmark model based on base flow investigations is reported by Meliga et al. [45], who highlights a bifurcation point where both single and double helical modes simultaneously become globally unstable at the instability threshold. The selected mode is subsequently identified through a weakly nonlinear analysis for the bifurcation point $Re = 71.95$ and $S = 1.436$. Nonlinear analyses of the vortex breakdown at low Reynolds number using numerical flow simulation focus on the formation of the bubble breakdown, the description of the flow patterns and the validation of vortex breakdown criterion initially derived by Squire [69]. These DNSs were performed in several configuration such as pipes by Lopez [140] or in close container by Escudier & Zehnder [61]. The first study that relaxed the radial confinement of the vortex breakdown was performed by Ruith et al. [57] with the aim to describe the linear stability of the first bifurcation state. Ruith et al. [57] have also reported, in addition, the onset of a low frequency for larger swirl number $S = 1.3$ and $Re = 200$ associated to a pulsant double-helical breakdown mode.

In contrast, studies investigating the nonlinear interactions of subsequent bifurcations were mainly performed in confined geometries. For example, spherical Couette flow (Wulf et al. [141]), Rayleigh-Bénard convection (Morris et al. [142] and Egolf et al. [143]) are typical fluid flow system presenting chaotic regimes. Turning back to swirling flow, Lagrangian chaos of vortex breakdown in closed containers was investigated by Sotiropoulos et al. [144] aiming at identifying basin of attractions of particle trajectories to improve species mixing in swirl burner applications. Quasi-periodic regime of Eulerian dynamics was reported by Serre & Bontoux [145] and Lopez [146] and Eulerian chaos was reported by Sorensen & Christensen [147] in the same configuration.

Confined geometries exacerbate fluctuations of the bulk flow through shear effect of the boundary layer and favor the system evolution to chaotic regime acting as a consequence of

Chapter 6. Nonlinear interaction of self-sustained instabilities in laminar swirling flows: Route to chaos

reflection and feedback mechanisms, before leading to spatio-temporal chaos and turbulence. Chaotic regimes in open flows were also reported in bounded geometries, like for instance the converging-diverging channel flow of Amon et al. [148] among others.

The route to chaos was found to follow three different possible universal scenarii (Newhouse et al. [149], Feigenbaum [150] and Pomeau & Manneville [151]). The first one is the period doubling or Feigenbaum scenario where consecutive period doubling transitions are successively observed until chaos is reached. The second is the Manneville-Pomeau intermittency regime. The third scenario is the Ruelle-Takens-Newhouse where chaos is observed after the apparition of a strange attractor with three incommensurate frequencies. In this scenario, the successive bifurcations yielding from a steady fixed point (so-called T0) solution to chaos proceed through the following states: a first Hopf bifurcation yields a limit cycle torus T1, followed by periodic k-period oscillations when the secondary instability sets in with a commensurable frequency or alternatively a quasiperiodic state with two non commensurable frequencies, the torus T2. A subsequent bifurcation can yield a torus T3, which eventually becomes unstable and yields chaos.

In the present study we investigate the appearance of Eulerian chaos in the open swirling wake flow in a semi-infinite domain.

The paper is organized as follows: the open geometry of Ruith et al. [57] leading to spiral vortex breakdown is described together with the governing equations in section 6.2. The numerical tools used to perform DNS and to study the emerging flow patterns by global stability analysis around the mean flow and double temporal-azimuthal Fourier decomposition are presented in section 6.3. The first part of the results explore the instantaneous axial vorticity snapshots of a specific set of bifurcation parameter (section 6.4), then a bifurcation diagram is presented (section 6.5) followed by a nonlinear time series analysis in a specific point (section 6.6). This local approach devoted to chaos theory and describing the flow state is then enriched by the identification of spatial modes involved and their nonlinear interactions. This part of the results are presented in section 6.7, before conclusions are drawn.

6.2 Flow configuration

We consider the dynamics of a Grabowsky & Berger [78] vortex, entering a semi-infinite domain Ω , governed by the incompressible Navier-Stokes equations. This vortex, defined as,

$$\begin{aligned} C_R(R) = 0, \quad C_\theta(R) = S\Psi, \quad C_Z(R) = 1, \quad \text{on } \Gamma_{in} \\ \Psi(R \leq 1) = R(2 - R^2), \quad \Psi(R > 1) = 1/R, \end{aligned} \tag{6.1}$$

is composed of a dimensionless vortex core size, with a prescribed tangential velocity C_θ assigned by the swirl number S , and uniform dimensionless axial velocity $C_Z = 1$. Here we have used the reference length scale defined by the vortex core size l and the reference velocity

scale defined by the axial velocity component C_0 so that the fluid motion governed by the incompressible Navier-Stokes equations write

$$\begin{aligned} \frac{\partial \mathbf{C}}{\partial t} + (\mathbf{C} \cdot \nabla) \mathbf{C} &= -\nabla P + Re^{-1} \nabla^2 \mathbf{C} \quad \text{in } \Omega \\ \nabla \cdot \mathbf{C} &= 0 \quad \text{in } \Omega, \end{aligned} \quad (6.2)$$

in dimensionless form, where $Re = lC_0/\nu$. This flow configuration is investigated for a constant swirl number $S = 1.095$, which restricts our study to the spiral vortex breakdown in contrast to pure bubble vortex breakdown or double helix vortex breakdown observed respectively at lower and larger swirl numbers (Ruith et al. [57] and Meliga et al. [45]). Although we focus on spiral vortex breakdown, this system is observed to reach several dynamical states as the Reynolds number is increased. A bifurcation analysis is, therefore, performed up to a Reynolds value of $Re = 300$, using classical tools to investigate dynamical systems such as nonlinear time series, attractor cross sections, frequency identification and sensitivity to initial conditions. This approach conducted in a single monitoring point is then enriched by the identification of the developing temporal and spatial 2-D axisymmetric modes by performing a global stability analysis around the mean flow and a double azimuthal-temporal Fourier decomposition of the direct numerical simulations (DNS).

6.3 Numerical methods

6.3.1 Direct numerical flow simulations

Direct numerical flow simulations (DNS) of the Navier-Stokes equations, eqn. (6.2), are performed on a 3-D cylindrical domain (fig. 6.1). These equations are completed with the

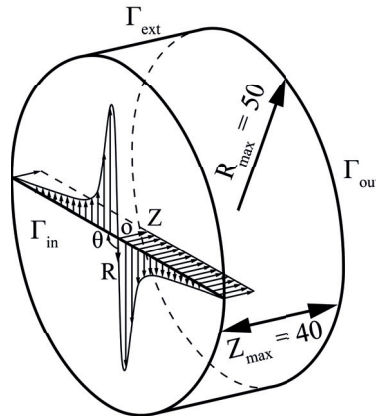


Figure 6.1 – 3D schematic of the flow configuration.

following boundary conditions: a Grabowsky and Berger vortex eqn. (6.1) at the inlet Γ_{in} , a free-outflow condition $(-P\mathbf{I} + Re^{-1} \cdot (\nabla \mathbf{C})) \cdot \mathbf{n} = 0$ on the external boundary Γ_{ext} and a convective

Chapter 6. Nonlinear interaction of self-sustained instabilities in laminar swirling flows: Route to chaos

condition $\partial_t \mathbf{C} + \mathbf{C}_c \cdot \partial_{\mathbf{n}} \mathbf{C} = 0$ at the outlet Γ_{out} . We have fixed the convective velocity equal to the free-stream velocity $\mathbf{C}_c = \mathbf{e}_Z$. The vortex breakdown resulting from this flow conditions is, in addition, known to be very sensitive to radial confinement as experimented by Ruith et al. [57]. To overcome this issue, Ruith et al. [57] imposed a convective boundary condition on the external boundary to mimic an infinite radial direction. We have, in contrast, imposed a ratio of fifty between the vortex core size c and the domain radial length, leading therefore to a domain size equals to $R_{max} = 50$ and $Z_{max} = 40$. In order to assess the absence of any confinement effects resulting from these choices, we have implemented a second boundary condition on Γ_{ext} , a no-slip condition and obtained very similar results, see appendix 6.9.1.

This flow system is solved numerically using the spectral element solver NEK5000 [100]. This solver is based on a cartesian coordinate system (X, Y, Z) and we have chosen to introduce a second, cylindrical, coordinate system (R, θ, Z) , which is preferably used to study swirling flows, to present our results. We defined the following convention: both systems are oriented in the trigonometric direction and share the same axial component Z pointing inside the domain, along the center axis. In addition, the mesh and the setup parameters are identical as in Pasche et al. [10]. The mesh contains 11040 hexahedral elements discretized using Gauss-Lobatto-Legendre (GLL) and Gauss-Legendre (GL) points of polynomial order P_{10} and P_8 to satisfy the inf-sup condition of the Navier-Stokes equations, and the time step defines a CFL number of 0.37 (see appendix 6.9.1 for a validation of this CFL choice). The simulations are initiated with a 3-D flow distribution provided by the inlet Grabowski & Berger vortex, eqn. (6.1), in the complete computational domain.

6.3.2 Temporal-azimuthal Fourier decomposition

The coherent flow patterns associated to the characteristic frequency of the DNS are extracted using a double azimuthal-temporal Fourier decomposition. This decomposition is performed for the selected Reynolds values $Re = [200, 220, 230, 250]$. The coherent flow fluctuations $\tilde{\mathbf{U}} = (\mathbf{C}, P)$ are therefore obtained by subtracting the time-average flow $\bar{\mathbf{U}}$ of the instantaneous flow \mathbf{U} yielding to following expression after Fourier decomposition:

$$\begin{aligned} \tilde{\mathbf{U}}(R, \theta, Z, t_q) &= \mathbf{U}(R, \theta, Z, t_q) - \bar{\mathbf{U}}(R, \theta, Z) = \\ \Re \left(\sum_{m=0}^{\infty} \frac{1}{N} \sum_{k=0}^{N-1} \left[\mathbf{A}_{mq}(R, Z) e^{-i\omega_k t_q} \cos(m\theta) + \mathbf{B}_{mq}(R, Z) e^{-i\omega_k t_q} \sin(m\theta) \right] \right) &= \\ = \Re \left(\sum_{m=0}^{M-1} \frac{1}{N} \sum_{k=0}^{N-1} \tilde{\mathbf{U}}_{mq}(R, Z) e^{i(m\theta - \omega_k t_q)} \right). \end{aligned} \quad (6.3)$$

where $\omega_k = k\Delta\omega = k2\pi/N$, and N the number of samples. This definition leads to the following relations $\Re(\tilde{\mathbf{U}}_{mq}) = \mathbf{A}_{mqr} = \mathbf{B}_{mqi}$ and $\Im(\tilde{\mathbf{U}}_{mq}) = \mathbf{A}_{mqi} = -\mathbf{B}_{mqr}$. The azimuthal decomposition is computed on the fly during the DNS using the FFTW package [152] embedded in NEK5000 [100]. At each time step, part of the domain from $R = 3$ to $Z = 30$ is interpolated on a cylindrical distribution of points using the spectral interpolation of NEK5000 with 10^{-13} accuracy. An

Azimuthal wave number	Boundary conditions
$m = 0$	$c_R = c_\theta = 0, \partial_R c_Z$
$m = \pm 1$	$c_Z = 0, \partial_R c_R = \partial_R c_\theta$
$m > 1$	$c_R = c_\theta = c_Z = 0$

Table 6.1 – Boundary conditions on the axisymmetric axis applied to the disturbances for different azimuthal wave numbers.

accurate Fourier decomposition of the flow has needed 16 azimuthal points, leading to $M = 17$ and a time series of $N = 320000$ samples for cases with low frequency, that represent a dimensionless time of 1600. The frequency spectrum associated to the temporal decomposition is then computed with the Matlab fast Fourier transform. As the modes are extracted during the DNS, this analysis can be viewed as an *a posteriori* description of the flow modes.

6.3.3 Global stability analysis

The small disturbance dynamics brings an *a priori* description of the coherent flow patterns by investigating the exponential growth of infinitesimal perturbations. Linear stability analysis about the time-average flow field $\bar{\mathbf{U}} = (\bar{\mathbf{C}}, \bar{P})$ of the Navier-Stokes equations are performed. We take advantage of the geometry and flow symmetry to compute the linear stability analysis in a 2-D axisymmetric domain Ω_a , i.e. a half section of the 3D domain Ω . Infinitesimal perturbations are therefore decomposed in normal mode expansion with respect to the time t and the azimuthal coordinate θ as,

$$\tilde{\mathbf{U}}(R, \theta, Z, t) = \mathbf{u}(R, Z) \exp(i(m\theta - \omega t)) + c.c., \quad (6.4)$$

with $m \in \mathcal{Z}$ the azimuthal wave number, ω the eigenvalue and *c.c.* the complex conjugate. The ensued eigenvalue problem is written in compact form as

$$(-i(\omega_r + i\omega_i)\mathcal{N} + \mathcal{L}_m(\bar{\mathbf{C}}))\mathbf{u} = \mathbf{0}, \quad \text{in } \Omega \quad (6.5)$$

where \mathcal{L}_m is the operator for the linearized Navier-Stokes equations of azimuthal wave number m and \mathcal{N} is the singular operator premultiplying the time-derivative. The associated boundary conditions of eqn. (6.5) are a zero disturbance at the inlet Γ_{in} , a free-outflow on the external boundary Γ_{ext} , boundary conditions on Γ_{axis} summarized in Table 6.1 which depend on the azimuthal wavenumber (Korhami [103]), while the convective boundary on Γ_{out} is converted to a free-outflow condition Γ_{out} without impacting the solution of the eigenvalue problem, see appendix 6.9.1.

Chapter 6. Nonlinear interaction of self-sustained instabilities in laminar swirling flows: Route to chaos

The global stability analysis is carried out by a finite element method implemented in the Freefem++ software [101]. The weak form of the eigenvalue problem is derived after being premultiplied by the radial coordinate R . The eigenvalue and eigenvectors are computed using by the implicit restarted Arnoldi method of the ARPACK library [104] with a tolerance of 10^{-6} . The 2-D axisymmetric mesh is made by approximately 400000 Taylor Hood triangular elements of $P_2 - P_1$ shape functions. The half section of the time-average flow from the 3-D DNS, which is computed on the fly in NEK5000, is interpolated on the 2-D axisymmetric mesh using the spectral interpolation tool of NEK5000, accurate at 10^{-13} .

6.4 Instantaneous flow

Three-dimensional representations of the vortex flow, materialized by iso-contours of axial vorticity are displayed in fig. 6.2 and illustrate the time history of the flow patterns observed at a Reynolds values of $Re = 220$ and a swirl number of $S = 1.095$. The presence of a bubble vortex breakdown at the beginning of the computational domain is always observed, which is followed by spiral vortices. At the first illustrated time (fig. 6.2a at $t = 2278$), a single spiral is observed, which is labeled primary spiral and is characteristic of the spiral vortex breakdown. This spiral indeed spins in the same direction as the inlet vortex and coils in the opposite direction, consistently with previous results of Ruith et al. [57]. The time evolution of this primary spiral shows a vorticity intensity modulation, which becomes stronger at the time step $t = 2289$ (fig. 6.2b) than at the later time step $t = 2368$ (fig. 6.2d).

Furthermore, a second vortical structure is observed for this Reynolds value, which is labeled downstream spiral and starts to be materialized by vorticity iso-contours for the time step $t = 2330$ (fig. 6.2c), around the location $Z = 10$. This downstream vortex develops separately from the primary spiral between the time step $t = 2330$ to $t = 2368$ and shows thinner and elongated vorticity iso-contours for the latter time step. In this figure, a third vortical structure is also observed in the near-wake of the bubble, which is well defined at the time step $t = 2341$ (fig. 6.2d) and is labeled near-wake spiral. While this vortex spins in this location, it has the particularity to reattach to the downstream spiral at time $t = 2356$ (fig. 6.2e) and to detach at the next illustrated time (fig. 6.2f). These three vortical structures will be later interpreted as three single helical vortex ($m = 1$ azimuthal wavenumber) in section 6.7 and not as double helical modes, which can be observed at larger swirl numbers.

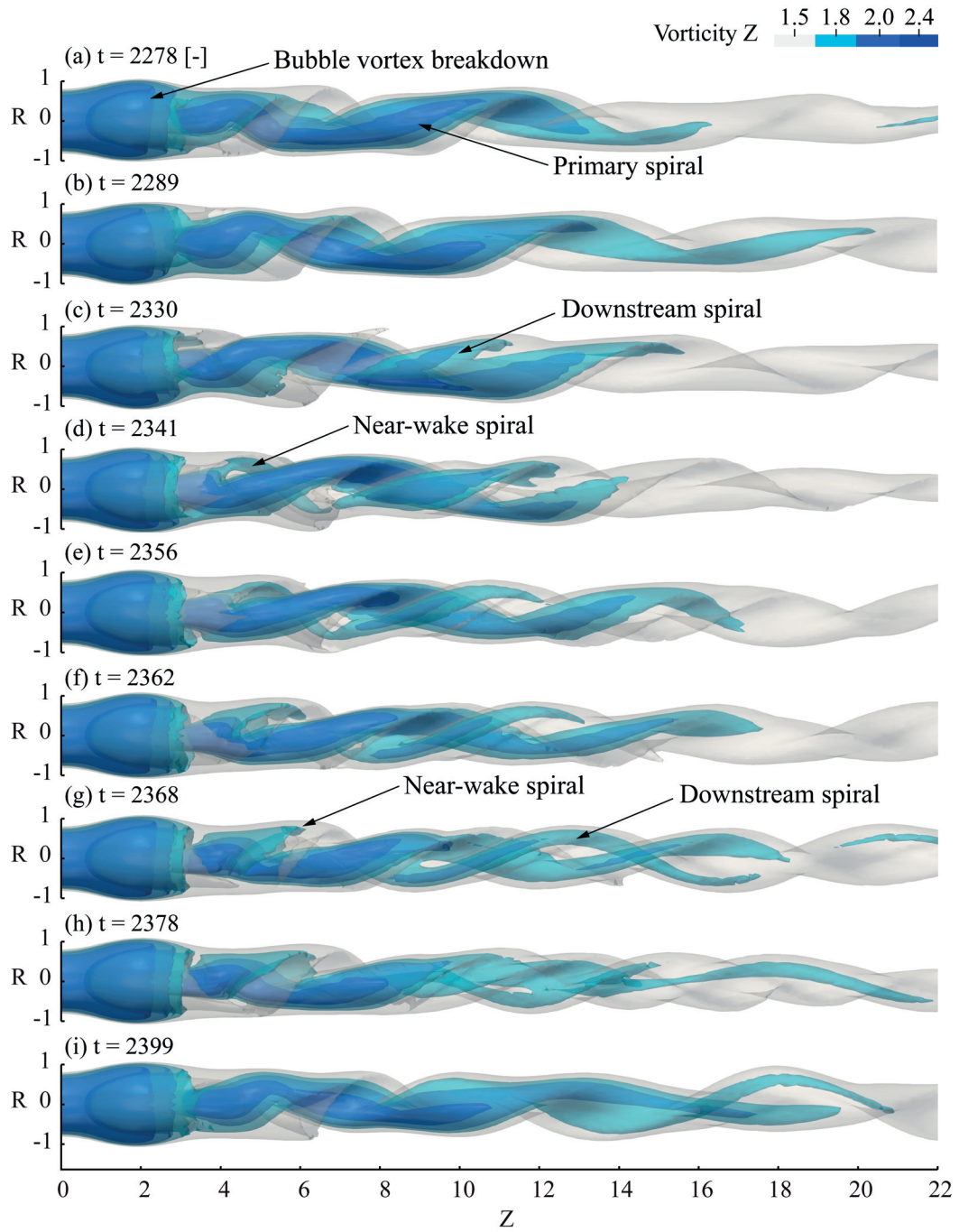


Figure 6.2 – Time evolution of the swirling flow induced by a Grabowski and Berger vortex for a swirl number of $S = 1.095$ and a Reynolds number of $Re = 220$, materialized by axial vorticity iso-contours.

6.5 Bifurcation analysis

A bifurcation diagram for the constant swirl number $S = 1.095$ and Reynolds numbers until $Re = 300$ is displayed in fig. 6.3. This diagram is built by identifying each maximum and minimum radial velocity of the time series monitored at the single point $(R, \theta, Z) = (0.1, 0.0, 6.0)$, after the system reaches its established state. Using this technique, fixed points are represented

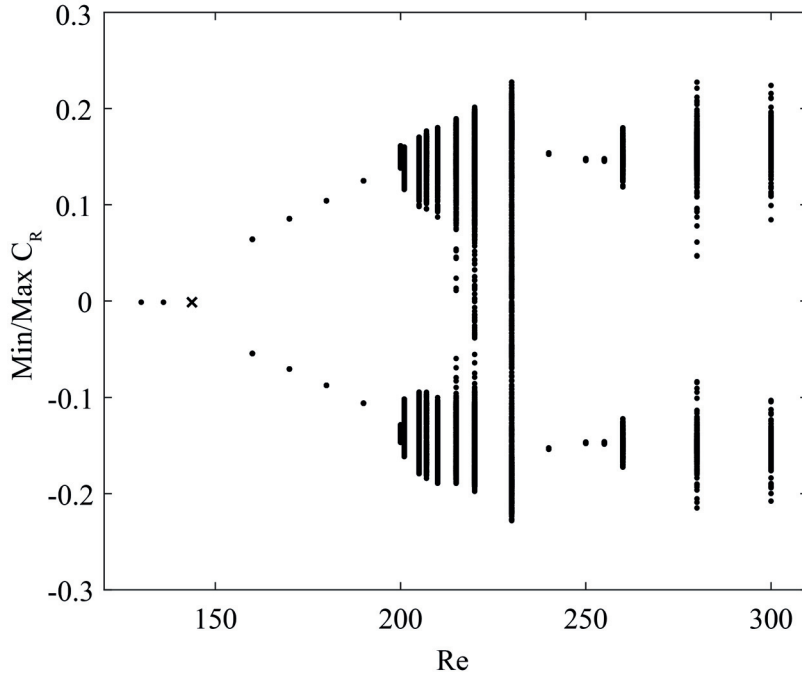


Figure 6.3 – Bifurcation diagram of the min/max temporal series of the radial velocity C_R at $(R, \theta, Z) = (0.1, 0.0, 6.0)$ (point symbole). The instability threshold of Pasche et al. [10], at $Re = 143.5$, is illustrated as a cross symbole.

by a single point, while higher dimensional states have either a finite number or a finite approximation of an infinite number of points, as a consequence of the finite length of the time series. In particular, a stable limit cycle (period-1 torus, T_1) has two repeated points (one repeated peak and one repeated trough), a period-2 cycle has four repeated points, a period- k cycle has $2k$ repeated points, and quasi-periodic on a m -torus T_m and chaotic regime have spread points bounded within a range of C_R .

At low Reynolds number, the system is attracted toward a fixed point solution, defined as the base flow of the governing equation, eqn. (6.2) and it occurs for Reynolds value less than $Re = 143.5$ as reported by Pasche et al. [10]. A supercritical Hopf bifurcation is then observed leading to a period-1 torus until a Reynolds value close to $Re = 200$, and it is characteristic of the spiral vortex breakdown phenomenon. Above $Re = 200$, several min/max values are observed, which means that this system is attracted towards higher dimensional states. Quasi-periodic and chaotic regimes will be observed, and further investigated in section 6.6. The ranges of radial velocity C_R increase until $Re = 230$, where the maxima and minima are mixed

and lead to a dense line of points in the present diagram (fig. 6.3). The system turns back into a period-1 torus between a Reynolds value of $Re = 240$ to $Re = 255$, characterized by two repeated points, and loses its stability above $Re = 255$. A second densification of the min/max values, which characterizes quasi-periodic or chaotic oscillations, is then observed and seems to persist over larger Reynolds values, although it is not further studied here.

6.6 Nonlinear time series analysis

6.6.1 Nonlinear time series

Nonlinear time series of the tangential velocity monitored at the location $(R, \theta, Z) = (0.1, 0.0, 6.0)$ are displayed in fig. 6.4 for several Reynolds values $Re = [180, 200, 205, 215, 220, 230, 250, 300]$. These time series are samples of the dynamical system for suitable time ranges after the transient phases has died out. The stable limit cycle T1 arising from a supercritical Hopf bifurcation associated to the spiral vortex breakdown is observed for $Re = 180$, in fig. 6.4(a). This periodic oscillation appears with the development of an unstable mode (Ruith et al. [57] and Gallaire et al. [75]), which saturates by nonlinearity of the governing equations, leading therefore to a finite amplitude oscillation of the flow. Then the system is attracted towards a quasi-periodic regime at $Re = 200$, in fig. 6.4(b), which is observed by the signal modulation of the time series. Above $Re = 205$ (fig. 6.4c), a low frequency is, in addition, observed and the temporal signals start to lose their regular oscillations. At $Re = [205, 230]$ only small irregular fluctuations are observed, while at $Re = [215, 220]$ larger bursts are identified. These irregular oscillations are followed by a synchronization regime, as illustrated at a Reynolds value of $Re = 250$ in fig. 6.4(g) which sets in between $Re = 230$ and $Re = 240$ and stops before $Re = 260$. After this synchronization regime the flow becomes quasi-periodic or chaotic again from $Re = 260$ until $Re = 300$ and apparently keeps this latter state favoring the turbulent transition.

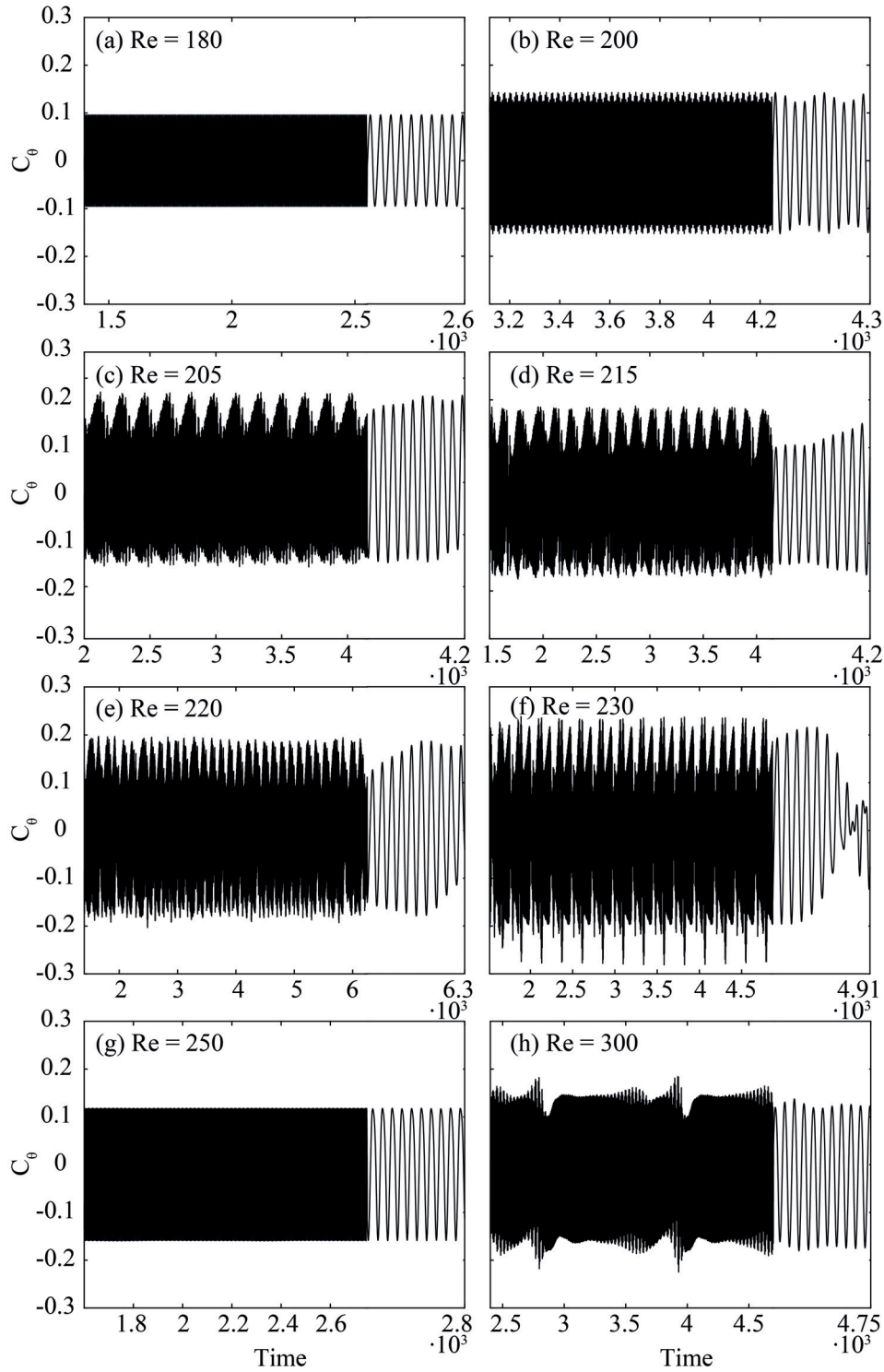


Figure 6.4 – Discrete temporal Fourier transform of the azimuthal time serie monitored at $(R, \theta, Z) = (0.1, 0.0, 6.0)$ for a swirl number of $S = 1.095$ and several Reynolds numbers, (a) $Re = 180$, (b) $Re = 200$, (c) $Re = 205$, (d) $Re = 215$, (e) $Re = 220$, (f) $Re = 230$, (g) $Re = 250$, (h) $Re = 300$. The end of each time series use a zoomed scale.

6.6.2 Sensitivity to initial disturbance

Sensitivity to initial disturbances is investigated to clarify the dynamical state at a Reynolds value of $Re = 205$ where a low frequency emerges in the time series, and at $Re = [215, 220]$, which are associated to irregular bursts of the time series. The separation distance $\|D\|$, assessed by the instantaneous L_2 -norm of the velocity on the monitoring point $(R, \theta, Z) = (0.1, 0.0, 6.0)$, between two flow solutions is therefore computed. These flow solutions are defined as a reference solution and a disturbed solution, which for the last is initiated by a random volume disturbance of amplitude 10^{-8} added to the reference solution. We should mention that the flow distribution from a restarted flow solution remains invariant in this setup and the high accuracy of spectral element method of NEK5000 allows us to carry out such approach.

The time series of the reference and disturbed flows are presented in fig. 6.5 at the Reynolds value of $Re = [215, 220]$. The separation of the two systems is visible after a time $t = 8.2 \cdot 10^3$ for the Reynolds value of $Re = 215$ and a time $t = 7 \cdot 10^3$ for the Reynolds value of $Re = 220$.

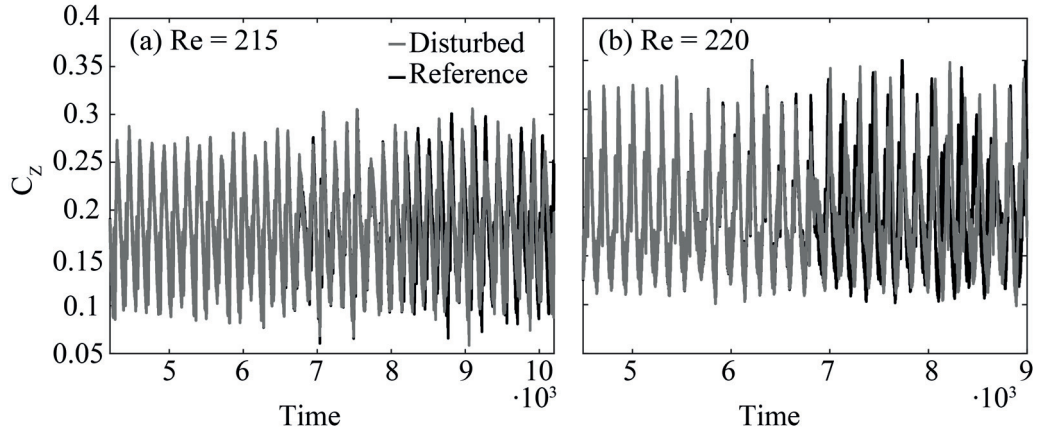


Figure 6.5 – Time series of the reference flow and the disturbed flow with a random noise of amplitude 10^{-8} at the initial time step at a Reynolds value of $Re = 215$ (a) and $Re = 220$ (b), at the location $(R, \theta, Z) = (0.1, 0.0, 6.0)$.

The separation distance of these signals are displayed in fig. 6.6 at the Reynolds value $Re = [215, 220]$ and also $Re = 205$. We observe at a Reynolds value of $Re = 205$ that the separation distance remains around 10^{-6} (fig. 6.6a). The system appears therefore as quasi-periodic even if a low frequency has emerged in the time series (see fig. 6.4c). In contrast, an exponential separation of the flow solutions is reported at a Reynolds value of $Re = 215$ and $Re = 220$ (fig. 6.6b and c). In the former case, a constant exponential coefficient can be extracted, while it is only approximate in the latter case due to a step change in the curve. Their exponential growths are close to zero, $\alpha = 6.6 \cdot 10^{-5}$, but nevertheless positive, which supports that these systems are tending towards chaotic attractors at the Reynolds numbers $Re = [215, 220]$.

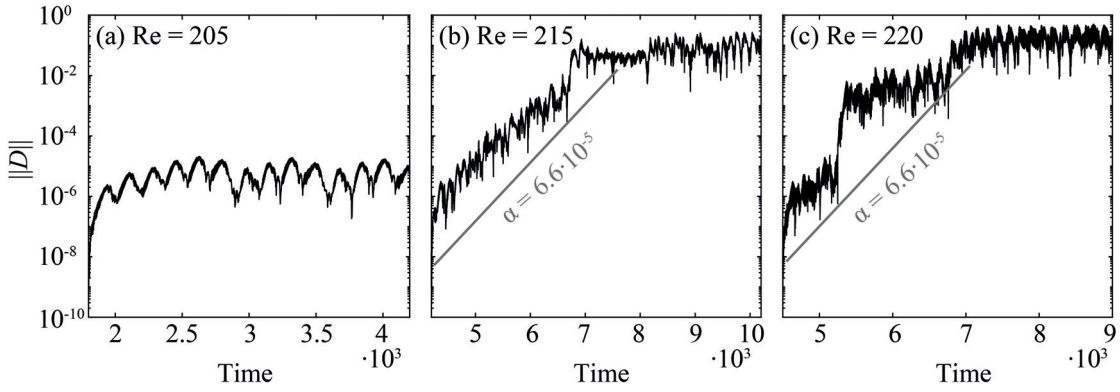


Figure 6.6 – L_2 -norm of the distance between the reference and disturbed dynamical state at the location $(R, \theta, Z) = (0.1, 0.0, 6.0)$ at a Reynolds value of $Re = 205$ (a), $Re = 215$ (b) and $Re = 220$ (c).

6.6.3 Attractor cross sections

Attractor cross sections of the time series at the location $(R, \theta, Z) = (0.1, 0.0, 6.0)$ are displayed in fig. 6.7 for the Reynolds values $Re = [180, 200, 205, 215, 220, 230, 250, 300]$. These cross sections were obtained by sampling the radial and axial velocity components associated to the constant tangential velocity component of value $C_\theta = 0.001$. We, therefore, display cross sections of the phase space, which is useful to define the topological structure of attractors and is similar to Poincaré section maps, with a double number of points because both crossing directions are extracted instead of only one direction for a Poincaré section map. Period-1 oscillations are represented as two points in the attractor cross section that is typically observed for Reynolds values of $Re = 180$ and $Re = 250$, in fig. 6.7(a) and (g) respectively. The first value is associated to the dynamics of the spiral vortex breakdown and the latter value corresponds to the frequency synchronization of the system. A quasi-periodic regime with two incommensurable frequencies is represented by a close path of the attractor cross section, typically at a Reynolds value of $Re = 200$ and in a more distorted way at $Re = 230$, where sensitivity to initial condition reports a converged solution. At $Re = 200$, The T2 torus results from a second supercritical Hopf bifurcation as reported by Pasche et al. [10]. In contrast, the T2 torus at $Re = 230$ observed in fig. 6.7(f), which presents complex patterns, is a consequence of frequency matching of the different vortices as will be discussed in sec. 6.6.4. The chaotic regime identified at $Re = [215, 220]$ have dense cross sections (fig. 6.7d and e) because the correlation dimension of chaotic attractors are not integer anymore, similar to fractal structures. The same structure of the attractor cross section is observed at $Re = 300$ (fig. 6.7h), which probably is also chaotic. At $Re = 205$, a dense attractor cross section is also observed (fig. 6.7c), we have seen in contrast that the flow is insensitive to initial disturbance (see fig. 6.6a). These two characteristics let us think that a stable quasi-periodic regime on a torus T3 is observed.

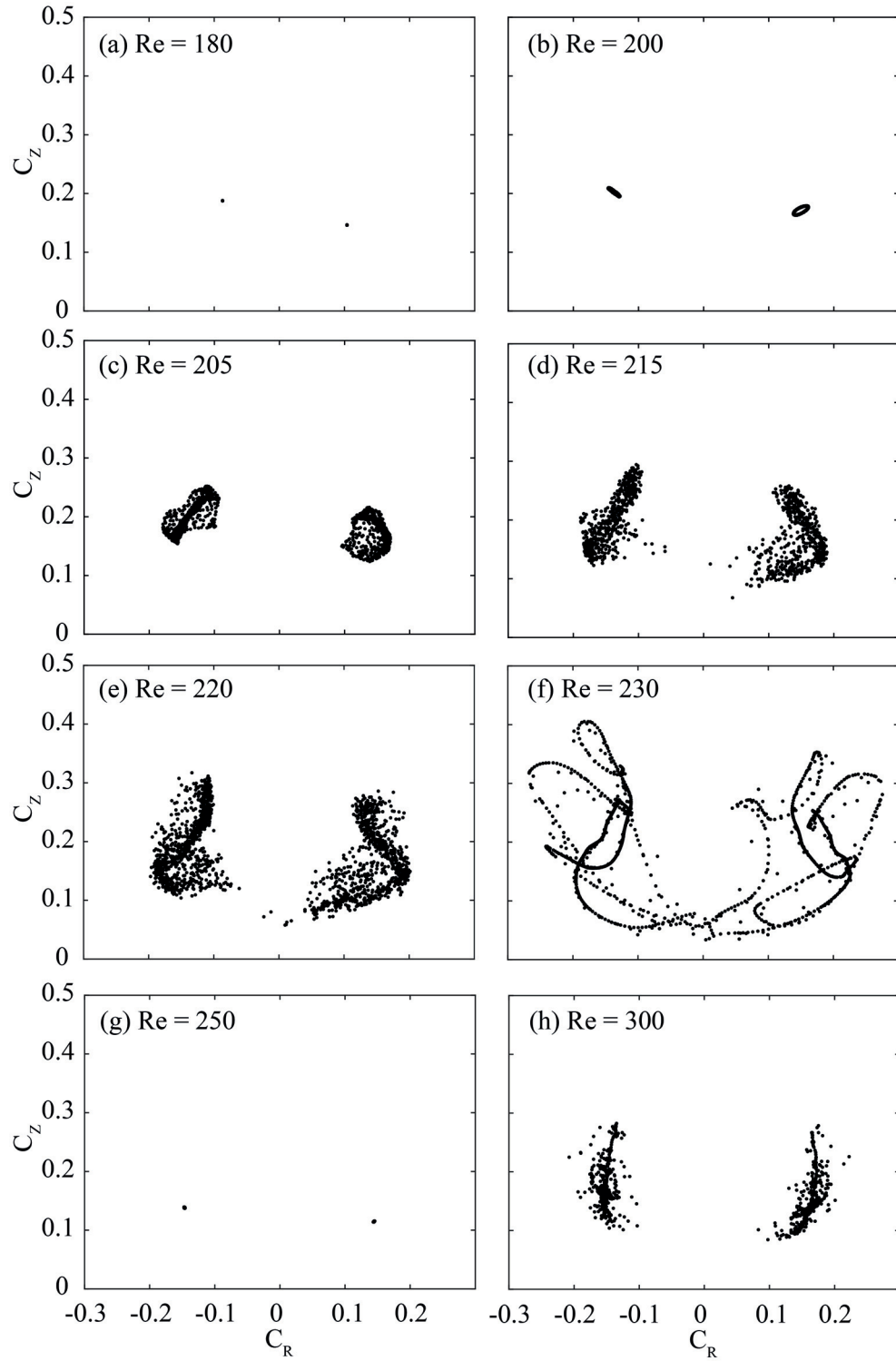


Figure 6.7 – Attractor cross section of the velocity time series at $(R, \theta, Z) = (0.1, 0.0, 6.0)$, for $C_\theta = 0.001$, a swirlnumber of $S = 1.095$ and several Reynolds numbers, (a) $Re = 180$, (b) $Re = 200$, (c) $Re = 205$, (d) $Re = 215$, (e) $Re = 220$, (f) $Re = 230$, (g) $Re = 250$, (h) $Re = 300$.

6.6.4 Amplitude Fourier spectrum

Amplitude Fourier spectrum of the time series (fig. 6.4) at the location $(R, \theta, Z) = (0.1, 0.0, 6.0)$ and snapshots of the axial vorticity iso-contours for the identical bifurcation parameters are presented in fig. 6.8. This method is investigated to corroborate the topological structure of the attractors, observed in the cross sections (fig. 6.7), to the frequency peaks of the amplitude Fourier spectrum. These frequency identifications are associated to vorticity iso-contours materializing the flow patterns. At $Re = 180$ the periodic signal of fundamental frequency f_1 is not purely sinusoidal, its first harmonic appears, therefore, in the frequency spectrum, labeled a in fig. 6.8(a). The associated vorticity iso-contours displayed in fig. 6.8(b), show the axisymmetric bubble and a well-defined single spiral spinning in the bubble wake, called primary spiral.

At $Re = 200$ (fig. 6.8d) the recirculation bubble starts precessing around an eccentric axis and a second vortex is observed beside the primary spiral, referred to as the downstream spiral, previously observed in fig. 6.2. A vorticity iso-contour of value 1.8 materializes this second spiral, which appears at a downstream location $Z = 12$ and has a weaker vorticity magnitude than the primary spiral. The dynamics of the system identified by Fourier amplitude spectrum is quasi-periodic on a torus T2, with two incommensurable frequencies $f_1 / f_2 = 1.2667$. This dynamics is also observed in the attractor cross section (fig. 6.7b). The quadratic nonlinear interaction of the primary and downstream spiral generates a frequency of smaller amplitude labeled $b = f_1 - f_2$ in fig.6.8(c). The frequency difference between these two spirals means that they periodically merge and separate, as seen in fig. 6.8(d).

A torus T3 appears at $Re = 205$ by the development of a third peak in the Fourier amplitude spectrum, associated to the frequency labeled f_3 in fig. 6.8(e). We can, therefore, identify three incommensurable frequencies $f_1 / f_3 = 1.0294$, $f_1 / f_2 = 1.2666$ and $f_2 / f_3 = 0.8127$ in this quasi-periodic attractor. Nonlinear interactions between these modes produce different frequencies, among all we have labeled $c = f_1 - f_3$ and $d = 2f_1 - f_3$. The low frequency modulation observed in the time series (fig. 6.4c) is associated to the frequency peak labeled c . The snapshot of vorticity iso-contours shows again the primary spiral and the downstream spiral associated to the frequency peak f_1 and f_2 . However no clearly visible vortical structure is identified for the frequency peak f_3 , see fig. 6.8(f).

The chaotic attractors at $Re = [215, 220]$ (fig. 6.8g and i) result from the destabilization of the torus T3 woven by these three incommensurable frequencies. Quasi-periodicity turns into a chaotic regime as the second frequency peak f_2 becomes closer to the first frequency peak f_1 . At $Re = 220$ (fig. 6.8j) several helical vortices are observed, the primary spiral of strong amplitude, the downstream spiral that now starts from $Z = 6.5$ and a near-wake spiral located behind the bubble at $Z = 5$, which are phase shifted compared to the primary spiral. These three vortical structures evolve in time according to the following sequence: while the bubble and the primary spiral keep spinning at a fixed location, the downstream and near-wake spiral start growing, attach together, as displayed in fig. 6.2, before being embedded in the primary

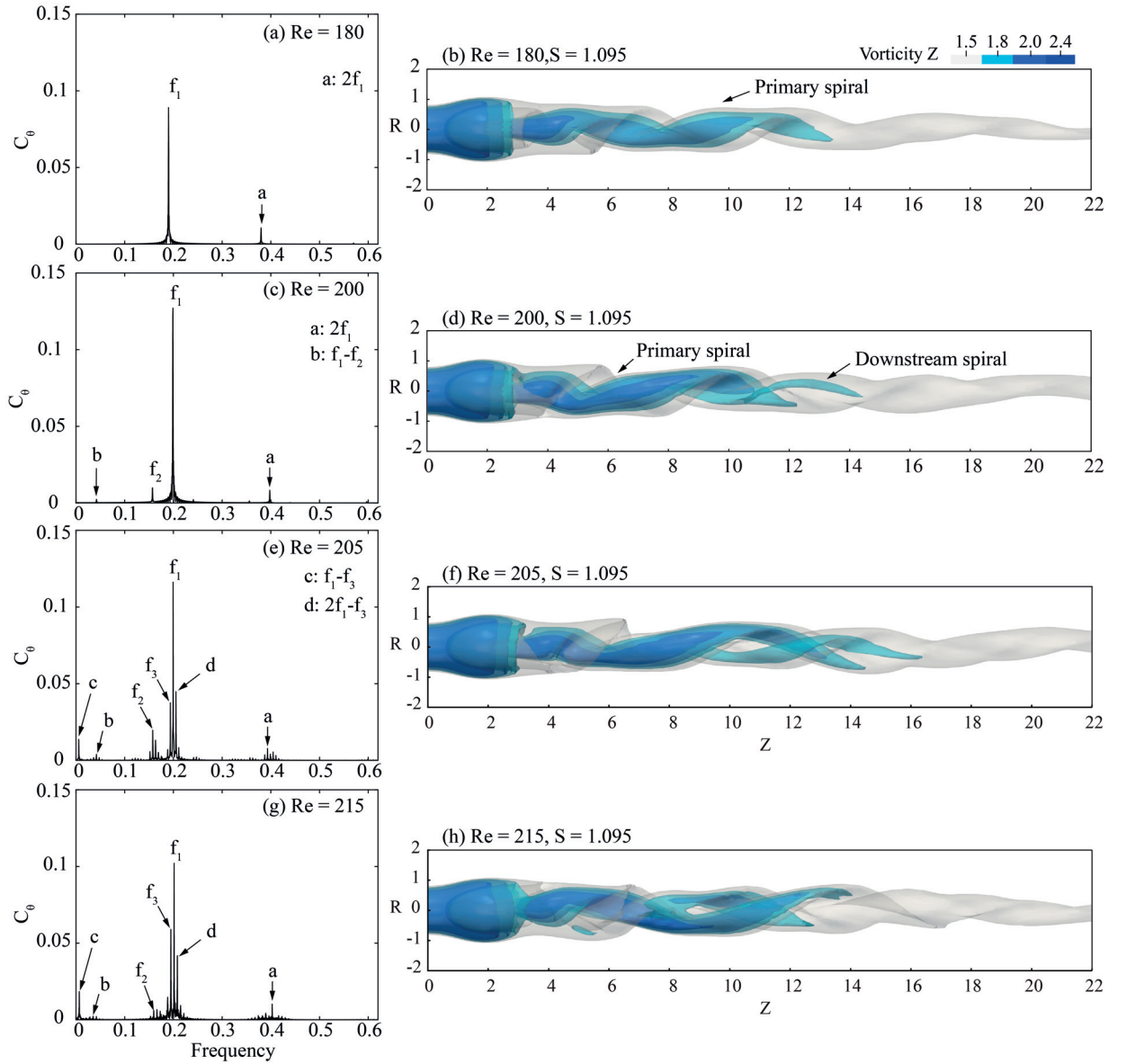


Figure 6.8 – Fast Fourier transform of the velocity time series at $(R, \theta, Z) = (0.1, 0.0, 6.0)$ for a swirl number of $S = 1.095$ and Reynolds numbers, (a, b) $Re = 180$, (c, d) $Re = 200$, (e, f) $Re = 205$, (g, h) $Re = 215$, and snapshots of the associated vorticity iso-contours.

Chapter 6. Nonlinear interaction of self-sustained instabilities in laminar swirling flows: Route to chaos

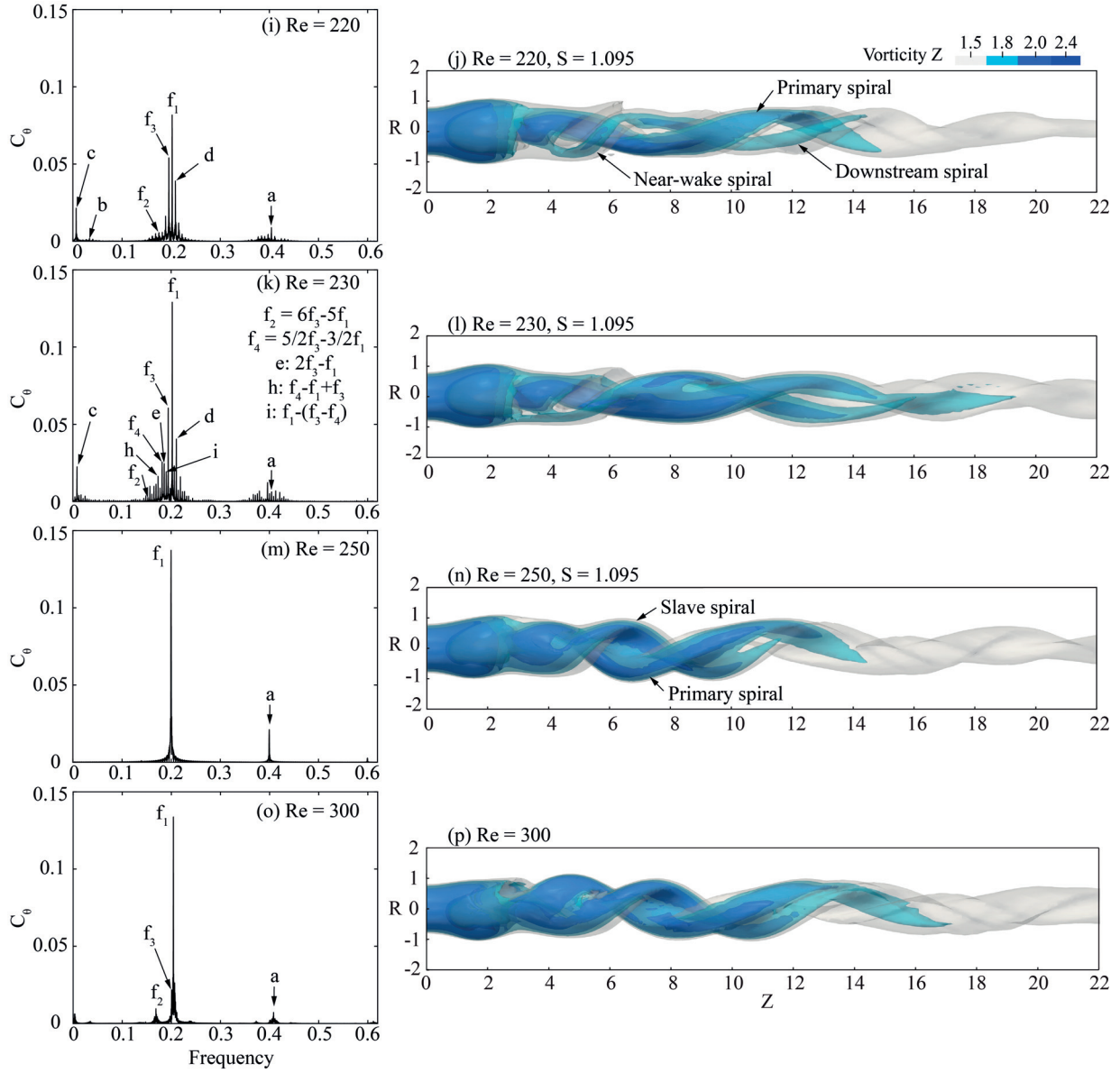


Figure 6.8 (Continued) – Fast Fourier transform of the velocity time series at $(R, \theta, Z) = (0.1, 0.0, 6.0)$ for a swirl number of $S = 1.095$ and Reynolds numbers, (i, j) $Re = 220$, (k, l) $Re = 230$, (m, n) $Re = 250$, (o, p) $Re = 300$, and snapshots of the associated vorticity iso-contours.

vortex cyclically. Movies for each value of bifurcation parameter investigated are available in the supplementary material.

Three successive Hopf bifurcations attracting the system towards a quasi-periodic regime on a torus T3 with three incommensurable frequencies can become unstable and lead to a chaotic regime. This scenario is a typical Ruelle-Takens-Newhouse route to chaos, which already appeared in several hydrodynamic examples (Gollub & Benson [153], Amon et al. [148], Wulf et al. [141], Egolf et al. [143] and Kashinath et al. [154], among others). In particular Oteski et al. [155] report this route to chaos including a stable three frequencies torus T3 in a confined two-dimensional differential convection case. In this scenario, the onset of the transition from a torus T3 to a strange attractor is not predictable (Eckmann [156]), only the computation of the first three maximum Lyapunov exponents can distinguish a stable from an unstable torus T3. The three largest Lyapunov exponents are equal to zero for a stable quasi-periodic T3 torus, which is in autonomous dissipative dynamical system (Grebogi et al. [157]), while a least one Lyapunov exponent must be positive for a chaotic state. In the present study, the Lyapunov exponents have not been computed due to the required computational time. However, the transition from the torus T3 observed at $Re = 205$, which appears to be stable in sight of its sensitivity to initial condition (fig. 6.6a), to the chaotic regime at $Re = 220$ is associated to the frequency migration of the downstream spiral to the primary spiral frequency, which emphasizes the nonlinear interactions.

The chaotic attractor turns into a torus T2 with two incommensurable frequencies for $Re = 230$ (fig. 6.8k), as seen in the attractor cross section (fig. 6.7f). This state is indeed made possible by the fact that the second frequency becomes a subharmonic of f_1 and f_3 by the relation: $f_2 = 6f_1 - 5f_3$. However to obtain the peak density observed in the Fourier amplitude spectrum, a fourth frequency appears as commensurable with the first and third frequencies $f_4 = 10f_3 - 6f_1$. The quasi-periodic regime is, therefore, due to the two incommensurable frequencies f_1 and f_3 , which govern the flow dynamics and drive the slaved modes of frequency f_2 and f_4 . In fig. 6.8(k), all the peaks of the Fourier amplitude spectrum are successfully identified by the use of these four frequencies, see appendix 6.9.2. A snapshot of axial vorticity contours corresponding to this amplitude Fourier spectrum is displayed in fig. 6.8(l). While several frequencies appear in this spectrum, we can only identify the vortical structures based on the result of the previous Reynolds number. The primary spiral has again the strongest vorticity and the near-wake spiral, in addition, attaches to the bubble crown and to the downstream spiral continuously at this time step.

The amplitude Fourier spectrum of the synchronization state observed at a Reynolds value of $Re = 250$ shows a well-defined peak f_1 and its associated harmonic $a = 2f_1$ (fig. 6.8m). The four frequencies observed in the quasi-periodic regime at $Re = 230$ are substituted for f_1 at $Re = 250$. The vorticity iso-contours, displayed in fig. 6.8(n), show not only a single spiral but two helical vortices. A primary spiral with a dense iso-contour of value 2.4, starting in the bubble wake, and a slaved spiral that has a modulated axial vorticity iso-contour of value 2.4. We can observe in fig. 6.8(n) that these two vortices are not in opposite phase but only slightly

Chapter 6. Nonlinear interaction of self-sustained instabilities in laminar swirling flows: Route to chaos

shifted. This indicates that this regime is not characterized by an $m = 2$ double helix, as one could have deduced at first sight from streaklines or iso-surfaces of vorticity, but rather by the co-existence of two $m = 1$ modes.

At $Re = 300$, the system turns into a chaotic regime identified by the dense attractor cross section (fig. 6.7h), the broad base of amplitude Fourier spectrum peaks and the identification of three incommensurable frequencies f_1 , f_2 and f_3 (fig. 6.8o). The flow patterns displayed in fig. 6.8(p), show two vortices similar to those observed at the previous Reynolds value, which are not in opposite phase but rather phase shifted.

6.7 Mode interactions

The nonlinear time series analysis characterizes the attractors of this autonomous dissipative dynamical system in a local monitoring point as the Reynolds number is increased. This local dynamics following from a stable attractor can change not only with the bifurcation parameter but also with the spatial coordinate along the dominant advection direction in open flows. In our system, where super-critical Hopf bifurcations are the starting point of new branches, local linear temporal stability analysis characterizes the stability properties of these branches but incorrectly predicts the frequency and the vortical structure associated to the new stable branch (Gallaire & Chomaz [72]). Since the dominant advection direction of the flow causes the failure of this prediction, it should be addressed by evaluating not only the growth in time but also in space of incoming fluctuations. This turns into the concept of spatio-temporal stability theory of Huerre & Monkewitz [44], which distinguishes the situation where advection dominates over growth and where instability waves are swept away while they grow (convective instability) from the one where growth dominates over advection and some instability waves withstand the advection and invade the entire domain (absolute instability). Convective instabilities are qualified as noise amplifiers and absolute instabilities are qualified as flow oscillators, which both are able to modify attractors along the advection direction. Typically Gallaire et al. [75] and Qadri et al. [80] identify two absolute regions in spiral vortex breakdown with two distinct frequencies, one frequency on the recirculation bubble and a second frequency in the bubble wake.

However, for strongly nonparallel flows, a so-called global stability analysis is preferably used, instead of a collection of velocity profiles at successive local streamwise stations. Globally unstable flows behave, therefore, as flow oscillators, while globally stable are best studied through the response to harmonic forcing. Therefore several globally unstable modes will act as coupled flow oscillators and their spatial core, sometimes called wavemaker, can induce different flow regimes along the streamwise direction, similar to a dynamical system subject to time-delay (Pimenov et al. [158]). Identifying the local frequencies observed in the amplitude Fourier spectrum as the consequence of global flow patterns is, therefore, essential to understand the system dynamical regimes. Since the present configuration consists of a semi-infinite unconfined domain, only purely hydrodynamic instabilities can generate

nonlinear dynamics. We, therefore, perform a global stability analysis to identify the unstable eigenmodes. This analysis is viewed as a predictive tool and it is then complemented by a double azimuthal-temporal Fourier series decomposition, which is viewed as an *a posteriori* analysis tool.

6.7.1 Stability analysis

A global stability analysis around the time-averaged flow is performed by solving the eigenvalue problem of eqn. (6.5). We have systematically compared the frequency prediction of the mean flow for azimuthal wave number $m = 0, 1, 2$ against the frequency of the DNS obtained by discrete Fourier transform of the time series. The results of this comparison are presented in fig. 6.9. The global stability analysis predicts successfully not only the primary spiral fre-

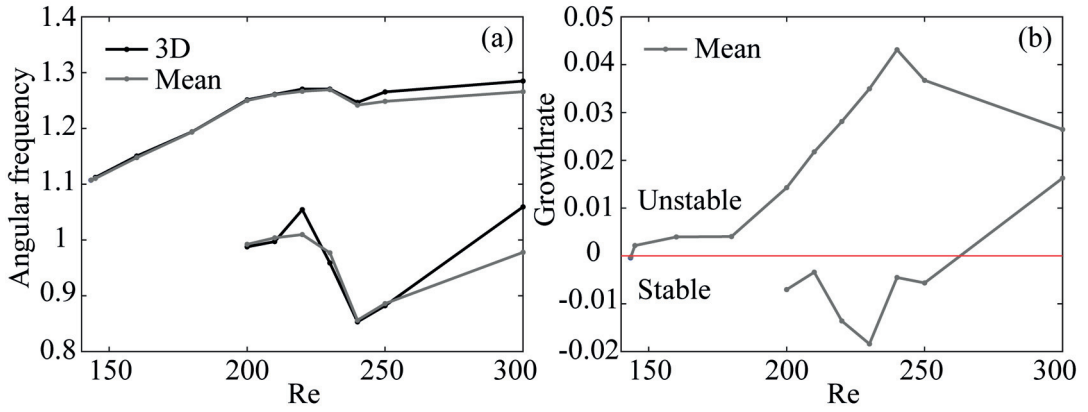


Figure 6.9 – Growth rate and angular frequency comparison of the 3D fft and the stability analysis for $m = 1$, eigemodes of azimuthal wavenumber ($m = 0, 2$) have no correlation with DNS frequencies.

quency (f_1) but also the frequency of the downstream spiral (fig. 6.9a), which is associated to the frequency f_2 in the amplitude Fourier spectrum of the time series (fig. 6.8). The growth rates of these eigenmodes displayed in fig. 6.9(b) show an unstable mode associated to the primary spiral as reported by Gallaire et al. [75], Meliga et al. [45] and Qadri et al. [80]. In contrast, the second eigenmode appears stable until a Reynolds value of $Re \approx 265$. In figure 6.9, only eigenmodes of azimuthal wavenumber $m = 1$ are represented for the following two reasons. First, the eigenmodes of azimuthal wavenumber $m = 2$ have no correlation with the first harmonic frequency of the amplitude Fourier spectrum (labeled a in fig. 6.8). Second, while two eigenmodes of the azimuthal wavenumber $m = 0$ could have the correct structure, their frequencies differ from those of the DNS (labeled c in fig. 6.8) and they have much larger damping rates when compared to the stable eigenmode of mode $m = 1$.

Axial velocity iso-contours of these two $m = 1$ eigenmodes are presented in fig. 6.10 at a Reynolds number of $Re = 200$, normalized with respect to the L_2 norm of the semi-inner product. The primary eigenmode (fig. 6.10a) shows two dissociated helices, a first helix

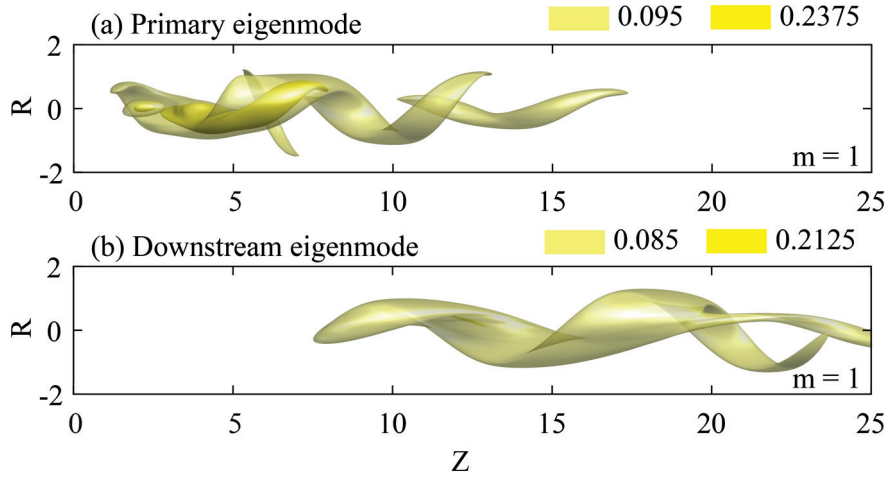


Figure 6.10 – Primary and downstream eigenmode axial velocity iso-contour at a Reynolds value of $Re = 200$.

at the beginning of the computational domain, which ends at $Z = 12$, and a second helix downstream centered at $Z = 14$. These helices contribute to the flow dynamics at the same frequency f_1 . The downstream eigenmode (fig. 6.10b) is centered at $Z = 15$ and forms a single helix precessing at the frequency f_2 located downstream of the primary eigenmode. These two eigenmodes appear associated respectively to the primary spiral and the downstream spiral of the DNS (fig. 6.8d) and as they overlap, strong nonlinear interactions are enabled.

Although the downstream spiral is found stable in the stability analysis, it finally develops and takes part in the dynamics of the system. This second eigenmode has the same azimuthal wavenumber as the first eigenmode and we can, therefore, expect an indirect excitation mechanism to be underpinning this development. Since only single helical eigenmodes are found unstable in the stability analysis, the system is governed by nonlinear interactions of single helical modes and the synchronization state observed at $Re = 250$ is also associated to the concordance of two single spirals. The chaotic attractor at $Re = 215$ and $Re = 220$, has a third incommensurable frequency that was not found associated to any of the available eigenmodes since their spatial locations and/or their frequency predictions could not be correlated with DNS results.

6.7.2 Temporal-azimuthal Fourier series cascade

The dynamics of the spiral vortex breakdown may be suitably described using a double temporal-azimuthal Fourier expansion. Because the description of the flow patterns appears as incomplete using global linear stability analysis, we perform indeed a temporal-azimuthal Fourier series decomposition of the DNS to further investigate the spatially developing modes. This decomposition is illustrated in fig. 6.11, and was performed for the selected Reynolds values $Re = [200, 220, 230, 250]$. The figure 6.11 displays the amplitude Fourier spectrum for

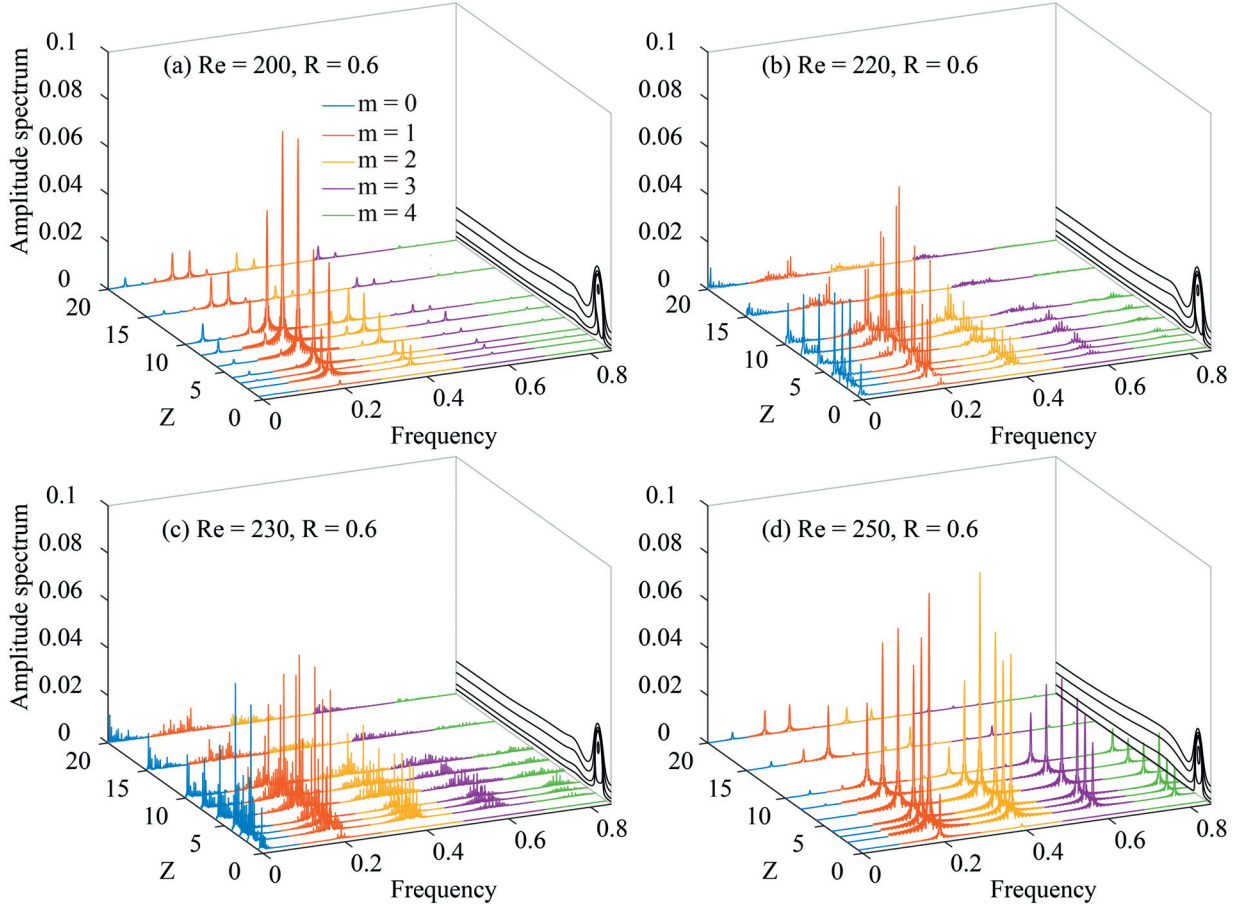


Figure 6.11 – Temporal-azimuthal Fourier decomposition of the DNS solutions for the Reynolds value $Re = 200$ (a), $Re = 220$ (b), $Re = 230$ (c) and $Re = 250$ (d). Amplitude Fourier spectrum for $R = 0.6$ along Z location ($Z = [0.6, 2, 3, 4, 6, 8, 10, 15, 20]$) with the fifth first azimuthal wavenumber m plotted in parallel with the streamlines of the time-average flow.

a radial value $R = 0.6$ along several Z stations for the five first azimuthal modes, plotted in parallel with the streamlines of the time-average flow to visualize the recirculation bubble position. The azimuthal modes are separated by frequency range, i.e. the low frequencies represent the azimuthal modes $m = 0$, the frequencies around $f \approx 0.2$ represent the azimuthal modes $m = 1$, the frequencies around $f \approx 0.4$ represent the azimuthal mode $m = 2$, etc.

In all the cases illustrated, a strong $m = 1$ oscillation of the recirculation bubble, in addition to the primary spiral precession, is observed until $Z = 10$. The amplitude of these $m = 1$ modes then suddenly drops until the end of the domain. This behavior can be correlated to the first and second helix appearing in the primary eigenmode (fig. 6.10a) where the intensity of the first helix is stronger than that of the second helix. As we will see later these two helices composing the primary spiral will be also observed for Reynolds number values of $Re = [220, 230, 250]$ (figs. 6.12, 6.13, 6.14 and 6.15).

Chapter 6. Nonlinear interaction of self-sustained instabilities in laminar swirling flows: Route to chaos

At $Re = 200$ (fig. 6.11a), the peaks associated to the primary spiral and the downstream spiral are well defined, f_1 and f_2 respectively. These two modes interact through the quadratic nonlinearity of the Navier-Stoke equations and produce an axisymmetric pulsation $m = 0$ (labeled b in fig. 6.8 and 6.8) as observed by Ruith et al. [57] at higher swirl number. This axisymmetric mode has its highest amplitude at $Z = 10$ where the first helix of the primary spiral and the downstream spiral overlap (fig. 6.10) and its starts at $Z = 3$ meaning that the downstream spiral impacts the system until the near-wake of the bubble. Moreover, the quasi-periodicity of the system encompasses the full streamwise length.

The chaotic attractor on which the system is folded at $Re = 220$ has three incommensurable frequencies displayed in fig. 6.11(b). The main $m = 1$ frequency represents the primary spiral while the downstream spiral associated to f_2 has a smaller amplitude than at $Re = 200$, although it remains present. In addition, the third incommensurable frequency f_3 , which corresponds to the closest peak of the frequency f_1 (fig. 6.8i), is mainly active in the same Z range as the primary spiral, i.e. between $Z = 0$ to $Z = 10$ and supports, therefore, the vortical structure development identified as the near-wake spiral in the DNS (fig. 6.2). The axisymmetric oscillation of the flow has a larger amplitude than at $Re = 200$ and its frequency corresponds to the difference of the primary and near-wake spiral frequency $c = f_1 - f_3$. Moreover, this chaotic regime is kept along an extended Z region, which can be viewed by dense attractor cross sections at different Z stations (not shown here).

At $Re = 230$, a quasi-periodic regime on a torus T2 shows several $m = 1$ frequencies but the dynamics is governed by the primary and the near-wake spirals f_1 and f_3 , as observed in fig. 6.8(k). We observe that the axisymmetric mode $m = 0$ has a comparable amplitude in the near-wake of the recirculation bubble than the azimuthal mode $m = 1$. This torus T2 starts to break down as we consider attractor cross sections progressing downstream because the downstream spiral starts to be more active in this region and, in addition, the amplitude of the primary spiral drops (not shown), while it is further upstream a sub-harmonic of f_1 and f_3 .

The synchronization regime at a Reynolds value of $Re = 250$ is made possible by the frequency match of the primary f_1 and near-wake f_3 spiral. This synchronization regime occurs only at Z stations upstream of $Z = 10$. The downstream spiral emerges downstream of $Z = 10$, which turns the torus T1 into a torus T2 (fig. 6.11d). In addition, the synchronized region has a first harmonic frequency $a \approx 0.4$ of amplitude comparable to that of the fundamental frequency f_1 , which suggests that its associated double helix super-harmonic mode can be involved in the nonlinear dynamics (fig. 6.8n).

6.7.3 Temporal-azimuthal Fourier series modes

The modes of the double temporal-azimuthal Fourier series decomposition, extracted using frequency selection, are displayed as axial velocity iso-contours to provide an overview of their structures in figs. 6.12, 6.13, 6.14 and 6.15. The juxtaposition of these structures with the cascade of amplitude Fourier spectra (fig. 6.11), the instability properties of the eigenmodes

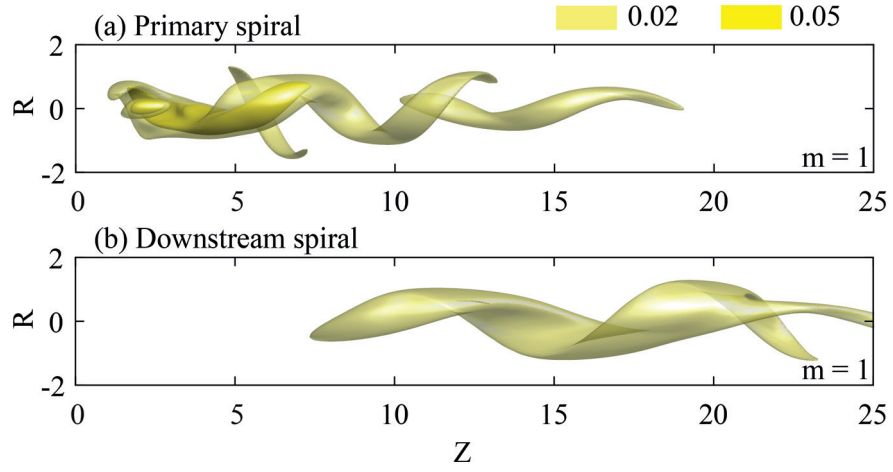


Figure 6.12 – Axial velocity iso-contour of temporal-azimuthal Fourier series modes at $Re = 200$, associated to the primary spiral at frequency f_1 (a) and the downstream spiral at frequency f_2 (b) at an arbitrary selected phase.

issuing from the global stability analysis (fig. 6.9) and the vortical structures identified in the DNS (fig. 6.8) enables the identification of the patterns, which contribute to the dynamics of this swirling flow. As previously demonstrated by the global stability analysis, the frequency f_1 and f_2 correspond to the primary and downstream spiral for all considered Reynolds values. Moreover, the axial velocity iso-contours of this Fourier series decomposition at a Reynolds value of $Re = 200$ (see fig. 6.12a and b) appear similar to the respective eigenmodes obtained by global linear stability analysis (fig. 6.10), while a different normalization is considered due to undefined magnitude of eigenmodes. The primary spiral has two single helices (fig. 6.12a), a first helix at the beginning of the computational domain and a second helix downstream. This first helix develops on the recirculation bubble and extends in its wake, which already emphasizes the oscillation of the bubble followed by a single spiral (see fig. 6.8d). The downstream spiral (fig. 6.12b) has only a single helix, which overlaps with both helices of the primary spiral.

The consistency of both methods at $Re = 200$ leads to investigate by Fourier series decomposition the third incommensurable frequency f_3 (the near-wake spiral), which turns the quasi-periodicity into a chaotic regime in the range of Reynolds values $Re = 215$ to $Re = 220$, while global stability analysis fails to identify this mode. Figure 6.13 displays the primary, downstream, near-wake spiral and the axisymmetric mode extracted respectively for the frequencies f_1 , f_2 , f_3 and c . The structure of the primary spiral is conserved, a first single helix developing on the recirculation bubble and extending in its wake as well as a second helix emerging downstream (fig. 6.13a). The downstream spiral, which has a smaller amplitude arises in the middle of the two helices of the primary spiral (fig. 6.13b). The near-wake spiral develops also on the recirculation bubble and its near-wake, and overlaps with both primary and downstream spirals (fig. 6.13c). The axisymmetric mode resulting from the nonlinear interactions of the primary, downstream and near-wake spirals, influences a large zone of the

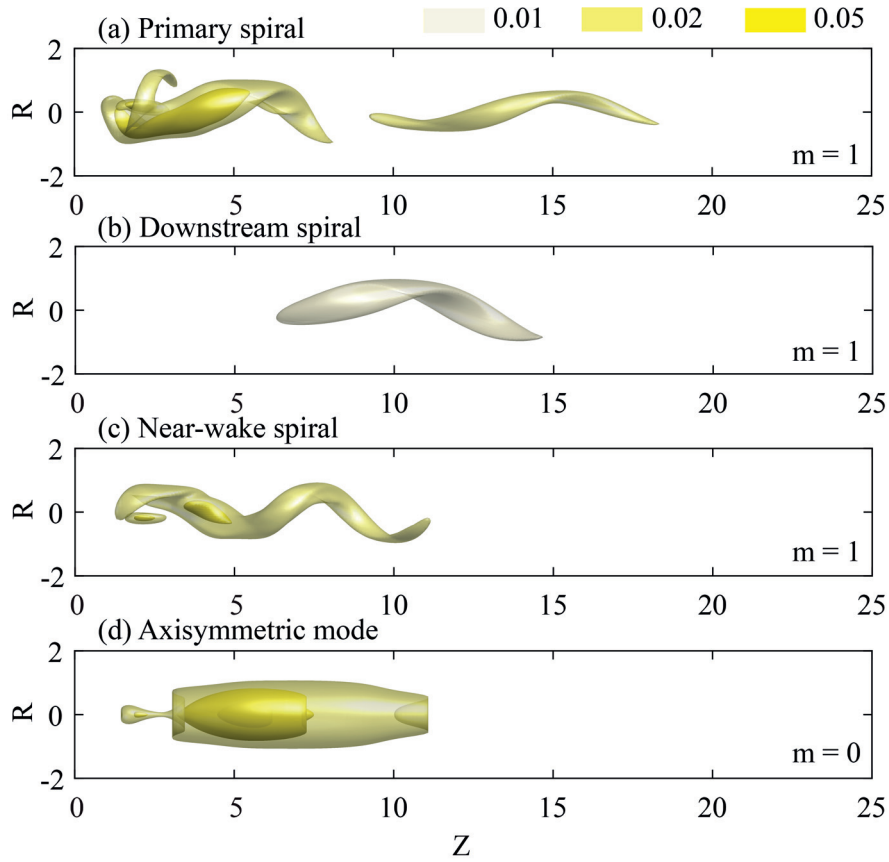


Figure 6.13 – Axial velocity iso-contour of temporal-azimuthal Fourier series modes at $Re = 220$, associated to the primary spiral at frequency f_1 (a), downstream spiral at frequency f_2 (b), near-wake spiral at frequency f_3 (c) and the axisymmetric pulsation at frequency c (d) at an arbitrary selected phase.

flow upstream of $Z = 11$ (fig. 6.13d).

At a Reynolds value of $Re = 230$, a T2 torus is observed (fig. 6.7f) and the Fourier modes associated to this quasi-periodic regime are displayed in fig. 6.14. The axial velocity iso-contours display the same patterns as for the previous Reynolds values. Two dissociated helices for the primary spiral (fig. 6.14a), a single downstream helix for the downstream spiral (fig. 6.14b) and a single helix in the near-wake of the recirculation bubble for the near-wake spiral (fig. 6.14c). In contrast, the axisymmetric mode (fig. 6.14d) is focused on the recirculation bubble, which suggests a better phase correlation of the different single helical modes diminishing nonlinear interactions and yielding, with the strategic repositioning of the frequencies, a torus T2.

The axial velocity iso-contours of the Fourier series decomposition for the synchronized regime at a Reynolds value of $Re = 250$, are displayed in fig. 6.15. The primary spiral (fig. 6.15a), which in this state embeds the near-wake spiral, shows a complex structure with

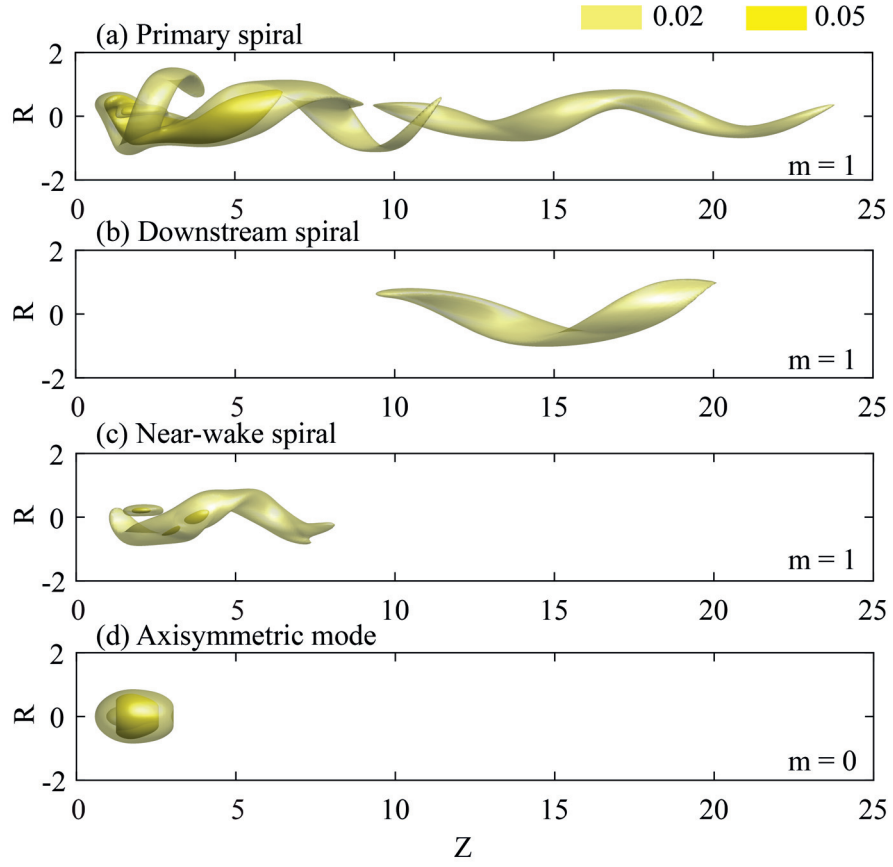


Figure 6.14 – Axial velocity iso-contour of temporal-azimuthal Fourier series modes at $Re = 230$, associated to the primary spiral at frequency f_1 (a), downstream spiral at frequency f_2 (b), near-wake spiral at frequency f_3 (c) and the axisymmetric pulsation at frequency c (d) at an arbitrary selected phase.

several single helices. The strongest helix at the beginning of the domain extends and overlaps with the second downstream helix, in contrast to $Re = 230$ and $Re = 220$ where these helices are spatially shifted. The downstream spiral migrates further downstream (fig. 6.15b), as observed in fig. 6.11(d), which is likely to result from the frequency synchronization regime at the beginning of the domain.

Since the first harmonic of the primary spiral (labeled *a*) has an amplitude comparable to that of the fundamental frequency f_1 in the cascade of amplitude Fourier spectra (fig. 6.11d), the mode associated to this harmonic, so-called double helix first harmonic, is displayed in fig. 6.15(c). This double spiral appears at the beginning of the domain and could, therefore, contribute to the nonlinear dynamics to form the two vortical structures observed in fig. 6.8(n).

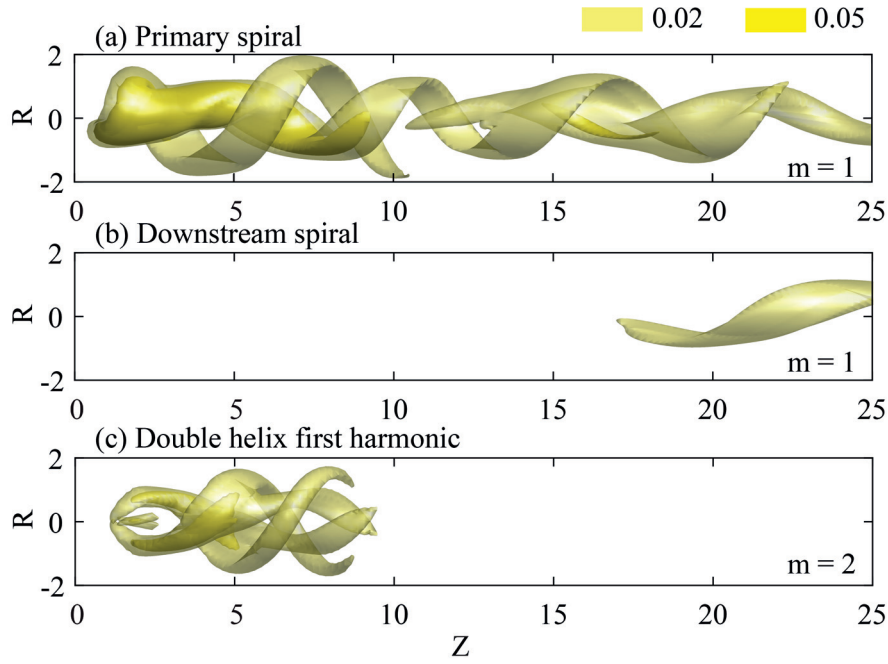


Figure 6.15 – Axial velocity iso-contour of temporal-azimuthal Fourier series modes at $Re = 250$, associated to the primary spiral at frequency f_1 (a), downstream spiral at frequency f_2 (b), double helix first harmonic (c) (labeled a in fig. 6.8m) at an arbitrary selected phase.

6.8 Conclusions

The nonlinear dynamics of the unconfined open swirling flow stemming from a Grabowski & Berger [78] vortex is studied for a fixed swirl number of $S = 1.095$ and a Reynolds number up to $Re = 300$. As the Reynolds number increases, this flow reveals a Ruelle-Takens-Newhouse route to chaos establishing a chaotic regime at a Reynolds value of $Re = 220$. A first supercritical Hopf bifurcation, leading to the spiral vortex breakdown (Ruith et al. [57] and Gallaire et al. [75]) is encountered at the instability threshold of $Re = 143.5$ (Meliga et al. [45] and Pasche et al. [10]), yielding the so-called primary spiral in the present study. A subsequent supercritical Hopf bifurcation turns the flow into a quasi-periodic regime on a torus T_2 at $Re = 200$ as shown by a global stability analysis around the base flow in Pasche et al. [10]. Then a quasi-periodic regime with three incommensurable frequencies is identified at a Reynolds value of $Re = 205$. Sensitivity to initial condition suggests that the present attractor is a stable torus T_3 , similar to Oteski et al. [155]. The interpretation of this regime as a stable torus T_3 is not in contradiction with the Ruelle-Takens-Newhouse route to chaos since the latter does not exclude such non chaotic states (Eckmann [156]).

Frequency identification based on amplitude Fourier spectra show that the first f_1 and third f_3 incommensurable frequency peaks become close to each other, while the second incommensurable frequency peaks f_2 remains at a lower frequency. As the Reynolds number is further increased, these three peaks become closer leading to a stronger axisymmetric mode at low

frequency (labeled c in fig. 6.8) generated by nonlinear interactions. Hence the potentially stable torus T3 observed at $Re = 205$ breaks down yielding a chaotic regime at Reynolds values from $Re = 215$ to $Re = 220$.

Since an unconfined geometry is considered, quasiperiodic or chaotic regime should be generated by nonlinear interactions of self-sustained instabilities. In fact, the first bifurcation of the flow associated to the spiral vortex breakdown is a hydrodynamic instability (Gallaire et al. [75], Meliga et al. [45] and Qadri et al. [80]). Local weakly non parallel stability analysis and global stability analysis around a fixed point solution successfully predict this instability threshold, while the prediction from the linearization around the base flow quickly fails to predict the limit cycle frequency as the Reynolds number is increased (Pasche et al. [10]). Global stability analysis around the mean flow, in contrast, successfully predicts the frequency of the spiral vortex breakdown and identifies two of the three incommensurable frequencies as single helical spiral of azimuthal wave number $m = 1$. The first frequency f_1 is an unstable eigenmode, the primary spiral, which has two spatial shifted single helices, a first helix on the recirculation bubble and in its near-wake, and a second downstream helix. The second frequency f_2 is associated to a linearly stable eigenmode, called the downstream spiral, which solely develops in the wake of the bubble. Hence an excitation mechanism induced by the advection of fluctuations should occur to lead the downstream spiral to develop its own oscillation.

In addition, the third incommensurable frequency f_3 , which is definitely needed to observe a chaotic regime, fails to be identified as an eigenmode from the global stability analysis. Moreover, axisymmetric $m = 0$ or double helical $m = 2$ modes cannot be associated to corresponding frequency or velocity distribution. A double temporal-azimuthal Fourier series decomposition is, therefore, performed and allows us to extract the flow pattern of these incommensurable frequencies and to corroborate also the previously identified eigenmodes. It appears that f_3 is a single helical mode developing in the near-wake of the recirculation bubble, which overlaps with the primary spiral. The successive emergence and the nonlinear interactions of the primary, downstream and near-wake single spirals, also observed as vortical structure in the DNS results, yields a Ruelle-Takens-Newhouse route to chaos.

A torus T2 with two incommensurable frequencies is observed at a larger Reynolds value of $Re = 230$, while three single spirals are identified at the previous Reynolds value of $Re = 220$. The following necessary frequency and mode reassortment is observed, the downstream spiral frequency becomes a sub-harmonic of those two incommensurable frequencies, and we identify, in addition, a fourth frequency as commensurable to the two driving frequencies. This attractor is ultimately characterized by two incommensurable frequencies, which are associated to the primary and near-wake spirals. The spatial location of these spirals appear, as a consequence, highly correlated to enable this torus T2, while at the chaotic regime $Re = 220$ these vortical structures are largely uncorrelated.

At a Reynolds value of $Re = 250$ a synchronized regime appears, formally identified in the

Chapter 6. Nonlinear interaction of self-sustained instabilities in laminar swirling flows: Route to chaos

frequency cascade of amplitude Fourier spectra. We could not determine if this results or originates from the migration of the downstream spiral associated to the frequency f_2 further downstream. Therefore a torus T1 is observed at the beginning of the domain by frequency synchronization of the primary and near-wake spiral, which turns into a torus T2 downstream of $Z = 10$. Vorticity iso-surfaces of the DNS results exhibits two spirals at $Re = 250$ (fig. 6.8n), which contrasts with the single peak of the amplitude Fourier spectrum (fig. 6.8m). We suggest that these nonlinear structures are a suitable phase and frequency combination of the two helices of the primary spiral and its double helical super-harmonic mode, associated to the frequency $a = 2f_1$. Actually, the amplitude of the first harmonic of the primary spiral a is comparable to that of its fundamental f_1 (see fig. 6.11d) and the double helix first harmonic overlaps with the first helix of the primary mode at the beginning of the domain (see fig. 6.15c). Although the double helix first harmonic appears to contribute to the flow dynamics, the origin of this synchronized state is the development of two single helical modes as demonstrated by the global stability analysis (see fig. 6.9), as for the other Reynolds values.

Finally, after this synchronization regime, the flow turns into a subsequent chaotic regime at $Re \approx 300$ with three incommensurable frequencies, which is suspected to definitely hold for larger Reynolds numbers, where the turbulence transition will be further exacerbated.

6.9 Appendix

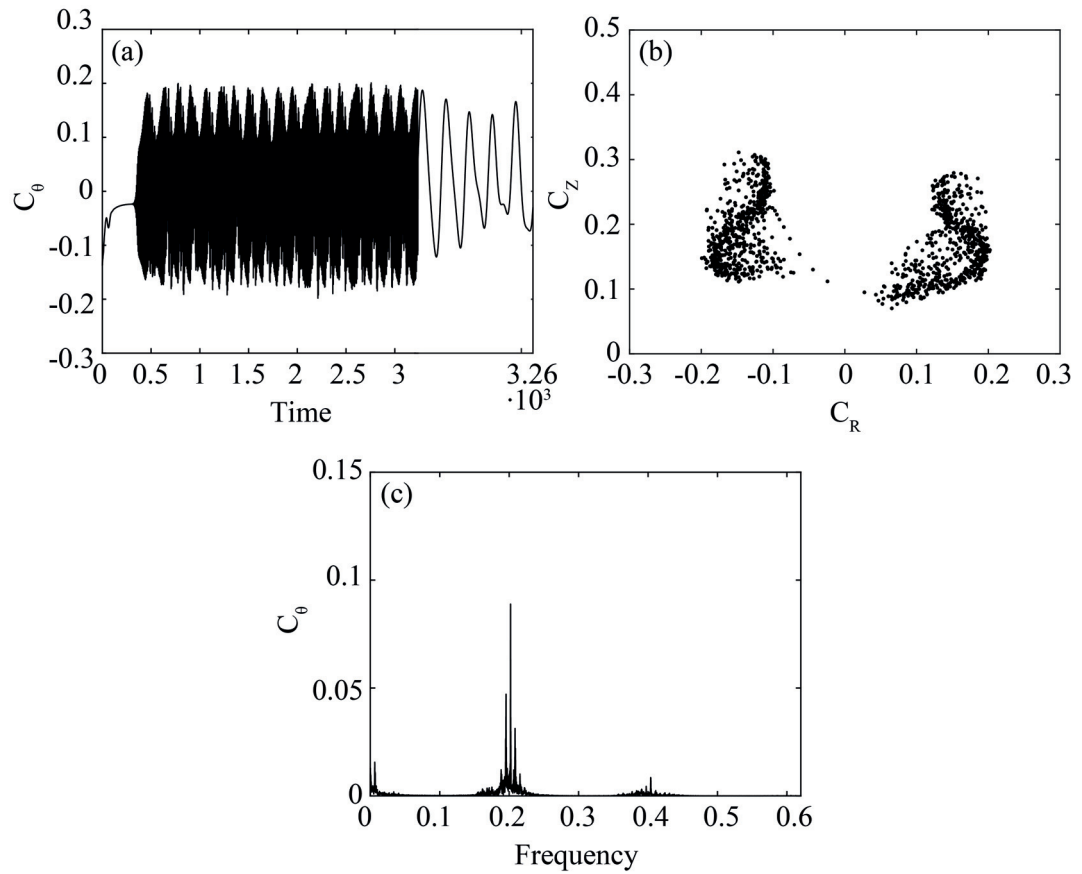
6.9.1 Validation of the 3D DNS

The 3D direct numerical flow simulations are validated by changing the mesh size, the mesh topology, the boundaries, the domain dimensions and the time step for a fixed swirl number $S = 1.095$ and Reynolds number $Re = 200$. The convergence criterion is based on the deviation of the frequency and the amplitude of the radial velocity component of the single helical vortex flow. These values are monitored at $(R, \theta, Z) = (0.1, 0.0, 6.0)$ which is located after the bubble, in the helix. The results of this convergence study is displayed on Table 6.2. The topology of the mesh is an O-grid type with two different cells arrangements in the center: diamonds cells that almost preserve the azimuthal symmetry of the problem and square cells. All cells have a P_{10} and P_8 spectral discretizations with a uniform number of nodes $n_x \times n_y \times n_z = 10 \times 10 \times 10$ and $n_x \times n_y \times n_z = 8 \times 8 \times 8$ for velocities and pressure respectively. The robustness of the solutions in front of the convective boundary condition on the outlet Γ_{out} is investigated by changing the length of the domain to $Z_{max} = 60$ for mesh M2 instead of $Z_{max} = 40$. The radial unconfinement is guaranteed by the invariance of the external boundary conditions. Two different types were investigated a free-stress boundary and a no-slip boundary, mesh M4. The CFL number invariance is investigated on mesh M5 and a refined mesh M3 concludes the convergence analysis. The mesh M1 is the reference mesh for this study.

The time series, the attractor cross section and the Fourier spectrum of the chaotic regime identified at a Reynolds value of $Re = 220$ are displayed in fig. 6.16 for the finer discretization

Case	Topology	BC on Γ_{ext}	L_z	L_r	n_e	CFL	3D (Amp,freq)	Eigenvalue
M1	Diamonds	Freestress	40	50	11040	0.37	(0.1299,0.1991)	(0.01427,1.25009)
M2	Diamonds	Freestress	60	50	16320	0.37	(0.1224,0.1991)	(0.01454,1.25193)
M3	Diamonds	Freestress	40	50	29696	0.44	(0.1284,0.1984)	(0.01475,1.25175)
M4	Squares	No slip	40	50	12512	0.34	(0.1231,0.1991)	-
M5	Diamonds	Freestress	40	50	11040	0.18	(0.1267,0.1991)	-

Table 6.2 – Convergence of the 3D numerical flow simulations and eigenvalues of mean flow

Figure 6.16 – Time series, attractor cross section and amplitude Fourier spectrum at the monitoring point $(R, \theta, Z) = (0.1, 0.0, 6.0)$ and at the Reynolds value of $Re = 220$ computed on the finer discretization M3.

M3. The irregular fluctuations of the time series is again observed for this computation.

6.9.2 Frequency validation

The frequency measured on the Fourier amplitude spectrum and the approximation based on the mean frequency are reported on Table 6.3. An excellent correspondence is observed. Note that the b frequency, resulting from the nonlinear interaction of the primary and the downstream spiral (respectively at f_1 and f_2) is not observed at this monitoring point for this Reynolds value.

Frequency	Measured	Approximation
f_1	0.202274	$0.202274 = f_1$
f_2	0.152683	$0.152492 = 6f_1 - 5f_3$
f_3	0.193977	$0.193977 = f_3$
f_4	0.181579	$0.181531 = 5/2f_3 - 3/2f_1$
a	0.40454	$0.40454 = 2f_1$
b	-	$0.049782 = f_1 - f_2$
c	0.008296	$0.008297 = f_1 - f_3$
d	0.210571	$0.210571 = 2f_1 - f_3$
e	0.185775	$0.18568 = 2f_3 - f_1$
h	0.173377	$0.173282 = f_4 - f_1 + f_3$
i	0.189876	$0.189876 = f_1 - (f_3 - f_4)$

Table 6.3 – Frequency interaction for $Re = 230$, $S = 1.095$ at $R = 0.2$, $Z = 6.0$ measured and approximated by the formulas using f_1 , f_2 , f_3 and f_4 .

7 Conclusions & Perspectives

7.1 Conclusions

The overarching objective of the present research work is the control of the cavitation vortex rope appearing in the draft tube of Francis turbines at part load operating conditions. This so-called part load vortex rope induces large pressure fluctuations, which restrict the operating range close to the best efficiency point of the turbine, while the extension of the operating range of Francis turbines is thought to be one of the main solutions to balance the electric consumption and the intermittent electric production arising from the foreseeable massive introduction of photovoltaic and wind energies in the electric distribution systems.

The control of the part load vortex rope is addressed using an optimal fluid flow control technique, based on the hydrodynamic instability properties of draft tube flow field. The main idea is to identify the part load vortex rope as a self-sustained instability, therefore caught by a global stability analysis, to define an objective function containing the growth rate of the most unstable eigenvalue as a target for a minimization algorithm. In this control strategy, the flow distribution is manipulated by an ideal volume force along the radial and axial components, which is expected to directly translate into an appendage or into a suitable actuation mechanism. This approach provides, therefore, a systematic and relevant tool to increase the operation flexibility of Francis turbines, by obtaining a quantifiable target about the vortex rope and by quenching the original nature of the vortex rope. However, first and foremost, the idealized uncluttered theoretical framework of fundamental research of hydrodynamic instability in laminar flows $Re = O(10^2)$ has to be transposed to include the inherent complexity of industrial design, embedding in particular turbulence modeling to reach high Reynolds number flows around $Re = O(10^6)$.

The control strategy adopted is first developed on an academic benchmark flow, the spiral vortex breakdown, to assess the feasibility and the validity of our approach. Global stability analyses around the base flow and the mean flow of the spiral vortex breakdown, issued from a semi-infinite domain, at a fixed swirl number $S = 1.095$ and Reynolds value up to $Re = 500$ are performed. The results confirm the correct frequency prediction of the mean flow stability

analysis obtained in recent swirling flows studies (Oberleithner et al. [49], Paredes et al. [50], Tammisola & Juniper [48]). The growth rate of the most unstable eigenvalue of the base and mean flow is then targeted by an adjoint-based minimization algorithm. The stabilization of these eigenvalues successfully quenches the self-sustained disturbance (the spiral vortex breakdown) close to the instability threshold $Re = 180$ and far away from it $Re = 300$. In addition, targeting the eigenvalue growth rate from the base or mean flow results in the same volume force and stabilized solution while a factor 10 exists between their growth rates at $Re = 180$. This result definitely emphasizes the physical significance and practical usefulness of mean flow stability analysis and related optimal control strategies, in situations where the eigenvalue growth rate of the mean flow is not neutral, in contrast to the case of the cylinder wake flow (Barkley [5] and Mantić-Lugo et al. [84]). The finite amplitude volume force results in a small variation of the flow solution with two active zones close to threshold ($Re = 180$), while further away from the threshold the optimal force completely changes the flow distribution by suppressing the flow recirculation bubble. Moreover, we underline the correct identification by the mean flow based linear sensitivity map of the minimum and maximum of the nonlinear receptivity regions, both close to the threshold $Re = 180$ and far away from it $Re = 300$. Linear sensitivity maps may therefore be sufficient to develop an appendage accessing these locations, although their validity cannot be ensured *a priori*.

The direct numerical flow simulations of the spiral vortex breakdown performed to compute the mean flow reveals the onset of chaos. A Ruelle-Takens-Newhouse route to chaos is identified with the successive onset of incommensurable frequencies as the Reynolds number increases. Chaos, which only appears in nonlinear dynamics with sufficient degrees of freedom, results in this unconfined configuration, from interactions of purely hydrodynamic self-sustained instabilities. Three incommensurable frequencies, as theoretically expected, are identified by spectral analysis of the chaotic regime, while the global stability analysis around the mean flow identifies only two out of them, an unstable eigenmode for the main incommensurable frequency, and a stable eigenmode for the second incommensurable frequency. The third incommensurable frequency is extracted by a temporal-azimuthal Fourier series decomposition of the unsteady flow distribution. We can question, therefore, the ability of the stability analysis around the mean flow to identify several unstable eigenmodes as well as the quantitative meaning of the obtained growth rates. In the present situation, we expect the transfer of energy from the unstable eigenmode to the stable eigenmode to occur by non-normality of the global linear evolution operator and to lead to the second incommensurable frequency.

With our success in addressing the optimal control of the spiral vortex breakdown, we turn our attention to the control of the part load vortex rope. In this industrial design, complexity reduction is a key feature to apply our minimization procedure. Instead of conducting an expensive full 3-D optimization, the main part of the algorithm is computed in a 2-D axisymmetric domain except for the mean flow obtained by successive time-averaging and azimuthal-averaging of the instantaneous 3-D flow field. This strategy is made possible thanks to the symmetry properties of the flow that can be caught by stability analysis using an az-

azimuthal Fourier decomposition of the disturbance and thanks to an auxiliary axisymmetric design of the draft tube, based on a discharge velocity conservation over the cross sections of the original elbow draft tube, which keeps the frequency and the flow distribution of the original vortex rope.

The global stability analysis of the part load vortex rope is addressed in this axisymmetric draft tube. This analysis requires the mean flow, which is computed on the fly during the URANS simulations of the draft tube flow field at $Re = O(10^6)$, and turbulence modeling, which is approximated by a diffusive term multiplied by the mean eddy viscosity extracted from the URANS simulations. The part load vortex rope is identified as a global unstable mode of azimuthal wave number $m = 1$ (single helical mode), whose frequency agrees well with the flow oscillations, and the eigenmode structure not only coils in space and spins in time rigorously identically as the vortex rope but also agrees well with the nonlinear disturbance distribution of the 3-D instantaneous vortex rope. In addition, the vortex rope captured as an instability in a "viscous framework" (in view of the large turbulent eddy viscosity) is found insensitive to different turbulence models used in the stability analysis (spatially varying eddy viscosity and constant eddy viscosity) and therefore suggests that the part load vortex rope is an inviscid instability. This global stability analysis exhibits the self-sustained character of the part load vortex rope, which is associated to a flow oscillator and comes from the emergence of an unstable disturbance out of the mean turbulent flow.

The linear framework offered by the global stability analysis of the part load vortex rope has allowed us to investigate the mechanism and the origin of the synchronous pressure fluctuations, a planar wave pulsating at the same frequency as the vortex rope, which can excite the hydraulic piping system eigenfrequency. This wave is only observed in elbow draft tube, we investigate it therefore in our axisymmetric draft tube by disturbing the draft tube wall through an eccentric displacement at selected circular sections. This disturbance defined as an azimuthal Fourier mode $m = 1$ is the key to separate the hydrodynamic mode from geometrical mode by azimuthal Fourier series decomposition of URANS flow solutions and to perform an asymptotic expansion around the mean turbulent flow to exhibit the generation mechanism of the synchronous wave. The part load vortex rope linear mode and the wall disturbance linear mode, obtained in our asymptotic expansion, interact and produce an axisymmetric pulsating force at the next order composed of their intercrossed Reynolds stresses, exciting therefore the synchronous wave at the frequency of the vortex rope. In our case the source is located on the wall disturbance but it is followed by an amplification mechanism in the axisymmetric elbow.

The mitigation of the pressure fluctuations in Francis turbines by minimizing the growth rate of the eigenvalue associated to the part load vortex rope is successfully addressed using the same adjoint-based minimization algorithm as for the spiral vortex breakdown. The growth rate during the minimization procedure decreases slowly until it suddenly drops at the ultimate iteration to therefore result in the stabilization of the part load vortex rope. This evolution contrasts with the case of the spiral vortex breakdown where the growth rate

decreases smoothly to zero. Our algorithm successfully stabilizes the part load vortex rope by pushing the fluid downstream in the draft tube center line starting after the recirculation region of the mean flow and sketches the design of a realistic control appendage. This result brings a promising solution to control the part load vortex rope by a volume force to increase the operation flexibility of Francis turbines. Moreover, the mean turbulent flow based sensitivity maps correctly identify the nonlinear receptivity region of the part load vortex rope. It may therefore appear sufficient to use the linear sensitivity maps to locate the receptivity region of the flow to design passive control appendage. An estimation of the control amplitude based on the linear sensitivity maps is however difficult to assess without computing 3-D solutions.

7.2 Perspectives

This research work investigates first the development of infinitesimal disturbance in swirling flows in a laminar regime with the spiral vortex breakdown and in a turbulent regime with the part load vortex rope, second the optimal control of self-sustained instability in both regimes, and third nonlinear fluid-fluid and fluid-solid interactions.

While the control of self-sustained instabilities is successfully performed by minimizing the growth rate of the most unstable eigenvalue of the mean flow, the physical significance of this growth rate still needs to be determined. We believe that it is, more than the measure of the exponential growth of the disturbance, merely also a measure of the variance between the linear and nonlinear modes.

Chaotic dynamics occurring from nonlinear interactions of self-sustained instabilities is observed in the spiral vortex breakdown. Global stability analysis on the mean flow results in the identification of two out of the three incommensurable frequencies observed in the direct numerical flow simulation. The question naturally arises if linear stability analysis is able to predict the growth rate of multiple self-sustained instabilities, while it correctly predicts the instability properties of a single self-sustained mode in many situations. We may also speculate how a chaotic state can be reached without having three self-sustained instabilities corresponding to three incommensurable frequencies.

The origin of the synchronous wave is investigated in the axisymmetric draft tube of a Francis turbine in the small deformation limit. The transposition to large wall deformation such as the elbow draft tube needs to be further investigated to obtain the real fluctuating pressure source location. One major difficulty to assess this location is to perform azimuthal Fourier series decomposition in evolving section shapes along the draft tube curvilinear axis, ranging from a circular to a rectangular via an oval section.

As far as flow control is concerned, the optimal volume forces obtained in the case of the two swirling flow investigated act along the axis center line. An important perspective is therefore to materialize this volume force by carrying out a shape optimization. This point is made difficult by the need to take into account the turbulence boundary layer on the control device.

We propose instead to design an appendage at the tip of the runner cone that will access the starting point of the distributed force on the axis and will accelerate the flow in the draft tube center line using either a convergent nozzle repatriating lateral mass flow or water jets from a conical appendage, or both simultaneously.

We have observed that the part load vortex rope is generated by its linear dynamics, which has enabled the correct identification of the nonlinear receptivity region of draft tube flow field by the linear sensitivity maps. Therefore these linear maps may appear sufficient to locate the receptivity region of the flow to design passive control appendage but caution should be exercised because the generality of this result is not guaranteed.

Bibliography

- [1] H. Häckert, *Wasserkraftmaschinen und Wasserkraftanlagen*. K.F. Koehler verlag Stuttgart, 1949.
- [2] J. Franck, F. Avellan, B. Belhadji, J. Billard, L. Briancon-Marjolet, D. Fréchou, D. Fruman, A. Karimi, J. Kueny, and J. Michel, *La Cavitation: Mécanismes Physiques et Aspects Industriels*. Collection Grenoble Sciences. Presse Universitaires de Grenoble, 1995.
- [3] M. V. Dyke, *An Album of Fluid Motion*. Stanford: The Parabolic Press, 1988.
- [4] F. Charru, *Hydrodynamic Instabilities*. Cambridge University Press, 2011.
- [5] D. Barkley, “Linear analysis of the cylinder wake mean flow,” *Europhysics Letters*, vol. 75, no. 5, p. 750, 2006.
- [6] O. Marquet, D. Sipp, and L. Jacquin, “Sensitivity analysis and passive control of cylinder flow,” *Journal of Fluid Mechanics*, vol. 615, pp. 221–252, 2008.
- [7] P. J. Strykowski and K. R. Sreenivasan, “On the formation and suppression of vortex ‘shedding’ at low reynolds numbers,” *Journal of Fluid Mechanics*, vol. 218, pp. 71—107, 1990.
- [8] J. Arpe and F. Avellan, “Pressure wall measurements in the whole draft tube: Steady and unsteady analysis,” in *Proceedings of the 21st IAHR Symposium on Hydraulic Machinery and Systems, Lausanne, Switzerland*, 2002.
- [9] G. Ciocan, M. Iliescu, T. Vu, B. Nenneman, and F. Avellan, “Experimental study and numerical simulation of the FLINDT draft tube rotating vortex,” *Journal of Fluids Engineering*, vol. 129, pp. 146–158, 2007.
- [10] S. Pasche, F. Gallaire, and F. Avellan, “Predictive control of spiral vortex breakdown,” *Manuscript submitted for publication*, 2017.
- [11] M. Nishi, T. Kubota, S. Matsunaga, and Y. Senoo, “Study on swirl flow and surge in an elbow type draft tube,” in *Proceedings, 10th IAHR Symposium, Tokyo, Japan*, 1980.
- [12] M. Nishi, T. Kubota, S. Matsunaga, and Y. Senoo, “Flow regimes in elbow type draft tube,” in *Proceedings, 11th Symposium of the International Association for Hydraulic*

Bibliography

- Research Section for Hydraulic Machinery Equipment and Cavitation, Amsterdam, the Netherlands*, 1982.
- [13] M. Nishi, S. Matsunaga, T. Kubota, and A. Senoo, "Surging characteristics of conical and elbow-type draft tubes," in *Proceedings of the 12th IAHR Symposium on Hydraulic Machinery and System, Stirling, Scotland*, 1984.
- [14] M. Nishi and S. Liu, "an outlook on the darft-tube-surge study," *International Journal of Fluid Machinery and Systems*, vol. 6, no. 1, pp. 33–48, 2013.
- [15] F. Avellan, "Flow investigation in a Francis draft tube: The FLINDT project," in *Proceedings of the 20th IAHR Symposium on Hydraulic Machinery and Systems, Charlotte, USA*, 2000.
- [16] M. Iliescu, G. Ciocan, and F. Avellan, "Analysis of the cavitating draft tube vortex in a Francis turbine using particule image velocimetry measurements in two phase flow," *Journal of Fluids Engineering*, vol. 130, pp. 021105 1–10, 2008.
- [17] A. Favrel, A. Müller, C. Landry, K. Yamamoto, and F. Avellan, "Study of the vortex-induced pressure excitation source in a Francis turbine draft tube by particle image velocimetry," *Experiments in Fluids*, vol. 56:215, 2015.
- [18] A. Ruprecht, T. Helmrich, T. Aschenbrenner, and T. Scheber, "Simulation of vortex rope in a turbine draft tube," in *Proceedings of the 21th IAHR Symposium on Hydraulic Machinery and Systems, Lausanne, Switzerland*, 2002.
- [19] S. Mauri, J. Kueny, and F. Avellan, "Werlé-Legendre separation in a hydraulic machine draft tube," *Journal of Fluids Engineering*, vol. 126, pp. 976–980, 2004.
- [20] J. Paik, F. Sotiropoulos, and M. J. Sale, "Numerical simulation of swirling flow in complex hydroturbine draft tube using unsteady statistical turbulence models," *Journal of Hydraulic Engineering*, vol. 131, no. 6, pp. 441–456, 2005.
- [21] O. Buntić, S. Dietze, and A. Ruprecht, "Numerical simulation of the flow in turbine-99 draft tube," in *Proceedings, 3rd IAHR/ERCOFTAG workshop on draft tube flow, Porjus, Sweden*, 2005.
- [22] Z. Wang and L. Zhou, "Simulations and measurements of pressure oscillations caused by vortex ropes," *Journal of Fluids Engineering*, vol. 128, no. 4, pp. 649–655, 2006.
- [23] C. Trivedi, C. M. J., and O. G. Dahlhaug, "Numerical techniques applied to hydraulic turbines: a perspective review," *Applied Mechanics Reviews*, vol. 68, no. 1, p. 010802, 2016.
- [24] J. Brammer, C. Segoufin, F. Duparchy, P. Lowys, A. Favrel, and F. Avellan, "Unsteady hydraulic simulation of the cavitating part load vortex rope in Francis turbines," in *IOP Conference Series: Earth and Environmental Science*, 813,1, 2017.

-
- [25] M. Nishi, X. M. Wang, K. Yoshida, T. Takahashi, and T. Tsukamoto, *An Experimental Study on Fins, Their Role in Control of the Draft Tube Surging*, pp. 905–914. Dordrecht: Springer Netherlands, 1996.
- [26] J. Kurokawa, I. Junichi, and C. Young-Do, “Effect of j-groove on the suppression of swirl flow in a conical diffuser,” *Journal of Fluids Engineering*, vol. 132, no. 7, p. 071101, 2010.
- [27] H. Brekke, “A review of some dynamic problems in hydropower plants,” in *Proc. 11th int. Meeting of IAHR Work Group on the Behaviours of Hydraulic Machinery under Steady Oscillatory Conditions, Stuttgart, Germany*, 2003.
- [28] Z. D. Qian, W. Li, W. X. Huai, and Y. L. Wu, “The effect of runner cone design on pressure oscillation characteristics in a Francis hydraulic turbine,” *Proceedings of the Institution of Mechanical Engineers, Part A: Journal of Power and Energy*, vol. 226, no. 1, pp. 137–150, 2012.
- [29] R. Susan-Resiga, T. C. Vu, S. Muntean, G. D. Ciocan, and B. Nennemann, “Jet control of the draft tube vortex rope in Francis turbines at partial discharge,” in *Proceedings of the 23th IAHR Symposium on Hydraulic Machinery and Systems, Yokohama, Japan*, 2006.
- [30] R. Zhang, F. Mao, J.-Z. Wu, S.-Y. Chen, Y.-L. Wu, and S.-H. Liu, “Characteristics and control of the draft-tube flow in part-load Francis turbine,” *Journal of Fluids Engineering*, vol. 131, no. 2, 2009.
- [31] H. Foroutan and S. Yavuzkurt, “Flow in the simplified draft tube of a Francis turbine operating at partial load—part I: Simulation of the vortex rope,” *Journal of Applied Mechanics*, vol. 81, no. 6, 2014.
- [32] G. Blommaert, J.-E. Prenat, F. Avellan, and A. Boyer, “Active control of Francis turbine operation stability,” in *Proceedings, 3rd ASME/JSME Joint FLuids Engineering Conference, San Francisco, California, USA*, 1999.
- [33] C. Landry, A. Favrel, A. Muller, C. Nicolet, K. Yamamoto, and F. Avellan, “Experimental investigation of the local wave speed in a draft tube with cavitation vortex rope,” in *IOP Conference Series: Earth and Environmental Science*, 22, 2014.
- [34] C. Nicolet, *Hydroacoustic modelling and numerical simulation of unsteady operation of hydroelectric systems*. PhD thesis, EPFL, 2007.
- [35] S. Alligné, C. Nicolet, Y. Tsujimoto, and F. Avellan, “Cavitation surge modelling in Francis turbine draft tube,” *Journal of Hydraulic Research*, vol. 52, no. 3, pp. 399–411, 2014.
- [36] C. Landry, *Hydroacoustic modeling of a cavitation vortex rope for a Francis turbine*. PhD thesis, EPFL, 2015.
- [37] W. Zielke and H. Hack, “Resonance frequencies and associated mode shapes of pressurized pipinf systems,” in *Proceedings of the international Conference Pressure Surges, Cranfield, UK, G1:1-13*, 1972.

Bibliography

- [38] M. Fanelli, “The vortex rope in the draft tube of Francis turbines operating at partial load: a proposal for a mathematical model,” in *IAHR W.G., Fort Collins*, 1989.
- [39] A. Gupta, D. Lilley, and N. Syred, *Swirl flows*. Abacus Press, 1986.
- [40] P. Schmid, “Nonmodal stability theory,” *Annual Review of Fluid Mechanics*, vol. 39, no. 1, pp. 129–162, 2007.
- [41] J. Chomaz, “Global instabilities in spatially developing flows: Non-normality and non-linearity,” *Annual Review of Fluid Mechanics*, vol. 37, no. 1, pp. 357–392, 2005.
- [42] L. Trefethen, A. Trefethen, S. Reddy, and T. Driscoll, “Hydrodynamic stability without eigenvalues,” *Science*, vol. 261, pp. 578–584, 1993.
- [43] A. Bers, “Linear waves and instabilities,” *Physique des Plasmas*, vol. 6, pp. 113–215, 1972.
- [44] P. Huerre and P. Monkewitz, “Local and global instabilities in spatially developing flows,” *Annual Review of Fluid Mechanics*, vol. 22, pp. 476–537, 1990.
- [45] P. Meliga, F. Gallaire, and J.-M. Chomaz, “A weakly nonlinear mechanism for mode selection in swirling jets,” *Journal of Fluid Mechanics*, vol. 699, pp. 216–262, 2012.
- [46] V. Theofilis, “Global linear instability,” *Annual Review of Fluid Mechanics*, vol. 43, pp. 319–352, 2011.
- [47] P. Meliga, G. Pujals, and E. Serre, “Sensitivity of 2-D turbulent flow past a D-shaped cylinder using global stability,” *Physics of Fluids*, vol. 24, no. 6, p. 061701, 2012.
- [48] O. Tammisola and M. P. Juniper, “Coherent structures in a swirl injector at $Re = 4800$ by nonlinear simulations and linear global modes,” *Journal of Fluid Mechanics*, vol. 792, p. 620–657, 2016.
- [49] K. Oberleithner, M. Stöhr, S. H. Im, C. M. Arndt, and A. M. Steinberg, “Formation and flame-induced suppression of the precessing vortex core in a swirl combustor: Experiments and linear stability analysis,” *Combustion and Flame*, vol. 162, no. 8, pp. 3100–3114, 2015.
- [50] P. Paredes, S. Terhaar, K. Oberleithner, V. Theofilis, and C. Passchereit, “Global and local hydrodynamic stability analysis as a tool for combustor dynamics modeling,” *Journal of Engineering for Gas Turbines and Power*, vol. 138, no. 2, pp. 021504–7, 2015.
- [51] T. Grimble, A. Agarwal, and M. Juniper, “Local linear stability analysis of cyclone separators,” *Journal of Fluid Mechanics*, vol. 816, p. 507–538, 2017.
- [52] S. Camarri, “Flow control design inspired by linear stability analysis,” *Acta Mechanica*, vol. 226, pp. 979–1010, 2015.

-
- [53] H. Kim and K. Chang, "Numerical study on vortex shedding from a circular cylinder influenced by a nearby control wire," *Computational Fluid Dynamics Journal*, vol. 4, pp. 151–164, 1995.
- [54] S. Mittal and A. Raghuvanshi, "Control of vortex shedding behind circular cylinder for flows at low reynolds numbers," *International Journal for Numerical Methods in Fluids*, vol. 35, pp. 421–447, 2001.
- [55] F. Giannetti and P. Luchini, "Structural sensitivity of the first instability of the cylinder wake," *Journal of Fluid Mechanics*, vol. 581, pp. 167–197, 2007.
- [56] V. Parezanović and O. Cadot, "Experimental sensitivity analysis of the global properties of a two-dimensional turbulent wake," *Journal of Fluid Mechanics*, vol. 693, p. 115–149, 2012.
- [57] M. R. Ruith, P. Chen, E. Meiburg, and T. Maxworthy, "Three-dimensional vortex breakdown in swirling jets and wakes: direct numerical simulation," *Journal of Fluid Mechanics*, vol. 486, pp. 331–378, 2003.
- [58] N. C. Lambourne and D. W. Bryer, "The bursting of leading-edge vortices - some observations and discussion of the phenomenon.," *Aeronautical Research Council*, vol. 3292, pp. 1–35, 1962.
- [59] M. G. Hall, "Vortex breakdown.," *Annual Review of Fluid Mechanics*, vol. 4, pp. 195–218, 1972.
- [60] S. Leibovich, "The structure of the vortex breakdown.," *Annual Review of Fluid Mechanics*, vol. 10, pp. 221–246, 1978.
- [61] M. P. Escudier and N. Zehnder, "Vortex-flow regimes.," *Journal of Fluid Mechanics*, vol. 115, pp. 105–121, 1982.
- [62] T. Sarpkaya, "On stationary and travelling vortex breakdowns.," *Journal of Fluid Mechanics*, vol. 45, no. 3, pp. 545–559, 1971.
- [63] C. European, "European policy: Climate strategies and targets," 2017.
- [64] R. Susan-Resiga, S. Muntean, V. Hasmatuchi, I. Anton, and F. Avellan, "Analysis and prevention of vortex breakdown in the simplified discharge cone of a Francis turbine," *Journal of Fluids Engineering*, vol. 132, 2010.
- [65] S. Pasche, F. Avellan, and F. Gallaire, "Part load vortex rope as a global unstable mode," *Journal of Fluids Engineering*, vol. 139, no. 5, p. 051102, 2017.
- [66] I. Gursul, Z. Wang, and E. Vardaki, "Review of flow control mechanisms of leading-edge vortices," *Progress in Aerospace Sciences*, vol. 43, no. 7, pp. 246 – 270, 2007.

Bibliography

- [67] C. Paschereit, P. Flohr, and E. Gutmark, "Combustion control by vortex breakdown stabilization," *Journal of Turbomachinery*, vol. 128, pp. 679–688, 2002.
- [68] N. Syred, "A review of oscillation mechanisms and the role of the precessing vortex core (pvc) in swirl combustion systems," *Progress in Energy and Combustion Science*, vol. 32, no. 2, pp. 93 – 161, 2006.
- [69] H. Squire, *Analysis of the Vortex Breakdown Phenomenon*. Imperial College of Science and Technology , Aeronautics Department, 1960.
- [70] T. B. Benjamin, "Theory of the vortex breakdown phenomenon," *Journal of Fluid Mechanics*, vol. 14, no. 4, pp. 593—629, 1962.
- [71] S. Wang and Z. Rusak, "The dynamics of a swirling flow in a pipe and transition to axisymmetric vortex breakdown," *Journal of Fluid Mechanics*, vol. 340, pp. 177—223, 1997.
- [72] F. Gallaire and J.-C. Chomaz, "Mode selection in swirling jet experiments: a linear stability analysis," *Journal of Fluid Mechanics*, vol. 494, pp. 223—253, 2003.
- [73] S. Leibovich and K. Stewartson, "A sufficient condition for the instability of columnar vortices," *Journal of Fluid Mechanics*, vol. 126, pp. 335—356, 1983.
- [74] I. Delbende, J.-C. Chomaz, and P. Huerre, "Absolute/convective instabilities in the batchelor vortex: a numerical study of the linear impulse response," *Journal of Fluid Mechanics*, vol. 355, pp. 229—254, 1998.
- [75] F. Gallaire, M. Ruith, E. Meiburg, J.-M. Chomaz, and P. Huerre, "Spiral vortex breakdown as a global mode.," *Journal of Fluid Mechanics*, vol. 549, pp. 71–80, 2006.
- [76] R. E. Spall, T. B. Gatski, and R. L. Ash, "The structure and dynamics of bubble-type vortex breakdown," *Proceedings of the Royal Society of London A: Mathematical, Physical and Engineering Sciences*, vol. 429, no. 1877, pp. 613–637, 1990.
- [77] W. Althaus, E. Krause, J. Hofhaus, and M. Weimer, "Vortex breakdown: Transition between bubble- and spiral-type breakdown.," *Meccanica*, vol. 29, no. 4, pp. 373–382, 1994.
- [78] W. J. Grabowski and S. A. Berger, "Solutions of the navier-stokes equations for vortex breakdown.," *Journal of Fluid Mechanics*, vol. 75, no. 3, pp. 525–544, 1976.
- [79] E. Vyazmina, J. W. Nichols, J.-M. Chomaz, and P. J. Schmid, "The bifurcation structure of viscous steady axisymmetric vortex breakdown with open lateral boundaries.," *Physics of Fluids*, vol. 21, no. 7, p. 074107, 2009.
- [80] U. A. Qadri, D. Mistry, and M. P. Juniper, "Structural sensitivity of spiral vortex breakdown," *Journal of Fluid Mechanics*, vol. 720, pp. 558–581, 2013.

-
- [81] Z. Rusak, J. Granata, and S. Wang, "An active feedback flow control theory of the axisymmetric vortex breakdown process.," *Journal of Fluid Mechanics*, vol. 774, pp. 488–528, 2015.
- [82] A. Maurel, V. Pagneux, and J. E. Wesfreid, "Mean-flow correction as non-linear saturation mechanism," *Europhysics Letters*, vol. 32, no. 3, p. 217, 1995.
- [83] D. Sipp and A. Lebedev, "Global stability of base and mean flows: a general approach and its applications to cylinder and open cavity flows," *Journal of Fluid Mechanics*, vol. 593, pp. 333–358, 2007.
- [84] V. Mantić-Lugo, C. Arratia, and F. Gallaire, "Self-consistent mean flow description of the nonlinear saturation of the vortex shedding in the cylinder wake," *Physical Review Letters*, vol. 113, p. 084501, Aug 2014.
- [85] J. Kim and T. R. Bewley, "A linear systems approach to flow control," *Annual Review of Fluid Mechanics*, vol. 39, pp. 383–417, 2007.
- [86] J. L. Lions, *Optimal control of systems governed by partial differential equations*. Springer-Verlag Berlin Heidelberg, 1971.
- [87] R. Joslin, M. Gunzburger, R. Nicolaides, G. Erlebacher, and M. Hussaini, "Self-contained automated methodology for optimal flow control," *AIAA Journal*, vol. 35, no. 5, pp. 816–824, 1997.
- [88] T. R. Bewley, P. Moin, and R. Temam, "DNS-based predictive control of turbulence: an optimal benchmark for feedback algorithms," *Journal of Fluid Mechanics*, vol. 447, pp. 179–225, 2001.
- [89] P.-Y. Passaggia and U. Ehrenstein, "Adjoint based optimization and control of a separated boundary-layer flow," *European Journal of Mechanics - B/Fluids*, vol. 41, pp. 169 – 177, 2013.
- [90] J. P. Goit and J. Meyers, "Optimal control of energy extraction in wind-farm boundary layers," *Journal of Fluid Mechanics*, vol. 768, pp. 5–50, 2015.
- [91] T. R. Bewley and S. Liu, "Optimal and robust control and estimation of linear paths to transition," *Journal of Fluid Mechanics*, vol. 365, pp. 305–349, 1998.
- [92] M. D. Gunzburger, "Sensitivities, adjoints and flow optimization," *International Journal for Numerical Methods in Fluids*, vol. 31, no. 1, pp. 53–78, 1999.
- [93] P. Luchini and A. Bottaro, "Adjoint equations in stability analysis.," *Annual Review of Fluid Mechanics*, vol. 46, pp. 493–517, 2014.
- [94] S. Camarri and A. Iollo, "Feedback control of the vortex-shedding instability based on sensitivity analysis," *Physics of Fluids*, vol. 22, no. 094102, 2010.

Bibliography

- [95] C. Mettot, D. Sipp, and H. Bézard, “Quasi-laminar stability and sensitivity analyses for turbulent flows prediction of low-frequency unsteadiness and passive control,” *Physics of Fluids*, vol. 26, no. 4, p. 045112, 2014.
- [96] M. Carini, C. Airiau, A. Debien, and J. Pralits, “Global stability and control of the confined turbulent flow past a thick flat plate,” *Physics of Fluids*, vol. 29, no. 2, 2017.
- [97] F. Gallaire, J.-C. Chomaz, and P. Huerre, “Closed-loop control of vortex breakdown: a model study,” *Journal of Fluid Mechanics*, vol. 511, pp. 67–93, 2004.
- [98] P. Meliga and F. Gallaire, “Control of axisymmetric vortex breakdown in a constricted pipe: Nonlinear steady states and weakly nonlinear asymptotic expansions,” *Physics of Fluids*, vol. 23, no. 8, p. 084102, 2011.
- [99] U. Lacis, N. Brosse, F. Ingremau, A. Mazzino, F. Lundell, H. Kellay, and S. Bagheri, “Passive appendages generate drift through symmetry breaking,” *Nature Communications*, vol. 5, 2014.
- [100] P. F. Fischer, J. W. Lottes, and S. G. Kerkemeier, “nek5000 Web page,” 2008. <http://nek5000.mcs.anl.gov>.
- [101] F. Hecht, “New development in freefem++,” *Journal of Numerical Mathematics*, vol. 20, no. 3-4, pp. 251–265, 2012.
- [102] T. A. Davis, “A column pre-ordering strategy for the unsymmetric-pattern multifrontal method,” *ACM Transactions on Mathematical Software*, vol. 30 (2), p. 165–195 available online from <http://www.cise.ufl.edu/research/sparse/umfpack/>, 2004.
- [103] M. R. Khorrami, “A chebyshev spectral collocation method using a staggered grid for the stability of cylindrical flows,” *International Journal for Numerical Methods in Fluids*, vol. 12, pp. 825–833, 1991.
- [104] R. B. Lehoucq, D. C. Sorensen, and C. Yang, “Arpack users’ guide: Solution of large-scale eigenvalue problems with implicitly restarted arnoldi methods,” 1998. SIAM, available online from <http://www.caam.rice.edu/software/ARPACK/>.
- [105] J. Marston, G. P. Chini, and S. M. Tobias, “Generalized quasilinear approximation: Application to zonal jets,” *Physical Review Letters*, vol. 116, p. 214501, 2016.
- [106] W. Rheingans, “Power swings in hydroelectric power plants,” *Transactions of the ASME*, vol. 62, no. 174, pp. 171–184, 1940.
- [107] E. Polak and G. Ribiere, “Note sur la convergence de méthodes de directions conjuguées,” *ESAIM: Mathematical Modelling and Numerical Analysis - Modélisation Mathématique et Analyse Numérique*, vol. 3, no. R1, pp. 35–43, 1969.
- [108] E. Polak, *Optimization Algorithms and Consistent Approximations*. Springer-Verlang New York, 1997.

-
- [109] E. Boujo and F. Gallaire, "Controlled reattachment in separated flows: a variational approach to recirculation length reduction," *Journal of Fluid Mechanics*, vol. 742, pp. 618–635, 2014.
- [110] S. Pasche, F. Gallaire, and F. Avellan, "Predictive control of part load vortex rope in Francis turbines," *Manuscript submitted for publication*, 2017.
- [111] T. Jacob, J. Prenat, and D. Maria, "Comportement dynamique d'une turbine Francis à forte charge. comparaisons modèle prototype," *La Houille Blanche* 3, vol. 3-4, pp. 293–300, 1988.
- [112] Y. Tsujimoto, Y. Yoshida, Y. Mackawa, S. Watanabe, and T. Hashimoto, "Observations of oscillating cavitation of an inducer," *Journal of Fluids Engineering*, vol. 119(4), pp. 775–781, 1997.
- [113] P. Dériaz, "A contribution to the understanding of flow in draft tubes of Francis turbines," in *International Association for Hydraulic Research, Hydraulic Machinery and Equipment Symposium, Nice, France*, 1960.
- [114] A. Müller, K. Yamamoto, S. Alligné, K. Yonezawa, Y. Tsujimoto, and F. Avellan, "Measurement of the self-oscillating vortex rope dynamics for hydroacoustic stability analysis," *Journal of Fluids Engineering*, vol. 138, no. 2, p. 021206, 2016.
- [115] P. Dörfler, "Modèle mathématique des oscillations excitées à charge partielle par la torche de cavitation dans les turbines Francis," in *Bulletin Escher Wyss No 1/2*, 1980.
- [116] R. Susan-Resiga, G. Ciocan, I. Anton, and F. Avellan, "Analysis of the swirling flow downstream a Francis turbine runner," *Journal of Fluids Engineering*, vol. 128, pp. 177–189, 2006.
- [117] P. Kuibin, V. Okulov, R. Resiga, and S. Muntean, "Validation of mathematical models for predicting the swirl flow and the vortex rope in a Francis turbine operated at partial discharge," in *Proceedings of the 25th IAHR Symposium on Hydraulic Machinery Systems, Timisoara, Roumania*, 2010.
- [118] R. Zhang, Q. Cai, J. Wu, Y. Wu, S. Liu, and L. Zhang, "The physical origin of severe low-frequency pressure fluctuations in giant Francis turbines," *Modern Physics Letters B*, vol. 19, no. 28 & 29, pp. 1527–1530, 2005.
- [119] M. Topor and D. Bristrian, "Localization of the most amplified perturbation in a vortex rope located in Francis turbine at partial discharge," in *AIP Conference Proceedings, Vol. 1493, pp. 1047–1053, Vienna, Austria*, 2012.
- [120] F. Pochyly, L. Cermak, P. Rudolf, V. Haban, and J. Koutnik, "Assessment of the steady swirling flow stability using amplitude- frequency characteristic," in *Proceedings of the 3rd IAHR International Meeting of the Workgroup on Cavitation and Dynamic Problems in Hydraulic Machinery and Systems, Brno, Czech Republic*, 2009.

Bibliography

- [121] Y. Egorov and F. Menter, “Development and application of sst-sas turbulence model in the desider project,” in *Second Symposium on the Hybrid RANS-LES Methods, Corfu, Greece*, 2007.
- [122] W. C. Reynolds and K. M. Hussain, “The mechanics of an organized wave in turbulent shear flow. part 3. theoretical models and comparisons with experiments,” *Journal of Fluid Mechanics*, vol. 54, pp. 263–288, 1972.
- [123] F. Viola, G. V. Iungo, S. Camarri, F. Porté-Agel, and F. Gallaire, “Prediction of the hub vortex instability in a wind turbine wake: stability analysis with eddy-viscosity models calibrated on wind tunnel data,” *Journal of Fluid Mechanics*, vol. 750, 2014.
- [124] C. Cossu, G. Pujals, and S. Depardon, “Optimal transient growth and very large-scale structures in turbulent boundary layers,” *Journal of Fluid Mechanics*, vol. 619, pp. 79–94, 2009.
- [125] J. C. Delàlamo and J. Jimenez, “Linear energy amplification in turbulent channels,” *Journal of Fluid Mechanics*, vol. 559, pp. 205–213, 2006.
- [126] F. Gallaire and J. Chomaz, “Instability mechanisms in swirling flows,” *Physics of Fluids*, vol. 15 (9), pp. 2622–2639, 2003.
- [127] T. Maxworthy and H. Liang, “An experimental investigation of swirling jets,” *Journal of Fluid Mechanics*, vol. 525, pp. 115–159, 2005.
- [128] S. Pasche, F. Gallaire, M. Dreyer, and M. Farhat, “Obstacle-induced spiral vortex breakdown,” *Experiments in Fluids*, vol. 55 (8), pp. 1–11, 2014.
- [129] O. Kirschner, A. Ruprecht, E. Gode, and S. Riedelbauch, “Experimental investigation of pressure fluctuations caused by a vortex rope in a draft tube,” in *Proceedings of the 26th IAHR Symposium on Hydraulic Machinery and Systems, Beijing, China, published in IOP Conference Series: Earth and Environmental Science*, vol. 15, 2012.
- [130] C. Landry, A. Favrel, A. Müller, C. Nicolet, and F. Avellan, “Local wave speed and bulk flow viscosity in Francis turbines at part load operation,” *Journal of Hydraulic Research*, vol. 54, no. 2, pp. 185–196, 2016.
- [131] A. I. Bosioc, R. Susan-Resiga, S. Muntean, and C. Tănasă, “Unsteady pressure analysis of a swirling flow with vortex rope and axial water injection in a discharge cone,” *Journal of Fluids Engineering*, vol. 134, no. 8, 2012.
- [132] L. Moody, “Moody,” Mar. 8 1932. US Patent 1,848,738.
- [133] C. Tănasă, R. Susan-Resiga, M. Sebastian, and A. I. Bosioc, “Flow-feedback method for mitigating the vortex rope in decelerated swirling flows,” *Journal of Applied Mechanics*, vol. 135, no. 6, 2013.

-
- [134] S. Alligné, *Forced and self oscillations of hydraulic systems induced by cavitation vortex rope of Francis turbines*. PhD thesis, EPFL, 2011.
- [135] T. Jacob, *Evaluation sur modèle réduit et prédiction de la stabilité de fonctionnement des turbines Francis*. PhD thesis, EPFL, 1993.
- [136] O. Pacot, C. Kato, Y. Guo, Y. Yamade, and F. Avellan, “Large eddy simulation of the rotating stall in a pump-turbine operated in pumping mode at a part-load condition,” *Journal of Fluids Engineering*, vol. 138, pp. 111102–11, 2016.
- [137] S. Wilhelm, G. Balarac, O. Métais, and C. Ségoufin, “Analysis of head losses in a turbine draft tube by means of 3d unsteady simulations,” *Flow, Turbulence and Combustion*, vol. 97, no. 4, pp. 1255–1280, 2016.
- [138] K. Oberleithner, M. Sieber, C. Nayeri, C. Petz, H.-C. Hege, R. R. Noack, and I. Wygnanski, “Three-dimensional coherent structures in a swirling jet undergoing vortex breakdown: stability analysis and empirical mode construction,” *Journal of Fluid Mechanics*, vol. 679, pp. 383–414, 2011.
- [139] O. Lucca-Negro and T. O’Doherty, “Vortex breakdown: a review,” *Progress in Energy and Combustion Science*, vol. 27, pp. 431–481, 2001.
- [140] J. M. Lopez, “On the bifurcation structure of axisymmetric vortex breakdown in a constricted pipe,” *Physics of Fluids*, vol. 6, no. 11, pp. 3683–3693, 1994.
- [141] P. Wulf, C. Egbers, and H. J. Rath, “Routes to chaos in wide-gap spherical couette flow,” *Physics of Fluids*, vol. 11, no. 6, pp. 1359–1372, 1999.
- [142] S. W. Morris, E. Bodenschatz, D. S. Cannell, and G. Ahlers, “Spiral defect chaos in large aspect ratio rayleigh-bénard convection,” *Physical Review Letters*, vol. 71, pp. 2026–2029, 1993.
- [143] D. Egolf, I. Melnikov, W. Pesch, and R. Ecke, “Mechanisms of extensive spatiotemporal chaos in rayleigh-benard convection,” *Nature*, vol. 404, pp. 733–736, 2000.
- [144] F. Sotiropoulos, Y. Ventikos, and T. Lackey, “Chaotic advection in three-dimensional stationary vortex-breakdown bubbles: sil’nikov’s chaos and the devil’s staircase,” *Journal of Fluid Mechanics*, vol. 444, pp. 257–297, 2001.
- [145] E. Serre and P. Bontoux, “Vortex breakdown in a three-dimensional swirling flow,” *Journal of Fluid Mechanics*, vol. 459, pp. 347–370, 2002.
- [146] J. M. Lopez, “Rotating and modulated rotating waves in transitions of an enclosed swirling flow,” *Journal of Fluid Mechanics*, vol. 553, p. 323–346, 2006.
- [147] J. Sorensen and E. Christensen, “Direct numerical simulation of rotating fluid flow in a closed cylinder,” *Physics of Fluids*, vol. 7, p. 764, 1995.

Bibliography

- [148] C. H. Amon, A. M. Guzmán, and B. Morel, “Lagrangian chaos, eulerian chaos, and mixing enhancement in converging–diverging channel flows,” *Physics of Fluids*, vol. 8, no. 5, pp. 1192–1206, 1996.
- [149] S. Newhouse, D. Ruelle, and F. Takens, “Occurrence of strange axiom a attractors near quasi periodic flows on tm , $m \geq 3$,” *Communications in Mathematical Physics*, vol. 64, no. 1, pp. 35–40, 1978.
- [150] M. J. Feigenbaum, “The metric universal properties of period doubling bifurcations and the spectrum for a route to turbulence,” *Annals of the New York Academy of Sciences*, vol. 357, no. 1, pp. 330–336, 1980.
- [151] Y. Pomeau and P. Manneville, “Intermittent transition to turbulence in dissipative dynamical systems,” *Communications in Mathematical Physics*, vol. 74, no. 2, pp. 189–197, 1980.
- [152] M. Frigo and S. G. Johnson, “The design and implementation of FFTW3,” *Proceedings of the IEEE*, vol. 93, no. 2, pp. 216–231, 2005. Special issue on “Program Generation, Optimization, and Platform Adaptation”.
- [153] J. Gollub and S. Benson, “Many routes to turbulent convection,” *Journal of Fluid Mechanics*, vol. 100, no. 3, p. 449–470, 1980.
- [154] K. Kashinath, I. Waugh, and M. Juniper, “Nonlinear self-excited thermoacoustic oscillations of a ducted premixed flame: bifurcations and routes to chaos,” *Journal of Fluid Mechanics*, vol. 761, p. 399–430, 2014.
- [155] L. Oteski, Y. Duguet, L. Pastur, and P. L. Quéré, “Quasiperiodic routes to chaos in confined two-dimensional differential convection,” *Phys. Rev. E*, vol. 92, p. 043020, 2015.
- [156] J.-P. Eckmann, “Roads to turbulence in dissipative dynamical systems,” *Reviews of Modern Physics*, vol. 53, pp. 643–654, 1981.
- [157] C. Grebogi, E. Ott, and J. Yorke, “Are three-frequency quasiperiodic orbits to be expected in typical nonlinear dynamical systems,” *Physical Review Letters*, vol. 51, pp. 339–342, 1983.
- [158] A. Pimenov, S. Slepneva, G. Huyet, and A. Vladimirov, “Dispersive time-delay dynamical systems,” *Physical Review Letters*, vol. 118, p. 193901, May 2017.

Simon Pasche

Ph.D in Mechanical Engineering

Born November 4th, 1986
Swiss citizenship
Impasse de la Combe 4,
1037 Etagnières,
simon.pasche@alumni.epfl.ch

Research interests

Flow instabilities, Vortex dynamics, Flow control, Asymptotic methods, Computational fluid dynamics.

Education

- 2013–2018 **PhD in Mechanical Engineering (EPFL)**, Research activity in the Laboratory for Hydraulic Machine (LMH) and in the Laboratory of Fluid Mechanics and Instabilities (LFMI) co-supervised by Prof. François Avellan and Prof. François Gallaire. Thesis title: “Dynamics and Optimal Control of Self-Sustained Instabilities in Laminar and Turbulent Swirling Flows: Application to the Part Load Vortex Rope in Francis Turbines”
- 2010–2012 **Master of Science MSc in Mechanical Engineering (EPFL)**, Specialization: fluid dynamics. Master thesis co-supervised by Dr. M. Farhat and Prof. F. Gallaire entitled: “Obstacle-induced spiral vortex breakdown”, published in Exp. Fluids
- 2006–2010 **Bachelor of Science in Mechanical Engineering at EPFL**
- 2002–2005 **Baccalauréat**, Gymnase d’Yverdon, orientation: math – physique

Work Experience

- 10th–12th Oct 2016 **Conference**, Aqua Media International Ltd, Publisher of Hydropower & Dams Journal. I assist the International Conference and Exhibition HYDRO 2016 as volunteer – Achievements, opportunities and challenges, Montreux, Switzerland, supervisor: Dr. L. Port
- 6th–10th Dec 2015 **Conference**, I assist in organizing the 9th International Symposium on Cavitation (CAV 2015), Lausanne, Switzerland, supervisor: Dr. M. Farhat
- Feb 2013–Oct 2013 **Scientific assistant in the Laboratory for Hydraulic Machine at EPFL**, writing of the SNSF proposal for my PhD studies and starting my PhD work, supervisor: Prof. Francois Avellan

- Oct2012–Jan2013: **Scientific assistant in the Laboratory of Fluid Mechanics and Instabilities at EPFL**, Continuation of my master project, ended with a publication in Exp. Fluids, supervisor: Prof. F. Gallaire & Dr. M. Farhat
- Aug2008–Sep2008: **Internship at Emile EGGER & Cie SA**, Swiss company active in the development and manufacture of pumps. Manufacturing a mechanical assembly by machining and acquisition of knowledge in the development and the manufacture of pumps, pump design steps, pump prototyping methods, wood modeling and stereolithography for casting
- Mar2006–Aug2006: **Military service in Swiss Armed Forces**, Soldier incorporated in Cp. EM. Bat. Car. 14
- Summers until 2012+ **Collaborator in family farm business**, worked in the family business which produces cereals and milk for Gruyère industry
- Aug2005–Feb2006:

Additional school and trainings

Transition to SLURM (for PBS users): course delivered by the HPC center of EPFL, 2014.

CATIA V8: course on the new feature in computer-aided design (CAO), 2015

ERCOFRAC Montestigliano Spring School, 17-23 April 2016, topic: “Reduced-order models for non-linear dynamics in fluid flows”, Montestigliano, Italy

Teaching and Student supervision

Teaching contributions:

Presentations in the Short Course on Hydraulic Machines Engineering, provided by the Laboratory for Hydraulic Machines (LMH) headed by Prof. F. Avellan., 2013-2017

Teaching assistant:

Mécanique des fluides incompressibles, Batchelor course in Mechanical Engineering at EPFL, 2013-2016, 4 semesters

Master thesis supervisor:

Shahab Eghbali: “Linear stability of spiral vortex breakdown in presence of a spherical object in constricted pipe”, 2017

Yves Pezzetta: “Mean flow of the oscillating cylinder”, 2016

Semester project supervisor:

Tutored four Master students at EPFL. Title of the project: “Optimal flapping and pitching motion of NACA airfoils for thrust generation”

Tutored one Master student at EPFL. Title of the project: “Automated meshing strategy for the design optimization of the counter-rotating runners of a microturbine”

Fellowship

SNSF grant N°200021 149818.1, 2013-2017, Current Phd thesis in Mechanical Engineering at EPFL, co-supervised by Prof. François Avellan and Prof. François Gallaire

Languages

French: native language

English: professional skills

German: A2 – TELC

Computer Skills

Math & Programming: C++, Fortran, Matlab, Octave

Analysis & Design: Fluent, Ansys, Gambit, Abaqus, Catia, NEK5000, Freefem++

Visualization & Plotting: Paraview, Visit

Drawing & Publishing: LaTeX, MS office, Adobe Illustrator

Membership

Member of the SCCER-SoE, Swiss competence center for energy research supply of electricity, since 2014

Member of the HYPERBOLE project, Hydropower plants performance and flexible operation towards lean integration of new renewable energies, ended Jan 2017

Reviewer for the 9th international symposium on cavitation (CAV 2015), Dec, 6-10, 2015, Lausanne, Switzerland

Publications

Peer-reviewed journal articles

Pasche S., Gallaire F., Dreyer M., Farhat M., **2014**, “Obstacle-induced spiral vortex breakdown“, Exp. Fluids, vol. 55, pp. 1784, doi: 10.1007/s00348-014-1784-7.

Pasche S., Avellan F., Gallaire F., **2017**, “Part load vortex rope as a global unstable mode”, J. Fluids Eng., vol. 139, pp. 051102, doi: 10.1115/1.4035640.

Papers submitted

Pasche S., Gallaire F., Avellan F., “Predictive control of spiral vortex breakdown”, **June 2017**, submitted in J. Fluid Mech.

Pasche S., Avellan F., Gallaire F., “Predictive control of part load vortex rope in Francis turbines”, **July 2017**, submitted in J. Fluids Eng.

Pasche S., Avellan F., Gallaire F., “Origin of the synchronous pressure fluctuations in the draft tube of Francis turbines operating at part load conditions“, **September 2017**, submitted in J. Fluids Struct.

Pasche S., Gallaire F., Avellan F., “Onset of chaos in helical vortex breakdown at low Reynolds number“, **October 2017**, submitted in Phys. Rev. Fluids.

Conferences contributed

Pasche S., Gallaire F., Avellan F., “Nonlinear optimal control of spiral vortex breakdown“, 11th European Fluid Mechanics Conference (EFMC11), Seville, Spain, September 13-16, 2016.

Pasche S., Gallaire F., Avellan F., “Onset of chaos in helical vortex breakdown at low Reynolds number“, 69th Annual Meeting of the APS Division of Fluid Dynamics, Portland, Oregon, USA, November 20-22, 2016.

Poster sessions

Pasche S., Gallaire F., Avellan F., “Stability analysis and optimal control of a Francis turbine vortex rope“, Poster session, SCCER-SoE annual conference, University of Neuchâtel, Neuchâtel, Switzerland, September 10-11, 2015.

Pasche S., Gallaire F., Avellan F., “Stability analysis and optimal control of a Francis turbine vortex rope“, Poster session, SCCER-SoE annual conference, HES-SO, Sion, Switzerland, September 12-13, 2016.

Pasche S., Gallaire F., Avellan F., “Extension of Francis Turbine Operating Conditions by Controlling the Part Load Vortex Rope“, Poster session, SCCER-SoE annual conference, WSL, Birmensdorf (ZH), Switzerland, September 14-15, 2017.

